

1-1-2011

Analytical and experimental investigations of ships impact interaction with one-sided barrier

Ihab M. Grace
Wayne State University,

Follow this and additional works at: http://digitalcommons.wayne.edu/oa_dissertations

Recommended Citation

Grace, Ihab M., "Analytical and experimental investigations of ships impact interaction with one-sided barrier" (2011). *Wayne State University Dissertations*. Paper 410.

This Open Access Dissertation is brought to you for free and open access by DigitalCommons@WayneState. It has been accepted for inclusion in Wayne State University Dissertations by an authorized administrator of DigitalCommons@WayneState.

**ANALYTICAL AND EXPERIMENTAL INVESTIGATIONS
OF SHIPS IMPACT INTERACTION WITH
ONE-SIDED BARRIER**

by

Ihab Mamdouh Fouad Grace

DISSERTATION

Submitted to the Graduate School of
Wayne State University,

Detroit, Michigan

in partial fulfillment of the requirements

for the degree of

DOCTOR OF PHILOSOPHY

2012

MAJOR: MECHANICAL ENGINEERING

Approved by:

Advisor

Date

COPYRIGHT BY

IHAB GRACE

2012

All Rights Reserved

DEDICATION

To my wife Amy, my daughter Hannah, expected son,
and my parents Mamdouh and Ragaa

ACKNOWLEDGMENTS

First, I would like to express my most profound gratitude to my adviser Professor Raouf Ibrahim for his excellent supervision and unwavering support throughout this work. His guidance, assistance, and encouragement led me to fulfill the greatest educational accomplishment, a doctoral degree. In fact, without Professor Ibrahim's insights and guidance, the technical content of this research would not have achieved its present depth. Also, I would like to thank Professor Victor Berdichevsky for his guidance and support. His vast knowledge helped me greatly in producing this work. I have learned a lot from him in Fundamentals of Mechanics, Fluid Dynamics, and Engineering Analysis.

I am expressing my deepest thanks to Professor Nabil Chalhoub for his continuous guidance, help, and encouragement. Special thanks to Professor Valery Pilipchuk for his endless patience and willingness to provide assistance. His guidance and advice helped me to continue this work. Professor Pilipchuk has offered many pertinent suggestions that helped in producing this work. Also, I would like to thank Professor Le Yi Wang for his help and support.

Kindly I wish to acknowledge all who are working in the machine shop of the Engineering College at Wayne State University for building the towing tank and the wave maker with high precision and professionalism.

Finally, every path of academic development has its darker moments. Those times were brightened by the confidence and support of my family.

This work was supported by a grant from Office of Naval Research (ONR) under Award No. N00014-05-1-0040.

2.2	Background and Terminology	36
2.3	Heave-Pitch-Roll Equations of Motion	41
2.3.1	Wave Motion Effects	47
2.3.2	Ships Roll Damping	49
2.3.3	Ship Inertia Forces and Moments	54
2.3.4	Governing Equations of Motion	55
2.3.4.1	Coupled Roll-Pitch Equations of Motion	57
2.3.4.2	Roll Equation of Motion	58
2.3.5	Memory Effect	60
2.4	Closing Remarks	62
Chapter 3	Elastic Impact of Ship Roll Motion with Solid Ice	63
3.1	Introduction	63
3.2	Modeling of Elastic Ice Impact Loading	63
3.3	Unperturbed Ship Dynamics	66
3.4	Ship Roll Motion under Sinusoidal Excitation	70
3.4.1	Excitation Amplitude as a Control Parameter	70
3.4.1.1	Excitation Frequency Ratio	70
3.4.1.2	Excitation Frequency Ratio	72
3.4.1.3	Excitation Frequency Ratio	74
3.4.1.4	Stability Fraction	75
3.4.2	Excitation Frequency as a Control Parameter	75
3.5	Closing Remarks	76
Chapter 4	Inelastic Impact of Ship Roll Dynamics with Soft Ice	96

4.1	Introduction	96
4.2	Constraint Eliminating Coordinate (Model 1)	97
4.2.1	Analytical Modeling	97
4.2.2	Numerical Simulation	99
4.3	Non-Smooth Coordinate-Velocity Transformation (Model 2)	118
4.3.1	Analytical Modeling	118
4.3.2	Numerical Simulation	120
4.4	Explicit Solution and validation of the Results	137
4.4.1	Runge-Kutta Method	137
4.4.2	Results and Discussion	139
4.5	Equivalent Viscous Damping Method	144
4.5.1	Derivation of the Equivalent Damping Term	144
4.5.2	Numerical Simulation	148
4.5.3	Validation of the Equivalent Damping Model Under Different Dynamic Conditions	156
4.5.3.1	Results and Discussion	157
4.5.4	Conclusions and Closing Remarks	160
Chapter 5	Experimental Investigation	169
5.1	Introduction	169
5.2	Ship Model	170
5.2.1	The Metacentric Height	170
5.2.2	Mass Moment of Inertia	171
5.2.3	Center of Gravity	172

5.3	Experimental Setup	176
5.3.1	Magnetic Angle Sensor	177
5.3.2	Resistive-Type Wave Gauge	177
5.4	Results and Discussion	185
5.5	Comparing Experimental Results to Analytical Solutions	205
5.5.1	Identification of the Model Parameters	206
5.5.1.1	Free Vibration Test	206
5.5.1.2	Nonlinear Restoring Moment Coefficients	207
5.5.1.3	Coefficient of Restitution	208
5.5.1.4	Forced Vibration Test	209
5.5.2	Numerical Simulation	210
5.6	Closing Remarks	210
Chapter 6	Conclusions and Recommendations for Future Work	215
Appendix A	219
Appendix B	224
References	227
Abstract	255
Autobiographical Statement	257

LIST OF FIGURES

Figure 1.1	Skematic sketch of the theoretical model by Matlock (1971).	17
Figure 1.2	Skematic sketch of theoretical model by Sodhi (1991)	17
Figure 1.3	Experimental data from indentation test carried out by Sodhi (1994)	18
Figure 1.4	Ice Floe-ship Impact by Aboulazm (1989)	23
Figure 1.5	Dependence of ratio of energy dissipated due to collision to initial kinetic energy on collision location of a supply vessel collides with a leg of a jack-up rig; Collision location is measured from the center of the ship (Pedersen and Zhang, 1998)	23
Figure 1.6	Spring-mass system with one sided barrier	29
Figure 1.7	Continuous representation of impact motion: (a) initial phase planer, and (b) auxiliary phase plane (Ivanov, 1994) .	29
Figure 2.1	Ship Schematic diagram showing the six degrees of freedom	36
Figure 2.2	(a) Possible locations of the metacenter and (b) the righting arm	40
Figure 2.3	Negative ship stability	40
Figure 2.4	Stability diagram	41
Figure 2.5	Ship schematic diagrams showing hydrostatic forces in a displaced position	46
Figure 3.1	Schematic diagram of one-sided barrier impact with ship in roll oscillation	65
Figure 3.2	(a) Restoring moment of the ship for the case of $q_i > 0$, and (b) Potential energy of the ship restoring moment in terms of Zhuravlev's non-smooth coordinate z	68
Figure 3.3	Phase portraits for $H = 0.11$ (impact orbit), $H = 0.0730283$ (Grazing impact), $H = 0.03$ (periodic oscillation)	69
Figure 3.4	The grazing orbit in Figure 3.3 divided into a huge number	

	of initial conditions	69
Figure 3.5	Section of time history response records for excitation frequency ratio $\nu = 0.88$, and excitation amplitude: (a) $a = 0.02$, (b) $a = 0.046$, (c) $a = 0.084$ (Chaotic), (d) $a = 0.094$ (Period four), (e) $a = 0.106$ (Period three), (f) $a = 0.11$ (Period seven)	78
Figure 3.6	FFT corresponding to the time history records of Figure 3.5 for excitation frequency ratio $\nu = 0.88$, and excitation amplitude: (a) $a = 0.02$, (b) $a = 0.046$, (c) $a = 0.084$ (Chaotic), (d) $a = 0.094$ (Period four), (e) $a = 0.106$ (Period three), (f) $a = 0.11$ (Period seven)	79
Figure 3.7	Phase portraits corresponding to the time history records of Figure 3.5 for excitation frequency ratio $\nu = 0.88$, and excitation amplitude: (a) $a = 0.02$, (b) $a = 0.046$, (c) $a = 0.084$ (Chaotic), (d) $a = 0.094$ (Period four), (e) $a = 0.106$ (Period three), (f) $a = 0.11$ (Period seven)	80
Figure 3.8	Poincaré maps corresponding to the time history records of Figure 3.5 for excitation frequency ratio $\nu = 0.88$, and excitation amplitude: (a) $a = 0.02$, (b) $a = 0.046$, (c) $a = 0.084$ (Chaotic), (d) $a = 0.094$ (Period four), (e) $a = 0.106$ (Period three), (f) $a = 0.11$ (Period seven)	81
Figure 3.9	Domains of attraction for different excitation amplitudes for excitation frequency $\nu = 0.88$: (a) $a = 0.04$, (b) $a = 0.096$, (c) $a = 0.10$, (d) $a = 0.112$, (e) $a = 0.116$, and (f) $a = 0.12$; Black region: bounded (safe) motion, and empty space: rollover dynamics	82
Figure 3.10	Bifurcation diagram for excitation frequency ratio $\nu = 0.88$. Period-one response, Modulated response, Multi - periodic response, Chaotic motion, and RM= Rollover Motion	83
Figure 3.11	Section of time history response records for excitation frequency ratio $\nu = 0.94$, and excitation amplitude: (a) $a = 0.008$, (b) $a = 0.04$ (period-two), (c) $a = 0.06$, (d) $a = 0.07$, (e) $a = 0.096$, and (f) $a = 0.12$ (period-three)	84
Figure 3.12	FFT corresponding to the time history records of Figure 3.11 for excitation frequency ratio $\nu = 0.94$, and excitation amplitude: (a) $a = 0.008$, (b) $a = 0.04$ (period-two), (c) $a = 0.06$, (d) $a = 0.07$, (e) $a = 0.096$, and (f) $a = 0.12$ (period-three)	85

Figure 3.13	Phase portraits corresponding to the time history records of Figure 3.11 for excitation frequency ratio $\nu=0.94$, and excitation amplitude: (a) $a=0.008$, (b) $a=0.04$ (period-two), (c) $a=0.06$, (d) $a=0.07$, (e) $a=0.096$, and (f) $a=0.12$ (period-three)	86
Figure 3.14	Poincaré maps corresponding to the time history records of Figure 3.11 for excitation frequency ratio $\nu=0.94$, and excitation amplitude: (a) $a=0.008$, (b) $a=0.04$ (period-two), (c) $a=0.06$, (d) $a=0.07$, (e) $a=0.096$, and (f) $a=0.12$ (period-three)	87
Figure 3.15	Domains of attraction for different excitation amplitudes for excitation frequency $\nu=0.94$; (a) $a=0.04$, (b) $a=0.072$, (c) $a=0.08$, (d) $a=0.088$, (e) $a=0.096$, and (f) $a=0.104$; Black region: bounded (safe) motion, and empty space: rollover (unsafe) motion	88
Figure 3.16	Bifurcation diagram for excitation frequency $\nu=0.94$. Period-one response, Period-one response experiencing impact, Period-two Response, Modulated response, Multi-periodic response, Chaotic motion, and RM= Rollover Motion	89
Figure 3.17	Section of time history response records for excitation frequency ratio $\nu=1.2$, and excitation amplitude: (a) $a=0.036$, and (b) $a=0.088$	90
Figure 3.18	FFT corresponding to the time history records of Figure 3.17 for excitation frequency ratio $\nu=1.2$, and excitation amplitude: (a) $a=0.036$, and (b) $a=0.088$	90
Figure 3.19	Phase portraits corresponding to the time history records of Figure 3.17 for excitation frequency ratio $\nu=1.2$, and excitation amplitude: (a) $a=0.036$, and (b) $a=0.088$	91
Figure 3.20	Poincaré maps corresponding to the time history records of Figure 3.17 for excitation frequency ratio $\nu=1.2$, and excitation amplitude: (a) $a=0.036$, and (b) $a=0.088$	91
Figure 3.21	Domains of attraction for different excitation amplitudes for excitation frequency $\nu=1.2$; (a) $a=0.04$, (b) $a=0.056$, (c) $a=0.064$, (d) $a=0.08$, (e) $a=0.104$, and (f) $a=0.12$; Black region: bounded (safe) motion, and empty space: rollover (unsafe) motion	92

Figure 3.22	Bifurcation diagram for excitation frequency $\nu = 1.2$. Period-one response, Period-one response experiencing impact, and RM= Rollover Motion	93
Figure 3.23	Dependence of stability fraction on excitation amplitude for three different values of excitation frequency $\nu = 0.88$, $\nu = 0.94$ and $\nu = 1.2$	93
Figure 3.24	Domains of attraction for different excitation frequencies for excitation amplitude $a = 0.08$: (a) $\nu = 0.6$, (b) $\nu = 0.92$, (c) $\nu = 0.96$, (d) $\nu = 1.0$, (e) $\nu = 1.12$, (f) $\nu = 1.2$, (g) $\nu = 1.28$, and (h) $\nu = 1.4$; Black region: bounded motion, and empty space: rollover motion	95
Figure 3.25	Amplitude versus excitation frequency diagram for excitation amplitude $a = 0.08$: Period-one response, Period-one response experiencing impact, Period-two Response, Modulated response, Multi - periodic response, Chaotic motion, and RM= Rollover Motion	95
Figure 4.1	Schematic diagram of one-sided ice barrier inelastic impact with ship in roll oscillation	104
Figure 4.2	Time History Records, FFT, Phase portraits, and Poincaré Maps for $\nu = 0.88$, and $a = 0.06$. Initial conditions $z_o = 0.01$, $z_o' = 0.01$ (a) Elastic impact $e = 1$, and (b) Inelastic impact (Model 1) $e = 0.8$	105
Figure 4.3	Time History Records, FFT, Phase portraits, and Poincaré Maps for $\nu = 0.88$, and $a = 0.06$. Initial conditions $z_o = 0.11$, $z_o' = -0.19$ (a) Elastic impact $e = 1$, and (b) Inelastic impact (Model 1) $e = 0.8$	106
Figure 4.4	Time History Records, FFT, Phase portraits, and Poincaré Maps for $\nu = 0.88$, and $a = 0.084$. Initial conditions $z_o = 0.15$, $z_o' = 0.31$. (a) Elastic impact $e = 1$, and (b) Inelastic impact (Model 1) $e = 0.8$	107
Figure 4.5	Time History Records, FFT, Phase portraits, and Poincaré Maps for $\nu = 0.88$, and $a = 0.084$. Initial conditions $z_o = 0.01$, $z_o' = 0.03$. (a) Elastic impact $e = 1$, and (b) Inelastic impact (Model 1) $e = 0.8$	108

Figure 4.6	Time History Records, FFT Phase portraits, and Poincaré Maps for $\nu=0.88$, and $a=0.104$. Initial conditions $z_o=0.01$, $z_o'=0.01$. (a) Elastic impact $e=1$, and (b) Inelastic impact (Model 1) $e=0.8$	109
Figure 4.7	Time History Records, FFT, Phase portraits, and Poincaré Maps for $\nu=0.88$, and $a=0.104$. Initial conditions $z_o=0.15$, $z_o'=-0.11$. (a) Elastic impact $e=1$, and (b) Inelastic impact (Model 1) $e=0.8$	110
Figure 4.8	Time History Records, FFT, Phase portraits, and Poincaré Maps for $\nu=0.88$, and $a=0.104$. Initial conditions $z_o=0.15$, $z_o'=0.09$. Elastic impact $e=1$, and (b) Inelastic impact (Model 1) $e=0.8$	111
Figure 4.9	Time History Records for $\nu=0.88$, and $a=0.104$. Initial conditions $z_o=0.65$, $z_o'=-0.23$; (a) Elastic impact $e=1$, and (b) Inelastic impact (Model 1) $e=0.8$	112
Figure 4.10	Domains of attraction for $\nu=0.88$, and $a=0.104$; Elastic impact $e=1$, and (b) Inelastic impact (Model 1) $e=0.8$: Black region: bounded (safe) motion, and empty space: rollover dynamics	112
Figure 4.11	Domains of attraction for different excitation amplitudes for $\nu=0.88$ as predicted by Model 1 for inelastic impact ($e=0.8$); (a) $a=0.08$, (b) $a=0.104$, (c) $a=0.12$, (d) $a=0.14$, (e) $a=0.16$, and (f) $a=0.18$; Black region: bounded (safe) motion, and empty space: rollover dynamics	113
Figure 4.12	Bifurcation diagram for $\nu=0.88$ as predicted by Model 1 for inelastic impact ($e=0.8$); Period-one response, Modulated response, Multi - periodic response, Chaotic motion, and RM= Rollover	114
Figure 4.13	Domains of attraction for different excitation amplitudes for $\nu=0.94$ as predicted by Model 1 for inelastic impact ($e=0.8$); (a) $a=0.04$, (b) $a=0.072$, (c) $a=0.08$, (d) $a=0.088$, (e) $a=0.096$, and (f) $a=0.104$; Black region: bounded (safe) motion, and empty space: rollover	

	dynamics	115
Figure 4.14	Bifurcation diagram for $\nu = 0.94$ as predicted by Model 1 for inelastic impact ($e = 0.8$); Period-one response, Period-one response experiencing impact, Period-two Response, Modulated response, Multi - periodic response, Chaotic motion, and RM= Rollover	116
Figure 4.15	Domains of attraction for different excitation amplitudes for $\nu = 1.2$ as predicted by Model 1 for inelastic impact ($e = 0.8$); (a) $a = 0.04$, (b) $a = 0.064$, (c) $a = 0.096$, (d) $a = 0.104$, (e) $a = 0.12$, and (f) $a = 0.136$; Black region: bounded (safe) motion, and empty space: rollover dynamics	117
Figure 4.16	Bifurcation diagram for $\nu = 1.2$ as predicted by Model 1 for inelastic impact ($e = 0.8$); Period-one response, Period-one response experiencing impact, and RM= Rollover	118
Figure 4.17	Ship time history records, FFT plots, phase portraits, and Poincaré Maps according to (a) Model 1, and (b) Model 2 for $\nu = 0.88$, $a = 0.084$, $e = 0.8$, and initial conditions $z_0 = 0.01$, $z'_0 = 0.01$	127
Figure 4.18	Ship time history records, FFT plots, phase portraits, and Poincaré Maps according to (a) Model 1, and (b) Model 2 for $\nu = 0.88$, $a = 0.12$, $e = 0.8$, and initial conditions $z_0 = 0.01$, $z'_0 = 0.01$	128
Figure 4.19	Ship time history records, FFT plots, phase portraits, and Poincaré Maps according to (a) Model 1, and (b) Model 2 for $\nu = 0.88$, $a = 0.12$, $e = 0.8$, and initial conditions $z_0 = 0.01$, $z'_0 = 0.03$	129
Figure 4.20	Ship time history records, FFT plots, phase portraits, and Poincaré Maps according to (a) Model 1, and (b) Model 2 for $\nu = 0.88$, $a = 0.12$, $e = 0.8$, and initial conditions $z_0 = 0.19$, $z'_0 = 0.13$	130
Figure 4.21	Domains of attraction according to (a) Model 1, and (b) Model 2 for $\nu = 0.88$, $a = 0.12$, $e = 0.8$, Black region: bounded (safe) motion, and empty space: rollover	

	dynamics	130
Figure 4.22	Domains of attraction for different excitation amplitudes for $\nu=0.88$ as predicted by Model 2 for inelastic impact ($e=0.8$); (a) $a=0.08$, (b) $a=0.128$, (c) $a=0.14$, (d) $a=0.16$, (e) $a=0.18$, and (f) $a=0.22$; Black region: bounded (safe) motion, and empty space: rollover dynamics	131
Figure 4.23	Bifurcation diagram for $\nu=0.88$ as predicted by Model 2 for inelastic impact ($e=0.8$); Period-one response, Modulated response, Multi - periodic response, and RM= Rollover Motion	132
Figure 4.24	Safety factor diagram for excitation frequency $\nu=0.88$; Purely elastic impact ($e=1$), and inelastic impact ($e=0.8$); Model 1 and Model 2	132
Figure 4.25	Domains of attraction for different excitation amplitudes for $\nu=0.94$ as predicted by Model 2 for inelastic impact ($e=0.8$); (a) $a=0.088$, (b) $a=0.096$, (c) $a=0.104$, (d) $a=0.12$, (e) $a=0.128$, and (f) $a=0.136$; Black region: bounded (safe) motion, and empty space: rollover dynamics	133
Figure 4.26	Bifurcation diagram for $\nu=0.94$ as predicted by Model 2 for inelastic impact ($e=0.8$); Period-one response, Period-one response experiencing impact, Period-two response, Multi - periodic response, and RM= Rollover Motion	134
Figure 4.27	Safety factor diagram for excitation frequency $\nu=0.94$; Purely elastic impact ($e=1$), and inelastic impact ($e=0.8$); Model 1, and Model 2	134
Figure 4.28	Domains of attraction for different excitation amplitudes for $\nu=1.2$ as predicted by Model 2 for inelastic impact ($e=0.8$); (a) $a=0.04$, (b) $a=0.096$, (c) $a=0.104$, (d) $a=0.12$, (e) $a=0.136$, and (f) $a=0.144$; Black region: bounded (safe) motion, and empty space: rollover dynamics	135

Figure 4.29	Bifurcation diagram for $\nu = 1.2$ as predicted by Model 2 for inelastic impact ($e = 0.8$); Period-one response, Period-one response experiencing impact, and RM= Rollover Motion . .	136
Figure 4.30	Safety factor diagram for excitation frequency $\nu = 1.2$; Purely elastic impact ($e = 1$), and inelastic impact ($e = 0.8$); Model 1, and Model 2	136
Figure 4.31	Estimates for stability boundaries due ship elastic impact ($e = 1$), and inelastic impact ($e = 0.8$) as predicted by Model 1 and Model 2. Unbounded motion is shown by grey area . .	137
Figure 4.32	(a) Amplitude history record, and (b) Velocity history record for $\nu = 0.88$, $a = 0.12$ and $e = 1$. Initial conditions $z_o = 0.2$, $z_o' = 0.0$	141
Figure 4.33	(a) Amplitude history record, and (b) Velocity history record for $\nu = 0.88$, $a = 0.12$ and $e = 0.9$. Initial conditions $z_o = 0.2$, $z_o' = 0.0$	142
Figure 4.34	(a) Amplitude history record, and (b) Velocity history record for $\nu = 0.88$, $a = 0.12$ and $e = 0.8$. Initial conditions $z_o = 0.2$, $z_o' = 0.0$	143
Figure 4.35	Typical response of ship roll experiencing impact with a barrier	150
Figure 4.36	(a) Amplitude history record, (b) Velocity history record, and (c) Phase Plot for $q_i = -0.2$, $\nu = 1.2$, $a = 0.08$, $z_o = 0.01$, $z_o' = 0.01$, and $e = 0.9$	151
Figure 4.37	(a) Amplitude history record, (b) Velocity history record, and (c) Phase Plot for $q_i = -0.2$, $\nu = 1.2$, $a = 0.08$, $z_o = 0.01$, $z_o' = 0.01$, and $e = 0.8$	152
Figure 4.38	(a) Amplitude history record, (b) Velocity history record, and (c) Phase Plot for $q_i = -0.2$, $\nu = 1.2$, $a = 0.08$, $z_o = 0.01$, $z_o' = 0.01$, and $e = 0.7$	153
Figure 4.39	(a) Amplitude history record, (b) Velocity history record, and	

	(c) Phase Plot for $q_i = -0.2$, $v = 1.2$, $a = 0.08$, $z_o = 0.01$, $z_o' = 0.01$, and $e = 0.6$	154
Figure 4.40	(a) Amplitude history record, (b) Velocity history record, and (c) Phase Plot for $q_i = -0.2$, $v = 1.2$, $a = 0.08$, $z_o = 0.01$, $z_o' = 0.01$, and $e = 0.6$	155
Figure 4.41	Amplitude history record for $q_i = -0.2$, $v = 1.2$, $a = 0.08$, $z_o = 0.01$, $z_o' = 0.01$ and $e = 0.998$	162
Figure 4.42	Total Energy for $q_i = -0.2$, $v = 1.2$, $a = 0.08$, $z_o = 0.01$, $z_o' = 0.01$ and $e = 0.998$	162
Figure 4.43	Amplitude history record for $q_i = -0.2$, $v = 1.2$, $a = 0.08$, $z_o = 0.01$, $z_o' = 0.01$ and $e = 0.995$	163
Figure 4.44	Total Energy for $q_i = -0.2$, $v = 1.2$, $a = 0.08$, $z_o = 0.01$, $z_o' = 0.01$ and $e = 0.995$	163
Figure 4.45	Amplitude history record for $q_i = -0.3$, $v = 0.8$, $a = 0.08$, $z_o = 0.01$, $z_o' = 0.01$, and $e = 0.90$	164
Figure 4.46	Total Energy for $q_i = -0.3$, $v = 0.8$, $a = 0.08$, $z_o = 0.01$, $z_o' = 0.01$, and $e = 0.90$	164
Figure 4.47	Error involved in equivalent damping method as a function of excitation frequency ratio v and coefficient of restitution e for $a = 0.08$, $z_o = 0.01$, $z_o' = 0.01$, and $q_i = -0.1$	165
Figure 4.48	Error involved in equivalent damping method as a function of excitation frequency ratio v and coefficient of restitution e for $a = 0.08$, $z_o = 0.01$, $z_o' = 0.01$, and $q_i = -0.2$	165
Figure 4.49	Error involved in equivalent damping method as a function of excitation frequency ratio v and coefficient of restitution e for $a = 0.08$, $z_o = 0.01$, $z_o' = 0.01$, and $q_i = -0.3$	166

Figure 4.50	Error involved in equivalent damping method as a function of excitation frequency ratio ν and coefficient of restitution e for $a = 0.08$, $z_o = 0.01$, $z_o' = 0.01$, and $q_i = -0.4$	166
Figure 4.51	Contour Plot for error involved in equivalent damping method for $a = 0.08$, $z_o = 0.01$, $z_o' = 0.01$, and $q_i = -0.1$: (a) $e = 0.9-1.0$, (b) $e = 0.99-1.0$	167
Figure 4.52	Contour Plot for error involved in equivalent damping method for $a = 0.08$, $z_o = 0.01$, $z_o' = 0.01$, and $q_i = -0.2$: (a) $e = 0.9-1.0$, (b) $e = 0.99-1.0$	167
Figure 4.53	Contour Plot for error involved in equivalent damping method for $a = 0.08$, $z_o = 0.01$, $z_o' = 0.01$, and $q_i = -0.3$: (a) $e = 0.9-1.0$, (b) $e = 0.99-1.0$	168
Figure 4.54	Contour Plot for error involved in equivalent damping method for $a = 0.08$, $z_o = 0.01$, $z_o' = 0.01$, and $q_i = -0.4$: (a) $e = 0.9-1.0$, (b) $e = 0.99-1.0$	168
Figure 5.1	The ship model used in the experiments and its dimensions (dimensions are in mm)	174
Figure 5.2	Inclination experiment to determine the metacentric height.	175
Figure 5.3	Determination of the vertical position of center of gravity of the ship model	175
Figure 5.4	Determination of the longitudinal position of the center of gravity of the ship model	175
Figure 5.5	Block diagram showing the experiment layout	180
Figure 5.6	A front view of the towing tank showing the tank, wave absorber, and the wave maker	181
Figure 5.7	The ship model showing the installed axle about which the model is restricted to roll against the one-sided barrier shown on the right side	182
Figure 5.8	A side view of the towing tank showing the wave maker and the resistive-type wave gauge	182

Figure 5.9	Calibration curve of the magnetic angle sensor	183
Figure 5.10	Schematic diagram for the electric circuit of the resistive-type wave gauge	184
Figure 5.11	Calibration curve of the wave gauge. Experimental data, and Fitting straight line	185
Figure 5.12	Free surface wave at wave maker motor speed $N_m = 2.4$ rad/s : (a) time history record of the water free surface, (b) magnification of few cycles showing the wave profile, and (c) FFT plot	191
Figure 5.13	Measured time history records of the model response under motor speed $N_m = 2.4$ rad/s : (a) in the absence of barrier, (b) in the presence of one-sided barrier at -40° , (c) at -30° , (d) at -20° , (e) at -10°	192
Figure 5.14	FFT plots of the model response of Figure 5.13. under motor speed $N_m = 2.4$ rad/s : (a) in the absence of barrier, (b) in the presence of one-sided barrier at -40° , (c) at -30° , (d) at -20° , (e) at -10°	193
Figure 5.15	Phase trajectory projections of the model response of Figure 5.13 under motor speed $N_m = 2.4$ rad/s : (a) in the absence of barrier, (b) in the presence of one-sided barrier at -40° , (c) at -30° , (d) at -20° , (e) at -10°	194
Figure 5.16	Free surface wave at wave maker motor speed $N_m = 2.8$ rad/s : (a) time history record of the water free surface, (b) magnification of few cycles showing the wave profile, and (c) FFT plot	195
Figure 5.17	Measured time history records of the model response under motor speed $N_m = 2.8$ rad/s : (a) in the absence of barrier, (b) in the presence of one-sided barrier at -40° , (c) at -30° , (d) at -20° , (e) at -10°	196
Figure 5.18	FFT plots of the model response shown in Figure 5.17 under motor speed $N_m = 2.8$ rad/s : (a) in the absence of barrier, (b) in the presence of one-sided barrier at -40° , (c) at -30° , (d) at -20° , (e) at -10°	197

Figure 5.19	Phase trajectory projections of the model response shown in Figure 5.17 under motor speed $N_m = 2.8$ rad/s : (a) in the absence of barrier, (b) in the presence of one-sided barrier at -40° , (c) at -30° , (d) at -20° , (e) at -10°	198
Figure 5.20	Morlet wavelet plots of the model response shown in Figure 5.16 under motor speed $N_m = 2.8$ rad/s : (a) in the absence of barrier, (b) in the presence of one-sided barrier at -40° , (c) at -30° , (d) at -20° , (e) at -10° , and (f) shows the quasi period versus scale relationship.	199
Figure 5.21	Free surface wave at wave maker motor speed $N_m = 2.2$ rad/s : (a) time history record of the water free surface, (b) magnification of few cycles showing the wave profile, and (c) FFT plot	200
Figure 5.22	Measured time history records of the model response under motor speed $N_m = 2.2$ rad/s : (a) in the absence of barrier, (b) in the presence of one-sided barrier at -40° , (c) at -30° , (d) at -20° , (e) at -10°	201
Figure 5.23	FFT plots of the model response of Figure 5.22. under motor speed $N_m = 2.2$ rad/s : (a) in the absence of barrier, (b) in the presence of one-sided barrier at -40° , (c) at -30° , (d) at -20°	202
Figure 5.24	Phase trajectory projections of the model response of Figure 5.22 under motor speed $N_m = 2.2$ rad/s : (a) in the absence of barrier, (b) in the presence of one-sided barrier at -40° , (c) at -30° , (d) at -20°	203
Figure 5.25	Phase trajectory projections of the model response of Figure 5.22(e) under motor speed $N_m = 2.2$ rad/s in the presence of one-sided barrier at -10°	204
Figure 5.26	%Reduction in response amplitude vs. impact angle. Black: $N_m = 2.4$ rad/s , and Gray: $N_m = 2.8$ rad/s	204
Figure 5.27	Dry friction damping term	211
Figure 5.28	Free vibration test result	211

Figure 5.29	Dependence of the coefficient of restitution on the impact velocity (with the fitting curve is $e = \text{Exp}\{-0.209 \dot{\phi}_- - 0.0296 \dot{\phi}_- ^2\}$)	212
Figure 5.30	FFT of excitation waves corresponding to Experimental record, and Fourier series representation.	212
Figure 5.31	Comparison between measured and predicted time-history record of ship response for $N_m = 2.4$ rad/s and different barrier positions, experimental measurement, and numerical simulation	213
Figure 5.32	Comparison between measured and predicted results FFT of ship time history responses shown in Fig. 13 for $N_m = 2.4$ rad/s and different values of barrier position. Experimental measurement and numerical simulation	214
Figure A.1	Key parts of a ship structure	223
Figure A.2	Definition of incident wave directions	223

NOMENCLATURE

- a = the excitation amplitude.
- a = nonlinear damping coefficient.
- B = damping moment.
- e = the coefficient of restitution.
- J_{xx} = the ship mass moment of inertia about roll axis.
- J_{yy} = the ship mass moment of inertia about pitch axis.
- $K_{\dot{\phi}}$ = the hydrodynamic added polar mass moment of inertia about the ship roll axis.
- $K_{\dot{\theta}}$ = the hydrodynamic added polar mass moment of inertia about the ship pitch axis.
- M_x = restoring moment of roll.
- $M_{\ddot{z}}$ = added inertia in pitch due to heave motion.
- q = non-dimensional roll angular displacement of the ship.
- q_i = non-dimensional angle of impact.
- W = the weight of water of displaced volume of the ship (equals to the weight of the ship).
- z = heave displacement of the ship.
- $Z_{\ddot{z}}$ = the hydrodynamic added mass in heave.
- $Z_{\dot{\theta}}$ = the hydrodynamic added inertia in heave due to pitch motion.
- δv = the difference in the submerged volume of the ship.

- $\bar{\zeta}$ = the linear damping ratio.
- ξ = the wave excitation.
- θ = pitch angular displacement of the ship.
- ν = the excitation frequency ratio.
- ϕ = roll angular displacement of the ship.
- ϕ_c = the roll capsize angle.
- ϕ_i = angle of impact.
- Φ = the beam sea hydrodynamic wave excitation moment.
- ω_n = the ship linear roll natural frequency.
- Ω = the roll excitation frequency.

CHAPTER 1

HISTORICAL ASSESSMENT OF SHIP-ICE INTERACTION

1.1 Motivation and Introduction

It has been a great challenge for ships navigating in arctic regions since it may experience impact with icebergs or ice floes. The Institute for Ocean Technology in Canada has reported more than 560 accidents of ship ice collisions¹ in the North Atlantic off Newfoundland and Labrador. In general, impact of ships with rigid or flexible barriers is an important factor to ship damage and is responsible for over half of all ship losses (Pedersen et al., 1996). For this reason there is continuing interest in ship-ice impact analyses despite the great complexity of the subject, which arises from the complexity of mathematical models. Studying the dynamics of interaction of ships with ice opens doors towards achieving the national interests in Arctic regions.

One of the major goals of the navy, ship builders and the US Coast Guard is to improve their ships' capability to navigate under different and severe environmental conditions. In arctic regions, considerable forces due to ice impact may result when an arctic vessel strikes an ice sheet or iceberg. The loads during interaction with ice become a major factor in the ships design process. The impact arises when drifting ice sheets, and ice floes and icebergs are moving with considerable speed under the action of environmental conditions, or when a moving ship strikes a stationary or moving ice feature. When collision occurs between an ice feature and a ship or offshore structure, the force of impact is irregular, random and

¹ <http://www.icedata.ca/index.php>

contains repetitive fluctuations. The random fluctuations are due to random variations of ice properties as well as ice failure at random locations along the contact area (Cammaert and Muggeridge, 1988).

Ice forces vary with time according to the resistance of the ice sheet. A typical cycle of ice force consists of gradual increase in the force until the ice sheet breaks, under which there is a sudden drop in the force. A new cycle begins when a new contact with another undamaged ice sheet occurs. This cycle may cause the offshore structure to vibrate at its natural frequency, resulting in a complicated ice-structure interaction.

One should note that the formulation of a collision theory for a ship striking a massive ice body is typically divided into two independent problems. One concerns the local structure damage, while the second involves the computation of global response. This separation corresponds to a parallel expression in the classical theory of ship collision dynamics dating from Minorski (1959). The literature shows considerable amount of work addressing the first problem, meanwhile, little work has been done in the area of computation of global response. There is a great importance to study the ship response or ocean structure when it experiences impact with an ice body. The response may exceed the physical acceptable levels for passengers and staff, and sometimes impact may lead to catastrophic results. This study pays particular attention to the response of ships experiencing impact with stationary icebergs and platforms.

This Chapter presents an overview of ship-ice interaction including its analytical modeling. The chapter is organized as follows: Section 1.2 addresses

icebergs and their classification, the problem of ice interaction with ships is described in Section 1.3 including different models of ice-structure interaction and ice loads. Section 1.4 presents an overview of vibro-impact systems and its analytical modeling. The scope of the present work is presented in Section 1.5.

1.2 Icebergs and their Classification

An iceberg is a large piece of freshwater ice that has broken off from a snow-formed glacier or ice shelf and is floating in open water. It may subsequently become frozen into pack ice. Alternatively, it may come to rest on the seabed in shallower water, causing ice scour (also known as ice gouging) or becoming an ice island. The word "iceberg" is from Dutch *ijsberg*, literally meaning "*ice mountain*", cognate to Danish *Isbjerg*. Icebergs are often referred to simply as "bergs". Because the density of pure ice is about 920 kg/m^3 , and that of sea water about 1025 kg/m^3 , typically only one-tenth of the volume of an iceberg is above water. The shape of the underwater portion can be difficult to judge by looking at the portion above the surface. This has led to the expression "*tip of the iceberg*", generally applied to a larger problem or difficulty, meaning that the visible trouble is only a small manifestation of a larger problem. Ralph et al. (2008) documented iceberg data during experiments near the northeast coast of Newfoundland including above water dimensions and underwater profiles. The total lengths of icebergs were in the range of 4-73 meters, with estimated masses of 21-22,000 tonnes. Generally, icebergs may range from 1 to 75 meters above sea level and weigh 20,000 to 2 million tons. Although most icebergs spent their entire life in polar zones, some are moved under the action of wind and

water currents to more temperate regions where they present a serious threat to ships and offshore structures. Motion of icebergs and factors affecting the speed were studied by Gaskill and Rochester (1984).

The International Ice Patrol² has established two useful schemes for iceberg classification. First classification system is based on the above-water shapes of icebergs. The classification includes:

- *Tabular*: horizontal or flat-topped with length to height ratio less than 5:1.
- *Blocky*: flat-topped with vertical sides.
- *Doomed*: round-topped.
- *Wedged*: vertical on one side and sloping on the other.
- *Pinnacled*: contains one or more large spires.

The second classification established by International Ice Patrol is based on iceberg size. It includes the following categories:

- *Growler*: A mass of glacial ice has calved from a berg, extends less than 1.5 m above water and has a water plane area around 20 m².
- *Bergy-bit*: A larger piece of floating glacier ice, height above water is in the range of 1.5-5 m and has a water plane area less than 300 m².
- *Iceberg*: A massive piece of glacier ice, with a height of more than 5 m and water plane area more than 300 m². Large icebergs have a height of 120 m above water-plane, and their masses are greater than 2 million tonnes.

² <http://www.uscg.mil/LANTAREA/IIP>

Glacial ice exhibits a wide range of mechanical properties depending upon strain rate, temperature, density, and grain size. The properties may also change during the life of the iceberg as a result of formation of internal cracks induced by mechanical and thermal stresses. El-Tahan et al. (1984) recorded values of 7.43 MPa and 5.04 GPa for unconfined compressive strength and Young's modulus of elasticity, respectively. Moreover, the strength of ice is affected by the temperature variation within the iceberg. Jones (2007) recorded a variation of uniaxial compressive strength from 5 MPa at $0 \text{ }^{\circ}\text{C}$, at water ice interface, to 8.5 MPa at $-20 \text{ }^{\circ}\text{C}$, 10-20 m inside iceberg. Also, it should be noted that the compressive strength of ice is dependent on strain rate and grain size (see Jones, 2007).

1.3 Ice Interaction with Ships

A moving ship against an ice sheet or iceberg exerts a force on the ice and the ice in turn, reacts with a force on the ship. The interaction between the two systems involves energy sharing in the form of ship oscillation and ice crushing. At a critical value of strain rate, the ice crushing strength decreases as the strain rate increases. This decrease in the crushing strength results in negative damping that may induce self-excited vibration. The concept of negative damping due to decreasing ice crushing strength was introduced by Blenkran (1970), Määttänen (1978, 1980, 1981 & 1983). The physical process involved in the interaction of ice masses with offshore structures including fracturing spalling, extrusion, and high pressure zone formation (most of the force is transmitted through small areas

termed as high pressure zones) are described in details by Jordaan (2001). Ibrahim et al. (2007) published a comprehensive review article on the interaction of ships and ocean structures with ice. The review also addresses the ship controls.

Croasdale and Marcellus (1981) described three stages during the interaction between a large ice feature and a structure. In the first stage, the ice feature slows down as the structure absorbs its momentum. Once the feature has stopped, the surrounding pack ice continues to move against it by stage two and three of interaction. Stage two involves ridge building behind ice feature, while stage three involves pack-ice drag on stationary rubble. These three stages are associated with two forces:

- *Limit-Momentum Load*: defined as the load required bringing the ice feature to stop after it impacts with the structure. It is the maximum force associated with stage one. It is the product of the maximum width of contact, the local ice thickness and the effective ice pressure. It should be noted here that the dimensions of the contact zone are significantly influenced by the initial kinetic energy of the ice feature.
- *Limit-Force Load*: defined as the maximum force associated with stages two and three, and governed by driving forces associated with ridge-building pressures exerted on an ice feature in contact with a structure and the drag forces on the feature caused by currents and winds. Usually limit-force loads are substantially less than the limit-momentum loads.

1.3.1 ICE IMPACT LOADS

For a designer or an engineer, choosing a design ice load has always been a challenge due to the uncertainties of ice loads. Sunder (1986) provided five principal areas of uncertainty; the mechanical properties of ice, analysis methods, interface modeling of contact forces, scale effects, and environmental factors as salt content and temperature. Zou (1996) showed that ice loads are highly localized within high pressure regions termed critical zones. These critical zones are formed due to fracture spilling during ice-structure interaction. A probability distribution of ice loads was estimated by probabilistic modeling of critical zones. Zou (1996) proposed a design curve for the estimation of extreme ice loads.

A considerable amount of research has been conducted to understand the process of impact damage initiation and growth along with the identification of impact governing parameters. The basic morphology of impact damage, its development and the parameters affecting its initiation, growth and final size are well documented by Arbate (1998). Ship hulls made of composite materials that are subjected to repeated ice impacts can experience damage consisting of delamination, matrix cracking, and fiber failure. Furthermore, it was reported that the delamination area increases linearly with the Kinetic energy of ice impacting the ship hull. Croasdale and Marcellus (1981) classified the occurrence of ice forces in two ways:

- A large ice sheet or pack ice moving and crushing against a structure, causing continuously repetitive ice force fluctuations known as *Ice Floe Impact Loads*.

- A single ice feature moving at a reasonably high velocity, causing a short-term transient loading known as *Iceberg Impact Loads*.

These two types of ice impact forces are discussed in the next subsections.

1.3.1.1 Ice Floe Impact Loads

As an ice floe moves against a structure, an initial impact occurs. This initial collision energy is absorbed by the structure itself. As the ice continues to move steadily or around the structure, the problem reduces to a quasistatic situation. The area of contact after collision depends on the size of the structure and the average thickness of the ice. Large transverse dimension of a structure relative to ice geometry results in local forces on the structure and ice failure. Small structural dimensions ensure an indentation mode of ice failure, which results in higher local and average forces on the structure (Cammaert, and Muggeridge 1988). Cammaert and Tsinker (1981) suggested that the impact scenario may be approximately modeled by neglecting the time-varying effects and selecting constant values of ice strength for the duration of impact. Since strain rate and contact geometry change significantly during impact, selection of the proper constants is difficult, and the effects of foundation on structural stability cannot be considered in the analysis.

Kreider (1984) presented a numerical time-domain solution for ice-floe impact in which the predominant ice-failure mode is crushing. For this model, the force exerted on a structure during impact is determined by solving the equation of motion for the floe. Ice failure was assumed to occur at the ice-structure contact. For a

direct, head-on collision, the equation of motion was written in the form (Kreider, 1984):

$$(M_i + m_i)\ddot{x} = F_c + F_w + F_a \quad (1.1)$$

where, M_i is the mass of ice floe, m_i is the added mass of floe, \ddot{x} is the acceleration of ice floe, F_c is the ice crushing force; is a function of x and \dot{x} ; displacement and velocity of ice floe, respectively. F_w is the water drag on floe and F_a is the wind drag on floe. Generally speaking, F_w and F_a are much smaller than F_c , and, when the added mass is small, equation (1.1) can be simplified to

$$M_i\ddot{x} = F_c(x, \dot{x}) \quad (1.2)$$

Bhat (1988) studied the impact ice loading and the phenomenon of floe splitting as a consequence of initiation and propagation of radial cracks in the impacting floe. It was shown that the splitting load or the fracture limit load may be reached relatively early in the radial crack propagation process, such as when the crack length is a small fraction of the floe size. Subsequently, the crack can propagate dynamically, splitting the floe into pieces and consequently, the load on the structure will fall.

Luk (1984) presented a theoretical analysis of an in-plane ice structure vibration problem due to a circular cylinder structure moving in the plane of an infinite ice sheet. The ice forces exerted on the structure as the motion occurs were estimated. The approach developed based on two-dimensional elastic wave theory. The results provide measures of ice sheet resistance to dynamic motion of structures surrounded by floating ice sheets of infinite extent. Vinogradov (1986)

described a methodology for the simulation of a non-steady random process of the interaction of ice floes with a vessel. The equations of motion are developed for a ship mooring in broken ice and interacting with a cluster of small floes having both variable mass and geometry.

1.3.1.2 Iceberg Impact Loads

The collision of an iceberg with a semi- submersible was modeled by Cammaert et al. (1983) by a single-degree-of-freedom system to allow a preliminary analysis of platform motions. The equation of motion was given by

$$M\ddot{x} + c\dot{x} + kx = F \quad (1.3)$$

where M is the mass of the platform and includes an added hydrodynamic mass, c is the damping coefficient and represents the viscous drag caused by the relative motion of the platform and the surrounding water, F is the impact force and k is the stiffness of the system. This model has a number of shortcomings. For example, the the impact force is required for the analysis. Also, only head-on collisions can be considered. To overcome these problems, Cammaert et al. (1983) and Curtis et al. (1984) developed several computer models to solve the equations of motion for a two-mass system to predict the collision force as a function of time as a direct outcome of the analysis. The interaction of ice floes with a rigid structure was modeled. All motions were restricted to the water-plane (i.e. surge, sway and yaw). The linearized equations of motion for the iceberg and platform anchored to the seabed were given by

$$\mathbf{M}_1\ddot{\mathbf{X}}_1 + \mathbf{C}_1\dot{\mathbf{X}}_1 = \mathbf{F}_1, \quad (1.4a)$$

$$\mathbf{M}_2 \ddot{\mathbf{X}}_2 + \mathbf{C}_2 \dot{\mathbf{X}}_2 + \mathbf{K}_2 \mathbf{X}_2 = \mathbf{F}_2 \quad (1.4b)$$

where \mathbf{M}_1 , and \mathbf{M}_2 are 3×3 mass matrices of the ice floe and platform, respectively including added masses; \mathbf{C}_1 and \mathbf{C}_2 are 3×3 damping matrices of the ice floe and platform, respectively; \mathbf{K}_2 is 3×3 stiffness matrix of platform, \mathbf{X}_1 and \mathbf{X}_2 are 3-row displacement vectors of ice floe and platform, respectively, a dot denotes differentiation with time, and \mathbf{F}_1 and \mathbf{F}_2 are 3-row force vectors containing collision forces due to deformation and hydrodynamic effects. The model was formulated based on the assumption that the ice floe and the platform only interact at the point of contact. The two bodies were considered as stiff, and all deformations were assumed to take place in a zone around the collision point.

Arockiasamy et al. (1984) presented three methods for the solution of the impact problem:

- *Energy approach*: This equates the kinetic energy of the oncoming berg to the total energy absorbed by the system.
- *Initial Velocity Condition approach*: This idealizes the system by certain initial velocity conditions.
- *Additional Degree of-Freedom for Local Deformation*: This reformulates the equations of motion for the semi submersible with the only approximation being that, during collision, the zone of impact provides stiffness coupling only not mass coupling.

El Tahan et al. (1985) considered two different types of elastic impact models, for the case of a moored semi submersible subjected to bergy-bit impact. The analytical results were verified by experiments on a hydrodynamic model of a semi

submersible in a wave tank. Matsuishi and Ettema (1986) reported some model tests in an ice tank to determine the effects of ice floe impacts on a floating platform with conical legs.

Fuglem et al. (1999) presented a probabilistic framework for determining global iceberg impact loads for offshore structures. The framework was set up to account for variations of population of icebergs, environmental conditions, wave induced velocities of different sized icebergs. The iceberg-structure model was used to account for rotation of iceberg about three natural principal axes. The model assumes small angular rotations. They found that the design impact load reduces significantly compared to when there is no rotation. The next subsection addresses different methods for modeling of ice-structure interaction.

1.3.2 MODELING OF ICE-STRUCTURE INTERACTION

When a structure vibrates under continuous crushing of ice, the dynamic characteristics of both are mutually dependent. Furthermore, the behavior of the structure depends on many factors as ice thickness and relative velocity of ice feature with respect to the structure. Besides, ice impact loads on offshore structures are random and non-smooth due to the nonhomogeneity and difference in ice microstructure. This is in addition to the fact that the salt and temperature result in great uncertainty in ice strength. The complexity of the interaction process makes it difficult to develop a complete model of the process.

Early attempts of mechanical models used to analyze the ice-structure interaction process include the study by Matlock et al. (1971). An impacting offshore

structure was represented by a mass-spring-dashpot system and the ice sheet was represented by a system of brittle elastic bars as shown in Figure 1.1. The ice bars fracture completely occurs at a characteristic deflection. This model captures in a simple manner the build up of contact stresses and subsequent failure of the ice. In Matlock's model, the spacing of the ice teeth is assumed constant, this has some basis in observations that ice may tend to break into fragments of a particular size distribution (Neil, 1976). Other interaction scenarios indicate a range of ice fragment sizes as shown, for example, by Timco and Jordaan (1987). Assuming that each ice tooth exhibits linear elastic deformation, Δ , then the force F exerted on ice tooth in contact with the mass; $F = K_2\Delta$ where K_2 is the stiffness of ice tooth, and $0 \leq \Delta < \Delta_{max}$, where Δ_{max} is maximum displacement of ice tooth. At $\Delta = \Delta_{max}$, the tooth is considered broken and discarded. The next tooth is then considered the active tooth. Referring to Figure 1.1, the governing equation of motion for the structure is therefore

$$M\ddot{x} + c\dot{x} + K_1x = F(t) \quad (1.5)$$

where,

$$F(t) = \begin{cases} 0 & \text{if no contact} \\ K_2\Delta & \text{if in contact} \end{cases} \quad (1.6)$$

The kinematic relationship between x , z , and Δ is given by

$$\Delta = \dot{z}t + z_0 - x - P(N-1) \quad (1.7)$$

where z_0 is the position of the ice sheet at time $t=0$, P is the distance between ice teeth (assumed constant), and N is the active tooth number. Substituting equations (1.6) and (1.7) into equation (1.5) yields

$$M\ddot{x} + c\dot{x} + K_1x = \begin{cases} 0, & \text{for } \Delta \leq 0, \text{ and } \Delta = \Delta_{\max} \\ K_2(\dot{z}t + z_0 - x - P(N-1)), & \text{for } 0 \leq \Delta < \Delta_{\max} \end{cases} \quad (1.8)$$

Note that if Δ is negative, there is no contact between the mass and the active tooth.

When using Matlock's model, Karr et al (1992) and Trosech et al (1992) found that periodic motions exist, and that the periodicity for a particular system depends upon initial conditions. Huang and Liu (2009) developed a discrete failure type of dynamic model by modifying Matlock's model to incorporate more properties of ice crushing such as discrete failure, dependence of the crushing strength on the ice velocity, and randomness of ice failure. They found that the dependence of ice crushing strength on the ice velocity plays an important role in the resonant frequency of vibration of the structure.

Sodhi (1991) conducted a series of indentation tests by pushing vertical flat indentors into the edges of floating ice sheets. Tests were conducted by varying the ice thickness, indentation velocity, indenter width, and stiffness of the indenter support system. Sodhi (1991) observed three modes of ice-structure interaction; creep deformation of ice during low-velocity indentation, intermittent crushing of ice during medium-velocity indentation, and continuous crushing of ice during high-velocity indentation. Later, Sodhi (1994) developed an analytical model to simulate ice-structure interaction during intermittent crushing. The model was developed on the basis of experimental results from indentation tests conducted by Sodhi (1991). The model consisted of a mass m , a spring of stiffness k , and viscous damper of coefficient c as shown in Figure 1.2. An ice sheet is assumed to be moving at constant velocity V and is depicted in the model by specifying the velocity of a point

in an ice sheet located far from the indenter. It was found that the interaction force generated at the ice-structure interface depends on the deformation and crushing of ice.

Furthermore, the ice structure interaction during ice crushing was found to constitute three phases shown in Figure 1.3. These are:

- *A loading Phase* in which the interaction force increases almost linearly with the relative displacement between ice and structure until ice fails as indicated by sudden decrease in the interaction force.
- *An extrusion phase* in which the structure moves forward at high velocity extruding the crushing ice in front of it.
- *A separation phase* between the ice and the structure in which the interaction force is zero while the structure experiences a transient motion until the gap is closed at the beginning of a new cycle.

Based on Sodhi's (1994) work, Liu et al. (2001) presented the dynamic equations of motion of both structure and ice-sheet for each phase when the ice sheet breaks in bending or buckling modes. They included also the crushed length of the moving ice sheet. Liu et al. (2001) studied the effect of different parameters of moving ice sheet and structure on the interaction process. Some of these are effective stiffness and strength of ice sheet, damping and stiffness of the structure, and natural frequency of the structure. It was concluded that Sodhi's model is very valuable for structural design against ice loads and mitigation of ice-induced vibration.

Marcellus et al. (1990) suggested a dynamic full scale ice-structure interaction model consisting of two-degrees-of-freedom for the structure and one-degree-of-freedom for the ice. The model includes Mohr-Coulomb³ representation for the force in the crushed layer, and determination of the peak load based upon accumulation of micro-cracks or damage in ice sheet in front of the indenter. Based on Marcellus et al. (1990) work, Morsy and Brown (1993) suggested the inclusion of more than one line of lumped masses. In each line, the ice mass is divided into intact, slightly damaged and highly damaged layers. The advantage of this model is that it permits the model to trace the behavior of ice sheet from undamaged field to rear field (fully damaged). Thus, the model is able to determine the average ice pressures and associated loads based on geometric and material properties of the ice sheet. Kärnä et al. (1999) developed a numerical model for predicting the dynamic ice forces on offshore structures.

Simple models of impact ice feature on structures include the evaluation of the risk of exceedance of initial translational energy of iceberg if probability distributions of iceberg mass, velocity and size were given (see, e.g., Maes and Jordaan, 1984). Maes and Jordaan (1984) considered phenomenological models that describe the gradual dissipation of the initial transitional energy of the berg during ice crushing at the structure interface.

³ Mohr–Coulomb representation is a mathematical model that describes the failure of brittle materials to shear stress as well as normal stress. Generally the theory applies to materials for which the compressive strength far exceeds the tensile strength.

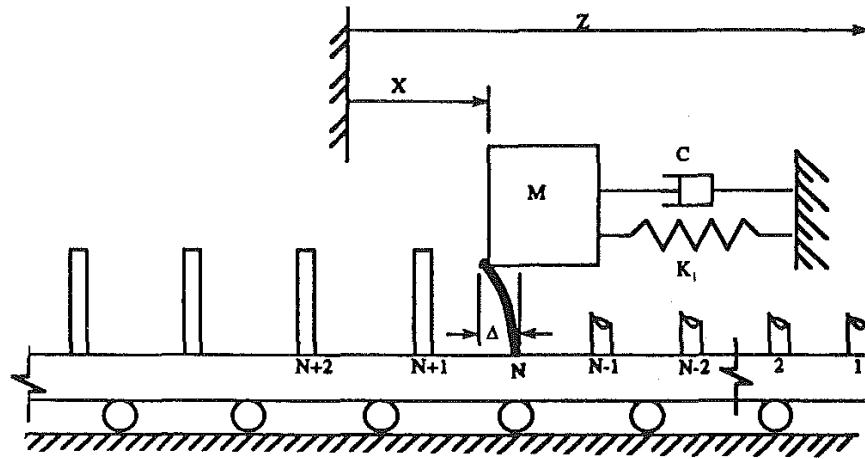


Figure 1.1. Schematic sketch of the theoretical model by Matlock (1971).

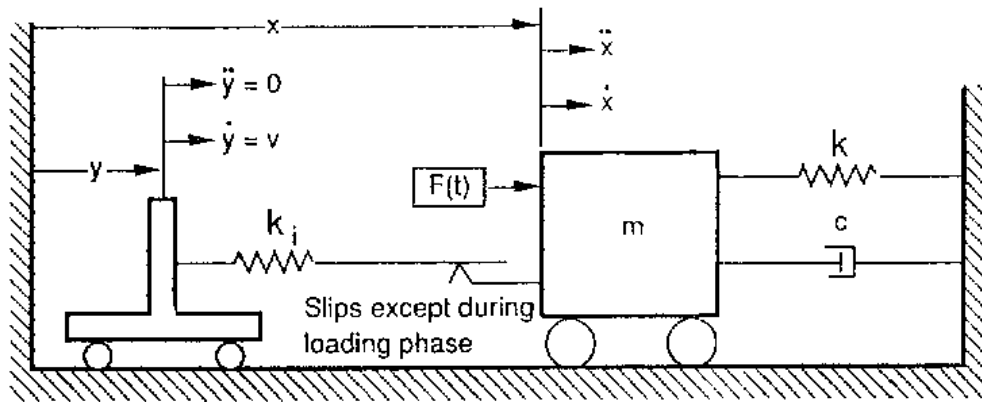


Figure 1.2. Schematic sketch of theoretical model by Sodhi (1991).

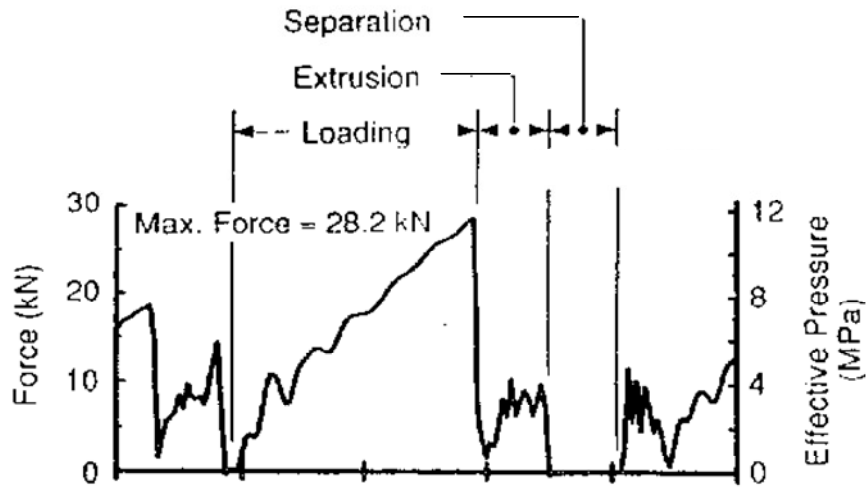


Figure 1.3. Experimental data from indentation test carried out by Sodhi (1994).

1.3.3 SHIP-ICE IMPACT

The study of ship-ice impact may be divided into two categories; calculating the total force on bow and the stress distribution along ship's hull, and studying vessel motions and its stability. The strong influence of ship speed prior to ship-ice collision upon the extent of structural damage has been studied by Aldwinckle and Lewis (1984). They analyzed the bow collapse in head-on collision with icebergs, assuming that all kinetic energy of the ship at the moment of impact is absorbed by local structural deformation (buckling) of ship only; i.e. no allowance for energy absorbed in global ship response or crushing of ice.

Koehler and Jorgensen (1985) presented a method for assessing the safe speed of ships navigating in arctic and subarctic waters. The method is based upon finite element analysis of the ship structural response under impact loading. Their

approach was based on the nonlinear ship-ship collision method developed by Valsgard and Jorgensen (1983). They replaced the struck ship by growler or multi-layer ice floe. Two separate models were introduced; one model for simulating the local damage process (inner mechanics model), and the second model for motions of the ship and ice feature during collision (outer mechanics model).

Philips (1994) and Philips and Tanaka (1994) developed a numerical procedure for predicting the stresses on the hull of icebreaking ships during head-on collision with multi-layer ice. The model involved the hydrodynamic forces associated with ship motions. They examined the requirement for exactly satisfying the kinematic boundary conditions on the ice interface when modeling ice forces on icebreaking ships. It was found that describing ice crushing strength in terms of the uniaxial compressive strength is sufficient, in conjunction with complete kinematic representation of the interface displacements. Daley et al. (1986) developed a technique to model dynamic ship-ice impact at model scale. The technique involved scaling of both vessel's rigid body motions (heave, roll, and pitch), and simulated multi-layer ice. Modal information was obtained from exciter tests and finite element analysis. They evaluated the force and bending moment distributions over ship hull at different speeds, and presented a practical solution to head-on impact problem. Jebaraj et al. (1988) presented a numerical study using finite element method to investigate ship/ice interaction problem. They considered the ice as plate subjected to dynamic edge loading. The ship was considered as a rigid indenter impacting the ice plate at different velocities; meanwhile the ice sheet was considered to be very large tending to infinity. Free vibration analysis was carried out using finite element

method to determine the frequencies and mode shapes for different indenter velocities.

Aboulazm (1989) employed the classical impact theory to study the interaction between the ship hull and ice floes. The ship was considered as a freely floating body advancing at speed V in the positive x – direction, see Figure 1.4. As a result of impact of a ship with an ice floe, momentum exchange takes place, such that the change of ship momentum is due to the impact force $P(t)$ which appears during collision duration t' with the ice floe. From the principle of conservation of momentum, the impulse and momentum equations for the ship can be written in the vector form as

$$\int_0^{t'} P(t) dt = M (V' - V) \quad (1.9)$$

where M is the mass of the ship, V is the ship velocity before impact, V' is the ship velocity after impact, $P(t)$ is the impact force and t' is the duration of impact. For a ship colliding with an ice floe, Aboulazm (1989) assumed that the ship is wall-sided at region of floe impacts. For one-degree-of-freedom case, the conservation of momentum represented by Equation (1.9) may be reduced to

$$MV + mv = MV' + mv' \quad (1.10)$$

where M and m are the masses of the ship and ice floe, respectively, V and v are the ship and ice floe speeds before impact, and V' and v' are the ship and ice floe speeds after impact, respectively. To determine velocities after impact, the following energy relation was introduced

$$MV'^2 + mv'^2 = e(MV^2 + mv^2) \quad (1.11)$$

where e is the coefficient of restitution and it is defined as

$$e = -(V' - v') / (V - v) \quad (1.12)$$

Substituting equation (1.12) in equations (1.10) and (1.11), velocities after impact can be written as

$$V' = V - (1 - e) \frac{m}{(M + m)} (V - v), \text{ and} \quad (1.13a)$$

$$v' = v + (1 - e) \frac{M}{(M + m)} (V - v) \quad (1.13b)$$

The change in kinetic energy of the system is given by

$$\delta E = \frac{1}{2} (MV'^2 + mv'^2) - (MV^2 + mv^2) \quad (1.14)$$

Substituting equations (1.13) in (1.14), loss of kinetic energy due to impact is written as

$$\delta E = \frac{1}{2} \frac{Mm}{(M + m)} (1 - e)^2 (V - v)^2 \quad (1.15)$$

Equation (1.15) was used in predicting the resistance of ship in broken ice. The predicted results showed good agreement to model testing results and available full scale tests.

It should be noted that the formulation of a collision theory for a ship striking a massive ice body corresponds to the classical theory of ship collision dynamics dating from Minorski (1959). Hence, one should not ignore the work done in this area. One of the major models to study the outer dynamics in ship collisions was developed by Petersen (1982) who developed a procedure for time simulation of ship response during collisions. The hydrodynamic forces acting on the ship hull

during the collision were calculated by the strip theory. The colliding ships were treated as essentially stiff bodies with all deformation taking place in the contact area. The structural response in the contact area was modeled by non-linear springs. The ships were supposed to be completely rough and inelastic. Pedersen and Zhang (1998) presented an analytical closed-form expression for the energy released for crushing and the impact impulse during ship collisions; ship-ship collisions, ship collisions with rigid walls and ship collisions with flexible offshore structures. The energy loss for dissipation by structural deformations of the involved structures was expressed in closed-form expressions. The derived general energy expressions were extended to the case of ship collisions with rigid walls and to collision between ships and flexible offshore platforms. The procedure was based on rigid-body mechanics, where it was assumed that there is negligible strain energy for deformation outside the contact region and that the contact region is local and small. It was considered that the collision is instantaneous and that each body is assumed to exert an impulsive force on the other at the point of contact. Also, they presented numerical illustrative examples for ship-ship collisions at different impact locations and impact angles. It was shown that for collision of ships with a rigid wall the energy loss due to collision depends mainly on the collision angle. Almost all the kinetic energy of the striking ship was assumed to be lost when the collision angle is greater than 60° . Also, they showed that the ratio of energy dissipated to the initial kinetic energy of the vessel before the collision becomes smaller if the flexibility of the platform is considered as shown in Figure 1.5.

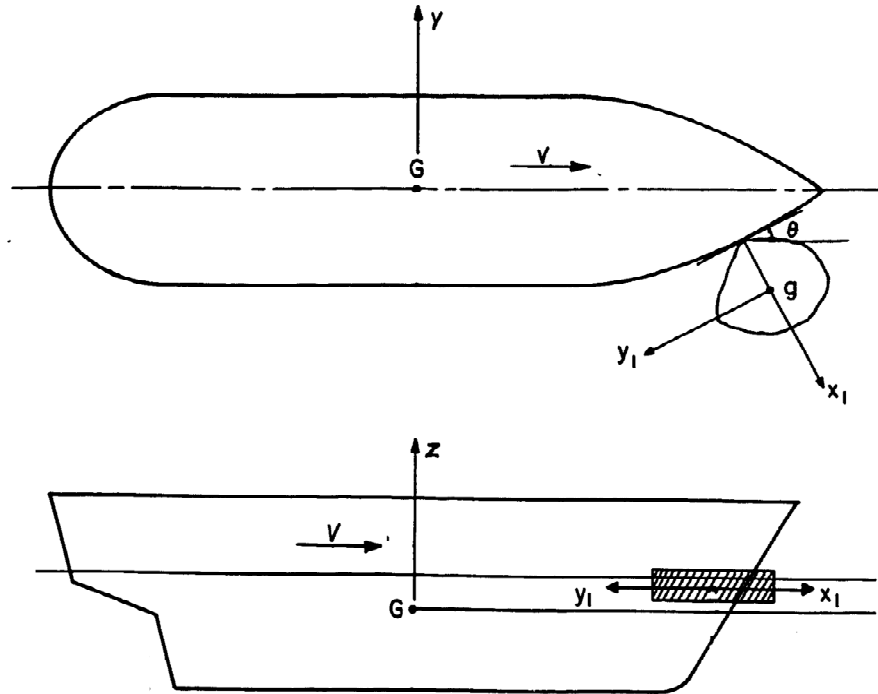


Figure 1.4. Ice floe-ship impact by Aboulazm (1989).

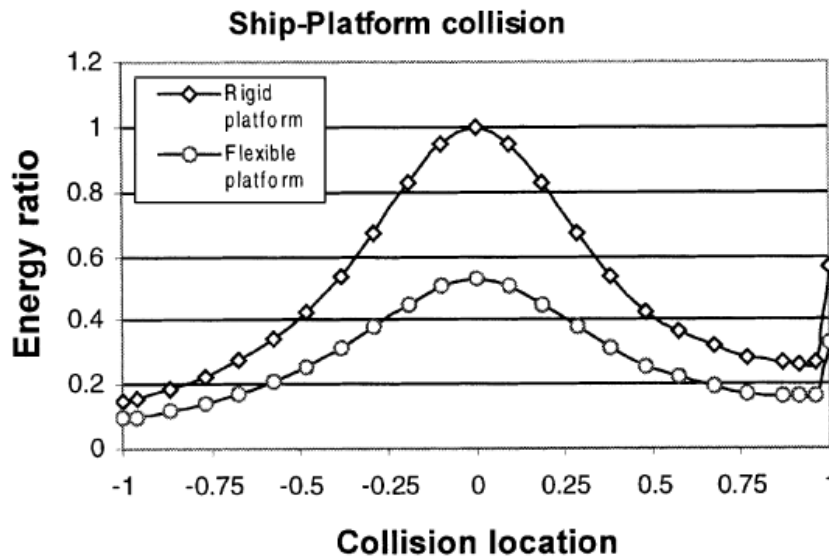


Figure 1.5. Dependence of ratio of energy dissipated due to collision to initial kinetic energy on collision location of a supply vessel collides with a leg of a jack-up rig; Collision location is measured from the center of the ship (Pedersen and Zhang, 1998).

1.4 Vibro-Impact Dynamics

Vibro-impact dynamics involves multiple impact interactions in the form of jumps in state space. In most cases there is energy loss due to impacts and the coefficient of restitution usually measures the degree of energy dissipation associated with impact event. The time scale involved during impact is much smaller than the time scale of the natural frequency of oscillation. The dynamics of vibro-impact systems in the presence or absence of friction is usually described by strongly nonlinear non-smooth differential equations. This strong nonlinearity is due to the fact that the velocity before and after impact experiences a sudden change in its direction. Vibro-impact systems are encountered in many engineering applications such as impact of floating ice with ships, ships colliding against fenders, collision of human vocal folds, automotive braking systems, and rubbing between the stator structure and rotor blades in turbomachinery.

1.4.1 MODELING OF VIBRO-IMPACT SYSTEMS

Vibro-impact systems together with the modeling of impact forces require special treatments and representations. These include Zhuravlev and Ivanov non-smooth coordinate transformation, phenomenological modeling, and Hertzian contact law. Since Zhuravlev and Ivanov coordinate transformations form the bases of the present work, the next two subsections outline the basic concepts of these two methods. Other models are well documented by Ibrahim (2009).

1.4.1.1 Zhuravlev Non-Smooth Coordinate Transformation

Zhuravlev (1976) introduced a non-smooth coordinate transformation that assumes rigid barriers as well as inelastic ones. The main rationale of such coordinate transformation is to convert the vibro-impact oscillator into an oscillator without barriers such that the corresponding equation of motion does not contain any impact terms. The transformed system is then solved using any asymptotic technique. For a system with one-sided rigid barrier, shown in Figure 1.6, the following transformation is used

$$x = z \operatorname{sgn}(z) - x_i \quad (1.16)$$

This transformation shifts the barrier to the axis $z = 0$ and maps the domain $x > -x_i$ of the phase plane trajectories on the original plane (x, \dot{x}) to the new phase plane (z, \dot{z}) . The first and second time derivatives are $\dot{x} = \dot{z} \operatorname{sgn}(z)$, and $\ddot{x} = \ddot{z} \operatorname{sgn}(z)$ respectively.

For the case of inelastic impact, the condition $\dot{x}_+ = e\dot{x}_-$ must be introduced, where e is the coefficient of restitution, \dot{x}_+ and \dot{x}_- are the ship velocities just before and after impact, respectively. Note that the additional damping associated with inelastic impact may be significant than the inherent linear and nonlinear damping terms. The coefficient e is assumed to be close to unity, such that $(1-e)$ is considered a small parameter. According to the coordinate transformation given by equation (1.16), the one sided impact occurs at $x = -x_i$, the impact condition $\dot{x}_+ = e\dot{x}_-$ specified at $x = -x_i$, is transformed to

$$\dot{z}_+ = e\dot{z}_- \text{ at } z = 0 \quad (1.17)$$

The transformed velocity jump is reduced by an amount proportional to $(1-e)$. It is possible to introduce this jump into the equation of motion using the Dirac delta-function, and thus one can avoid using condition (1.17). The additional term due to inelastic impact may be written in the form

$$(\dot{z}_+ - e\dot{z}_-)\delta(t-t_i) = (1-e)\dot{z}\delta(t-t_i), \text{ provided } |\dot{z}_+| < |\dot{z}| < |\dot{z}_-| \quad (1.18)$$

where t_i is the time instant of impact. By writing $z(t) = z(t_i) + \dot{z}(t)(t-t_i)$, since $z(t_i) = 0$, one can write $(t-t_i) = z(t)/\dot{z}(t_i)$. Thus $\delta(t-t_i) = \delta(z(t)/\dot{z}(t_i))$. Now consider

$$\int_{-\infty}^{\infty} f(z)\delta(z)dz = f(0), \text{ and } \int_{-\infty}^{\infty} f(z)\delta(\lambda z)dz = \left[\int_{-\infty}^{\infty} f(u/\lambda)\delta(u)du \right] / \lambda = f(0)/\lambda,$$

one can write $\delta(\lambda z) = \delta(z)/\lambda$, provided that $\lambda > 0$, thus $\delta(t-t_i) = |\dot{z}|\delta(z)$, in this case, equation (1.18) can be written in the form

$$(1-e)\dot{z}\delta(t-t_i) = (1-e)\dot{z}|\dot{z}|\delta(z) \quad (1.19)$$

Equation (1.19) represents the damping term associated with inelastic impact as $(1-e)\dot{z}'|\dot{z}'|\delta(z)$. Dimentberg (1996) provided a systematic description of Zhuravlev coordinate transformation and demonstrated its application to vibro-impact systems under random excitation.

1.4.1.2 Ivanov Transformation

For the case of inelastic impact, Ivanov (1994) developed a modified non-smooth coordinate transformation. In terms of the generalized coordinates, q_0, q_1, \dots ,

q_n , subject to the unilateral constraint $q_0 \geq 0$, these systems may be described by the following set of equations in the vector form

$$\dot{\mathbf{X}} = \mathbf{F}(t, \mathbf{X}), \quad \mathbf{F}(t+T, \mathbf{X}) = \mathbf{F}(t, \mathbf{X}) \quad (1.20)$$

Where $\mathbf{X} = \{q_0, \dot{q}_0, q_1, \dots, q_n, p_1, \dots, p_n\}^T$, p_i are the generalized momenta. The functions $\mathbf{F}(t, \mathbf{X})$ are periodic with period T , and the superscript T denotes transpose. At the instant of impact, $t = t_i$, one may write

$$q_0(t_i) = 0, \text{ and } \dot{q}_0(t_i) < 0 \quad (1.21)$$

The impact reaction force R_i involves energy dissipation and can be expressed by the visco-elastic model

$$R_i = \begin{cases} -\alpha q_0 - 2\eta\alpha\dot{q}_0 & \text{if } q_0 < 0 \\ 0 & \text{if } q_0 > 0 \end{cases} \quad (1.22)$$

where α is large and $\eta \in [0, 1)$. The equation of motion of the impact trajectory in the region $q_0 < 0$ is

$$\ddot{q}_0 + 2\eta\alpha\dot{q}_0 + \alpha^2 q_0 = F_2 \quad (1.23)$$

The solution of this equation subject to the initial conditions (1.21) is

$$q_0 = \frac{\mathbf{F}_2^0(t_i, \mathbf{X}(t_i))}{\alpha^2} \left[1 - \frac{e^{-\eta\alpha}}{\sqrt{1-\eta^2}} \sin(\alpha\sqrt{1-\eta^2}\tau + \arcsin\sqrt{1-\eta^2}) \right] + \frac{\dot{q}_0(t_i)e^{-\eta\alpha}}{\alpha\sqrt{1-\eta^2}} \sin(\alpha\sqrt{1-\eta^2}\tau + O(\tau)) \quad (1.24)$$

where $\tau = t - t_i$ and $X_j(t) = X_j(t_i) + O(\tau)$, $j = 3, \dots, 2n+2$. Note that $\tau = O(\alpha^{-1})$, which implies that the duration of impact is very small, and thus the vibration X_j do not

change during impacts. On the other hand, the displacement q_0 and velocity \dot{q}_0 , experience two distinct limiting regimes. The first regime is the impact regime in which $\alpha|\dot{q}_0(t_i)| \gg |\mathbf{F}_2^0|$ and the duration of the impact τ is close to $\pi/(\alpha\sqrt{1-\eta^2})$. The restitution law gives

$$\dot{q}_0(t_i+0) = -e\dot{q}_0(t_i-0), \quad e = e^{-\pi\eta/\sqrt{1-\eta^2}} \in [0,1] \quad (1.25)$$

Ivanov (1994) introduced the new coordinate transformation

$$\mathbf{Y} = \{s, v, q_1, \dots, q_n, p_1, \dots, p_n\}^T, \quad (1.26)$$

$$q_0 = s \operatorname{sgn}(s), \text{ and } \dot{q}_0 = Rv \operatorname{sgn}(s)$$

where $R = 1 - k \operatorname{sgn}(sv)$, $k = [(1-e)/(1+e)]$, s and v are the new coordinate transformation of q_0 and \dot{q}_0 according to the transformation (1.27) where the values of s and v are not restricted. The substitution $\mathbf{Y} \rightarrow \mathbf{X}$ is irreversible since each vector \mathbf{X} has two inverses for which $s_1 = -s_2$, and $v_1 = -v_2$. However, for every \mathbf{Y} there exists a unique image \mathbf{X} in accordance with the transformation

$$\mathbf{X} = \mathbf{S}\mathbf{Y} \quad (1.27)$$

$$\mathbf{S} = \operatorname{diag}\{\operatorname{sgn}(s), R \operatorname{sgn}(s), 1, \dots, 1\}$$

where the matrix \mathbf{X} is diagonal of dimension $2n+2$. The equations of motion (1.20) will take the transformed form

$$\dot{\mathbf{Y}} = \mathbf{S}^{-1}\mathbf{F}(t, \mathbf{S}\mathbf{Y}) = \mathbf{G}(t, \mathbf{Y}) \quad (1.28)$$

Equation (1.28) possess a discontinuous right-hand side due to the presence of terms such as $\operatorname{sgn}(s)$ and $\operatorname{sgn}(sv)$. However, their solutions are continuous vector

functions in the time domain, and differentiable provided that $z\dot{v} \neq 0$. For $n=0$, Ivanov coordinate transformation given by equation (1.26) is illustrated in Figure 1.7.

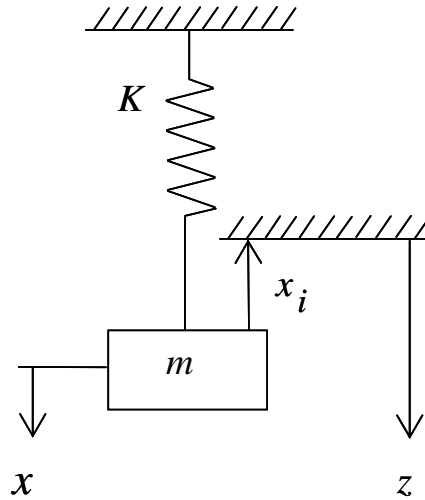


Figure 1.6. Spring-mass system with one sided barrier.

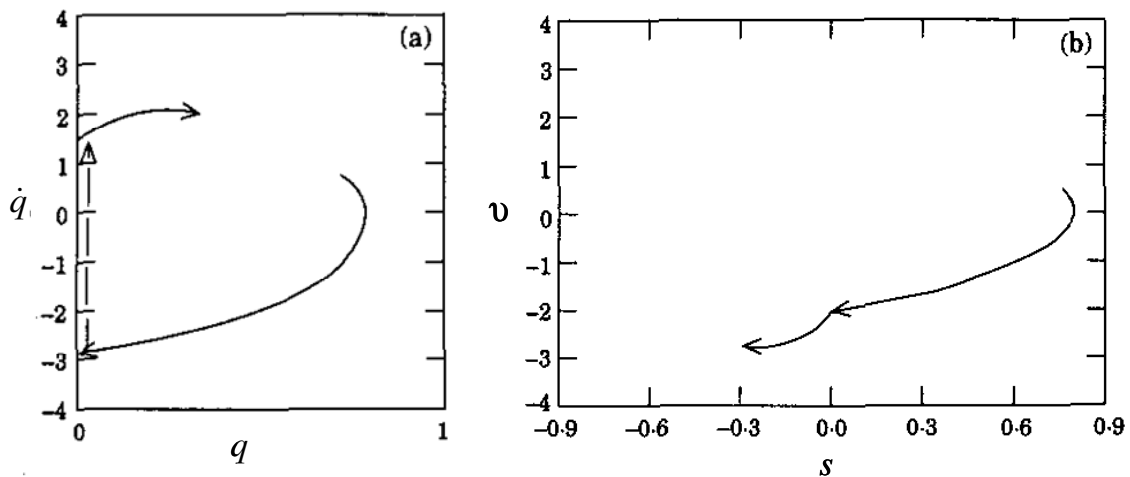


Figure 1.7. Continuous representation of impact motion: (a) initial phase planer, and (b) auxiliary phase plane (Ivanov, 1994).

1.5 Scope of the Present Work

The formulation of a collision theory for a ship striking an iceberg or a rigid platform is typically divided into two problems. One addresses concerns about local structure damage, while the second deals with the global response of a ship interacting with a barrier. The literature showed extensive amount of work dealing with the first problem. However, there is a great importance to study the global response of ships or ocean structures when they experience impact with an ice body. The response may exceed the physical acceptable levels for passengers, and sometimes impact may lead to catastrophic results. Of the six motions of the ship, the roll oscillation is the most critical motion that can lead to the ship capsizing. This study is denoted to the impact of ship roll interaction with stationary icebergs and platforms.

The objective of the current work is to develop different analytical models of ship roll motion interacting with stationary ice in the form of one-sided barrier. Chapter 2 presents a general analytical modeling of ship roll dynamics and its coupling with heave and pitch. The special case of uncoupled ship roll dynamics is included for the purpose of this study. An analytical model of ship roll motion interacting with one-sided barrier will be developed based on Zhuravlev (1976) and Ivanov (1994) non-smooth coordinate transformations in chapters 3 and 4, respectively. These transformations have the advantage of converting the vibro-impact oscillator into an oscillator without barriers such that the corresponding equation of motion does not contain any impact term. A comparison between response characteristics for two cases of impact; elastic and inelastic impacts will be

carried out to study the significance of damping associated with inelastic impact. Another two approaches will be introduced based on the numerical integration of the equation of motion using Runge-Kutta fourth-order and equivalent viscous damping of impact damping at the moment of impact. The validation of the proposed analytical methods will be carried out by comparing the results obtained from these models to each other.

Experimental investigation conducted on ship model interacting with a stationary one-sided barrier using the towing tank at Wayne State University will be discussed in chapter 5. A comparison between analytical and experimental results is carried out in order to determine the usefulness of the analytical models. The importance of this study is that it represents the first attempt to explore the interaction of ship roll motion with floating ice and platforms. Furthermore, the current study presents different analytical models of ship roll motion interacting with stationary barriers. The use of the proposed analytical models saves time and high cost required by experimental analysis.

CHAPTER 2

MODELING OF SHIP ROLL DYNAMICS AND ITS COUPLING WITH HEAVE AND PITCH

2.1 Introduction

In order to study the dynamic behavior of ships navigating in severe environmental conditions it is imperative to develop their governing equations of motion taking into account the inherent nonlinearity of large-amplitude ship motion. The purpose of this chapter is to present the coupled nonlinear equations of motion in heave, roll and pitch based on physical grounds. The special cases of coupled roll-pitch and purely roll equations of motion are the obtained from the general formulation. The ingredients of the formulation are comprised of three main components. These are the inertia forces and moments, restoring forces and moments, and damping forces and moments with an emphasis to the roll damping moment. In the formulation of the restoring forces and moments, the influence of large-amplitude ship motions will be considered together with ocean wave loads.

Generally, ships can experience three types of displacement motions (heave, sway or drift and surge) and three angular motions (yaw, pitch and roll) as shown in Figure (2.1). The general equations of motion have been developed either by using Lagrange's equation (see, e.g., Nayfeh et al., 1973, 1974; Nayfeh and Mook, 1979; and Suleiman, 2000) or by using Newton's second law (see, e.g., Fossen, 1994; Lewandowski, 2004; and Perez, 2005). In order to derive the hydrostatic and hydrodynamic forces and moments acting on the ship, two approaches have been used in the literature. The first approach utilizes a mathematical development based

on a Taylor expansion of the force function (see, e.g., Paulling, 1959; Kinney, 1961; Haddara, 1971; and Neves et al., 2006 and 2007). The second group employs the integration of hydrodynamic pressure acting on the ship's wetted surface to derive the external forces and moments (see, e.g., Vugts, 1971; Newman, 1977; Edward, 1989; Chu, 1998; Lee, 2001; and Khalid, 2007). Stability against capsizing in heavy seas is one of the fundamental requirements in ship design. Capsizing is related to the extreme motion of the ship and waves. Of the six motions of the ship, the roll oscillation is the most critical motion that can lead to the ship capsizing. For small angles of roll motions, the response of ships can be described by a linear equation. However, as the amplitude of oscillation increases, nonlinear effects come into play. Nonlinearity can magnify small variations in excitation to the point where the restoring force contributes to capsizing. The nonlinearity is due to the nature of restoring moment and damping. The environmental loadings are nonlinear and beyond the control of the designer. The nonlinearity of the restoring moment depends on the shape of the righting-arm diagram.

Abkowitz (1964) presented a significant development of the forces acting on a ship in surge, sway, and yaw motions. He used Taylor series expansions of the hydrodynamic forces about a forward cruising speed. The formulation resulted in an unlimited number of parameters, and can model forces to an arbitrary degree of accuracy. Thus, it can be reduced to linear and extended to nonlinear equations of motion. Later, Abkowitz (1975, 1981), Hwang (1980) and Källström and Åström (1981) provided different approaches to estimate the coefficients of these models. Son and Nomoto (1982) extended the work of Abkowitz (1964) to include ship roll

motion in deriving the forces and moments acting on the ship. Ross (2009) developed the nonlinear equations of motion of a ship maneuvering through waves using Kirchhoff's (1869) convolution integral formulation of the added mass. Kirchhoff's equations are a set of relations used to obtain the equations of motion from the derivatives of the system kinetic energy. They are special cases of the Euler-Lagrange equations. The derived equations also give the Coriolis and centripetal forces (Milne-Thomson, 1968; and Fossen, 2002).

Rong (1994) considered some problems of weak and strong nonlinear sea loads on floating marine structures. The weak nonlinear problem considers hydrodynamic loads on marine structures due to wave-current-body interaction. The strong nonlinear problem considers slamming loads acting on conventional and high-speed vessels. Theoretical and numerical methods to analyze wave-current interaction effects on large-volume structure were developed. It is known that large-amplitude ship motions result in strongly nonlinear, even chaotic behavior (Alford et al., 2008). The current trends toward high-speed and unique hull-form vessels in commercial and military applications have broadened the need for robust mathematical approaches to studying the dynamics of these ships.

Various models of roll motion containing nonlinear terms in damping and restoring moments have been studied by many researchers (De Kat and Paulling, 1989; Witz et al., 1989; Denise, 1983). Bass and Haddara (1987, 1988) considered various forms for the roll damping moment and introduced two techniques to identify the parameters of the various models together with a methodology for their evaluation. Taylan (2000) demonstrated that different nonlinear damping and

restoring moment formulations reported in the literature may result in completely different roll amplitudes, and further yielded different ship stability characteristics. Since ship capsizing is strongly dependent on the magnitude of roll motion, an accurate estimation of roll damping is crucial to the prediction of the ship motion responses. Moreover, the designer should consider the influence of waves on roll damping, especially nonlinear roll damping of large-amplitude roll motion, and subsequently on ship stability. Different models for the damping moment introduced in the equation of roll motion were proposed by Dalzell (1978), Cardo (1982), and Mathisen and Price (1984). They contain linear-quadratic or linear-cubic terms in the angular roll velocity. El-Bassiouny (2007) studied the dynamic behavior of ships roll motion by considering different forms of damping moments consisting of the linear term associated with radiation, viscous damping, and a cubic term due to frictional resistance and eddies behind bilge keels and hard bilge corners.

This chapter presents the derivation of the equations of motion based on physical grounds. The equations of motion will then be simplified to consider the roll-pitch coupling, which is very critical in studying the problem of ship capsizing. It begins with a basic background and terminology commonly used in Marine Engineering. This is followed by considering the hydrostatics of ships in calm water and the corresponding contribution due to sea waves. An account of nonlinear damping in ship roll oscillation will be made based on the main results reported in the literature. The chapter includes an overview of ship roll dynamic stability.

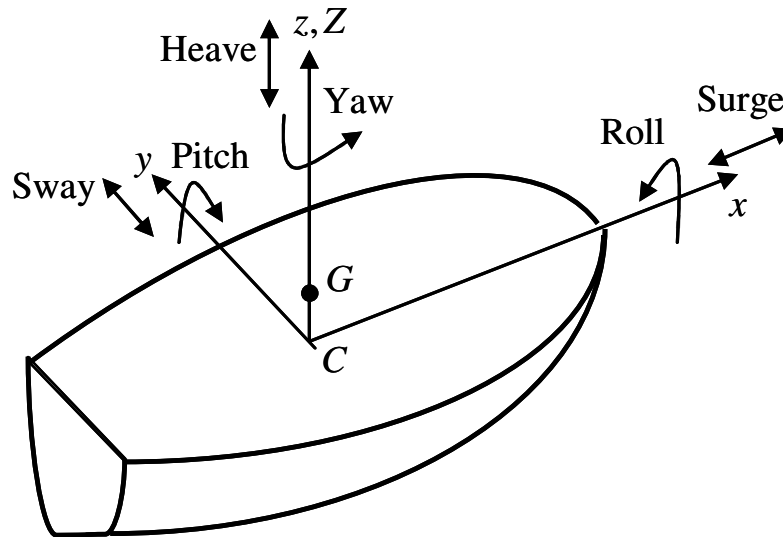


Figure 2.1. Ship Schematic diagram showing the six degrees of freedom.

2.2 Background and Terminology

In marine engineering community one should be familiar with naval architecture terminology. These include key stability terms that are used in the design and analysis of vessels and their structure components. A list of the main terms is provided in Appendix A. The purpose of this section is to introduce the fundamental concept of ship roll stability. A floating ship displaces a volume of water equal to the weight of the ship. The ship will be buoyed up by a force equal to the weight of the displaced water. The ship will be buoyed up by a force equal to the weight of the displaced water. The *metacenter* M (see Figure 2.2) is a theoretical point through which the buoyant forces act at small angles of *list* (roll). At these small angles the center of buoyancy tends to follow an arc subtended by the metacentric radius BM , which is the distance between the metacenter and the center of

buoyancy B . As the vessels' draft changes so does the metacenter moving up with the center of buoyancy when the draft increases and vice versa when the draft decreases. For small angle stability it is assumed that the Metacenter does not move.

The *center of Buoyancy* B is a theoretical point through which the buoyant forces acting on the wetted surface of the hull. The position of the center of buoyancy changes depending on the attitude of the vessel in the water. As the vessel increases or reduces its draft (drawing or pulling), its center of buoyancy moves up or down respectively caused by an increase in water displaced. As the vessel *lists* the center of buoyancy moves in a direction governed by the changing shape of the submerged part of the hull as demonstrated in Figure 2.2b. For small angles, the center of buoyancy moves towards the side of the ships, which becomes more submerged. This is true for consideration of small angle stability and for vessels with sufficient freeboard. When the water line reaches and moves above the main deck level a relatively smaller volume of the hull is submerged on the lower side for every centimeter movement as the water moves up the deck. The center buoyancy will now begin to move back towards centerline.

As a vessel rolls its center of buoyancy moves off centerline. The center of gravity, however, remains on centerline. For small roll angles up to $\phi = 10^\circ$ depending on hull geometry, the righting arm \overline{GZ} is

$$\overline{GZ} = \overline{GM} \times \sin \phi \quad (2.1)$$

It can be seen that the greater the metacenter height the greater the righting arm is and therefore the greater the force restoring the vessel (Righting Moment

RM) to the upright position. This is valid as long as the metacenter is above the center of gravity. When the metacenter is at or very near the centre of gravity then it is possible for the vessel to have a permanent list due to the lack of an adequate righting arm. Note that this may occur during loading operations and it is often the case that once the small angle restrictions are passed the metacentric height increases and a righting arm prevents further listing. A worst case occurs when the metacenter is substantially located below the center of gravity as shown in Figure 2.3. This situation will lead to the ship capsizing. As long as the metacenter is located above the ship center of gravity, the righting arm has a stabilizing effect to bring the ship back to its normal position. If, on the other hand, the righting arm is displaced below the center of gravity, the ship will lose its roll stability and capsize.

Hydrostatic and hydrodynamic characteristics of ships undergo changes because of the varying underwater volume, *centers of buoyancy* and gravity and pressure distribution. Another factor is the effect of forward speed on ship stability and motions, particularly on rolling motion in synchronous *beam* waves. Taylan (2004) examined the influence of forward speed by incrementing its value and determining the roll responses at each speed interval. Various characteristics of the \overline{GZ} -curve for a selected test vessel were found to change systematically. The roll stability of a ship is usually measured by the stability diagram shown in Figure 2.4. The diagram shows the dependence of the right arm on the roll angle and plays an important design guide for ships' roll stability.

The roll oscillation of a ship is associated with a restoring moment to stabilize the ship about the x -axis given by the expression

$$M_x = W \overline{GM} \sin \phi \quad (2.2)$$

where W is the weight of water of displaced volume of the ship which is equal to the weight of the ship. If the ship experiences pitching motion of angle θ the righting arm $\overline{GM} \sin \phi$ will be raised by an increment $\overline{GM} \sin \phi \sin \theta$. In this case the net roll moment becomes

$$M_x = W \overline{GM} \sin \phi (1 + \sin \theta) \approx W \overline{GM} \phi (1 + \theta) \quad (2.3)$$

Note that the static stability is governed by the minimum value that the metacenter height, \overline{GM} , should have and the shape of the static stability curve with respect to the roll angle. This approach is still being applied in the assessment of stability criterion. The dynamic stability approach, on the other hand, is based on the equation of rolling motion. This involves constructing a model for a ship rolling in a realistic sea. The linear restoring parameters can be easily obtained from ship hydrostatics.

The curve for the righting arm, known also as the restoring lever, may be represented by an odd-order polynomial up to different degrees (Nayfeh and Balachandran, 1995; Arnold et al., 2004; Surendran et al., 2005; and Bulian, 2005). Different representations of the restoring moment were proposed in the literature. For example, Roberts (1982a,b), Falzarano and Zhang (1993), Huang et al. (1994), and Senjanović et al. (2000) represented $M_x(\phi)$ by the polynomial

$$M_x(\phi) = k_1 \phi + k_3 \phi^3 + k_5 \phi^5 + k_7 \phi^7 + \dots \quad (2.4)$$

where $k_1 > 0$, $k_3 < 0$, $k_5 > 0$, and $k_7 < 0$ for a damaged vessel, but $k_7 = 0$ for an intact vessel. Moshchuk et al. (1995) proposed the following representation

$$M_x(\phi) = k_0 \sin(\pi\phi / \phi_s) + \tilde{\gamma}(\pi\phi / \phi_s) \tag{2.5}$$

where ϕ_s is the capsizing angle, and the function $\tilde{\gamma}(\pi\phi / \phi_s)$ accounts for the difference between the exact function $M_x(\phi)$ and $k_0 \sin(\pi\phi / \phi_s)$.

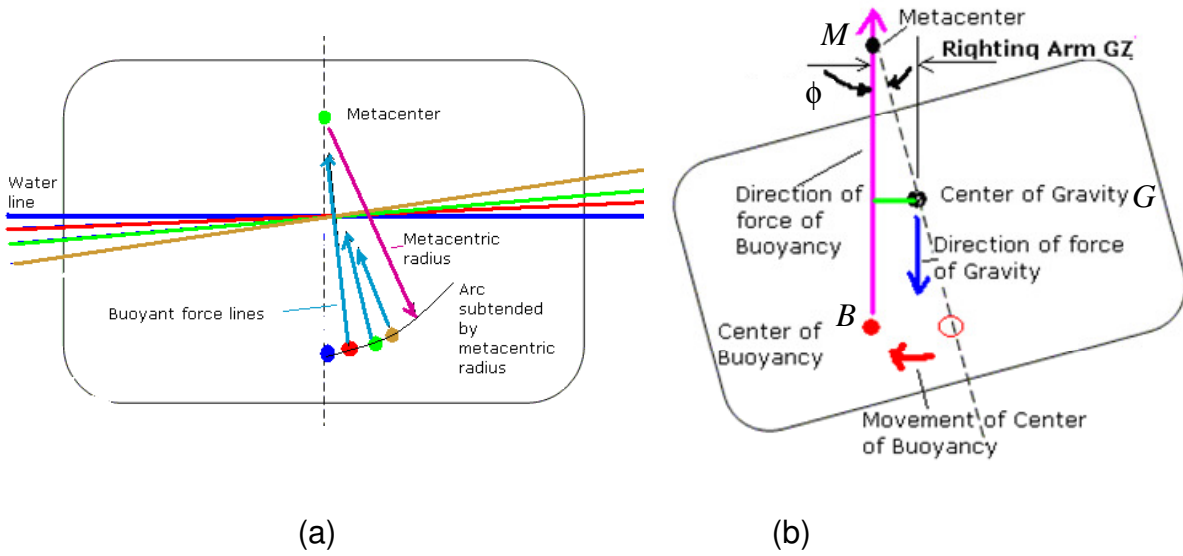


Figure 2.2. (a) Possible locations of the metacenter and (b) the righting arm.

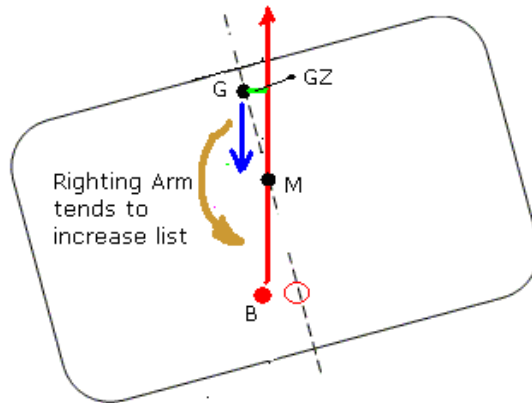


Figure 2.3. Negative ship stability.

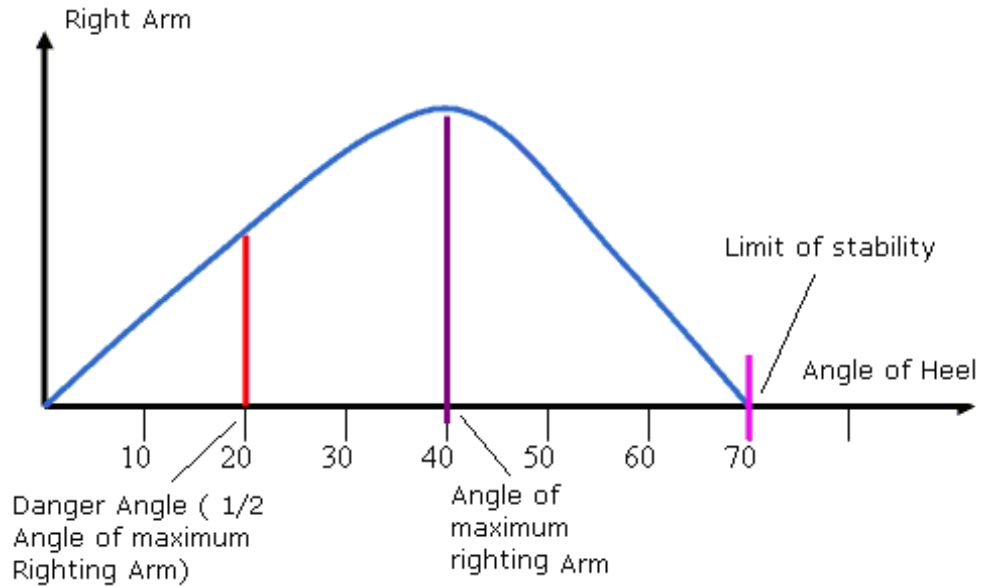


Figure 2.4. Stability diagram.

2.3 Heave-Pitch-Roll Equations of Motion

Consider a ship sitting in its static equilibrium position with a submerged volume v_0 . During its motion, its instantaneous submerged volume is v_1 , and the difference in the submerged volume is $\delta v = v_1 - v_0$. The inertial frame of axes is XYZ with unit vectors \mathbf{I} , \mathbf{J} , and \mathbf{K} along X , Y , and Z axes, respectively. On the other hand, the body frame that moves with the ship is xyz with unit vectors \mathbf{i} , \mathbf{j} , and \mathbf{k} along x , y , and z axes, respectively. Figure 2.5 shows the instantaneous buoyant center located at point B_1 and the corresponding instantaneous force is $\mathbf{F}_1 = \rho g v_1 \mathbf{K} = \rho g (v_0 + \delta v) \mathbf{K}$. The weight of the ship is $\mathbf{W} = -\rho g v_0 \mathbf{K}$. In this case the instantaneous restoring hydrostatic force is

$$\mathbf{F}_H = \rho g \delta v \mathbf{K} \quad (2.6)$$

The restoring moment is the resultant between the moments of weight and instantaneous buoyancy

$$\mathbf{M}_H = \rho g \left[v_0 \mathbf{K} \times (\overline{OG} - \overline{OB}_o) + \int \overline{Ob}_i \times dv_i \mathbf{K} \right] \quad (2.7)$$

where dv_i is the volume of the infinitesimal prism of height h_i , $\overline{OG} = \bar{z}_G \mathbf{k}$, \bar{z}_G is the center of mass location from O , $\overline{OB}_o = \bar{z}_{BO} \mathbf{k}$, $\overline{Ob}_i \approx x_{Ai} \mathbf{I} + y_{Ai} \mathbf{J} + \frac{h_i}{2} \mathbf{K}$, $\mathbf{k} = \sin \theta \mathbf{I} - \sin \phi \mathbf{J} + \mathbf{K}$, \bar{z}_G is the vertical coordinate of the center of gravity, $\delta v = \int h_i dA_i = \int h dA$, and \bar{z}_{BO} is the vertical coordinate of the center of gravity of the submerged volume, and (x_A, y_A) are the coordinates of the elemental prism in the instantaneous plane with respect to the inertial frame $CXYZ$. Substituting these parameters in equation (2.7) gives

$$\mathbf{M}_H = -\mathbf{I} \rho g \left[v_0 (\bar{z}_{BO} - \bar{z}_G) \sin \phi - \int y_A h dA \right] - \mathbf{J} \rho g \left[v_0 (\bar{z}_{BO} - \bar{z}_G) \sin \theta + \int x_A h dA \right] \quad (2.8)$$

The elemental prism height $h_i = h$ can be written in terms of the heave displacement z of the origin O above the water level, the pitch, θ , and roll, ϕ , angles as

$$h_i = -z - y_{Ai} \sin \phi + x_{Ai} \sin \theta \quad (2.9)$$

The volume variation δv is

$$\begin{aligned} \delta v &= \int dv = \int (-z - y_A \sin \phi + x_A \sin \theta) dA \\ &= -z \int dA - \sin \phi \int y_A dA + \sin \theta \int x_A dA \end{aligned} \quad (2.10)$$

The above summations are dependent on z , ϕ , and θ . They represent the following geometric properties

$\int dA = A(z, \phi, \theta)$ area of instantaneous plane of floatation,

$$\int y_A dA = A_x(z, \phi, \theta) \text{ first static moment of the area about } x\text{-axis,} \quad (2.11)$$

$\int x_A dA = A_y(z, \phi, \theta)$ first static moment of area about y -axis.

In this case, one may write the volume variation in the form (see, e.g., Neves and Rodrigues, 2006)

$$\delta v = -zA(z, \phi, \theta) - \sin \phi A_x(z, \phi, \theta) + \sin \theta A_y(z, \phi, \theta) \quad (2.12)$$

Note the above summations could have been replaced by integrals. The instantaneous restoring hydrostatic force given by equation (2.6) takes the form

$$\mathbf{F}_H = -\rho g \left[zA(z, \phi, \theta) + \sin \phi A_x(z, \phi, \theta) - \sin \theta A_y(z, \phi, \theta) \right] \mathbf{K} \quad (2.13)$$

In scalar form, the absolute value of the restoring force is

$$F_H = \rho g \left[zA(z, \phi, \theta) + \sin \phi A_x(z, \phi, \theta) - \sin \theta A_y(z, \phi, \theta) \right] \quad (2.14)$$

The summations in equation (2.8) can also be written in terms of equation (2.9) as

$$\begin{aligned} \int y_A h dA &= \int y_A (-z - y_A \sin \phi + x_A \sin \theta) dA \\ &= -zA_x(z, \phi, \theta) - \sin \phi I_{xx}(z, \phi, \theta) + \sin \theta I_{xy}(z, \phi, \theta) \end{aligned} \quad (2.15a)$$

$$\begin{aligned} \int x_A h dA &= \int x_A (-z - y_A \sin \phi + x_A \sin \theta) dA \\ &= -zA_y(z, \phi, \theta) - \sin \phi I_{xy}(z, \phi, \theta) + \sin \theta I_{yy}(z, \phi, \theta) \end{aligned} \quad (2.15b)$$

where

$$I_{xx}(z, \phi, \theta) = \int y_A^2 dA, \quad I_{yy}(z, \phi, \theta) = \int x_A^2 dA, \quad \text{and} \quad I_{xy}(z, \phi, \theta) = \int x_A y_A dA \quad (2.16)$$

Introducing (2.15a,b) into equation (2.8) and writing the result in the absolute and scalar form, gives

$$M_{xH} = \rho g \left[A_x z + v_0 (\bar{z}_{BO} - \bar{z}_G) \sin \phi + I_{xx} \sin \phi - I_{xy} \sin \theta \right] \quad (2.17)$$

$$M_{yH} = \rho g \left[-A_y z - I_{xy} \sin \phi + v_0 (\bar{z}_{BO} - \bar{z}_G) \sin \theta + I_{yy} \sin \theta \right]$$

Note that the geometrical parameters (2.11) and (2.16) depend on the instantaneous displacements of the ship (z, ϕ, θ) . These properties may be expanded in multi-variable Taylor series around the average position, i.e.,

$$A(z, \phi, \theta) = A_0 + \left. \frac{\partial A}{\partial z} \right|_0 z + \left. \frac{\partial A}{\partial \theta} \right|_0 \theta + \frac{1}{2} \left. \frac{\partial^2 A}{\partial z^2} \right|_0 z^2 + \left. \frac{\partial^2 A}{\partial z \partial \theta} \right|_0 z \theta + \frac{1}{2} \left. \frac{\partial^2 A}{\partial \phi^2} \right|_0 \phi^2 + \frac{1}{2} \left. \frac{\partial^2 A}{\partial \theta^2} \right|_0 \theta^2$$

$$A_x(z, \phi, \theta) = \left. \frac{\partial A_x}{\partial \phi} \right|_0 \phi + \left. \frac{\partial^2 A_x}{\partial z \partial \phi} \right|_0 z \phi + \left. \frac{\partial^2 A_x}{\partial \phi \partial \theta} \right|_0 \phi \theta$$

$$A_y(z, \phi, \theta) = A_y|_0 + \left. \frac{\partial A_y}{\partial z} \right|_0 z + \left. \frac{\partial A_y}{\partial \theta} \right|_0 \theta + \frac{1}{2} \left. \frac{\partial^2 A_y}{\partial z^2} \right|_0 z^2 + \left. \frac{\partial^2 A_y}{\partial z \partial \theta} \right|_0 z \theta + \frac{1}{2} \left. \frac{\partial^2 A_y}{\partial \phi^2} \right|_0 \phi^2 + \frac{1}{2} \left. \frac{\partial^2 A_y}{\partial \theta^2} \right|_0 \theta^2 \quad (2.18)$$

$$I_{xx}(z, \phi, \theta) = I_{xx}|_0 + \left. \frac{\partial I_{xx}}{\partial z} \right|_0 z + \left. \frac{\partial I_{xx}}{\partial \theta} \right|_0 \theta + \frac{1}{2} \left. \frac{\partial^2 I_{xx}}{\partial z^2} \right|_0 z^2 + \left. \frac{\partial^2 I_{xx}}{\partial z \partial \theta} \right|_0 z \theta + \frac{1}{2} \left. \frac{\partial^2 I_{xx}}{\partial \phi^2} \right|_0 \phi^2 + \frac{1}{2} \left. \frac{\partial^2 I_{xx}}{\partial \theta^2} \right|_0 \theta^2$$

$$I_{yy}(z, \phi, \theta) = I_{yy}|_0 + \left. \frac{\partial I_{yy}}{\partial z} \right|_0 z + \left. \frac{\partial I_{yy}}{\partial \theta} \right|_0 \theta + \frac{1}{2} \left. \frac{\partial^2 I_{yy}}{\partial z^2} \right|_0 z^2 + \left. \frac{\partial^2 I_{yy}}{\partial z \partial \theta} \right|_0 z \theta + \frac{1}{2} \left. \frac{\partial^2 I_{yy}}{\partial \phi^2} \right|_0 \phi^2 + \frac{1}{2} \left. \frac{\partial^2 I_{yy}}{\partial \theta^2} \right|_0 \theta^2$$

$$I_{xy}(z, \phi, \theta) = \left. \frac{\partial I_{xy}}{\partial \phi} \right|_0 \phi + \left. \frac{\partial^2 I_{xy}}{\partial z \partial \phi} \right|_0 z \phi + \left. \frac{\partial^2 I_{xy}}{\partial \phi \partial \theta} \right|_0 \phi \theta$$

where A_0 , $A_y|_0$, $I_{xx}|_0$, and $I_{yy}|_0$ are the geometric properties evaluated at the average plane of floatation. Note that the variation of first moment of area about the x -axis is dependent on an odd-order of roll angle. That dependence does not exist in variations of other geometrical parameters. Paulling and Rosenberg (1959)

showed that the dependencies of the heave and pitch coefficients on roll are of even-order, while the coefficients in roll due to heave and pitch are odd.

The restoring hydrodynamic force and moments given by equations (2.13) and (2.8) take the form

$$\begin{aligned}
F_H = \rho g \left\{ z A_0 - A_y \Big|_0 \sin \theta + \frac{\partial A}{\partial z} \Big|_0 z^2 + \frac{\partial A}{\partial \theta} \Big|_0 z (\theta + \sin \theta) + \frac{\partial A_x}{\partial \phi} \Big|_0 \phi \sin \phi \right. \\
\left. - \frac{\partial A_y}{\partial \theta} \Big|_0 \theta \sin \theta + \frac{1}{6} \frac{\partial^2 A}{\partial z^2} \Big|_0 z^3 + \frac{\partial^2 A}{\partial z \partial \theta} \Big|_0 z^2 (\theta + \sin \theta) + \frac{1}{2} \frac{\partial^2 A}{\partial \phi^2} \Big|_0 z \phi \left(\frac{\phi}{2} + \sin \phi \right) \right. \\
\left. + \frac{\partial^2 A_x}{\partial \phi \partial \theta} \Big|_0 \phi \left(\theta \sin \phi + \frac{\phi}{2} \sin \theta \right) + \frac{\partial^2 A}{\partial \theta^2} \Big|_0 z \theta \left(\frac{\theta}{2} + \sin \theta \right) - \frac{1}{2} \frac{\partial^2 A_y}{\partial \theta^2} \Big|_0 \theta^2 \sin \theta \right\} \quad (2.19a)
\end{aligned}$$

$$\begin{aligned}
M_{xH} = \rho g \left\{ v_0 (\bar{z}_{BO} - \bar{z}_G) \sin \phi + I_{xx} \Big|_0 z \sin \phi + \frac{\partial I_{xx}}{\partial z} \Big|_0 z (\phi + \sin \phi) + \frac{\partial I_{xx}}{\partial \theta} \Big|_0 (\theta \sin \phi + \phi \sin \theta) \right. \\
\left. + \frac{\partial^2 I_{xx}}{\partial z^2} \Big|_0 z^2 \left(\phi + \frac{1}{2} \sin \phi \right) + \frac{1}{2} \frac{\partial^2 I_{xx}}{\partial \theta^2} \Big|_0 \theta (\theta \sin \phi + \phi \sin \theta) \right. \\
\left. + \frac{\partial^2 I_{xx}}{\partial z \partial \theta} \Big|_0 z (\phi \theta + \theta \sin \phi + \phi \sin \theta) + \frac{1}{2} \frac{\partial^2 I_{xx}}{\partial \phi^2} \Big|_0 \phi^2 \sin \phi \right\} \quad (2.19b)
\end{aligned}$$

$$\begin{aligned}
M_{yH} = \rho g \left\{ v_0 (\bar{z}_{BO} - \bar{z}_G) \sin \theta - A_y \Big|_0 z + I_{yy} \Big|_0 \sin \theta - \frac{\partial A_y}{\partial z} \Big|_0 z^2 + \frac{\partial I_{yy}}{\partial z} \Big|_0 z (\theta + \sin \theta) \right. \\
\left. - \frac{\partial I_{xy}}{\partial \phi} \Big|_0 \phi \sin \phi + \frac{\partial I_{yy}}{\partial \theta} \Big|_0 \theta \sin \theta - \frac{1}{6} \frac{\partial^2 A_y}{\partial z^2} \Big|_0 z^3 + \frac{\partial^2 I_{yy}}{\partial z^2} \Big|_0 z^2 \left(\theta + \frac{1}{2} \sin \theta \right) - \frac{\partial^2 I_{xy}}{\partial z \partial \phi} \Big|_0 z \phi \left(\frac{\phi}{2} + \sin \phi \right) \right. \\
\left. + \frac{\partial^2 I_{yy}}{\partial z \partial \theta} \Big|_0 z \theta \left(\frac{\theta}{2} + \sin \theta \right) - \frac{\partial^2 I_{xy}}{\partial \phi \partial \theta} \Big|_0 \phi \theta \sin \phi + \frac{1}{2} \frac{\partial^2 I_{yy}}{\partial \phi^2} \Big|_0 \phi^2 \sin \theta + \frac{1}{2} \frac{\partial^2 I_{yy}}{\partial \theta^2} \Big|_0 \theta^2 \sin \theta \right\} \quad (2.19c)
\end{aligned}$$

In achieving the above equations use has been made of the following equalities verified by Neves and Rodrigues (2006)

$$\begin{aligned} \frac{\partial A}{\partial \theta} \Big|_0 &= -\frac{\partial A_y}{\partial z} \Big|_0, & \frac{\partial A_x}{\partial \phi} \Big|_0 &= \frac{\partial I_{xx}}{\partial z} \Big|_0, & \frac{\partial I_{xx}}{\partial \theta} \Big|_0 &= -\frac{\partial I_{xy}}{\partial \phi} \Big|_0, & \frac{\partial I_{yy}}{\partial z} \Big|_0 &= -\frac{\partial A_y}{\partial \theta} \Big|_0 \\ \frac{\partial^2 A}{\partial \phi^2} \Big|_0 &= \frac{\partial^2 A_x}{\partial z \partial \phi} \Big|_0 = \frac{\partial^2 I_{xx}}{\partial z^2} \Big|_0, & \frac{\partial^2 A}{\partial \theta^2} \Big|_0 &= -\frac{\partial^2 A_y}{\partial z \partial \theta} \Big|_0 = \frac{\partial^2 I_{yy}}{\partial z^2} \Big|_0, & \frac{\partial^2 A}{\partial z \partial \theta} \Big|_0 &= -\frac{\partial^2 A_y}{\partial z^2} \Big|_0 \\ -\frac{\partial^2 I_{xx}}{\partial z \partial \theta} \Big|_0 &= -\frac{\partial^2 I_{xy}}{\partial z \partial \phi} \Big|_0 = \frac{\partial^2 A_x}{\partial \phi \partial \theta} \Big|_0 = -\frac{\partial^2 A_y}{\partial \phi^2} \Big|_0, & \frac{\partial^2 I_{xx}}{\partial \theta^2} \Big|_0 &= -\frac{\partial^2 I_{xy}}{\partial \phi \partial \theta} \Big|_0 = \frac{\partial^2 I_{yy}}{\partial \phi^2} \Big|_0, & \frac{\partial^2 I_{yy}}{\partial z \partial \theta} \Big|_0 &= -\frac{\partial^2 A_y}{\partial \theta^2} \Big|_0 \end{aligned} \quad (2.20)$$

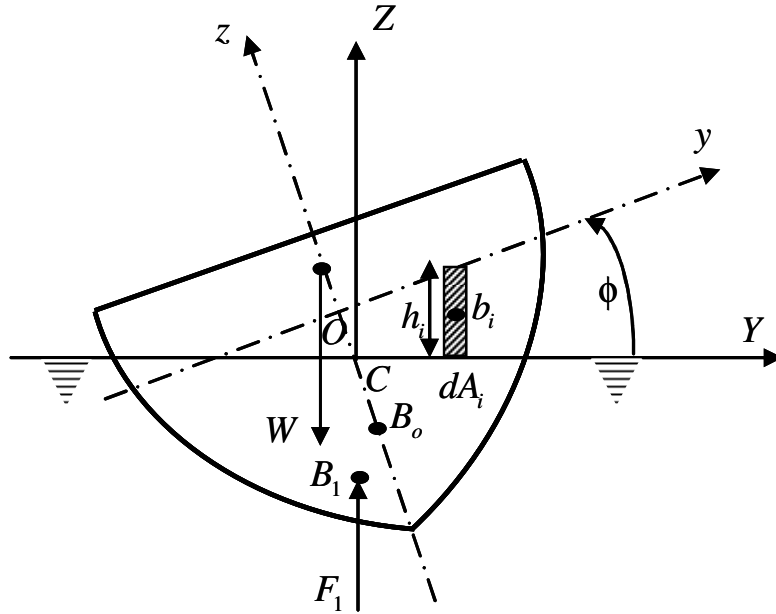


Figure 2.5. Ship schematic diagrams showing hydrostatic forces in a displaced position.

2.3.1 WAVE MOTION EFFECTS

The influence of incident sea waves of arbitrary direction along the hull is to change the average submerged shape defined by the instantaneous position of the wave. These waves exert external forces and moments in heave, roll, and pitch in addition they introduce an additional restoring forces and moments. For the case of head sea, Neves and Rodriguez (2006, 2007) considered the Airy linear theory in representing longitudinal waves (along x -axis) defined by the expression (Newman, 1977)

$$\eta(x, y, t; \chi) = \eta_0 \cos(kx + \omega_e t) \quad (2.21)$$

where η_0 is the wave amplitude, $k = \omega_w^2 / g = 2\pi / \lambda$ is the wave number, ω_w is the wave frequency, λ is the wave length, g is the gravitational acceleration, χ is the wave incidence, $\omega_e = (\omega_w - kU \cos \chi)$ is the encounter frequency of the wave by the ship when the ship advances with speed U .

Note that h_i expressed by equation (2.9) should read

$$h_i = -[z - \eta(x_{Ai}, y_{Ai}, t)] - y_{Ai} \sin \phi + x_{Ai} \sin \theta \quad (2.22)$$

The contributions of longitudinal waves to the restoring force, F_η , and the restoring moments, $M_{x\eta}$ and $M_{y\eta}$, obtained using Taylor series expansion about the average position up to third-order terms are given by the expressions (Neves and Rodriguez, 2006, 2007)

$$F_\eta = \left. \frac{\partial^2 F_\eta}{\partial \eta \partial z} \right|_0 z + \left. \frac{\partial^2 F_\eta}{\partial \eta \partial \theta} \right|_0 \theta + \left. \frac{\partial^3 F_\eta}{\partial \eta \partial z^2} \right|_0 z^2 + \left. \frac{\partial^3 F_\eta}{\partial \eta \partial z \partial \theta} \right|_0 z \theta + \left. \frac{\partial^3 F_\eta}{\partial \phi^2 \partial \eta} \right|_0 \phi^2 + \left. \frac{\partial^3 F_\eta}{\partial \eta^2 \partial \theta} \right|_0 \theta + \left. \frac{\partial^3 F_\eta}{\partial \eta \partial \theta^2} \right|_0 \theta^2 \quad (2.23a)$$

$$M_{x\eta} = \frac{\partial^2 M_{x\eta}}{\partial \eta \partial \phi} \Big|_0 \phi + \frac{\partial^3 M_{x\eta}}{\partial \eta \partial z \partial \phi} \Big|_0 z \phi + \frac{\partial^3 M_{x\eta}}{\partial \eta^2 \partial \phi} \Big|_0 \phi + \frac{\partial^3 M_{x\eta}}{\partial \eta \partial \phi \partial \theta} \Big|_0 \phi \theta \quad (2.23b)$$

$$M_{y\eta} = \frac{\partial^2 M_{y\eta}}{\partial \eta \partial z} \Big|_0 z + \frac{\partial^2 M_{y\eta}}{\partial \eta \partial \theta} \Big|_0 \theta + \frac{\partial^3 M_{y\eta}}{\partial \eta^2 \partial z} \Big|_0 z + \frac{\partial^3 M_{y\eta}}{\partial \eta \partial z^2} \Big|_0 z \theta + \frac{\partial^3 M_{y\eta}}{\partial \phi^2 \partial \eta} \Big|_0 \phi^3 + \frac{\partial^3 M_{y\eta}}{\partial \eta^2 \partial \theta} \Big|_0 \theta + \frac{\partial^3 M_{y\eta}}{\partial \theta^2 \partial \eta} \Big|_0 \theta^2 \quad (2.23c)$$

where the derivatives of the above equations are given by the following expressions:

$$\frac{\partial^2 F_\eta}{\partial \eta \partial z} \Big|_0 = 2\rho g \int_L \frac{\partial y}{\partial z} \eta dx, \quad \frac{\partial^2 F_\eta}{\partial \eta \partial \theta} \Big|_0 = -2\rho g \int_L x \frac{\partial y}{\partial z} \eta dx,$$

$$\frac{\partial^3 F_\eta}{\partial \phi^2 \partial \eta} \Big|_0 = -\rho g \int_L \left[2y \left(\frac{\partial y}{\partial z} \right)^2 + y \right] \eta dx,$$

$$\frac{\partial^3 F_\eta}{\partial \eta \partial z^2} \Big|_0 = \frac{\partial^3 F_\eta}{\partial \eta \partial z \partial \theta} \Big|_0 = \frac{\partial^3 F_\eta}{\partial \eta^2 \partial \theta} \Big|_0 = \frac{\partial^3 F_\eta}{\partial \eta \partial \theta^2} \Big|_0 = 0$$

$$\frac{\partial^2 M_{x\eta}}{\partial \eta \partial \phi} \Big|_0 = 2\rho g \int_L y^2 \frac{\partial y}{\partial z} \eta dx,$$

$$\frac{\partial^3 M_{x\eta}}{\partial \eta \partial z \partial \phi} \Big|_0 = -2\rho g \int_L \left[2y \left(\frac{\partial y}{\partial z} \right)^2 + y \right] \eta dx,$$

$$\frac{\partial^3 M_{x\eta}}{\partial \eta^2 \partial \phi} \Big|_0 = \rho g \int_L \left[2y \left(\frac{\partial y}{\partial z} \right)^2 + y \right] \eta^2 dx$$

$$\frac{\partial^3 M_{x\eta}}{\partial \eta \partial \phi \partial \theta} \Big|_0 = 2\rho g \int_L \left[2xy \left(\frac{\partial y}{\partial z} \right)^2 + xy \right] \eta dx \quad (2.24)$$

$$\frac{\partial^2 M_{y\eta}}{\partial \eta \partial z} \Big|_0 = -2\rho g \int_L x \frac{\partial y}{\partial z} \eta dx,$$

$$\frac{\partial^2 M_{y\eta}}{\partial \eta \partial \theta} \Big|_0 = 2\rho g \int_L x^2 \frac{\partial y}{\partial z} \eta dx,$$

$$\frac{\partial^3 M_{y\eta}}{\partial \phi^2 \partial \eta} \Big|_0 = \rho g \int_L \left[2xy \left(\frac{\partial y}{\partial z} \right)^2 + xy \right] \eta dx$$

$$\frac{\partial^3 M_{y\eta}}{\partial \eta^2 \partial z} \Big|_0 = \frac{\partial^3 M_{y\eta}}{\partial \eta \partial z^2} \Big|_0 = \frac{\partial^3 M_{y\eta}}{\partial \theta^2 \partial \eta} \Big|_0 = \frac{\partial^3 M_{y\eta}}{\partial \eta^2 \partial \theta} \Big|_0 = 0$$

Equations (2.23) constitute the restoring forces and moments taking into account the effects of ocean waves.

2.3.2 SHIPS ROLL DAMPING

The surface waves introduce inertia and drag hydrodynamic forces. The inertia force is the sum of two components. The first is a buoyancy force acting on the structure in the fluid due to a pressure gradient generated from the flow acceleration. The buoyancy force is equal to the mass of the fluid displaced by the structure multiplied by the acceleration of the flow. The second inertia component is due to the added mass, which is proportional to the relative acceleration between the structure and the fluid. This component accounts for the flow entrained by the structure. The drag force is the sum of the viscous and pressure drags produced by the relative velocity between the structure and the flow. This type of hydrodynamic drag is proportional to the square of the relative velocity.

Viscosity plays an important role in ship responses especially at large-amplitude roll motions in which the wave radiation damping is relatively low. The effect of the *bilge keel* on the roll damping was first discussed by Bryan (1900). Hishida (1952, 1954, 1955) proposed an analytical approach to roll damping for ship hulls in simple oscillatory waves. The regressive curve of the roll damping obtained from the experiments by Kato (1958) has been widely used in the prediction of ship

roll motions. Since amplitudes and frequencies are varying in random waves, the hydrodynamic coefficients are time-dependent and irregular. Several experimental investigations were conducted to measure the effect of *bilge keels* on the roll damping (see, e.g., Martin, 1958; Tanaka, 1957, 1958, 1959, 1961; Kato, 1965, Moody, 1961; Motter, 1967; and Jones 1978, 1979).

It was indicated by Bishop and Price (1978) that existing information on the structural damping of ships is far from satisfactory. It cannot be calculated and it can only be measured in the presence of hydrodynamic damping, whose nature and magnitude are also somewhat obscure. Yet it is very important. Much less is known about antisymmetric responses to waves, either as regards to the means of estimating them or the appropriate levels of hull damping. Vibration at higher frequencies, due to excitation by machinery (notably propellers), is limited by structural damping to a much greater extent than it is by the fluid actions of the sea. Damping measurements at these frequencies therefore give more accurate estimates of hull damping. The damping moment of ships is related to multiplicity of factors such as hull shape, loading condition, *bilge keel*, rolling frequency and range of rolling angle. For small roll angles, the damping moment is directly proportional to the angular roll velocity. But with increasing roll angle, non-linear damping will become significant. Due to the occurrence of strong viscous effects, the roll damping moment can not be computed by means of potential theory. Himeno (1981) provided a detailed description of the equivalent damping coefficient and expressed it in terms of various contributions due to hull skin friction damping, hull eddy shedding

damping, free surface wave damping, lift force damping, and bilge keel damping.

The viscous damping is due to the following sources:

- Wave-making moment, B_W .
- Skin-friction damping moment, B_F .
- The moment resulting from the bare hull arising from separation and eddies mostly near the bilge keels, B_E .
- Lift damping moment due to an apparent angle of attack as the ship rolls, B_L .
- Bilge-keel damping moment, B_{BK} .

Damping due to bilge keels can be decomposed into the following components:

- Bilge keels moment due to normal force, B_{BKN} .
- Moment due to interaction between hull and bilge keel, B_{BKH} .
- Modification to wave making due to the presence of bilge keels, B_{BKW} .

The damping components B_F , B_L , B_W , and B_{BKW} are linear, while B_E , B_{BKN} , and B_{BKH} are nonlinear. The linear and nonlinear damping moments can be expressed as follows

$$B_{lin} = B_F + B_L + B_W + B_{BKW} \tag{2.25}$$

$$B_{nonlin} = B_E + B_{BKN} + B_{BKH}$$

A pseudo-spectral model for nonlinear ship-surface wave interactions was developed by Lin et al. (2005). The algorithm is a combination of spectral and boundary element methods. All possible wave-wave interactions were included in

the model. The nonlinear bow waves at high Froude numbers⁴ from the pseudo-spectral model are much closer to the experimental results than those from linear ship wave models. One of the main problems in modeling ship-wave hydrodynamics is solving for the forcing (pressure) at the ship boundary. With an arbitrary ship, singularities occur in evaluating the velocity potential and the velocities on the hull. Inaccuracies in the evaluation of the singular terms in the velocity potential result in discretization errors, numerical errors, and excessive computational costs. Lin and Kuang (2006, 2008) presented a new approach to evaluating the pressure on a ship. They used the digital, self-consistent, ship experimental laboratory (DiSSEL) ship motion model to test its effectiveness in predicting ship roll motion. It was shown that the implementation of this roll damping component improves significantly the accuracy of numerical model results. Salvesen (1979) reported some results pertaining numerical methods such as large amplitude motion program (LAMP) used to evaluate hydrodynamic performance characteristics. These methods were developed for solving fully three-dimensional ship-motions, ship-wave-resistance and local-flow problems using linearized free-surface boundary conditions. Lin and Salvesen, 1997 and Lin, et al., 1998) examined the capabilities of the 3-D nonlinear time domain LAMP for the evaluation of fishing vessels operating in extreme waves. They extended their previous work to the modeling of maritime casualties, including a time domain simulation of a ship capsizing in stern quartering seas.

⁴ Froude number is a dimensionless number defined as the ratio of the body inertia to gravitational force. It is used to determine the resistance of an object moving through water.

The damping characteristics of a variety of ship shapes and offshore structures undergoing roll oscillation in the presence of ocean waves have been assessed by Chakrabarti (2001). Chakrabarti (2001) relied on empirical formulas derived from a series of model experiments reported by Ikeda (1984), Ikeda et al. (1978a,b, 1993). These experiments were performed on two-dimensional shapes. The damping roll moment $B(\dot{\phi})$ is nonlinear and may be expressed by the expression (Chakrabarti, 2001; and El-Bassiouny, 2007).

$$B(\dot{\phi}) = c_1\dot{\phi} + c_2\dot{\phi}|\dot{\phi}| + c_3\dot{\phi}^3 + \dots = \sum_{k=1}^K c_k\dot{\phi}|\dot{\phi}|^{k-1} \quad (2.26)$$

The first term is the usual linear viscous damping, the second is the quadratic damping term originally developed by Morison et al. (1950). It is in phase with the velocity but it is quadratic because the flow is separated and the drag is primarily due to pressure rather than the skin friction. Sarpkaya and Isaacson (1981) provided a critical assessment of Morison's equation, which describes the forces acting on a pile due to the action of progressive waves. The third term is cubic damping. The total damping may be replaced by an equivalent viscous term in the form

$$B(\dot{\phi}) = c_{eq}\dot{\phi} \quad (2.27)$$

where c_{eq} is the equivalent damping coefficient. This coefficient can be expressed in terms of the nonlinear coefficients as

$$c_{eq} = c_1 + \frac{8}{3\pi}c_2(\omega\phi_0) + \frac{3}{4}c_3(\omega\phi_0)^2 \quad (2.28)$$

where ω is the wave frequency and ϕ_0 is the amplitude of the ship roll angle.

Dalzell (1978) replaced the nonlinear damping term $\dot{\phi}|\dot{\phi}|$ by an equivalent smooth non-linear polynomial given by

$$\dot{\phi}|\dot{\phi}| = \sum_{k=1,3,\dots} \alpha_k \frac{\dot{\phi}^k}{(\dot{\phi}_c)^{k-2}} \cong \frac{5}{16} \dot{\phi}_c \dot{\phi} + \frac{35}{48} \frac{\dot{\phi}^3}{\dot{\phi}_c} \quad (2.29)$$

where $\dot{\phi}_c$ is the maximum amplitude of roll velocity. The numerical coefficients α_k were estimated by using least-square fitting.

Haddara (1992) employed the concept of the random decrement⁵ in the damping identification of linear systems. He extended the concept of the random decrement for a ship performing roll motion in random beam waves. Wave excitation was assumed to be a Gaussian white noise process. The equations were used to identify the parameters of the nonlinear roll damping moment. Wu et al. (2005) conducted an experimental investigation to measure the nonlinear roll damping of a ship in regular and irregular waves.

2.3.3 SHIP INERTIA FORCES AND MOMENTS

The inertia forces and moments in heave, roll and pitch motions are mainly due to the ship mass and mass moment of inertia and the corresponding added mass terms. These are well documented in Neves and Rodriguez (2006) and are given in the form

⁵ The random decrement technique is a time domain procedure, where the system responses to applied loads are transformed into random decrement functions. These functions are proportional to the correlation functions of the system responses or can, equivalently, be considered as free vibration responses.

$$F_{zI} = (m + Z_z) \ddot{z} + Z_{\theta} \ddot{\theta}$$

$$M_{xI} = (J_{xx} + K_{\phi}) \ddot{\phi} \quad (2.30)$$

$$M_{yI} = (J_{yy} + K_{\theta}) \ddot{\theta} + M_z \ddot{z}$$

where m is the ship mass, J_{xx} and J_{yy} are the ship mass moment of inertia about roll and pitch axes, Z_z is the hydrodynamic added mass in heave, Z_{θ} is the hydrodynamic added inertia in heave due to pitch motion, K_{ϕ} and K_{θ} are the hydrodynamic added polar mass moment of inertia about the ship roll and pitch axes, respectively, and M_z is the added inertia in pitch due to heave motion. The added inertia parameters may be evaluated using the potential theory as described by Salvesen et al. (1970) and Meyers et al. (1975).

2.3.4 GOVERNING EQUATIONS OF MOTION

Applying Newton's second law, the equations governing heave-roll-pitch motion may be written in the form:

The heave equation of motion is,

$$\begin{aligned} (m + Z_z) \ddot{z} + Z_{\theta} \ddot{\theta} + C_z \dot{z} + \rho g \left\{ z A_0 - A_y \right\}_0 \sin \theta + \left. \frac{\partial A}{\partial z} \right|_0 z^2 + \left. \frac{\partial A}{\partial \theta} \right|_0 z (\theta + \sin \theta) + \left. \frac{\partial A_x}{\partial \phi} \right|_0 \phi \sin \phi \\ - \left. \frac{\partial A_y}{\partial \theta} \right|_0 \theta \sin \theta + \left. \frac{1}{6} \frac{\partial^2 A}{\partial z^2} \right|_0 z^3 + \left. \frac{\partial^2 A}{\partial z \partial \theta} \right|_0 z^2 (\theta + \sin \theta) + \left. \frac{1}{2} \frac{\partial^2 A}{\partial \phi^2} \right|_0 z \phi \left(\frac{\phi}{2} + \sin \phi \right) \\ + \left. \frac{\partial^2 A_x}{\partial \phi \partial \theta} \right|_0 \phi \left(\theta \sin \phi + \frac{\phi}{2} \sin \theta \right) + \left. \frac{\partial^2 A}{\partial \theta^2} \right|_0 z \theta \left(\frac{\theta}{2} + \sin \theta \right) - \left. \frac{1}{2} \frac{\partial^2 A_y}{\partial \theta^2} \right|_0 \theta^2 \sin \theta \end{aligned}$$

$$+2\rho g z \int_L \frac{\partial y}{\partial z} \eta(t) dx - 2\rho g \theta \int_L x \frac{\partial y}{\partial z} \eta(t) dx - \rho g \phi^2 \int_L \left[2y \left(\frac{\partial y}{\partial z} \right)^2 + y \right] \eta(t) dx = Z(t) \quad (2.31)$$

The roll moment equation of motion taking into account the beam sea hydrodynamic wave excitation moment, $\Phi(t)$, is,

$$\begin{aligned} & (J_{xx} + K_{\phi}) \ddot{\phi} + \sum_{k=1}^K c_k \dot{\phi} |\dot{\phi}|^{k-1} + \rho g \left\{ v_0 (\bar{z}_{BO} - \bar{z}_G) \sin \phi + I_{xx} \Big|_0 z \sin \phi + \frac{\partial I_{xx}}{\partial z} \Big|_0 z (\phi + \sin \phi) \right. \\ & \left. + \frac{\partial I_{xx}}{\partial \theta} \Big|_0 (\theta \sin \phi + \phi \sin \theta) + \frac{\partial^2 I_{xx}}{\partial z^2} \Big|_0 z^2 \left(\phi + \frac{1}{2} \sin \phi \right) + \frac{1}{2} \frac{\partial^2 I_{xx}}{\partial \theta^2} \Big|_0 \theta (\theta \sin \phi + \phi \sin \theta) \right. \\ & \left. + \frac{\partial^2 I_{xx}}{\partial z \partial \theta} \Big|_0 z (\phi \theta + \theta \sin \phi + \phi \sin \theta) + \frac{1}{2} \frac{\partial^2 I_{xx}}{\partial \phi^2} \Big|_0 \phi^2 \sin \phi \right\} \\ & + 2\rho g \phi \int_L y^2 \frac{\partial y}{\partial z} \eta(t) dx - 2\rho g z \phi \int_L \left[2y \left(\frac{\partial y}{\partial z} \right)^2 + y \right] \eta(t) dx + \rho g \phi \int_L \left[2y \left(\frac{\partial y}{\partial z} \right)^2 + y \right] \eta^2(t) dx \\ & + 2\rho g \phi \theta \int_L \left[2xy \left(\frac{\partial y}{\partial z} \right)^2 + xy \right] \eta(t) dx = \Phi(t) \end{aligned} \quad (2.32)$$

The pitch moment equation of motion taking into account the beam sea hydrodynamic wave excitation moment, $\Theta(t)$, is,

$$\begin{aligned} & (J_{yy} + K_{\theta}) \ddot{\theta} + M_{\ddot{z}} \ddot{z} + C_{\dot{\theta}} \dot{\theta} + \rho g \left\{ v_0 (\bar{z}_{BO} - \bar{z}_G) \sin \theta - A_y \Big|_0 z + I_{yy} \Big|_0 \sin \theta - \frac{\partial A_y}{\partial z} \Big|_0 z^2 \right. \\ & \left. + \frac{\partial I_{yy}}{\partial z} \Big|_0 z (\theta + \sin \theta) - \frac{\partial I_{xy}}{\partial \phi} \Big|_0 \phi \sin \theta + \frac{\partial I_{yy}}{\partial \theta} \Big|_0 \theta \sin \theta - \frac{1}{6} \frac{\partial^2 A_y}{\partial z^2} \Big|_0 z^3 + \frac{\partial^2 I_{yy}}{\partial z^2} \Big|_0 z^2 \left(\theta + \frac{1}{2} \sin \theta \right) \right. \\ & \left. - \frac{\partial^2 I_{xy}}{\partial z \partial \phi} \Big|_0 z \phi \left(\frac{\phi}{2} + \sin \phi \right) + \frac{\partial^2 I_{yy}}{\partial z \partial \theta} \Big|_0 z \theta \left(\frac{\theta}{2} + \sin \theta \right) - \frac{\partial^2 I_{xy}}{\partial \phi \partial \theta} \Big|_0 \phi \theta \sin \phi + \frac{1}{2} \frac{\partial^2 I_{yy}}{\partial \phi^2} \Big|_0 \phi^2 \sin \theta \right. \\ & \left. + \frac{1}{2} \frac{\partial^2 I_{yy}}{\partial \theta^2} \Big|_0 \theta^2 \sin \theta \right\} - 2\rho g z \int_L x \frac{\partial y}{\partial z} \eta(t) dx + 2\rho g \theta \int_L x^2 \frac{\partial y}{\partial z} \eta(t) dx \end{aligned}$$

$$+\rho g \phi^3 \int_L \left[2xy \left(\frac{\partial y}{\partial z} \right)^2 + xy \right] \eta(t) dx = \Theta(t) \quad (2.33)$$

where $C_{\dot{z}}$ and $C_{\dot{\theta}}$ are linear damping coefficients associated with heave and pitch motions, respectively. $Z(t)$, $\Phi(t)$, and $\Theta(t)$ are the external excitations due to sea waves. One can extract from the above three equations the coupled roll-pitch equations of motion or the purely roll equation of motion.

2.3.4.1 Coupled Roll-Pitch Equations of Motion

Considering the coupled roll-pitch equations of motion, equations (2.32) and (2.33) take the form

$$\begin{aligned} (J_{xx} + K_{\phi}) \ddot{\phi} + \sum_{k=1}^K c_k \dot{\phi} |\dot{\phi}|^{k-1} + \rho g \left\{ v_0 (\bar{z}_{BO} - \bar{z}_G) \sin \phi + \frac{\partial I_{xx}}{\partial \theta} \Big|_0 (\theta \sin \phi + \phi \sin \theta) \right. \\ \left. + \frac{1}{2} \frac{\partial^2 I_{xx}}{\partial \theta^2} \Big|_0 \theta (\theta \sin \phi + \phi \sin \theta) + \frac{1}{2} \frac{\partial^2 I_{xx}}{\partial \phi^2} \Big|_0 \phi^2 \sin \phi \right\} + 2\rho g \phi \int_L y^2 \frac{\partial y}{\partial z} \eta(t) dx \\ + \rho g \phi \int_L \left[2y \left(\frac{\partial y}{\partial z} \right)^2 + y \right] \eta^2(t) dx + 2\rho g \phi \theta \int_L \left[2xy \left(\frac{\partial y}{\partial z} \right)^2 + xy \right] \eta(t) dx = \Phi(t) \end{aligned} \quad (2.34a)$$

$$\begin{aligned} (J_{yy} + K_{\theta}) \ddot{\theta} + C_{\dot{\theta}} \dot{\theta} + \rho g \left\{ v_0 (\bar{z}_{BO} - \bar{z}_G) \sin \theta + I_{yy} \Big|_0 \sin \theta - \frac{\partial I_{xy}}{\partial \phi} \Big|_0 \phi \sin \phi + \frac{\partial I_{yy}}{\partial \theta} \Big|_0 \theta \sin \theta \right. \\ \left. - \frac{\partial^2 I_{xy}}{\partial \phi \partial \theta} \Big|_0 \phi \theta \sin \phi + \frac{1}{2} \frac{\partial^2 I_{yy}}{\partial \phi^2} \Big|_0 \phi^2 \sin \theta + \frac{1}{2} \frac{\partial^2 I_{yy}}{\partial \theta^2} \Big|_0 \theta^2 \sin \theta \right\} + 2\rho g \theta \int_L x^2 \frac{\partial y}{\partial z} \eta(t) dx \\ + \rho g \phi^3 \int_L \left[2xy \left(\frac{\partial y}{\partial z} \right)^2 + xy \right] \eta(t) dx = \Theta(t) \end{aligned} \quad (2.34b)$$

Note that the nonlinear coupling terms may result in nonlinear internal resonances among pitch and roll motions (see, e.g., Nayfeh et al., 1974; and Nayfeh and Mook, 1979).

2.3.4.2 Roll Equation of Motion

The prediction of ship stability during the early stages of design is very important from the point of a vessel's safety. Of the six motions of a ship, the critical motion leading to capsize is the rolling motion. Thus for studying roll stability in beam seas one should consider the nonlinear roll equation

$$\begin{aligned} (J_{xx} + K_{\dot{\phi}}) \ddot{\phi} + \sum_{k=1}^K c_k \dot{\phi} |\dot{\phi}|^{k-1} + \rho g \left[v_0 (\bar{z}_{BO} - \bar{z}_G) + \frac{1}{2} \frac{\partial^2 I_{xx}}{\partial \phi^2} \Big|_0 \phi^2 \right] \sin \phi \\ + 2\rho g \phi \int_L y^2 \frac{\partial y}{\partial z} \eta(t) dx + \rho g \phi \int_L \left[2y \left(\frac{\partial y}{\partial z} \right)^2 + y \right] \eta^2(t) dx = \Phi(t) \end{aligned} \quad (2.35)$$

In formulating the roll equation in beam seas one should realize that the hydrodynamic roll moments on the ship are dependent on the relative motion of ship and wave, rather than upon the absolute roll motion. In a beam sea the relative roll is defined as $(\phi - \alpha)$, where α is the local wave slope in a long-crested regular beam sea. In this case, the nonlinear equation of roll motion may be written in the form (Wright and Marshfield, 1979)

$$J_{xx} \ddot{\phi} = -\delta J_{xx} (\ddot{\phi} - \ddot{\alpha}) - H(\dot{\phi} - \dot{\alpha}) - E(\phi - \alpha) + B \quad (2.36)$$

where δJ_{xx} is the roll added inertia and B is the bias moment created by several sources such as a steady beam wind, a shift of cargo, or water or ice on deck. Setting $\phi_r = \phi - \alpha$, equation (2.36) takes the form (see, e.g., Kuo and Odabasi, 1974)

$$(J_{xx} + \delta J_{xx})\ddot{\phi}_r + H\dot{\phi}_r + E\phi_r = B - J_{xx}\ddot{\alpha} \quad (2.37)$$

Wright and Marshfield (1979) solved equation (2.37) for small nonlinear restoring moment and small linear and cubic damping near the resonance frequency using three different approximate techniques: perturbation method, averaging method, and harmonic balance. Lin and Salvesen (1997) presented an assessment of the Large Amplitude Motion Program (LAMP) for evaluating ship performance in extreme seas. The study included a time domain simulation of a ship capsizing in beam seas. It was shown that capsizing can happen due to dynamic effects even for ships that satisfy the minimum righting arm requirement. Surendran and Reddy (2002, 2003) evaluated the performance of a ship in beam seas using strip theory. The critical condition in the rolling motion of a ship is when it is subjected to synchronous beam waves (i.e., the encounter frequency coincides with the wave frequency). They considered various representations of damping and restoring terms to identify the effect of wave amplitude, wave frequency, and metacentric height (represented by a quintic polynomial).

Contento et al. (1996) reported some results of experimental tests on nonlinear rolling in a regular beam sea of a Ro-Ro ship model by varying both the wave steepness and the wave frequency. They adopted a parameter estimation technique based on the least squares fitting of the stationary numerical solution of the nonlinear rolling motion differential equation. It was possible to extract information on the damping model and on the linear and nonlinear damping coefficients. These exhibit a quite strong dependence on frequency that reduces the efficiency of constant coefficients rolling equation to simulate large amplitude

nonlinear rolling. The results indicated that a good quality prediction model of nonlinear rolling cannot be based on constant coefficients time-domain simulations. The analysis indicated also a marked dependence of the effective wave slope coefficient on wave amplitude. The effect of the excitation modeling on the fitting capability of the nonlinear roll motion equation to experimental data was studied by Francescutto et al. (1998). Several frequency dependent and constant effective wave slope coefficients were derived for five different scale models corresponding to different ship typologies by a parameter identification technique. Later, Francescutto and Contento (1999) studied the steady rolling response in a regular beam sea of a 1:50 scale model of a destroyer in the bare hull condition. In view of the softening characteristics of the restoring moment, bifurcations with jump in amplitude and phase at two different wave frequencies were observed experimentally. Exact numerical solutions were used to obtain reliable values of the coefficients of the mathematical model to be used for the roll motion simulation.

Mahfouz (2004) presented a robust method for the identification of linear and nonlinear damping and restoring parameters in the equation describing the rolling motion of a ship using only its measured response at sea. The parameters were identified using a combination of the random decrement technique, auto- and cross-correlation functions, a linear regression algorithm, and a neural-network technique.

2.3.5 MEMORY EFFECT

Note that the previous formulation did not account for the hydrodynamic memory effect. The hydrodynamic load due to the ship motion is a function of its

frequency of oscillation. When the ship oscillates, waves will be generated on the free surface. As time increases, these waves will propagate outward from the body, but they continue to affect the fluid pressure and hence the body force for all subsequent times (Newman, 1977). In the time domain, this force or moment can be represented by a convolution integral of the impulse response function as outlined by Cummins (1962), i.e.,

$$F_{ij} = -\alpha_{ij}(\infty)\dot{V}_j - \int_{-\infty}^t K_{ij}(t-\tau)V_j(\tau)d\tau, \quad i, j=1,2,3 \quad (2.38)$$

where $i, j=1,2,3$ indicate surge, sway, and yaw, respectively. $V_j(\tau)$ is the ship velocity along the axis j , α_{ij} is the ship added mass, and $K_{ij}(t-\tau)$ is the retardation function and can be expressed in terms of the velocity potential function φ as

$$K_{ij}(t-\tau) = \rho \iint_S \frac{\partial \varphi_j(t-\tau)}{\partial \tau} s_i d\sigma \quad (2.39)$$

where s_i is the i th component of the normal vector of the surface element $d\sigma$. Chung and Bernitsas (1997) evaluated these forces in details.

A component of this force initiated at a certain moment continues to attribute its influence on the system for a period of time. This is referred to as the hydrodynamic memory effect (Chung and Bernitsas, 1997). It was indicated that calculating this effect in the time domain is very time-consuming. Tick (1959) represented the convolution integral by a set of recursive differential equations with constant coefficients. These coefficients are determined by curve-fitting the added mass and damping in the frequency domain. This method was used for estimating

the memory effect on ship maneuvering by McCreight (1986), a single-point mooring tanker by Jiang et al. (1987) and Sharma et al. (1988), and other motions by Schmiechen (1974, 1975).

2.4 Closing Remarks

The nonlinear dynamic modeling of ship motions in roll, pitch and heave has been formulated. The formulation has been adopted from the work of Neves et al. (2006, 2007). One can use the coupled nonlinear equations motion to examine only the ship motion in roll oscillations under regular and random sea waves. Other issues related to this modeling deal with the effect of roll damping and hydrodynamic memory effect arising from the ship motion. An extended version of this chapter has been published by Ibrahim and Grace (2010). The literature has not addressed the interaction of roll dynamics with icebergs or rigid barriers which will be addressed in the next chapter.

CHAPTER 3

ELASTIC IMPACT OF SHIP ROLL MOTION WITH SOLID ICE

3.1 Introduction

The previous chapter presented the ship coupled nonlinear equations of motion in heave, roll and pitch. From these equations the uncoupled equation of motion in roll was extracted in its general form. This chapter considers the dynamic behavior of ships' roll motion under elastic impact with one sided ice barrier or rigid structure. The uncoupled equation of ship roll motion developed in Chapter 2 is considered under beam wave sinusoidal excitation. The ship response is expected to be periodic as long as the roll angle does not exceed the barrier angle. However, as soon the ship reaches the barrier at zero velocity it then experiences what is known as the *grazing bifurcation*. In order to examine the dynamic behavior of the ship experiencing impact with the barrier, Zhuravlev non-smooth coordinate transformation will be introduced to transform the equation of motion in a form that does not include impact. The unperturbed ship roll dynamics will be studied to identify the grazing orbit in terms of initial conditions. For all initial conditions covered by the grazing orbit, the perturbed ship dynamics is estimated numerically in terms of excitation amplitude and frequency due to wave roll moment. The basins of attraction of safe operation are obtained in order to determine the safe conditions for operation.

3.2 Modeling of Elastic Ice Impact Loading

In the absence of pitch, the nonlinear equation of roll motion of ship was given

by equation (2.37) in Chapter 2 in the form

$$\begin{aligned} & (J_{xx} + K_{\ddot{\phi}})\ddot{\phi} + \sum_{k=1}^K c_k \dot{\phi} |\dot{\phi}|^{k-1} + \rho g \left[v_0 (\bar{z}_{BO} - \bar{z}_G) + \frac{1}{2} \frac{\partial^2 I_{xx}}{\partial \phi^2} \Big|_0 \phi^2 \right] \sin \phi \\ & + 2\rho g \phi \int_L y^2 \frac{\partial y}{\partial z} \eta(t) dx + \rho g \phi \int_L \left[2y \left(\frac{\partial y}{\partial z} \right)^2 + y \right] \eta^2(t) dx = \Phi(t) \end{aligned} \quad (3.1)$$

where ϕ is the roll angle, $\Phi(t)$ is the beam sea hydrodynamic wave excitation moment, η is the longitudinal wave which is a function of wave height, wave number, and wave length. In the absence of longitudinal waves, and after dividing both sides of equation (3.1) by $(J_{xx} + K_{\ddot{\phi}})$, one may write equation (3.1) in the form

$$\ddot{\phi} + 2\zeta\omega_n\dot{\phi} + a\dot{\phi}|\dot{\phi}| + \omega_n^2\phi + C_3\phi^3 + C_5\phi^5 = \xi(t) \quad (3.2)$$

where the third expression in equation (3.1) was expanded in polynomial through curve fitting. ζ is the linear damping ratio, ω_n is the undamped natural frequency, the third term on the left hand side in equation (3.2) represents the nonlinear damping moment where a is constant and can be determined experimentally, $\xi(t) = \Phi(t)/(J_{xx} + K_{\ddot{\phi}})$, and the coefficients $C_1 > 0$, $C_3 < 0$, and $C_5 > 0$ can be obtained experimentally. Introducing the non-dimensional parameters $\tau = \omega_n t$ and $q = \phi/\phi_c$, $q_i = \dot{\phi}_i/\dot{\phi}_c$, where ϕ_c is the ship capsizing angle, equation (3.2) takes the form

$$q'' + \bar{\zeta}q' + \gamma q'|q'| + q + \bar{C}_3q^3 + \bar{C}_5q^5 = Z(\tau) \quad (3.3)$$

where a prime denotes differentiation with respect to the non-dimensional time parameter τ , $\bar{\zeta} = 2\zeta$, $\bar{C}_3 = C_3(\phi_c^2/\omega_n^2)$, $\bar{C}_5 = C_5(\phi_c^4/\omega_n^2)$, $Z(\tau) = \xi(t)/\omega_n^2\phi_c$ and

$\gamma = a\phi_c^2$. Equation (3.3) is a nonlinear differential equation describing the ship roll dynamics under nonlinear hydrodynamic sea waves. One can adopt a non-smooth coordinate transformation introduced by Zhuravlev (1976). Zhuravlev assumed rigid barriers and converts the vibro-impact system into an oscillator without barriers such that the equations of motion do not contain any impact terms. The transformed system is then solved using any asymptotic technique. For the one-sided-barrier shown in Figure 3.1, and placed at $q = -q_i$, the following transformation may be introduced

$$q = z \operatorname{sgn}(z) - q_i \quad (3.4)$$

This transformation shifts the barrier to the axis $z = 0$ and maps the domain $q > -q_i$ of the phase plane trajectories on the original plane (q, q') to the new phase plane (z, z') . The ship equation of motion takes the following form

$$z'' + \bar{\zeta} z' + \gamma z'^2 \operatorname{sgn}(z') + z + \operatorname{sgn}(z) [-q_i + \bar{C}_3 (z \operatorname{sgn}(z) - q_i)^3 + \bar{C}_5 (z \operatorname{sgn}(z) - q_i)^5] = Z(\tau) \operatorname{sgn}(z) \quad (3.5)$$

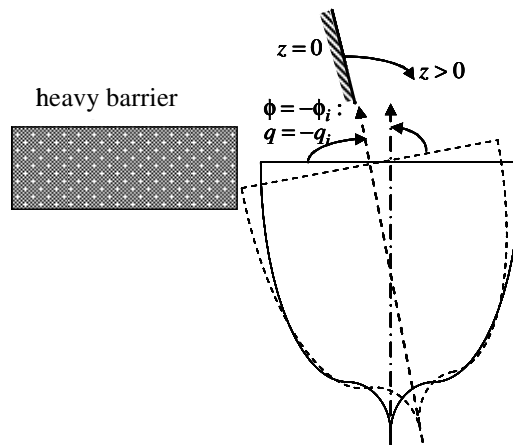


Figure 3.1. Schematic diagram of one-sided barrier impact with ship in roll oscillation.

3.3 Unperturbed Ship Dynamics

In the absence of damping the unperturbed motion equation (3.5) takes the form

$$z'' + \Gamma(z) = 0 \quad (3.6)$$

where $\Gamma(z) = z + \text{sgn}(z) \left[-q_i + \bar{C}_3 (z \text{sgn}(z) - q_i)^3 + \bar{C}_5 (z \text{sgn}(z) - q_i)^5 \right]$ is the nonlinear restoring moment of the ship and is shown in Figure 3.2(a) for an impact angle $q_i = -0.4$, and nonlinear coefficients $\bar{C}_3 = -1.1$, and $\bar{C}_5 = 0.1$. It is seen that the restoring moment vanishes at $z = 0.4$. The potential energy, $\Pi(z)$, is obtained by integrating the restoring moment $\Gamma(z)$ over the limits q_i and z , i.e.,

$$\Pi(z) = \int_{q_i}^z \Gamma(y) dy = a_6 z^6 + a_5 z^5 + a_4 z^4 + a_3 z^3 + a_2 z^2 + a_1 z + a_0 \quad (3.7)$$

where, $a_0 = \frac{q_i^2}{12} \left[-6 + 21C_3 q_i^2 - 62C_5 q_i^4 + 4 \text{sgn}(z)(3 - 6C_3 q_i^2 + 16C_5 q_i^4) \right]$,

$$a_1 = -q_i \text{sgn}(z) (1 - C_3 q_i^2 + C_5 q_i^4), \quad a_2 = \frac{1}{2} (1 - 3C_3 q_i^2 + 5C_5 q_i^4),$$

$$a_3 = \frac{1}{3} q_i \text{sgn}(z) (3C_3 - 10C_5 q_i^2), \quad a_4 = -\frac{1}{4} (C_3 - 10C_5 q_i^2), \quad a_5 = -C_5 q_i \text{sgn}(z), \quad a_6 = \frac{1}{6} C_5.$$

Note that the lower limit, q_i , is chosen such that at q_i the potential energy is minimum as shown in Figure 3.2(b). It is seen at $z = 0$ (corresponding to ship angle $q = -q_i$) the potential has a maximum of $\Pi(z = 0) = 0.0730283$. The Hamiltonian of system (3.5), $H = \frac{1}{2} Z'^2 + \Pi(z)$, possesses the first integral of motion

$$z' = \pm \sqrt{2[H - \Pi(z)]} \quad (3.8)$$

As long as $H > \Pi(z)$ the phase diagram is periodic closed orbit in the phase space $\{z, z'\}$ as shown in Figure 3.3. With reference to Figure 3.2(b), H reaches its maximum value $H_{\max} = \Pi(z=0) = 0.0730283$. The periodic orbits are only restricted inside the domain $D = \{(z, z') \mid H \leq H_c\}$, where $H_c = H_{\max} - \Delta H$, and ΔH is sufficiently small. H_c is the critical energy level above which impact of the ship will take place, and the trajectories of motion will be structurally unstable. The motion corresponding to $H_{\max} = 0.0730283$ follows a critical orbit shown by the dashed curve in Figure 3.3. This orbit describes the grazing impact of the ship with one-side barrier.

Let the system be given an initial velocity z_0' , i.e., $H = z_0'^2/2$. The period of oscillation, T , can be estimated from equation (3.8) as

$$T = \frac{1}{\sqrt{2}} \int_0^z \frac{dz}{\sqrt{(z_0'^2/2) - \Pi(z)}} \quad (3.9)$$

Note that $\Pi(z) < 0.0730283$ for the entire range of the ship motion before capsizing as shown in Figure 3.3. The character of motion depends on the value of initial velocity ($z_0'^2/2$). For $z_0'^2/2 < 0.0730283$ the integrand is always real and z can assume any value within a range governed by the condition $(z_0'^2/2) - \Pi(z) = 0$. For a given initial energy, $z_0'^2/2 < 0.0730283$, the ship will oscillate between two values z_1 and z_2 and the corresponding period of oscillation is

$$T = \frac{1}{\sqrt{2}} \int_{z_2}^{z_1} \frac{dz}{\sqrt{\left(\frac{z_0'^2}{2}\right) - \Pi(z)}} \quad (3.10)$$

If $z_0'^2/2 = 0.0730283$, the integrand is real and approaches ∞ and the ship is at the verge of capsizing. If $z_0'^2/2 > 0.0730283$, the integrand is always real and the value of z increases indefinitely. In this case, the motion is unbounded and the ship will acquire a rollover motion.

The grazing orbit shown in Figure 3.3 by the dashed closed curve is divided in a large number of elements as shown in Figure 3.4. Each element has an average value of (z_0, z_0') , represent an initial condition given to the ship. Equation (3.5) will be solved numerically for each of these conditions. The results are discussed in the next section.

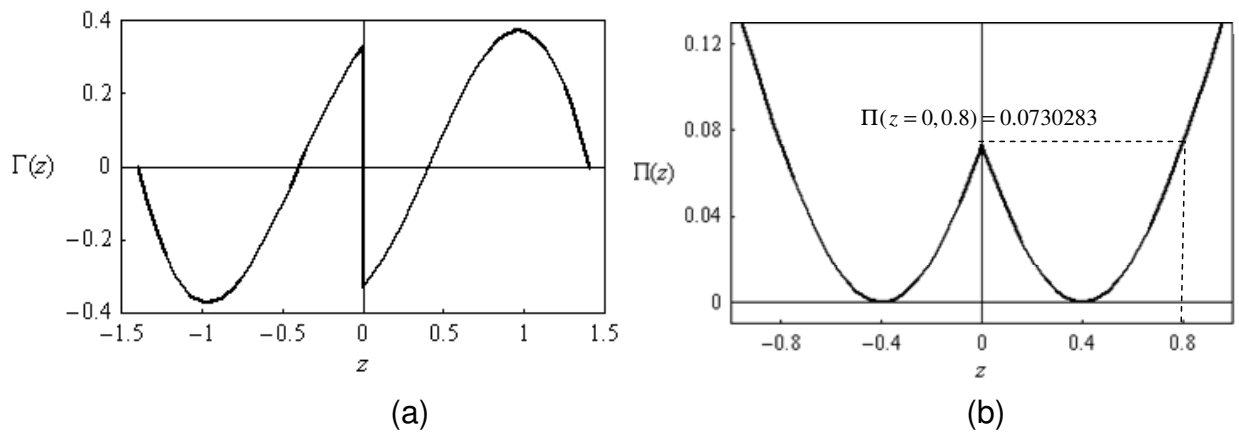


Figure 3.2. (a) Restoring moment of the ship for the case of $q_i > 0$, and
 (b) Potential energy of the ship restoring moment in terms of Zhuravlev's non-smooth coordinate z .

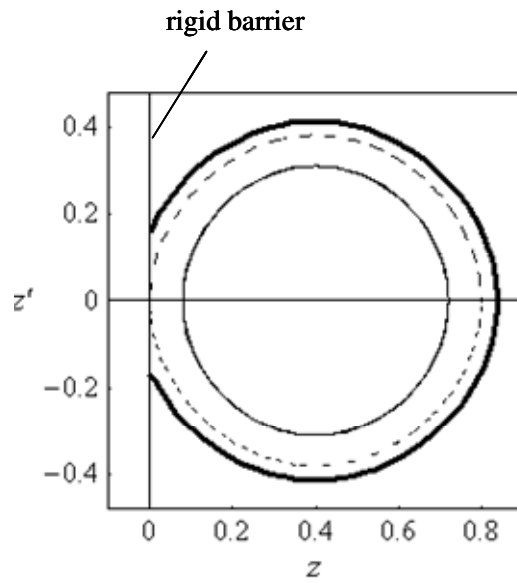


Figure 3.3. Phase portraits for — $H = 0.11$ (impact orbit),
 --- $H = 0.0730283$ (Grazing impact), — $H = 0.03$ (periodic oscillation).

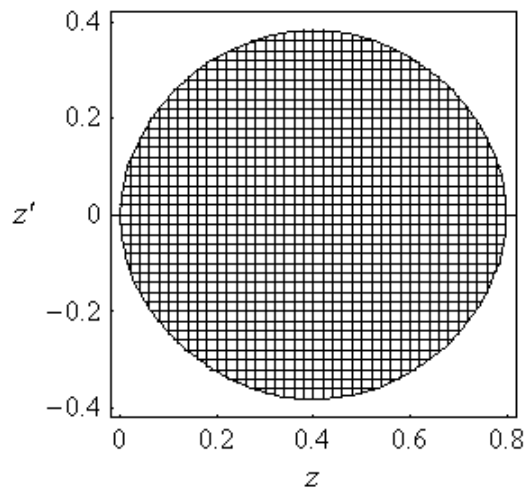


Figure 3.4. The grazing orbit in Figure 3.3 divided into a huge number of initial conditions.

3.4 Ship Roll Motion under Sinusoidal Excitation

Under sinusoidal excitation $Z(\tau) = a \sin \nu \tau$, where a is the nondimensional excitation amplitude of the roll excitation moment, and ν the excitation frequency ratio; $\nu = \Omega / \omega_n$, Ω is the roll excitation frequency, equation (3.5) was solved numerically under different values of excitation amplitude and frequency. The numerical solution was obtained for all initial conditions occupying the grazing orbit shown in Figure 3.4. In section 3.4.1, the effect of excitation amplitude on ship roll motion is examined for three different values of excitation frequency; $\nu = 0.88, 0.94,$ and 1.2 . In section 3.4.2, the effect of excitation frequency is examined for an excitation amplitude; $a = 0.08$.

3.4.1 EXCITATION AMPLITUDE AS A CONTROL PARAMETER

3.4.1.1 Excitation Frequency Ratio $\nu = 0.88$

For excitation frequency $\nu = 0.88$, Figures 3.5(a) through 3.5(f) show six selected samples of the response time history records for six different values of excitation amplitude, $a = 0.02, 0.046, 0.084, 0.094, 0.106,$ and 0.11 respectively. It is seen that for a relatively low excitation amplitude, $a = 0.02$, the response is periodic and the ship roll amplitude does not reach the barrier as shown in Figure 3.5(a). The Fast Fourier Transform (FFT) shown in Figure 3.6(a) shows periodic response. This is confirmed by the phase portrait shown in Figure 3.7(a) and the Poincaré map shown in Figure 3.8(a) reveals period-1 fixed point. As the excitation amplitude increases the response experiences grazing bifurcation and assumes amplitude modulated pattern as shown in Figure 3.5(b) for $a = 0.046$. Figures 3.6(b), 3.7(b) and

3.8(b) show the corresponding FFT, phase diagram, and Poincaré map respectively. The response experiences one impact per 10 excitation periods. At excitation amplitude $a = 0.084$, the response is bounded chaotic with multi-impacts as shown in Figures 3.5(c) through 3.8(c). As the excitation amplitude increases, e.g., $a = 0.094$, the response possesses periodic motion with period-four as shown in Figures 3.5(d) through 3.8(d). The response experiences one impact per two excitation periods. It then assumes period-three for excitation amplitude $a = 0.106$ as shown in Figures 3.5(e) through 3.8(e). This motion is characterized by one impact every three excitation periods. This is followed by period-7 for excitation amplitude $a = 0.11$ as revealed in Figures 3.5(f) through 3.8(f). For any excitation amplitude, $a \geq 0.12$, the ship experiences rollover motion indicating the occurrence of capsizing. Note that these scenarios are obtained for given sets of initial conditions. However, for other initial conditions there is a possibility of other attractors that may coexist under the same excitation parameters.

Figure 3.9 shows samples of safe basins of attraction for different values of excitation amplitude and for excitation frequency parameter $\nu = 0.88$. The black region denotes bounded (safe) motion, while the blank region represents the rollover dynamics (ship capsizing). It is seen that for relatively small values of excitation amplitude (for example $a = 0.04$) the entire domain bounded by the grazing orbit experiences bounded oscillations as shown in Figure 3.9(a). As the excitation amplitude gradually increases, for example, for $a = 0.096$ the domain is eroded by empty space for ship capsizing as shown in Figure 3.9(b). By increasing the excitation amplitude, the eroded area representing the rollover motion increases as

shown in Figures 3.9 (c) through (f) up to excitation amplitude $a \leq 0.132$. Above that excitation amplitude the entire region belongs to ship rollover dynamics or capsizing (i.e., all initial conditions lead to ship capsizing).

Figure 3.10 shows the bifurcation diagram on the plane of response-excitation amplitudes for frequency ratio $\nu = 0.88$. This diagram reveals the coexistence of different solutions for the same excitation level depending on initial conditions; non-impact bounded oscillations of period-one as shown by the black square, modulated motion shown by the symbol \diamond , multi-periodic oscillation shown by empty squares, and chaotic motion shown by black circle. Also, it can be seen from Figure 3.10 that rollover motion exists for excitation amplitude $a \geq 0.084$.

3.4.1.2 Excitation Frequency Ratio $\nu = 0.94$

For $\nu = 0.94$, Figures 3.11(a) through 3.11(f) show six selected samples of the response time history records for six different values of excitation amplitude, $a = 0.008, 0.04, 0.06, 0.07, 0.096, \text{ and } 0.12$ respectively. It is seen that for relatively low excitation amplitude, $a = 0.008$, the response is periodic and the ship does not experience impact as shown in Figure 3.11(a). This is confirmed by the FFT, phase portrait, and Poincaré map shown in Figures 3.12(a), 3.13(a) and 3.14(a), respectively. As the excitation amplitude increases the response experiences period doubling as shown in Figure 3.11(b) for $a = 0.04$. Figures 3.12(b), 3.13(b) and 3.14(b) show the corresponding FFT, phase diagram, and Poincaré map, respectively. At excitation amplitude $a = 0.06$, the response is periodic and the ship experiences impact with the barrier as shown in Figures 3.11(c), 3.12(c),

3.13(c), and 3.14(c). The ship experiences one impact every excitation period. For $a = 0.07$, the response possesses modulated motion as shown in Figures 3.11(d), 3.12(d), 3.13(d), and 3.14(d). It then assumes multi-periodic response for excitation amplitude $a = 0.096$ as shown in Figures 3.11(e), 3.12(e), 3.13(e), and 3.14(e). This is followed by period-three for excitation amplitude $a = 0.12$ as revealed in Figures 3.11(f), 3.12(f), 3.13(f), and 3.14(f).

Samples of safe basins of attraction for different values of excitation amplitude are shown in Figure 3.15. It is seen that for relatively small values of excitation amplitude the entire domain bounded by the grazing orbit experiences bounded oscillations as shown in Figure 3.15(a). As the excitation amplitude gradually increases, for example, for $a = 0.072$ the domain is eroded by empty space representing rollover motion as shown in Figure 3.15(b). By increasing the excitation amplitude, the eroded area representing the unsafe motion increases as shown in Figures 3.15(c) through 3.15(f) up to excitation amplitude $a \leq 0.192$. Above that excitation amplitude the entire region belongs to ship rollover motion or capsizing. Figure 3.16 shows the bifurcation diagram on the plane of response-excitation amplitudes for frequency ratio $\nu = 0.94$. The figure summarizes possible regimes of ship dynamics. It can be seen from Figure 3.16 that rollover motion exists for excitation amplitude $a \geq 0.064$. Comparing this value to the one calculated in subsection 3.4.1.1 for excitation frequency ratio $\nu = 0.88$, one may conclude that as the excitation frequency ratio increases, the excitation at the occurrence of capsizing decreases.

3.4.1.3 Excitation Frequency Ratio $\nu = 1.2$

For excitation frequency ratio $\nu = 1.2$, and relatively small values of excitation amplitude, (e.g., $a = 0.036$) the ship response is periodic and does not experience impact with the barrier as shown in Figures 3.17(a), 3.18(a), 3.19(a), and 3.20(a). However, for larger values of excitation amplitude, (e.g. $a = 0.088$) some initial conditions yield to periodic response which experiences impact every excitation period as revealed in Figures 3.17(b), 3.18(b), 3.19(b), and 3.20(b). Samples of safe basins of attraction for different values of excitation amplitude for excitation frequency ratio $\nu = 1.2$ are shown in Figure 3.21. It is seen that for relatively small values of excitation amplitude the entire domain bounded by the grazing orbit experiences bounded oscillations as shown in Figure 3.21(a) for $a = 0.04$. As the excitation amplitude gradually increases, for example for $a = 0.056$ the domain is eroded by empty space for rollover motion as shown in Figure 3.21(b). By increasing the excitation amplitude, the eroded area representing the rollover motion increases as shown in Figures 3.21(c) through 3.21(f) up to excitation amplitude $a \leq 0.16$. Above that excitation amplitude the entire region belongs to ship rollover motion or capsizing. Figure 3.22 shows the bifurcation diagram on the plane of response-excitation amplitudes for frequency ratio $\nu = 1.2$. It can be seen that the periodic non-impact motion occupies a wider range of excitation amplitude however, it coexists with rollover motion for $a \geq 0.044$ and also with periodic impact motion over the excitation amplitude range $0.064 \leq a \leq 0.156$. Also, one may conclude that as the excitation frequency ratio increases, the excitation at the occurrence of capsizing decreases.

3.4.1.4 Stability Fraction

Figure 3.23 shows the dependence of stability fraction, S_f , on excitation amplitude for three different values of excitation frequency, $\nu = 0.88, 0.94$, and 1.20 . The stability fraction is also known as the safety integrity factor (S.I.F.). It is obtained by estimating the ratio of the area of the stable region in the phase plane (area of the safe basin) to the total area encompassed by the grazing orbit, which is the safe basin in the absence of external excitation. For excitation amplitudes less than a critical value, governed by the excitation frequency, there is no erosion at all for the safe basin. Above this critical value, the value of the safe basin area shrinks and the stability fraction drops. It is seen that as the excitation frequency ratio increases, the excitation amplitude at which capsizing exists decreases. This is attributed to the fact that less force is required to cause large response amplitude as the excitation frequency increases. Another important feature of the decreasing curve of the stability fraction is that it becomes progressively less steep when the excitation frequency increases above the resonant frequency.

3.4.2 EXCITATION FREQUENCY AS A CONTROL PARAMETER

Figure 3.24 shows samples of safe basins of attraction for different values of excitation frequency and for excitation amplitude $a = 0.08$. It is seen that for relatively small values of excitation frequency and below resonance (for example $\nu = 0.6$) the entire domain bounded by the grazing orbit experiences bounded oscillations as shown in Figure 3.24(a) by the black region. As the excitation frequency gradually increases and for $\nu = 0.92$ the region is eroded by regions of rollover motion as

shown in Figure 3.24(b). As the excitation frequency increases and up to $\nu = 1.12$, the eroded area representing the unsafe motion increases. For excitation frequency $\nu \geq 1.12$ the area belongs to rollover motion decreases until $\nu = 1.4$ at which the entire domain belongs to bounded motion. Figure 3.25 shows the bifurcation diagram on the plane of response-excitation frequency for excitation amplitude $a = 0.08$. An important feature is that ship capsizing occurs for a certain excitation frequency range which is close to resonance.

3.5 Closing Remarks

In this chapter extensive numerical simulations were carried out to determine the safe conditions for operation of a ship that suffers one-sided impact with solid ice or rigid barriers. The bifurcation diagrams were obtained and reveal the coexistence of different response regimes such non-impact periodic oscillations, modulation impact motion, period added impact oscillations, chaotic impact motion and unbounded rollover motion. The stability fraction for three different values of excitation frequency was obtained. It was shown that for a certain excitation frequency, there exists a critical value of excitation amplitude above which the stability fraction decreases. As the excitation amplitude increases the stability fraction decreases until it reaches zero. Another important conclusion from this study is that the excitation frequency range leading to ship capsizing enlarges as the excitation amplitude increases. The importance of this chapter is that it represents the first attempt to explore the purely elastic impact interaction of ship roll motion with floating ice. In this chapter the ice barrier was assumed rigid and purely elastic

and the analysis did not take into account the damping due to inelastic impact which represents a more realistic case. The inelastic impact of ship roll motion with ice will be studied in chapter 4.

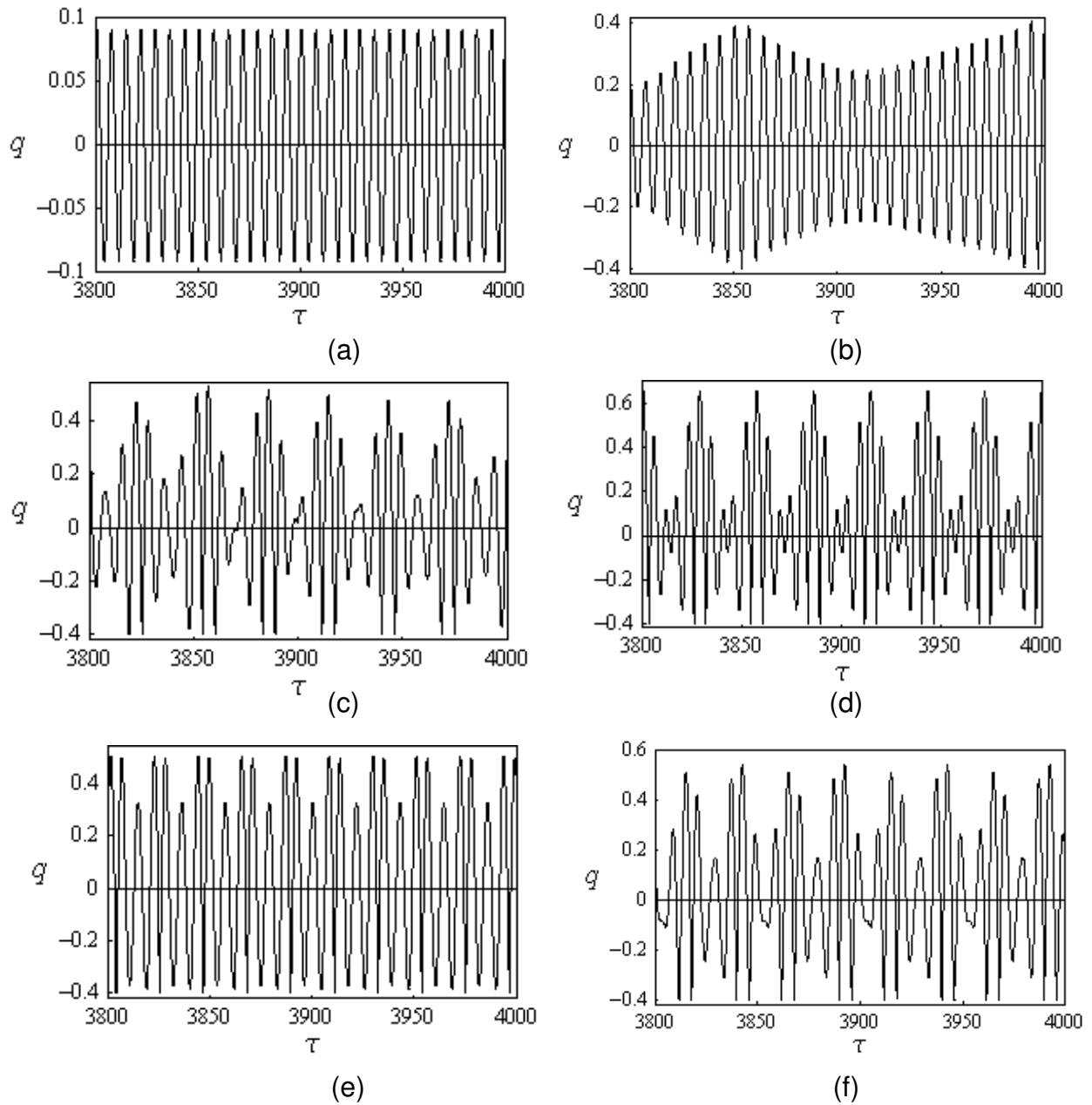


Figure 3.5. Section of time history response records for excitation frequency ratio $\nu = 0.88$, and excitation amplitude:

- (a) $a = 0.02$, (b) $a = 0.046$, (c) $a = 0.084$ (Chaotic), (d) $a = 0.094$ (Period four),
 (e) $a = 0.106$ (Period three), (f) $a = 0.11$ (Period seven).

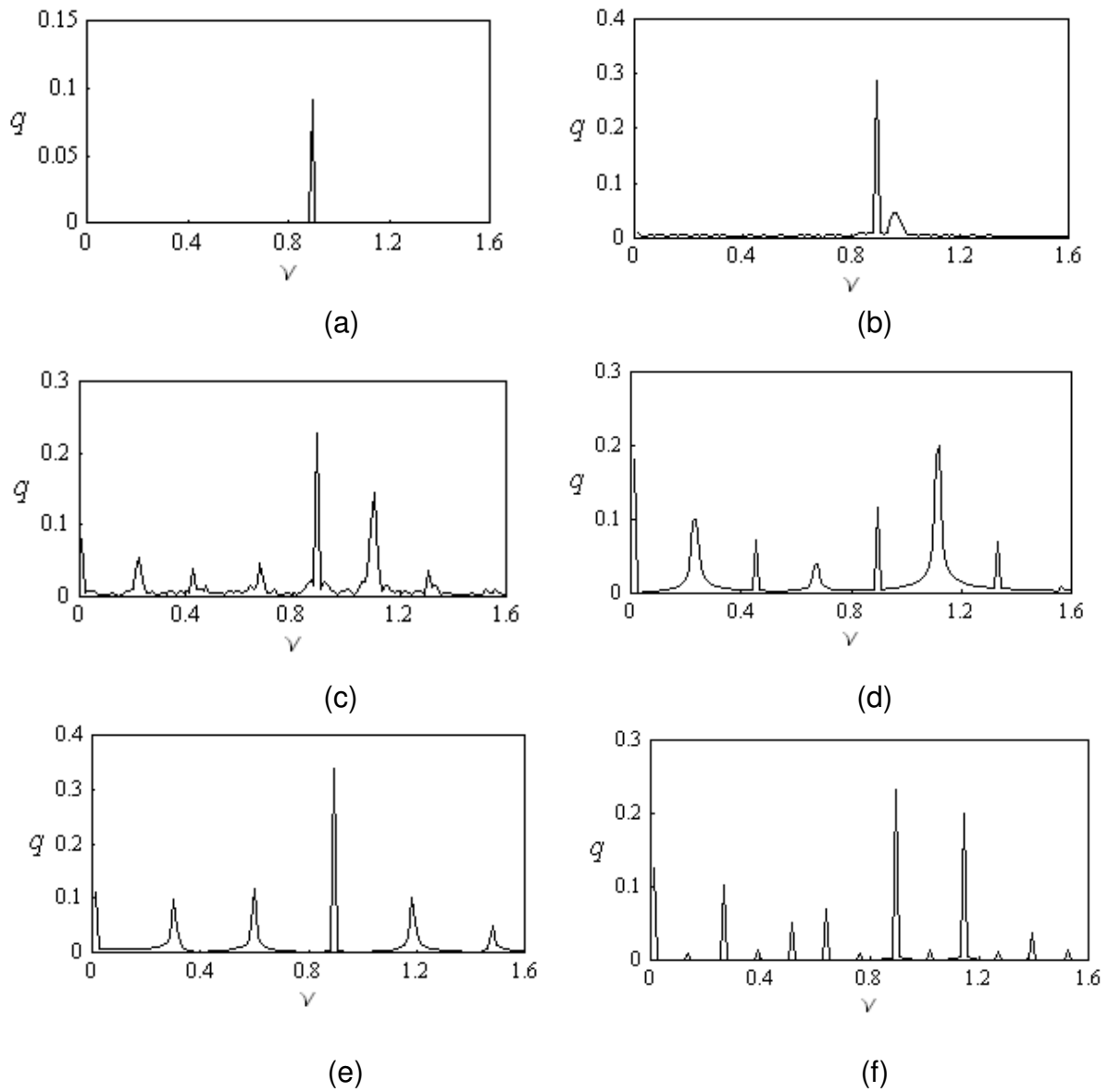


Figure 3.6. FFT corresponding to the time history records of Figure 3.5 for excitation frequency ratio $\nu = 0.88$, and excitation amplitude: (a) $a = 0.02$, (b) $a = 0.046$, (c) $a = 0.084$ (Chaotic), (d) $a = 0.094$ (Period four), (e) $a = 0.106$ (Period three), (f) $a = 0.11$ (Period seven).

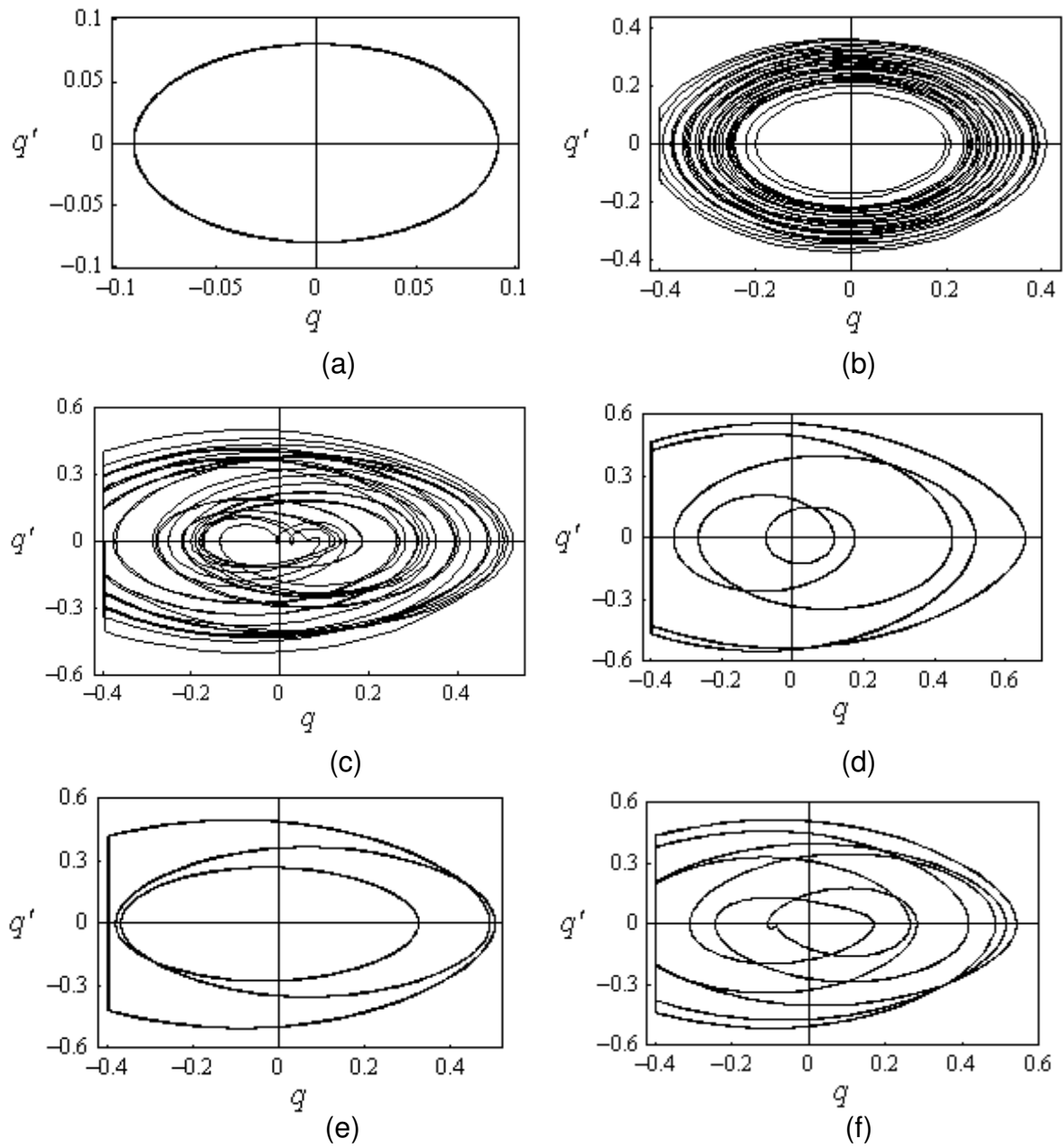


Figure 3.7. Phase portraits corresponding to the time history records of Figure 3.5 for excitation frequency ratio $\nu = 0.88$, and excitation amplitude: (a) $a = 0.02$, (b) $a = 0.046$, (c) $a = 0.084$ (Chaotic), (d) $a = 0.094$ (Period four), (e) $a = 0.106$ (Period three), (f) $a = 0.11$ (Period seven).

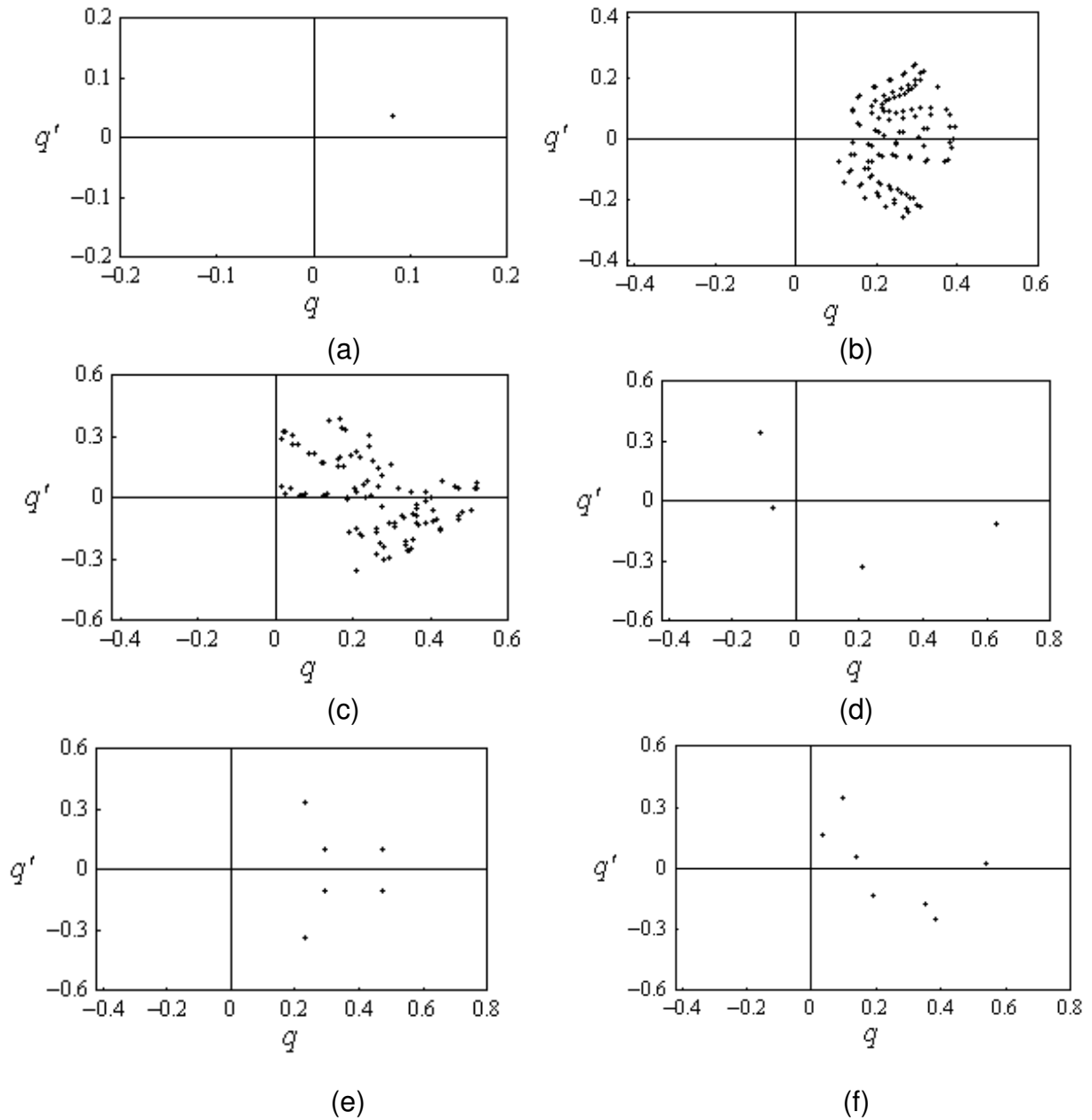


Figure 3.8. Poincaré maps corresponding to the time history records of Figure 3.5 for excitation frequency ratio $\nu = 0.88$, and excitation amplitude: (a) $a = 0.02$, (b) $a = 0.046$, (c) $a = 0.084$ (Chaotic), (d) $a = 0.094$ (Period four), (e) $a = 0.106$ (Period three), (f) $a = 0.11$ (Period seven).

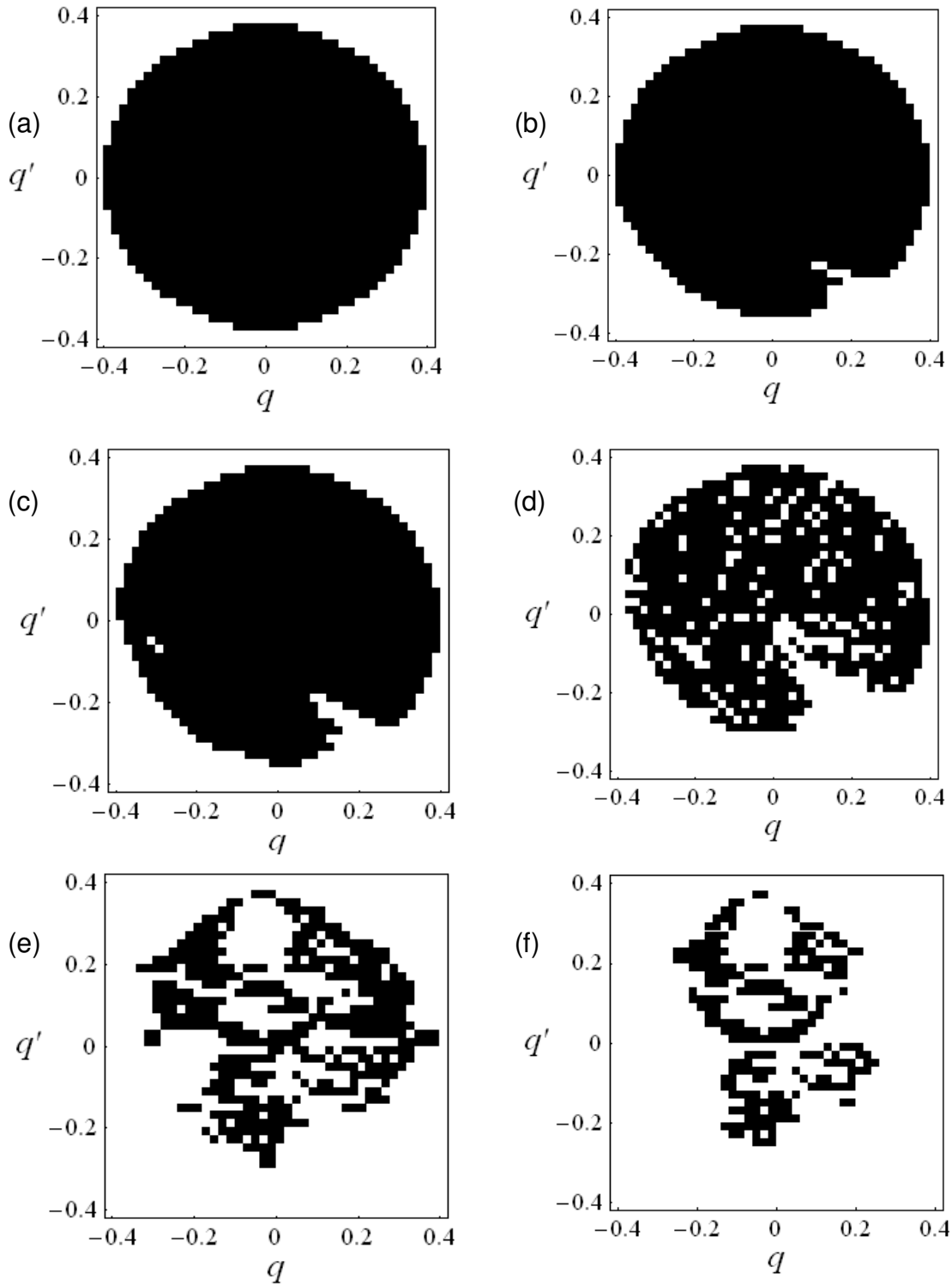


Figure 3.9. Domains of attraction for different excitation amplitudes for excitation frequency $\nu = 0.88$: (a) $a = 0.04$, (b) $a = 0.096$, (c) $a = 0.10$, (d) $a = 0.112$, (e) $a = 0.116$, and (f) $a = 0.12$; Black region: bounded (safe) motion, and empty space: rollover dynamics.

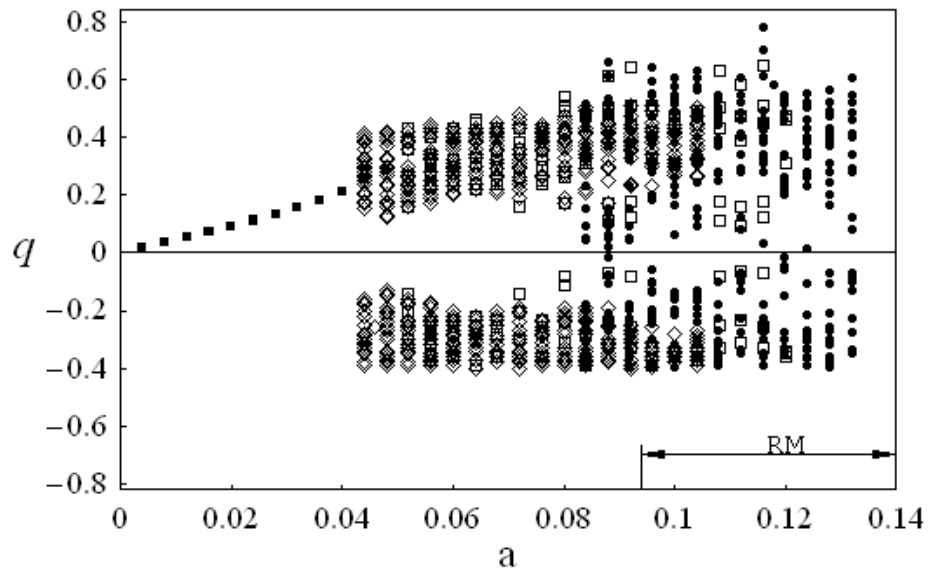


Figure 3.10. Bifurcation diagram for excitation frequency ratio $\nu = 0.88$.
 ■ Period-one response, \diamond Modulated response, \square Multi - periodic response,
 ● Chaotic motion, and RM= Rollover Motion.

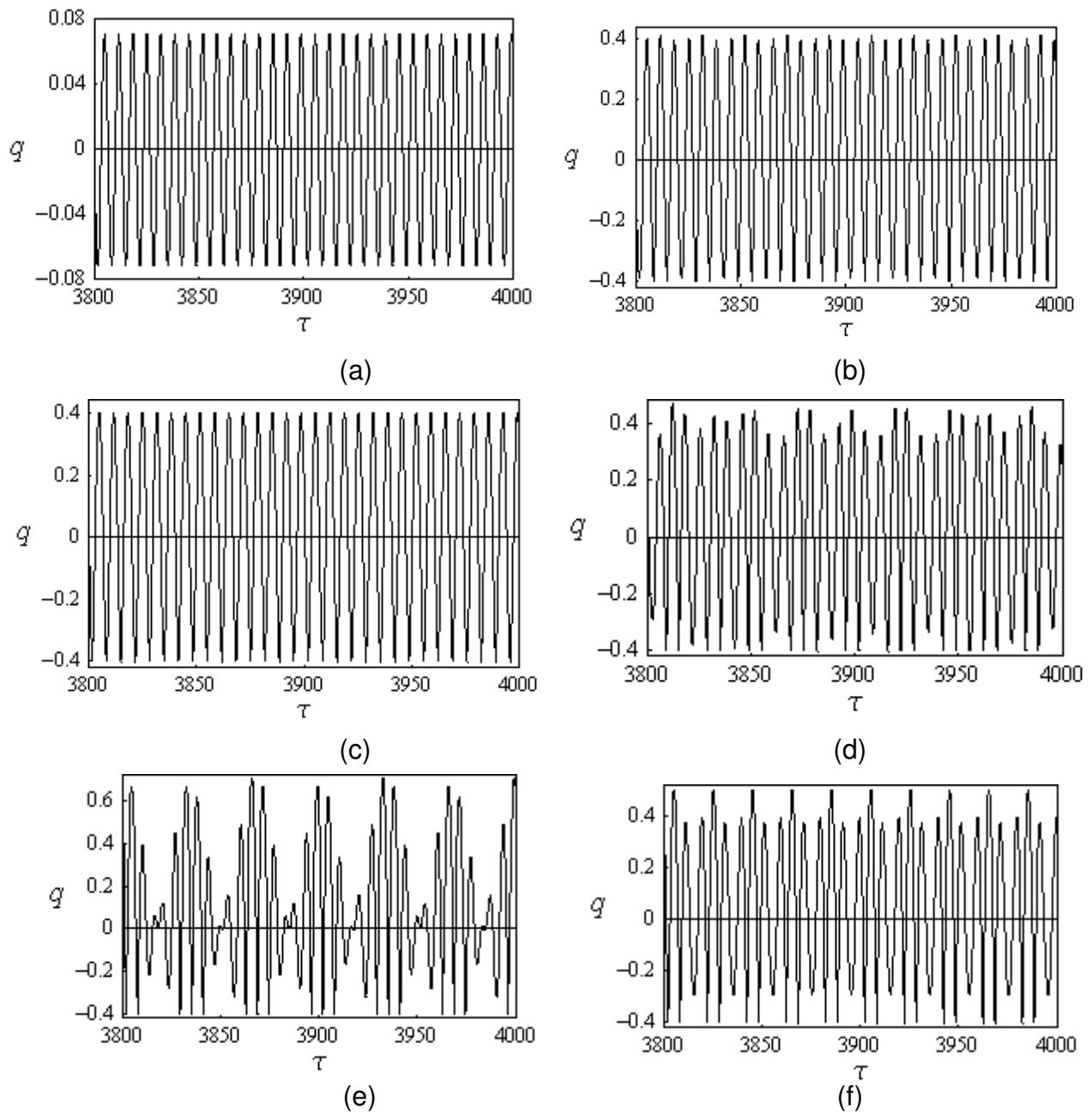


Figure 3.11 Section of time history response records for excitation frequency ratio $\nu = 0.94$, and excitation amplitude: (a) $a = 0.008$, (b) $a = 0.04$ (period-two), (c) $a = 0.06$, (d) $a = 0.07$, (e) $a = 0.096$, and (f) $a = 0.12$ (period-three).

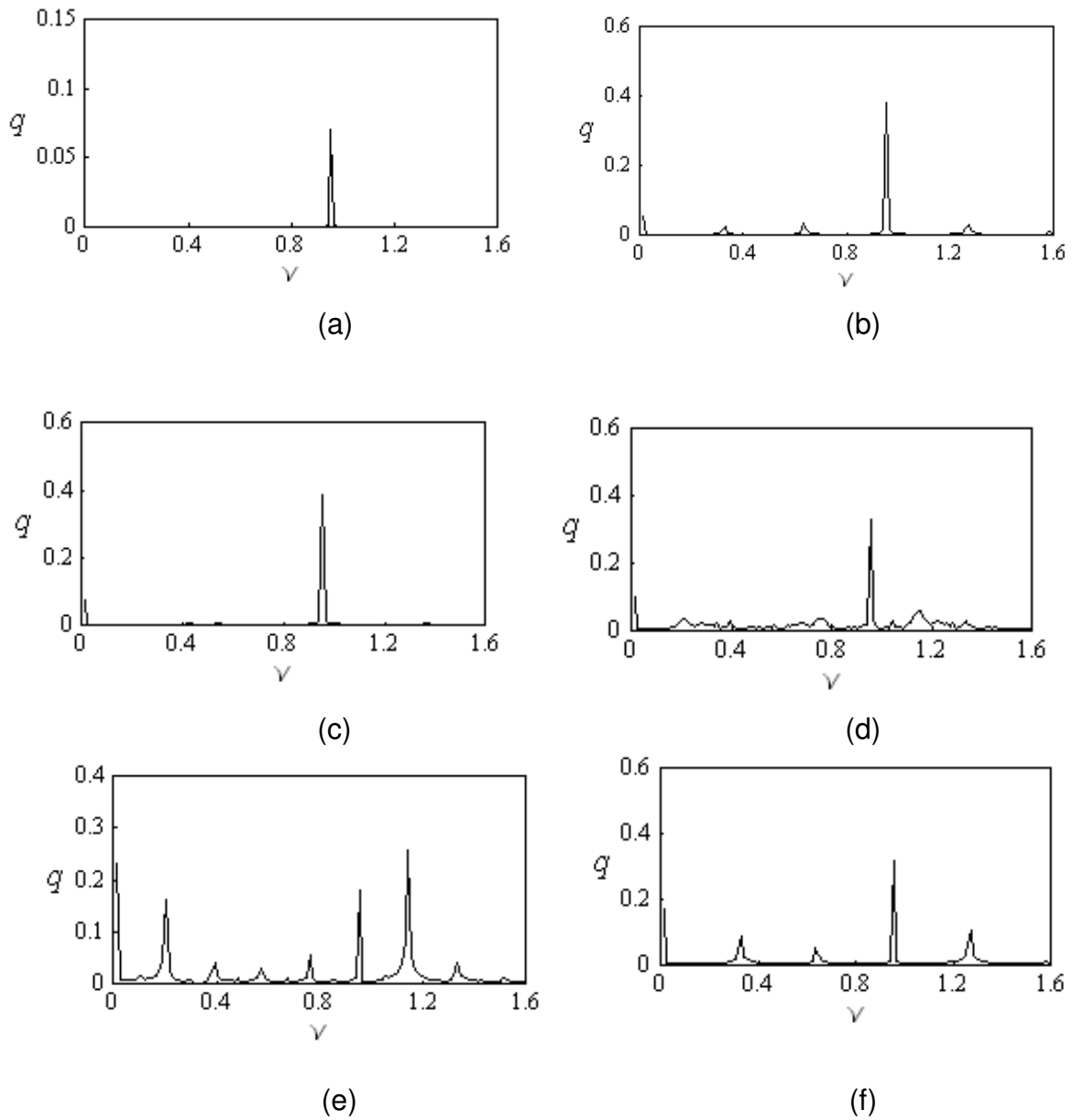


Figure 3.12. FFT corresponding to the time history records of Figure 3.11 for excitation frequency ratio $v = 0.94$, and excitation amplitude: (a) $a = 0.008$, (b) $a = 0.04$ (period-two), (c) $a = 0.06$, (d) $a = 0.07$, (e) $a = 0.096$, and (f) $a = 0.12$ (period-three).

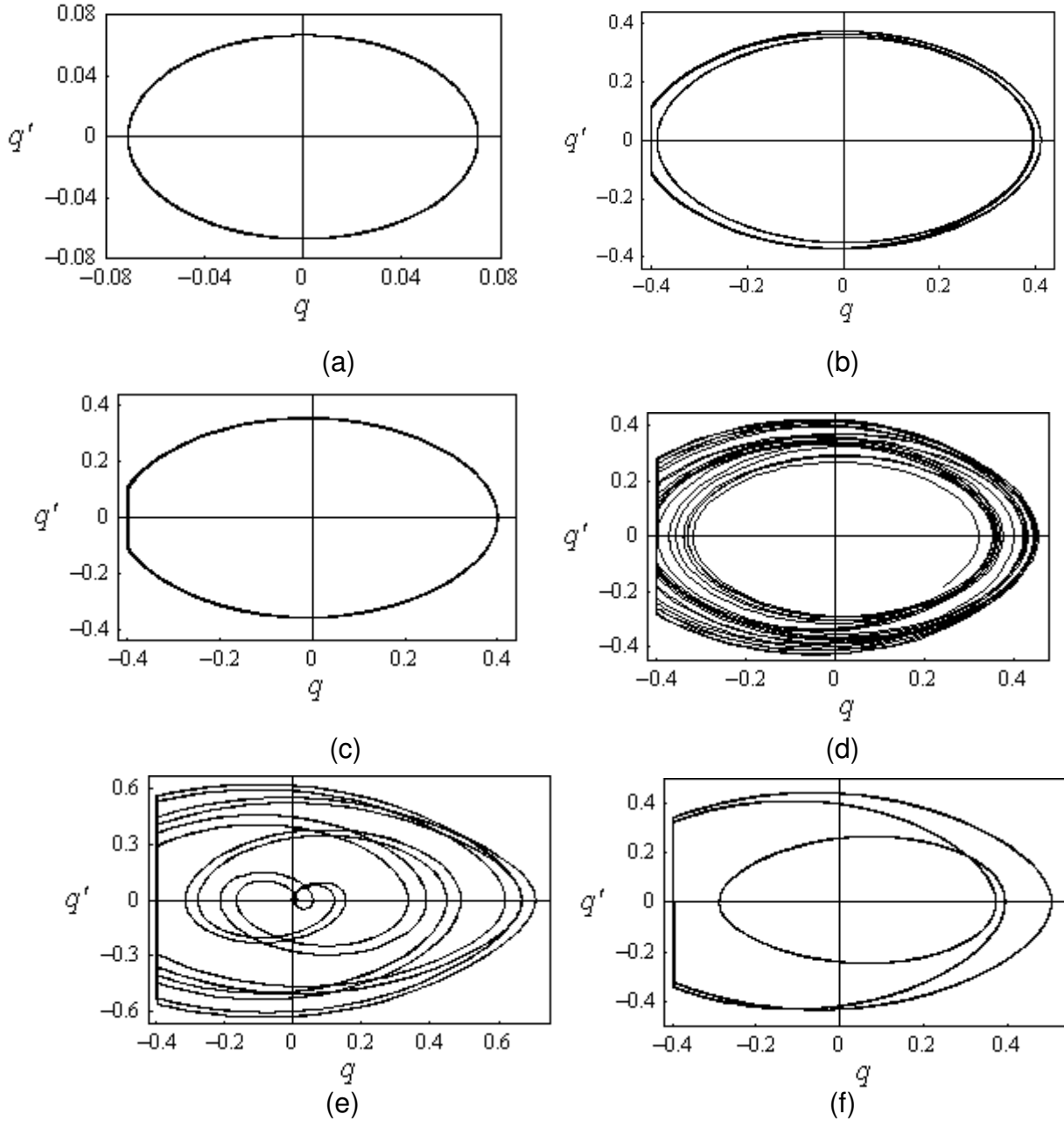


Figure 3.13. Phase portraits corresponding to the time history records of Figure 3.11 for excitation frequency ratio $\nu = 0.94$, and excitation amplitude: (a) $a = 0.008$, (b) $a = 0.04$ (period-two), (c) $a = 0.06$, (d) $a = 0.07$, (e) $a = 0.096$, and (f) $a = 0.12$ (period-three).

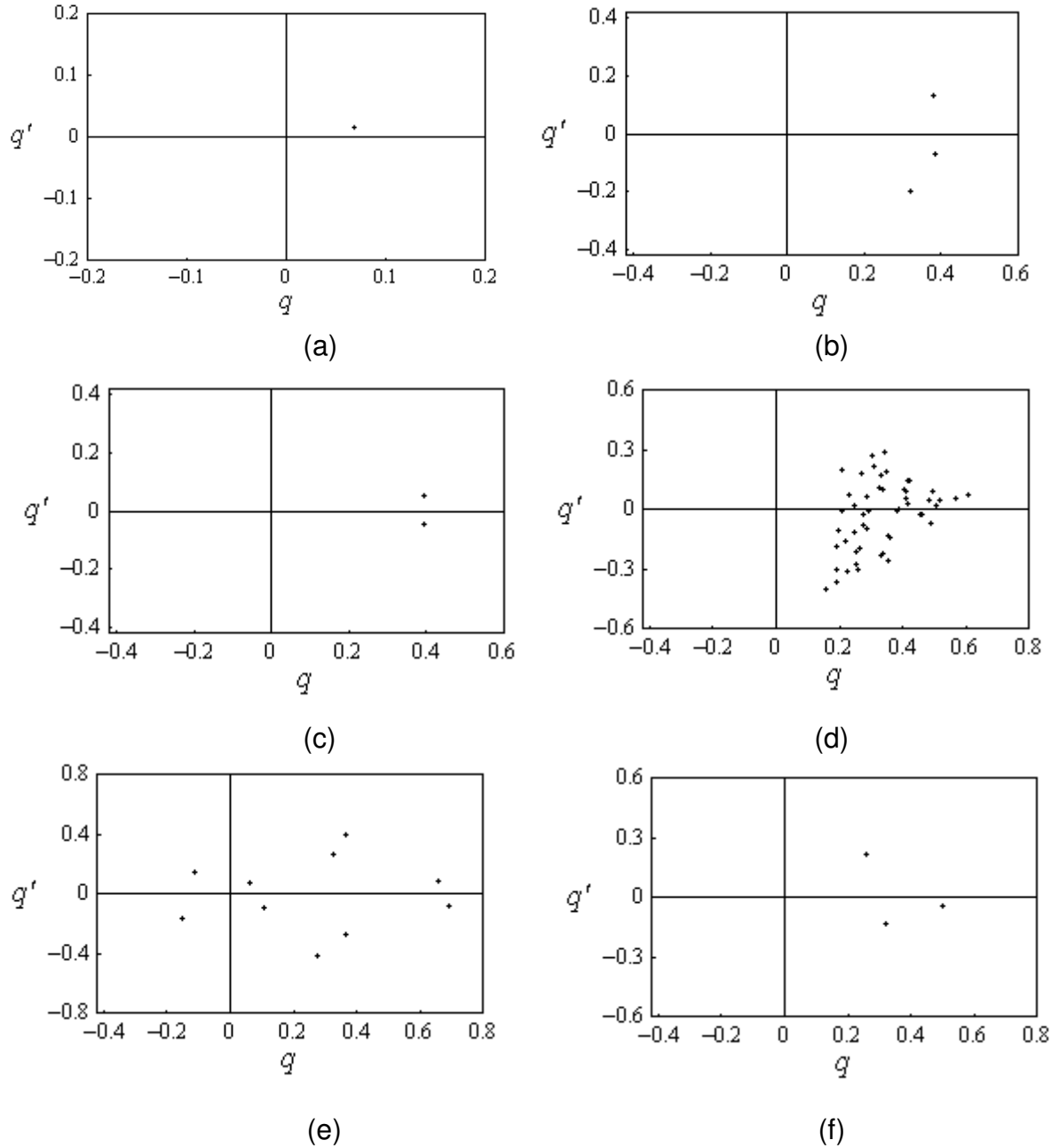


Figure 3.14. Poincaré maps corresponding to the time history records of Figure 3.11 for excitation frequency ratio $\nu = 0.94$, and excitation amplitude: (a) $a = 0.008$, (b) $a = 0.04$ (period-two), (c) $a = 0.06$, (d) $a = 0.07$, (e) $a = 0.096$, and (f) $a = 0.12$ (period-three).

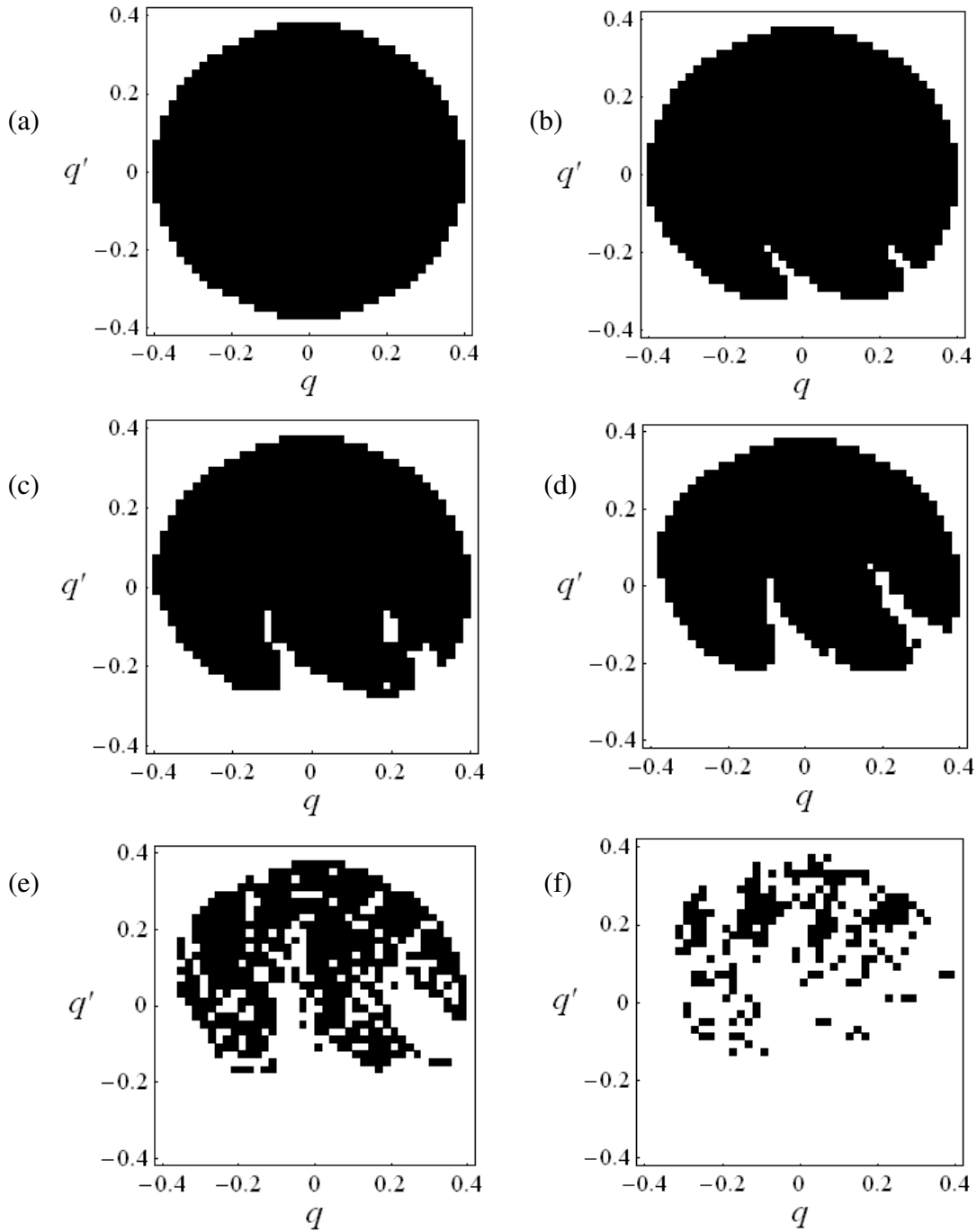


Figure 3.15. Domains of attraction for different excitation amplitudes for excitation frequency $\nu = 0.94$; (a) $a = 0.04$, (b) $a = 0.072$, (c) $a = 0.08$, (d) $a = 0.088$, (e) $a = 0.096$, and (f) $a = 0.104$; Black region: bounded (safe) motion, and empty space: rollover dynamics.

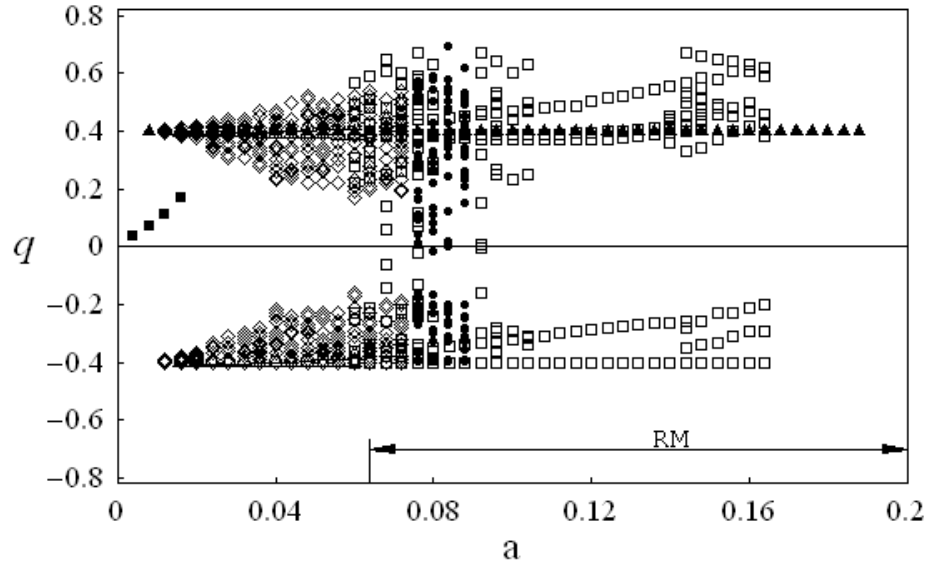
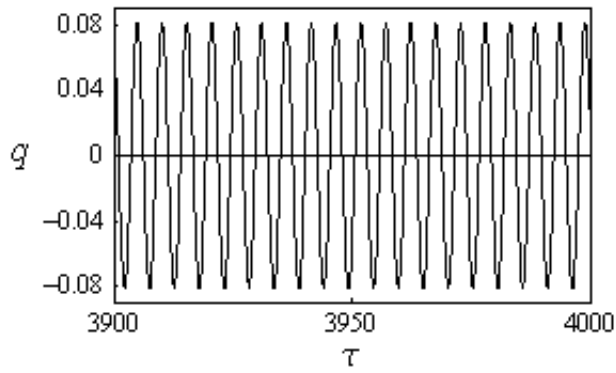
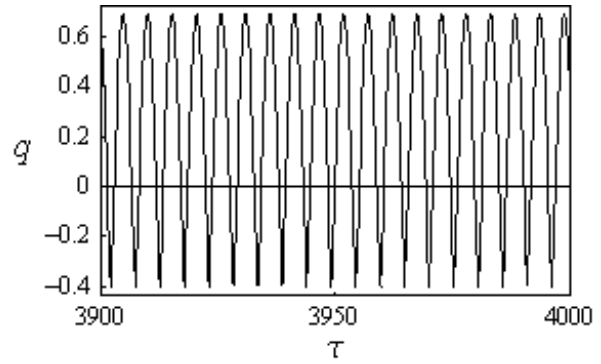


Figure 3.16. Bifurcation diagram for excitation frequency $\nu = 0.94$.
 ■ Period-one response, ▲ Period-one response experiencing impact, △ Period-two Response, ◇ Modulated response, □ Multi - periodic response,
 ● Chaotic motion, and RM= Rollover Motion.

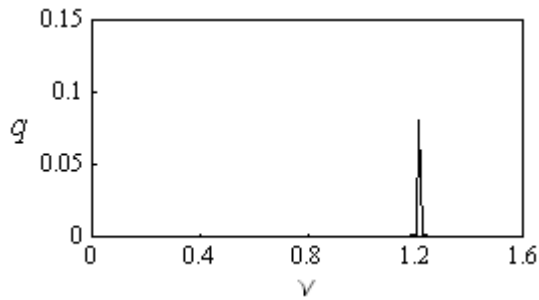


(a)

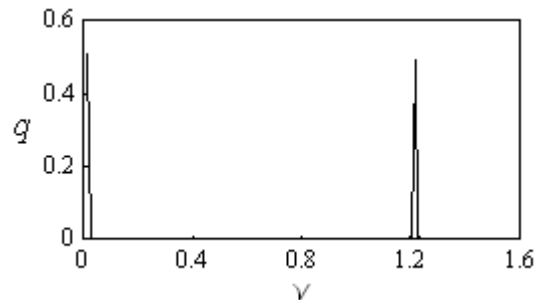


(b)

Figure 3.17 Section of time history response records for excitation frequency ratio $\nu = 1.2$, and excitation amplitude: (a) $a = 0.036$, and (b) $a = 0.088$.



(a)



(b)

Figure 3.18. FFT corresponding to the time history records of Figure 3.17 for excitation frequency ratio $\nu = 1.2$, and excitation amplitude: (a) $a = 0.036$, and (b) $a = 0.088$.

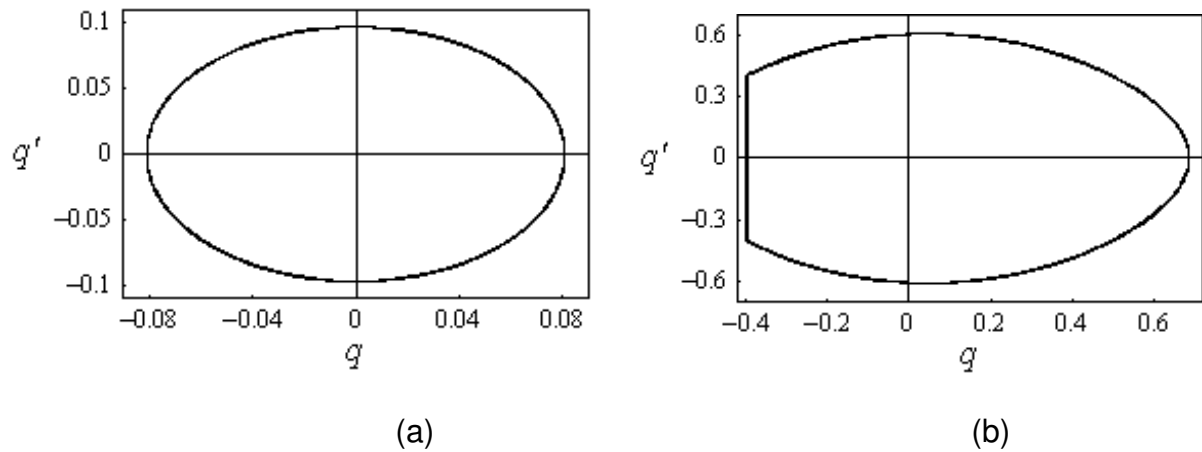


Figure 3.19. Phase portraits corresponding to the time history records of Figure 3.17 for excitation frequency ratio $\nu = 1.2$, and excitation amplitude: (a) $a = 0.036$, and (b) $a = 0.088$.

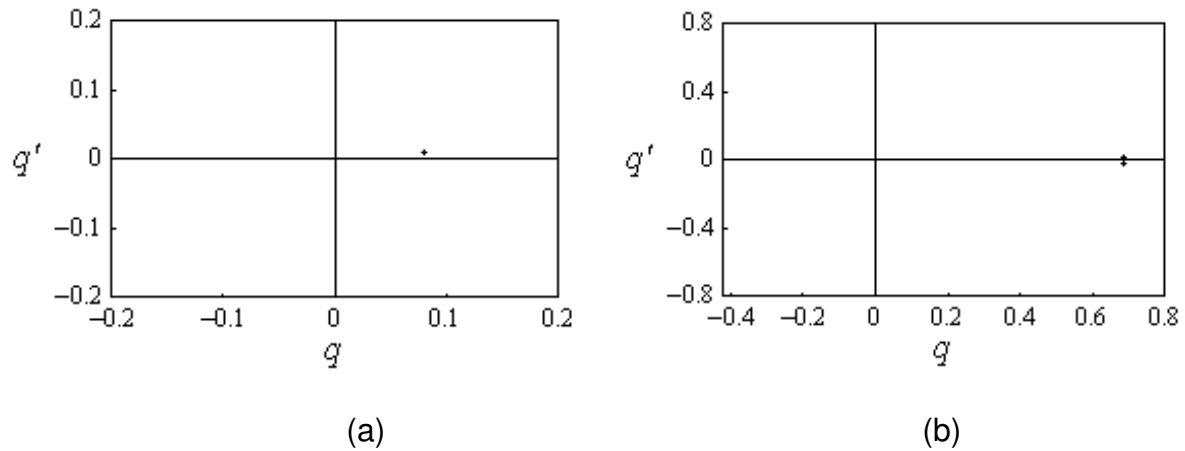


Figure 3.20. Poincaré maps corresponding to the time history records of Figure 3.17 for excitation frequency ratio $\nu = 1.2$, and excitation amplitude: (a) $a = 0.036$, and (b) $a = 0.088$.

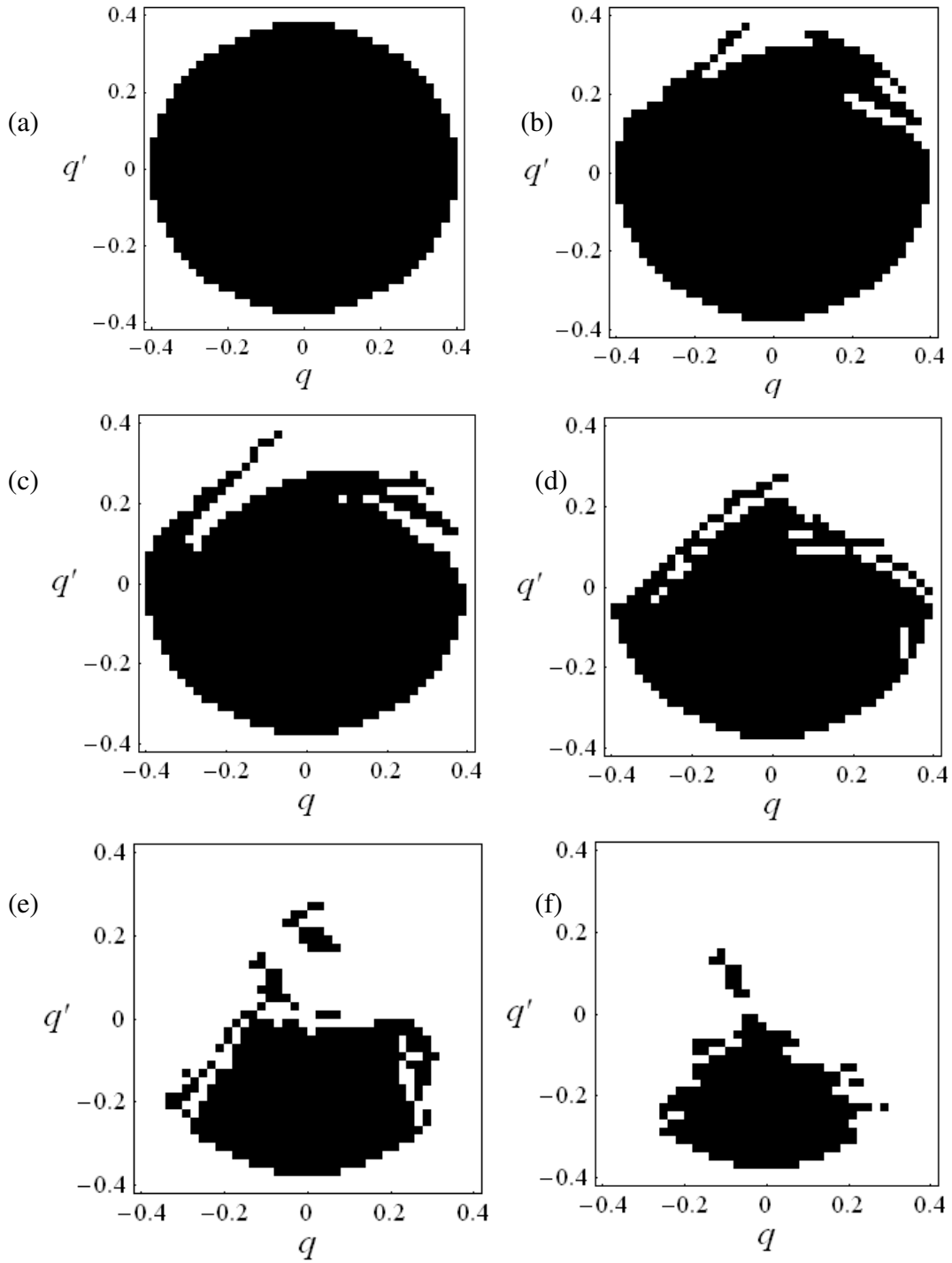


Figure 3.21. Domains of attraction for different excitation amplitudes for excitation frequency $\nu = 1.2$; (a) $a = 0.04$, (b) $a = 0.056$, (c) $a = 0.064$, (d) $a = 0.08$, (e) $a = 0.104$, and (f) $a = 0.12$; Black region: bounded (safe) motion, and empty space: rollover (unsafe) motion.

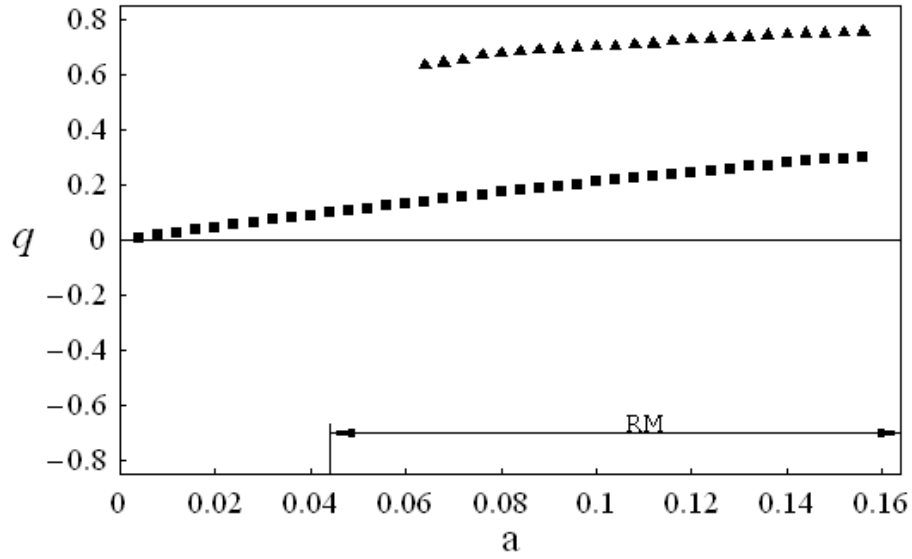


Figure 3.22. Bifurcation diagram for excitation frequency $\nu = 1.2$.
 ■ Period-one response, ▲ Period-one response experiencing impact,
 and RM= Rollover Motion

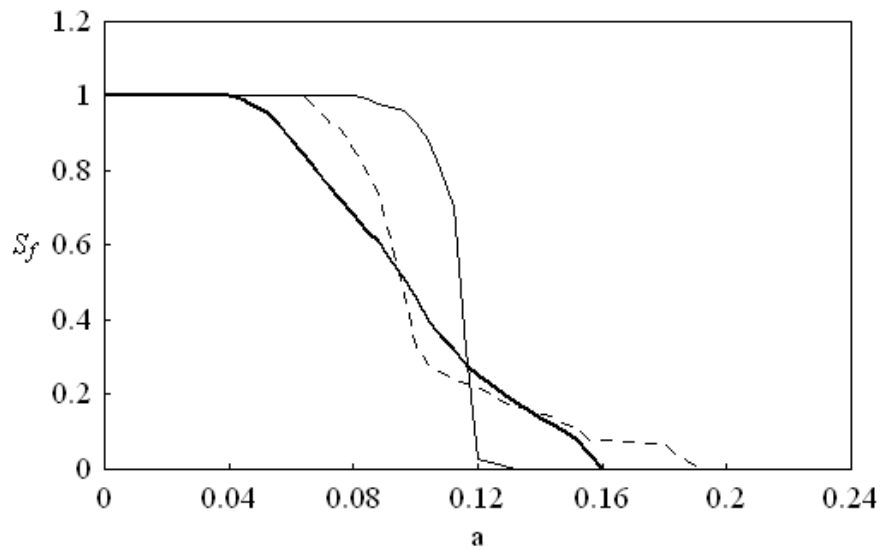
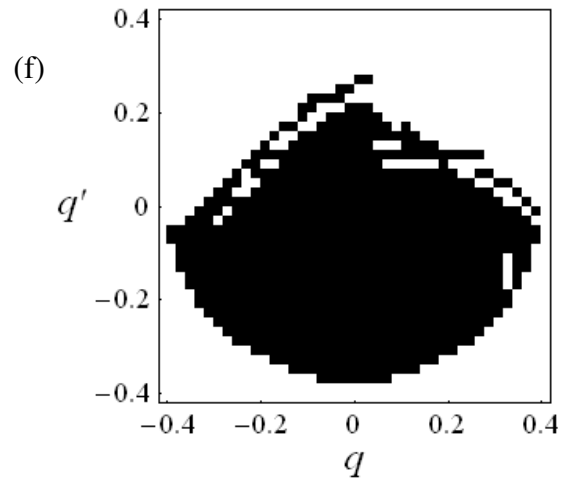
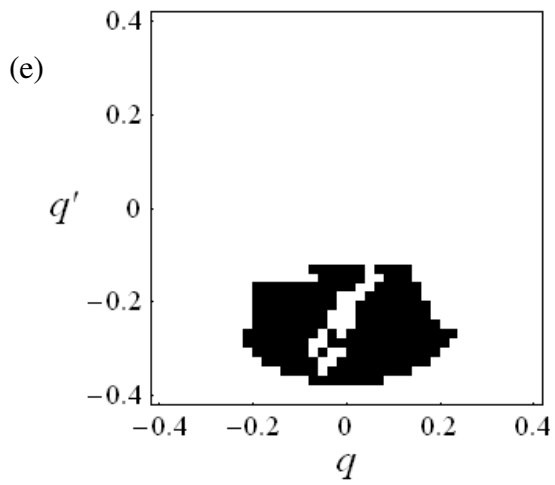
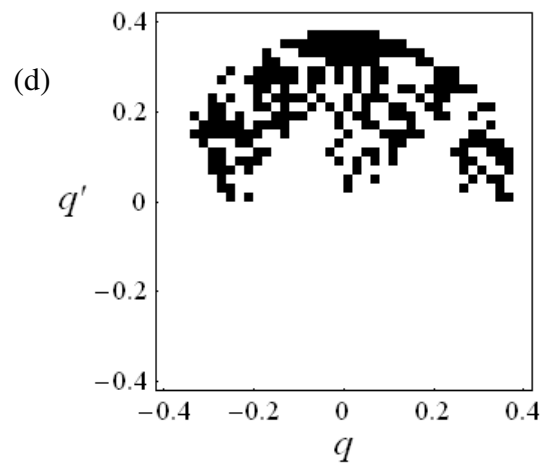
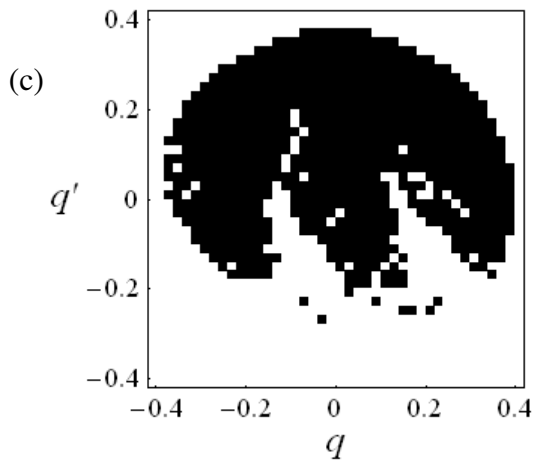
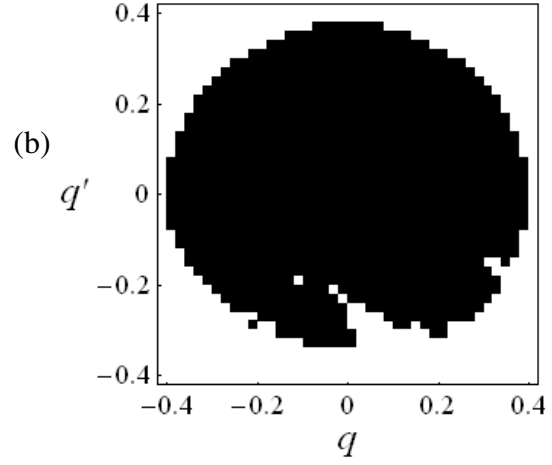
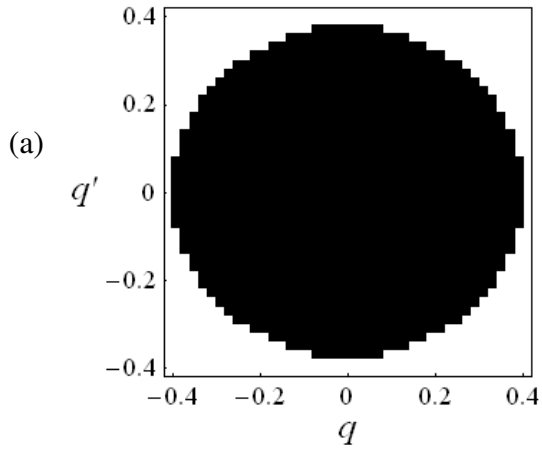


Figure 3.23. Dependence of stability fraction on excitation amplitude for three different values of excitation frequency
 — $\nu = 0.88$, $\nu = 0.94$, — $\nu = 1.2$.



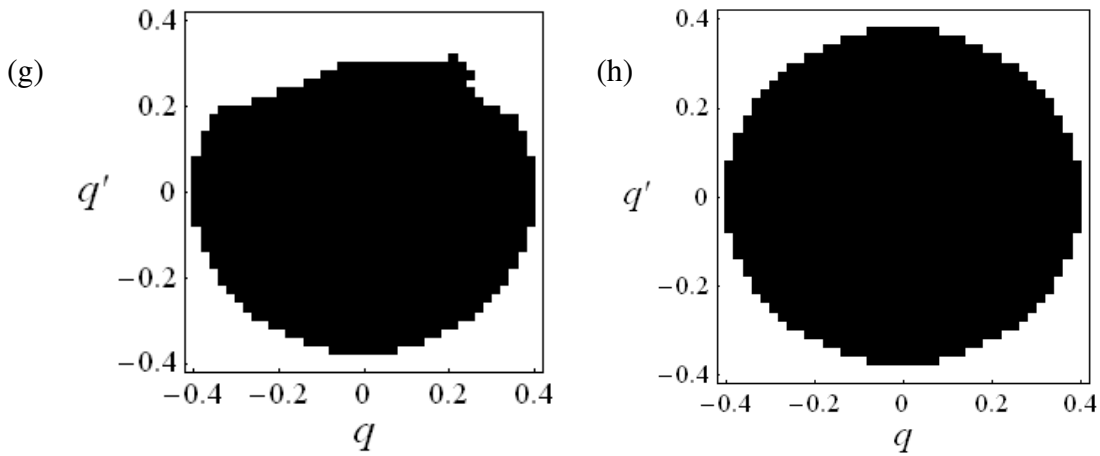


Figure 3.24. Domains of attraction for different excitation frequencies for excitation amplitude $a = 0.08$: (a) $\nu = 0.6$, (b) $\nu = 0.92$, (c) $\nu = 0.96$, (d) $\nu = 1.0$, (e) $\nu = 1.12$, (f) $\nu = 1.2$, (g) $\nu = 1.28$, and (h) $\nu = 1.4$; Black region: bounded motion, and empty space: rollover motion.

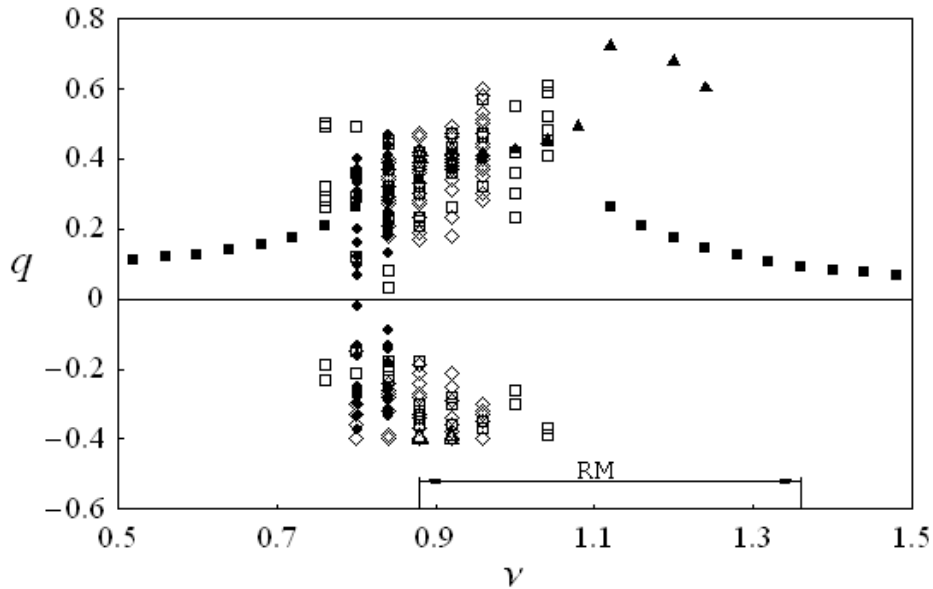


Figure 3.25. Amplitude versus excitation frequency diagram for excitation amplitude $a = 0.08$: ■ Period-one response, ▲ Period-one response experiencing impact, △ Period-two Response, ◇ Modulated response, □ Multi - periodic response, ● Chaotic motion, and RM= Rollover Motion.

CHAPTER 4

INELASTIC IMPACT OF SHIP ROLL DYNAMICS WITH SOFT ICE

4.1 Introduction

The previous chapter explored the elastic impact interaction of ship roll motion with floating ice and rigid barriers. However for realistic cases, impact phenomena are accompanied by energy loss. Energy is lost through the generation of heat during localized inelastic deformation of the material, through the generation and dissipation of elastic stress waves within the colliding bodies, and through the generation of sound energy. As a result, the velocity of a ship after impact with a rigid barrier is smaller than its velocity before impact. The purpose of this chapter is to study the influence of inelastic impact on ships roll dynamics.

Different methods for modeling inelastic impact of ship roll with stationary soft ice or rigid barriers are presented in this chapter. Model 1 extends Zhuravlev (1976) transformation (Zh.T.) presented in chapter 3 to involve the damping term associated with inelastic impact (Section 4.2). Ship response is estimated numerically for different values of excitation amplitude and excitation frequency. A comparison of the response characteristics for both cases; elastic impact ($e=1$) and inelastic impact ($e<1$) is carried out. Model 2 introduces Ivanov (1994) non-smooth coordinate transformation (Iv.T.), which handles both cases of elastic and inelastic impact. A comparison between response characteristics as predicted by both models 1 and 2 is carried out for same conditions and coefficient of restitution (Section 4.3). Section 4.4 presents an explicit solution to the equation of motion using Runge-Kutta (R.K.) method. The results are compared to solutions predicted

by both models 1 and 2. Section 4.5 presents another method to determine the response of ship roll motion experiencing inelastic impact with ice based on physical foundation. This method is based on simulating the impact phenomenon with a viscous damper in terms of coefficient of restitution. In this case, the damping term in the equation of motion will be a summation of the inherent linear damping and equivalent viscous damping. The main advantage of such modeling is that it eliminates singularities associated with sudden change in velocity and hence simplifies analytical description. The present work, in particular, highlights the fact that the impact dynamics may have qualitatively different response characteristics to different dissipation models.

4.2 Constraint Eliminating Coordinate (Model 1)

4.2.1 ANALYTICAL MODELING

For the case of inelastic impact, the condition $q'_+ = eq'_-$ must be introduced; where e is the coefficient of restitution, q'_- and q'_+ are the ship nondimensional velocities just before and after impact, respectively, see Figure 4.1. The coefficient e is assumed to be close to unity, such that $(1-e)$ is considered a small parameter. The one-sided impact occurs at $q = -q_i$. In line with Zh.T. introduced in chapter 3 and given by equation (3.4); $q = z \operatorname{sgn}(z) - q_i$, the impact condition $q'_+ = eq'_-$ specified at $q = -q_i$, is transformed to

$$z'_+ = ez'_- \text{ at } z = 0 \quad (4.1)$$

The transformed velocity jump is reduced by an amount proportional to $(1-e)$. It is possible to introduce this jump into the equation of motion using the Dirac delta-function, and thus one can avoid using condition (4.1). In Section 1.4.1.1, it was shown that the additional term due to inelastic damping is given by the expression

$$(1-e)z'\delta(\tau-\tau_i)=(1-e)z'|z'|\delta(z) \quad (4.2)$$

Equation (4.2) represents the damping term associated with inelastic impact as $(1-e)z'|z'|\delta(z)$. One may introduce a new function δ_- stands for a specific

distribution applied to some testing function $\Theta(t)$ such that $\int_{-\infty}^{\infty} \Theta(t) \delta_-(t) dt = \Theta(0_-)$. In

contrast to the conventional Dirac Delta function, $\delta_-(t)$ takes the value of $\Theta(t)$ on the left of zero but not exactly at zero. Note that using the conventional Dirac delta function in equation (4.2) would not be correct due to the continuous factor $z'|z'|$ at $z=0$. Accordingly, the term $(1-e)z'|z'|\delta_-(z)$ provides only approximate description for the energy loss at the barrier $z=0$, which is justified under the condition $e \ll 1$.

Equation (4.2) can be written as

$$(1-e)z'\delta(\tau-\tau_i)=(1-e)z'|z'|\delta_-(z) \quad (4.3)$$

Introducing the damping term associated with inelastic impact, $(1-e)z'|z'|\delta_-(z)$ to equation (3.5), the equation of motion in case of inelastic impact of ships with soft ice may be written as

$$z'' + \bar{\zeta}z' + \gamma z^2 \text{sgn}(z') + z + \text{sgn}(z)[-q_i + \bar{C}_3(z \text{sgn}(z) - q_i)^3 + \bar{C}_5(z \text{sgn}(z) - q_i)^5] + (1-e)z'|z'|\delta_-(z) = Z(\tau) \text{sgn}(z) \quad (4.4)$$

Under sinusoidal excitation $Z(\tau) = a \sin \nu \tau$, and for coefficient of restitution $e = 0.8$, equation (4.4) is solved numerically under different values of excitation amplitude and frequency. Same values of the coefficients of equation (4.4) used in chapter 3 are used in solving equation (4.4); $\bar{\zeta} = 0.01$, $\gamma = 0.005$, $\bar{C}_3 = -1.1$, $\bar{C}_5 = 0.1$, and $q_i = -0.4$. A comparison between the responses in the two cases elastic ($e = 1$) and inelastic ($e = 0.8$) impacts is carried out for three different values of excitation frequency ratio $\nu = 0.88$, 0.94 and 1.2 . Safe basins of attraction and bifurcation diagrams are generated for the three cases.

4.2.2 NUMERICAL SIMULATION

A comparison between the results of elastic and inelastic impacts for $\nu = 0.88$, and $a = 0.06$ is shown in Figures 4.2 and 4.3 for two different sets of initial conditions. It can be seen from Figure 4.2 that for initial conditions, $z_o = 0.01$, $z_o' = 0.01$, both coefficients of restitution, $e = 1$, and $e = 0.8$ yield the multi-periodic motion (period six) characterized by one impact every three excitation periods. However, for $z_o = 0.11$, $z_o' = -0.19$, elastic impact yields modulated response characterized by one impact every four excitation periods, while inelastic impact yields multi-periodic response characterized by one impact every seven excitation periods, as seen in Figure 4.3. As the excitation amplitude increases, for example for $a = 0.084$, and for initial conditions $z_o = 0.15$, $z_o' = 0.31$, elastic impact yields chaotic motion as shown in Figures 4.4(a), on the other hand, inelastic impact yields periodic motion as seen in Figure 4.4(b). Other initial conditions may yield similar

response for both cases of impact. For example, for $z_o = 0.01$, $z_o' = 0.03$, both cases lead to period-four response as shown in Figure 4.5.

Figures 4.6 through 4.9 show a comparison between the response for elastic and inelastic impact cases for $\nu = 0.88$, $a = 0.104$. Some initial conditions yield same response characteristics. For example, for two sets of initial conditions $z_o = 0.01$, $z_o' = 0.01$, and $z_o = 0.15$, $z_o' = -0.11$, both cases yield same response characteristics as shown in Figures 4.6 and 4.7, respectively. For initial conditions $z_o = 0.01$, $z_o' = 0.01$, both cases yield period three response as shown in Figure 4.6, and for $z_o = 0.15$, $z_o' = -0.11$ both cases yield chaotic response as shown in Figure 4.7. Meanwhile, for initial conditions $z_o = 0.15$, $z_o' = 0.09$, elastic impact yields chaotic motion and inelastic impact yields period-three motion as shown in Figure 4.8. On the other hand, some initial conditions may lead to ship rollover (ship capsizing) in case of elastic impact, meanwhile, inelastic impact yields safe motion. For example, for $z_o = 0.65$, $z_o' = -0.33$, Figure 4.9 shows that $e = 1$ yields ship capsizing, while $e = 0.8$ yields multi-periodic motion. Domains of attraction for $\nu = 0.88$, $a = 0.104$ are shown in Figure 4.10. It can be seen that elastic impact yields larger eroded area of ship rollover or ship capsizing than for inelastic impact.

For different values of excitation amplitude, the domains of attraction generated for inelastic impact ($e = 0.8$) according to Model 1 is shown in Figure 4.11. It is seen that for relatively small values of excitation amplitude ($a < 0.092$) the entire domain bounded by the grazing orbit experiences bounded oscillations as shown in

Figure 4.11(a). As the excitation amplitude gradually increases, for example, for $a = 0.104$ the domain is eroded by empty space indicating ship capsizing as shown in Figure 4.11(b). By increasing the excitation amplitude, the eroded area representing the ship capsizing increases as shown in Figures 4.11 (c) through 4.11(f) up to excitation amplitude $a \leq 0.192$. Above that excitation amplitude the entire region belongs to ship capsizing. Comparing the safe basins of attraction generated for inelastic impact to those generated for elastic impact shown in Figure 3.9, one may conclude that for same excitation parameters the eroded area representing regions of rollover dynamics in case of inelastic impact is less than that for elastic impact.

A summary of different response regimes for inelastic impact (Model 1) for $e = 0.8$, and excitation frequency ratio $\nu = 0.88$ are summarized in the bifurcation diagram shown in Figure 4.12. This diagram reveals the coexistence of different solutions for the same excitation level depending on initial conditions; non-impact bounded oscillations of period-one as shown by the black square, modulated motion shown by the symbol \diamond , multi-periodic oscillation shown by empty squares, and chaotic motion shown by black circle. Also, it can be seen from Figure 4.12 that rollover motion exists for excitation amplitude $a \geq 0.092$. Comparing the bifurcation diagram shown in Figure 4.12 to the corresponding one for purely elastic impact shown in Figure 3.10, reveals that for elastic impact, rollover motion exists for $a \geq 0.084$. However for inelastic impact, $e = 0.8$, the value of excitation amplitude at which rollover motion exists increases to $a \geq 0.092$. On the other hand, for the case

of $e=1$, the entire domain is unsafe (i.e. all initial conditions lead to ship capsizing) for $a \geq 0.132$. Meanwhile, for $e=0.8$, this value is raised up to $a \geq 0.196$.

For excitation frequency ratio $\nu=0.94$, and different values of excitation amplitude, the domains of attraction generated for inelastic impact ($e=0.8$) according to Model 1 is shown in Figure 4.13. It is seen that for relatively small values of excitation amplitude ($a < 0.068$) the entire domain bounded by the grazing orbit experiences bounded oscillations as shown in Figure 4.13(a). As the excitation amplitude gradually increases, for example, for $a=0.072$ the domain is eroded indicating rollover motion as shown in Figure 4.13(b). By increasing the excitation amplitude, the eroded area representing the ship capsizing increases as shown in Figures 4.13 (c) through 4.13(f) up to excitation amplitude $a \leq 0.212$. Above that excitation amplitude the entire region belongs to ship capsizing. Comparing the safe basins of attraction generated for inelastic impact to those generated for elastic impact shown in Figure 3.15, one may conclude that for same excitation parameters the eroded area representing regions of rollover dynamics in case of inelastic impact is less than that for elastic impact.

A summary of different response regimes for inelastic impact (Model 1), $e=0.8$, and excitation frequency ratio $\nu=0.94$ are summarized in the bifurcation diagram shown in Figure 4.14. This diagram reveals the coexistence of different solutions for the same excitation level depending on initial conditions. Also, it can be seen from Figure 4.14 that rollover motion exists for excitation amplitude $a \geq 0.068$. Comparing the bifurcation diagram shown in Figure 4.14 to the corresponding one for purely elastic impact shown in Figure 3.16, reveals that for elastic impact, rollover

motion exists for $a \geq 0.064$. However for inelastic impact, $e = 0.8$, the value of excitation amplitude at which rollover motion exists increases to $a \geq 0.068$. On the other hand, for the case of $e = 1$, the entire domain yield ship capsizing for $a \geq 0.192$. Meanwhile, for $e = 0.8$, this value is raised up to $a \geq 0.216$. It can be seen that the significance of the damping due to inelastic impact is not as beneficiary as it was for excitation frequency ratio $\nu = 0.88$, i.e., as the excitation frequency ratio approaches to resonance (i.e., $\nu = 1.0$), the damping due to inelastic impact becomes less significant.

For excitation frequency ratio $\nu = 1.2$, the domains of attraction generated for inelastic impact case ($e = 0.8$) is shown in Figures 4.15. Comparing the results to those for elastic impact given in Figure 3.21, it can be seen that in case of inelastic impact, the area of rollover dynamics is less than that for elastic impact. The results for inelastic impact case can be summarized in the bifurcation diagram shown in Figure 4.16. This diagram reveals the coexistence of two solutions for the same excitation level depending on initial conditions; non-impact bounded oscillations of period-one as shown by the black square and period-one oscillations experiencing impact with the barrier indicated by the black triangle. Comparing the bifurcation diagram shown in Figure 4.16 to the corresponding one for purely elastic impact shown in Figure 3.22, reveals that for elastic impact, rollover motion exists for $a \geq 0.044$, however, for inelastic impact, $e = 0.8$, rollover motion exists for $a \geq 0.048$. On the other hand, for the case of $e = 1$, the entire domain is unsafe for $a \geq 0.16$. Meanwhile, for $e = 0.8$, this value is raised up to $a \geq 0.176$.

The importance of this section is that it emphasizes the contribution of the additional damping associated with inelastic impact given by the last term on the left hand side in equation (4.4). For coefficient of restitution less than one, this term plays an important role in ship roll motion and results in reducing the area to region of unsafe motion when compared to purely elastic impact.

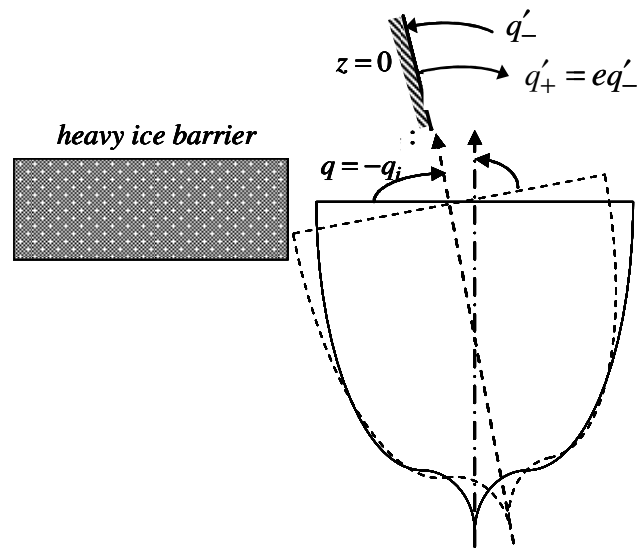


Figure 4.1. Schematic diagram of one-sided ice barrier inelastic impact with ship in roll oscillation.

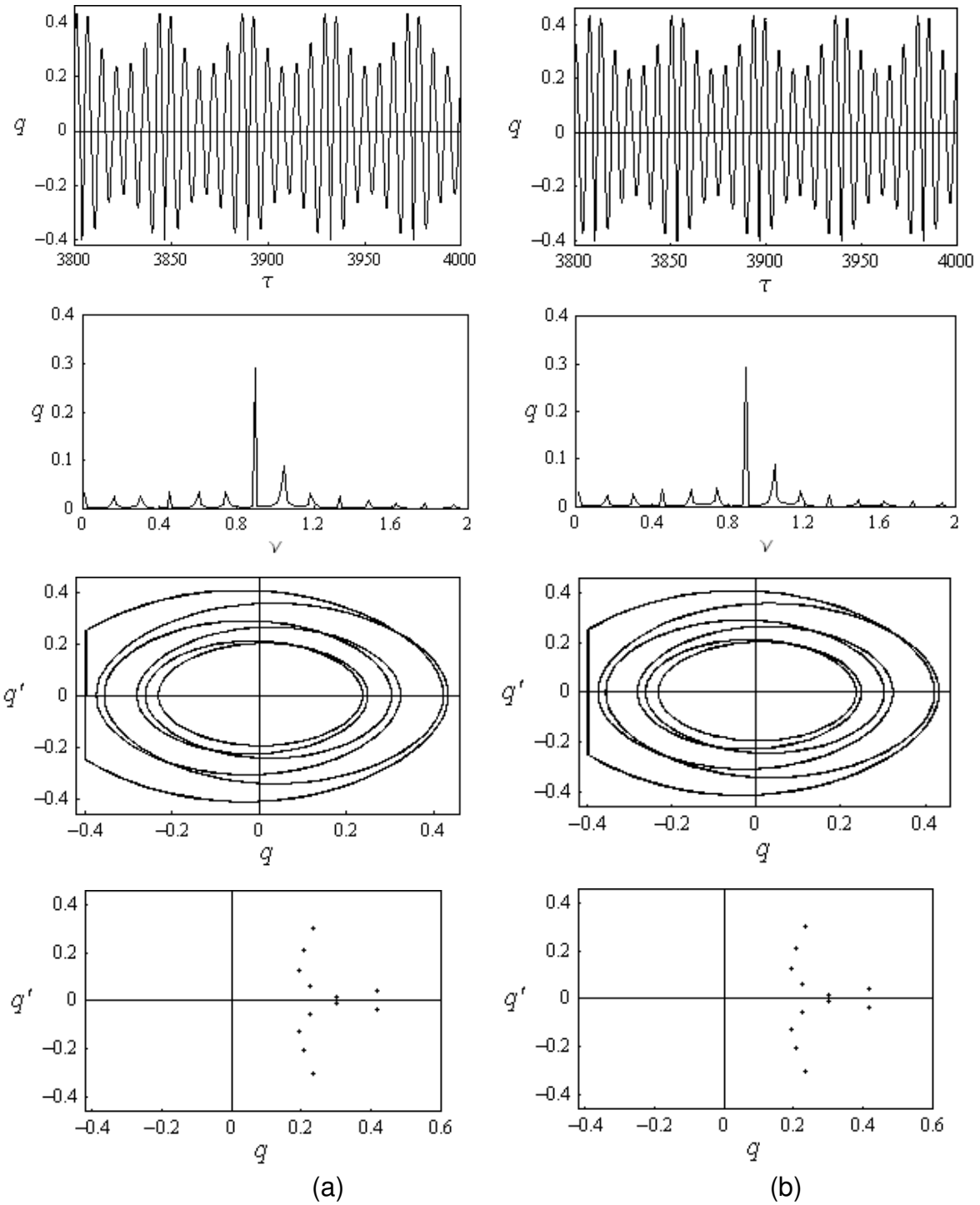


Figure 4.2. Time History Records, FFT, Phase portraits, and Poincaré Maps for $\nu = 0.88$, and $a = 0.06$. Initial conditions $z_o = 0.01$, $z_o' = 0.01$.
 (a) Elastic impact $e = 1$, and (b) Inelastic impact (Model 1) $e = 0.8$.

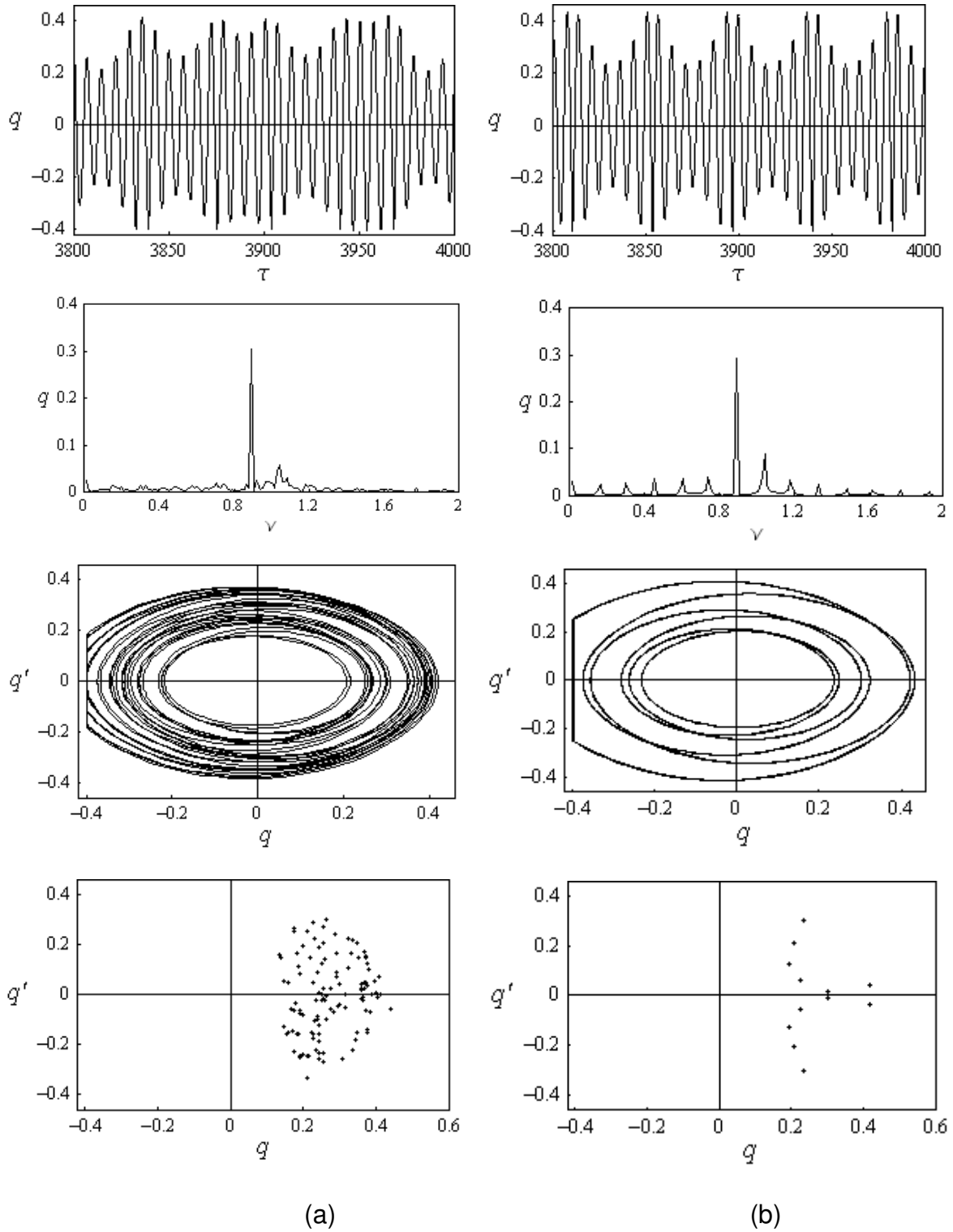


Figure 4.3. Time History Records, FFT, Phase portraits, and Poincaré Maps

for $\nu = 0.88$, and $\alpha = 0.06$. Initial conditions $z_o = 0.11$, $z_o' = -0.19$.

(a) Elastic impact $e = 1$, and (b) Inelastic impact (Model 1) $e = 0.8$.

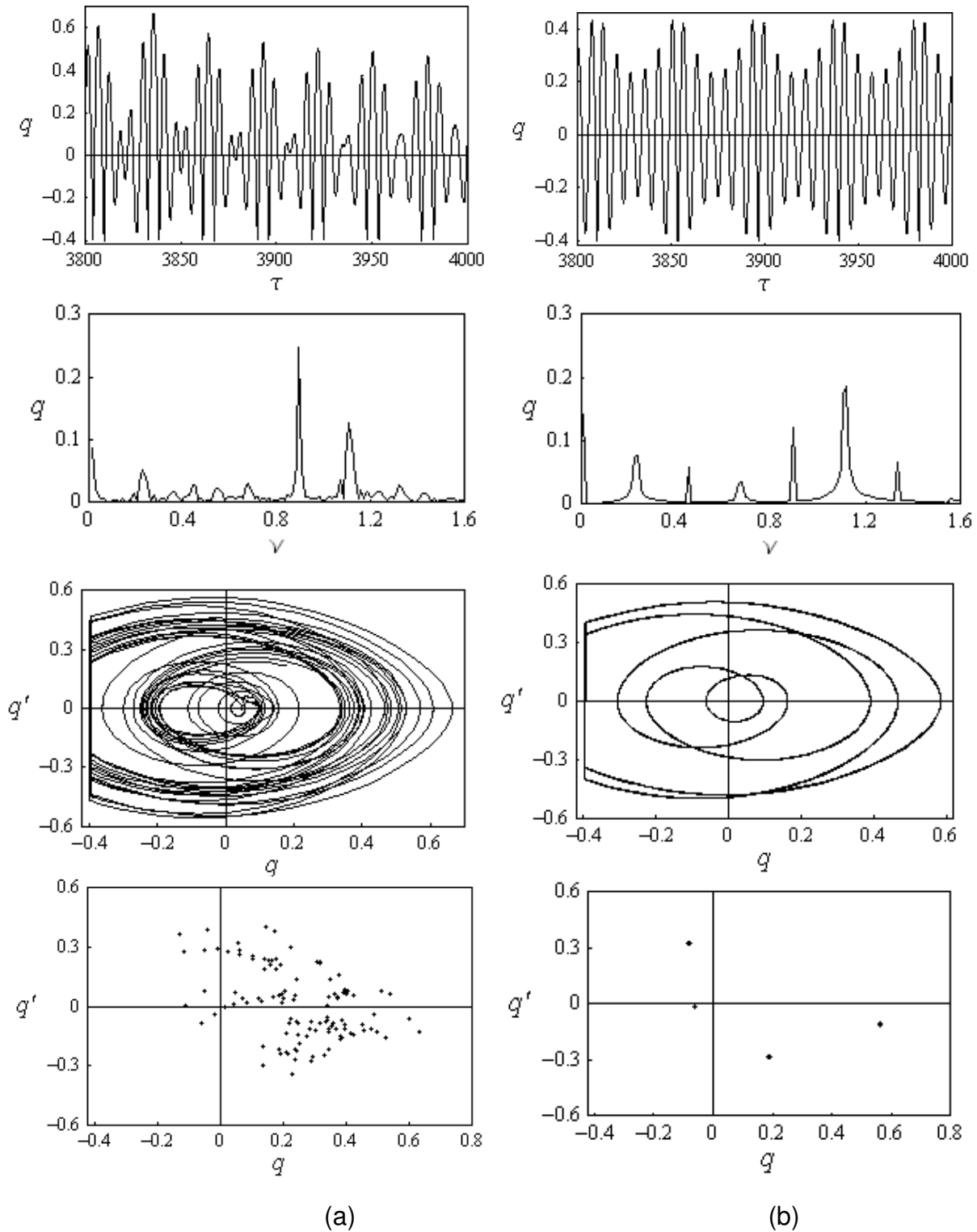


Figure 4.4. Time History Records, FFT, Phase portraits, and Poincaré Maps

for $\nu = 0.88$, and $a = 0.084$. Initial conditions $z_o = 0.15$, $z_o' = 0.31$.

(a) Elastic impact $e = 1$, and (b) Inelastic impact (Model 1) $e = 0.8$.

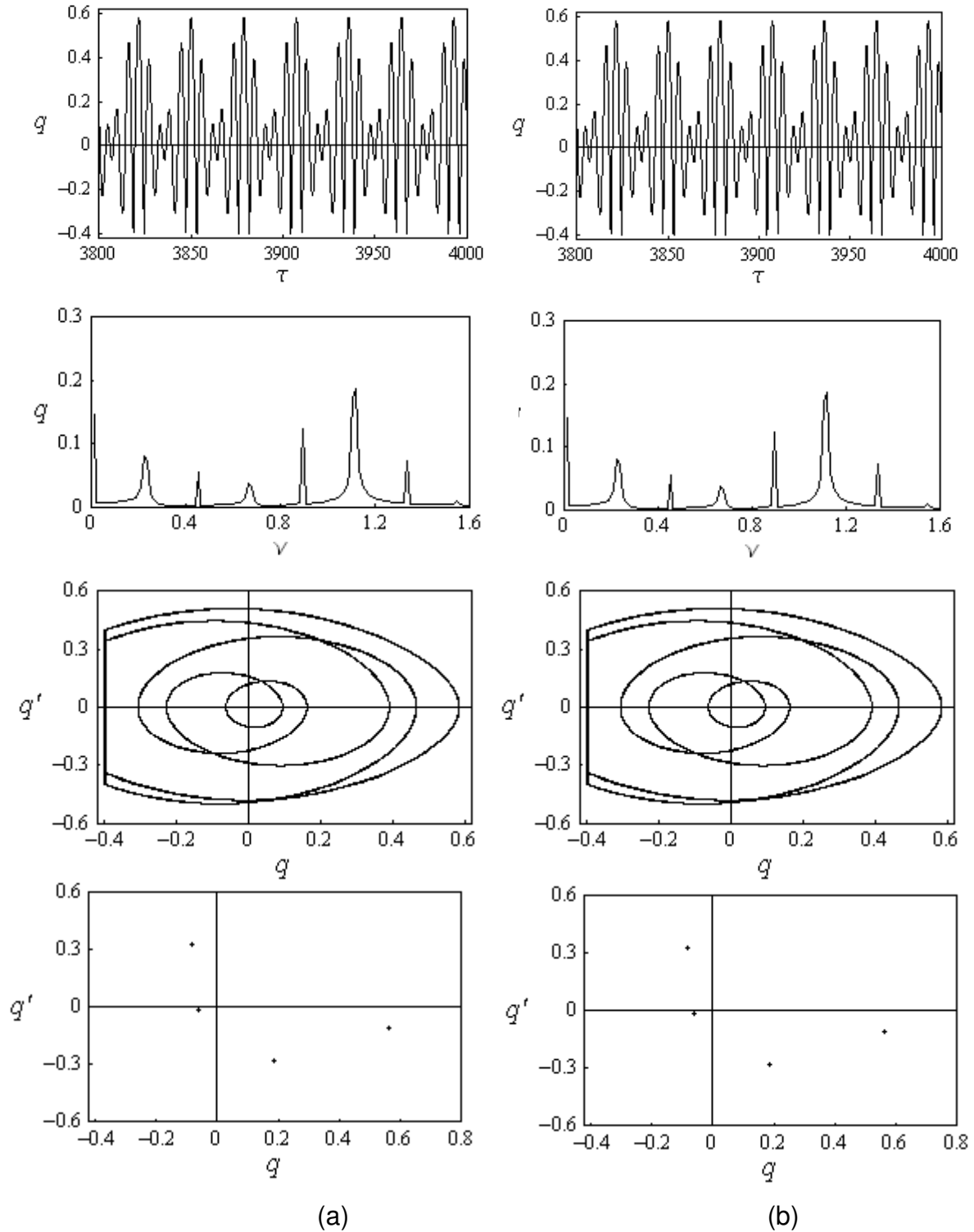


Figure 4.5. Time History Records, FFT, Phase portraits, and Poincaré Maps

for $\nu = 0.88$, and $a = 0.084$. Initial conditions $z_o = 0.01$, $z_o' = 0.03$.

(a) Elastic impact $e = 1$, and (b) Inelastic impact (Model 1) $e = 0.8$.

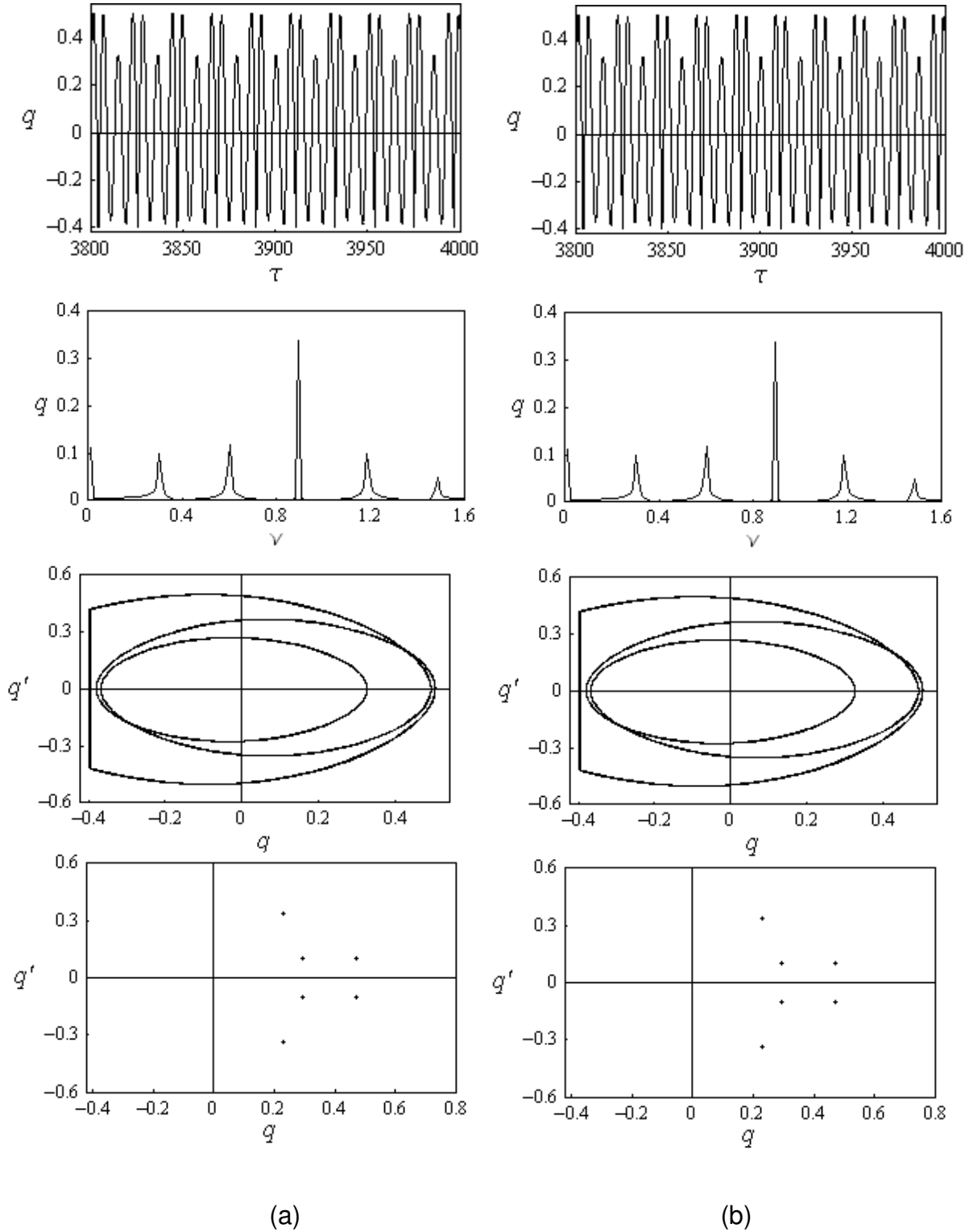


Figure 4.6. Time History Records, FFT Phase portraits, and Poincaré Maps for $\nu = 0.88$, and $a = 0.104$. Initial conditions $z_o = 0.01$, $z_o' = 0.01$.

(a) Elastic impact $e=1$, and (b) Inelastic impact (Model 1) $e=0.8$.

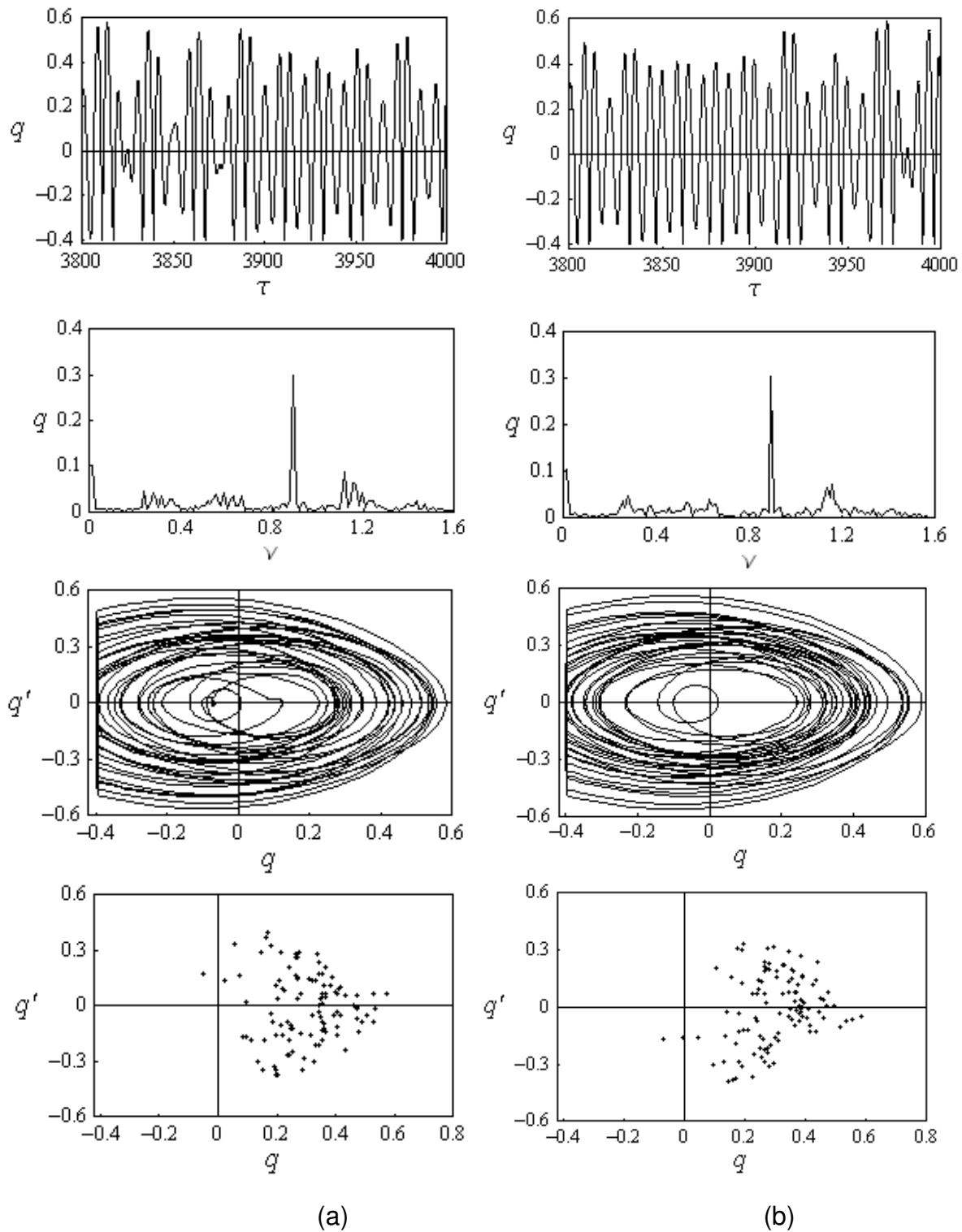


Figure 4.7. Time History Records, FFT, Phase portraits, and Poincaré Maps for $\nu = 0.88$, and $a = 0.104$. Initial conditions $z_o = 0.15$, $z_o' = -0.11$.

(a) Elastic impact $e=1$, and (b) Inelastic impact (Model 1) $e=0.8$.

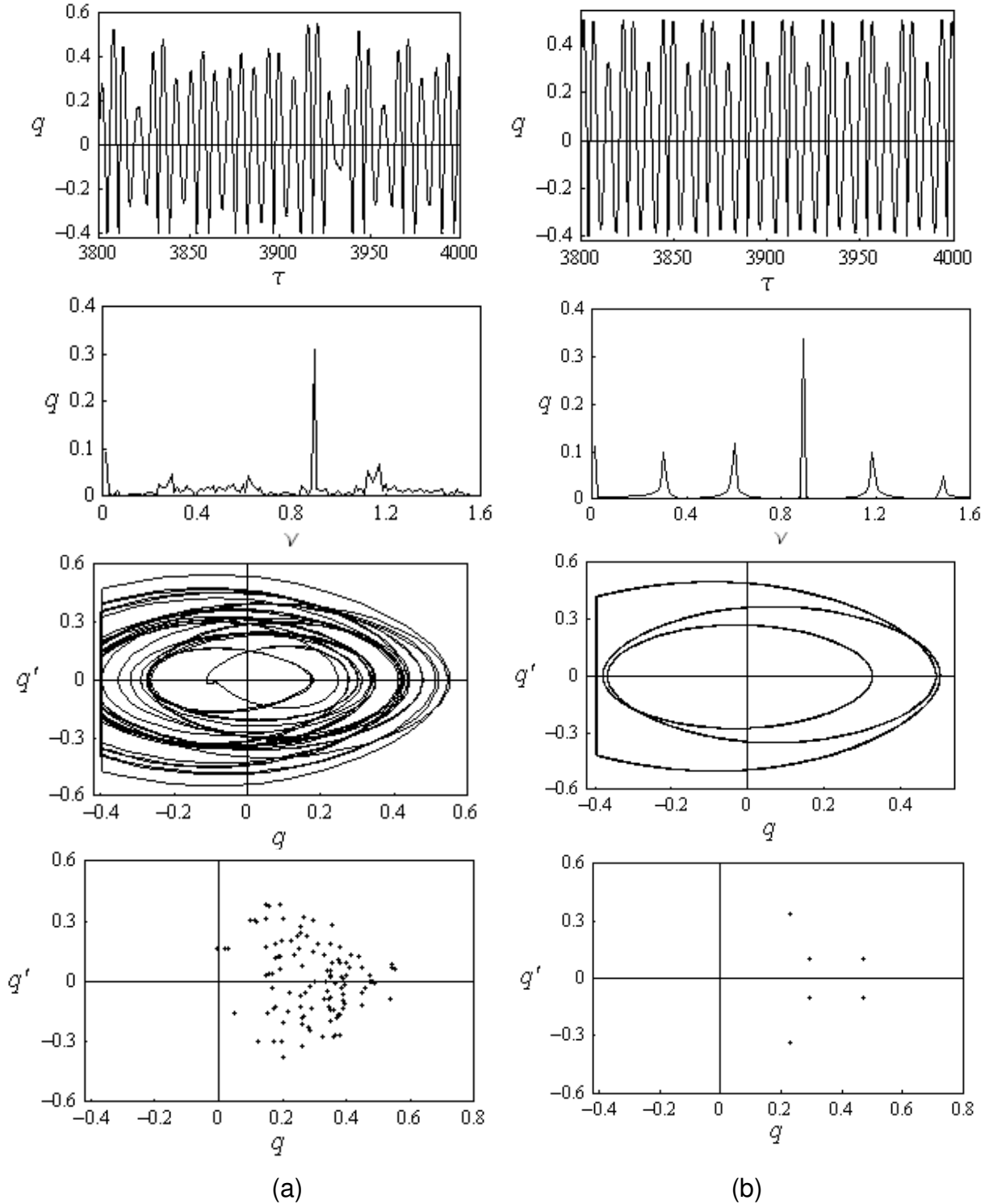


Figure 4.8. Time History Records, FFT, Phase portraits, and Poincaré Maps

for $\nu = 0.88$, and $a = 0.104$. Initial conditions $z_o = 0.15$, $z_o' = 0.09$.

(a) Elastic impact $e=1$, and (b) Inelastic impact (Model 1) $e=0.8$.

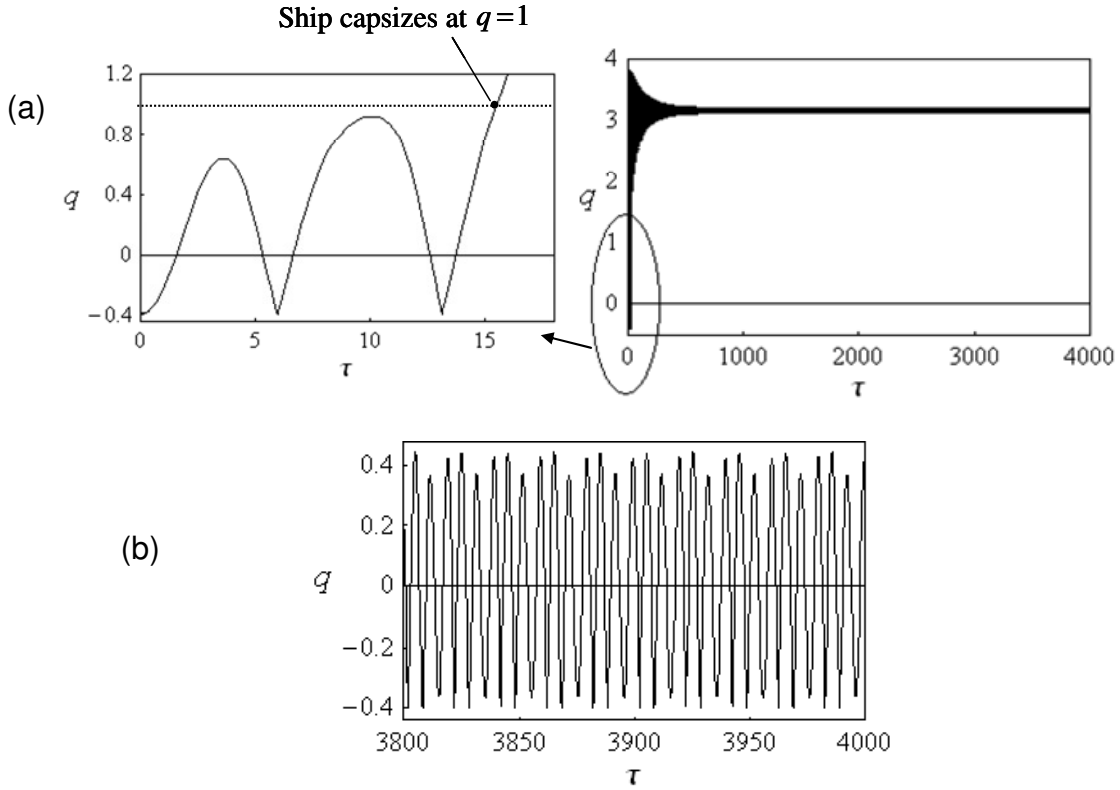


Figure 4.9. Time History Records for $\nu = 0.88$, and $a = 0.104$. Initial conditions $z_o = 0.65$, $z_o' = -0.23$; (a) Elastic impact $e = 1$, and (b) Inelastic impact (Model 1) $e = 0.8$.

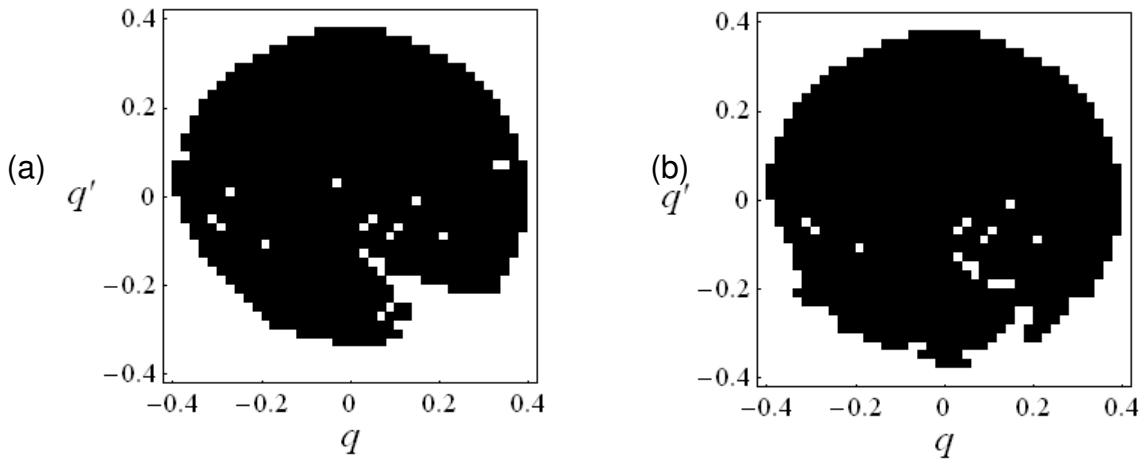


Figure 4.10. Domains of attraction for $\nu = 0.88$, and $a = 0.104$; (a) Elastic impact $e = 1$, and (b) Inelastic impact (Model 1) $e = 0.8$: Black region: bounded (safe) motion, and empty space: rollover dynamics.

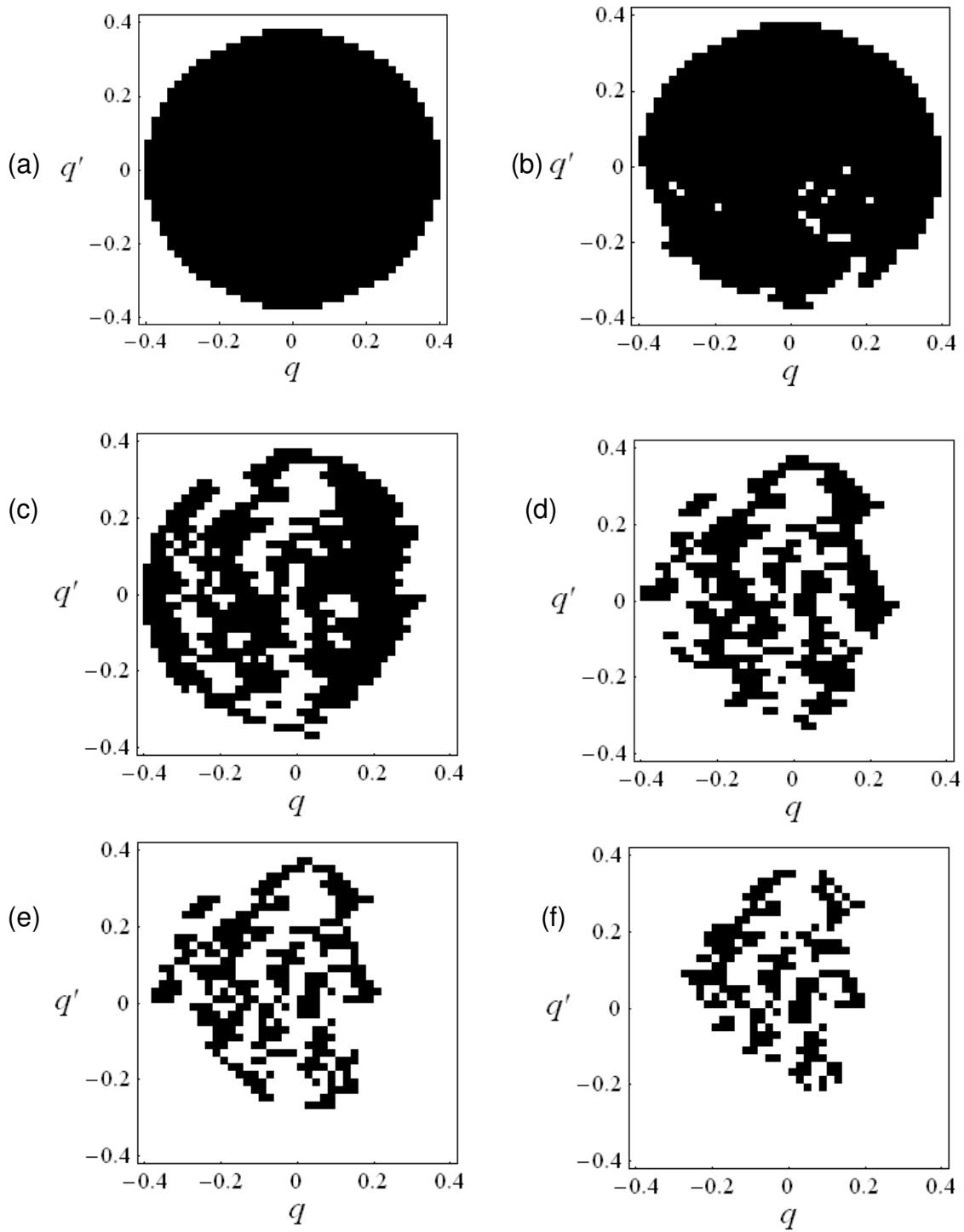


Figure 4.11. Domains of attraction for different excitation amplitudes for $v = 0.88$ as predicted by Model 1 for inelastic impact ($e = 0.8$); (a) $a = 0.08$, (b) $a = 0.104$, (c) $a = 0.12$, (d) $a = 0.14$, (e) $a = 0.16$, and (f) $a = 0.18$; Black region: bounded (safe) motion, and empty space: rollover dynamics.

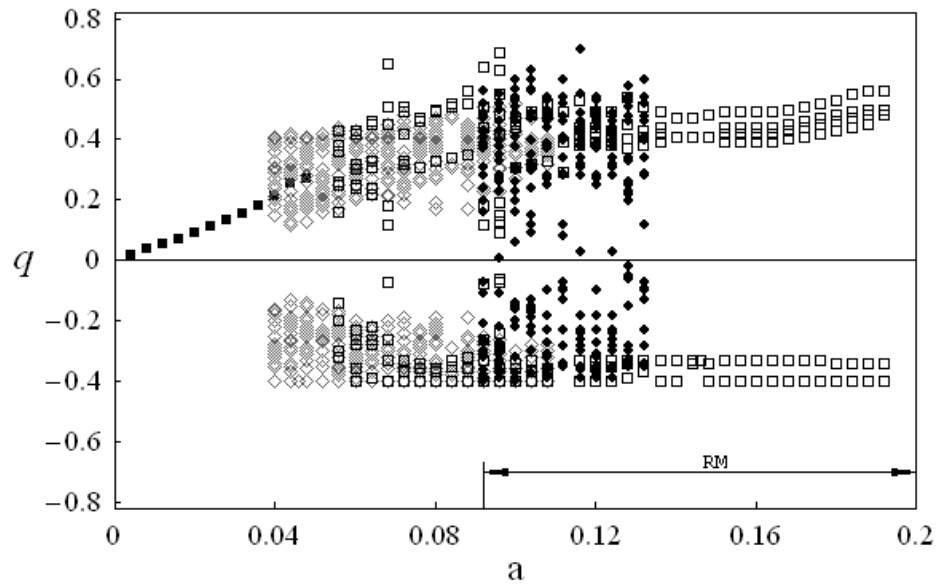


Figure 4.12. Bifurcation diagram for $v = 0.88$ as predicted by Model 1 for inelastic impact ($e = 0.8$); ■ Period-one response, ◊ Modulated response, □ Multi-periodic response, ● Chaotic motion, and RM= Rollover Motion.

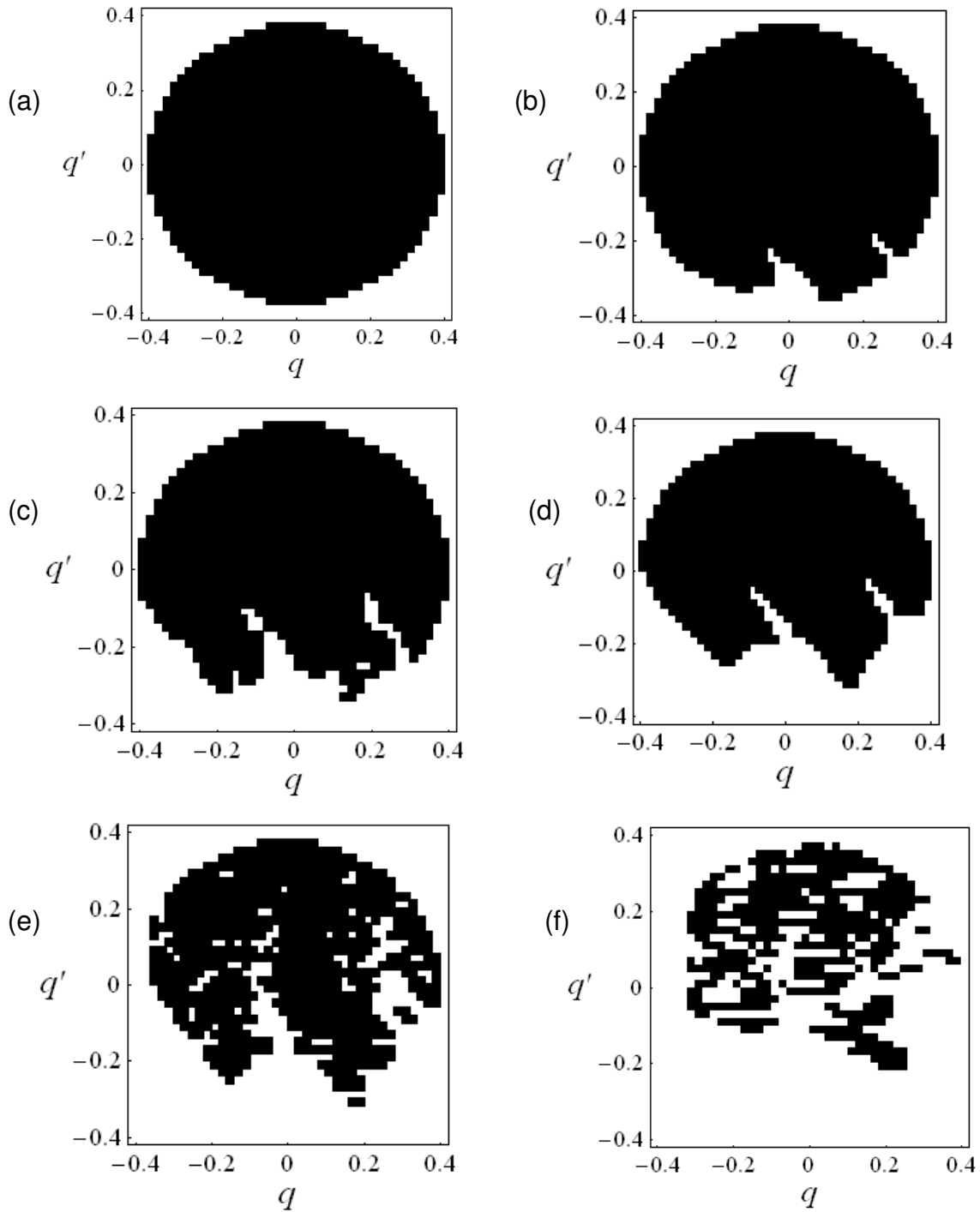


Figure 4.13. Domains of attraction for different excitation amplitudes for $v = 0.94$ as predicted by Model 1 for inelastic impact ($e = 0.8$); (a) $a = 0.04$, (b) $a = 0.072$, (c) $a = 0.08$, (d) $a = 0.088$, (e) $a = 0.096$, and (f) $a = 0.104$; Black region: bounded (safe) motion, and empty space: rollover dynamics.

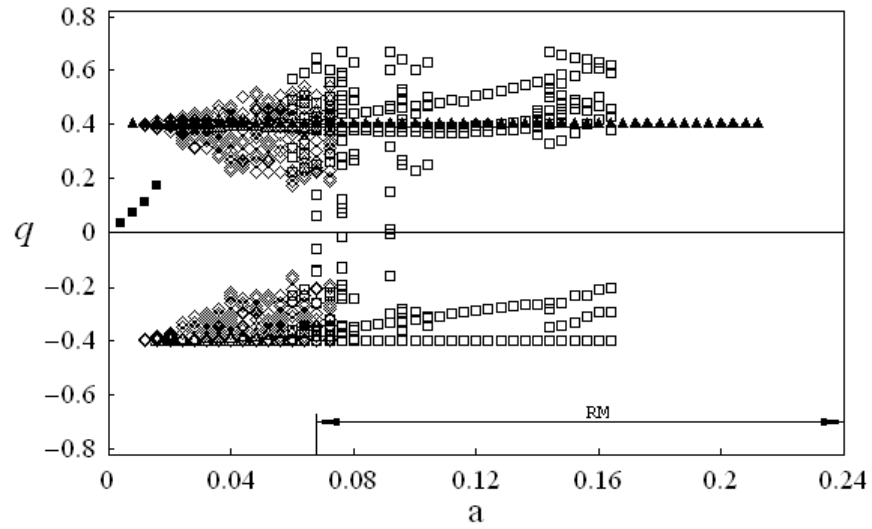


Figure 4.14. Bifurcation diagram for $\nu = 0.94$ as predicted by Model 1 for inelastic impact ($e = 0.8$); \blacksquare Period-one response, \blacktriangle Period-one response experiencing impact, \triangle Period-two Response, \diamond Modulated response, \square Multi - periodic response, \bullet Chaotic motion, and RM= Rollover Motion.

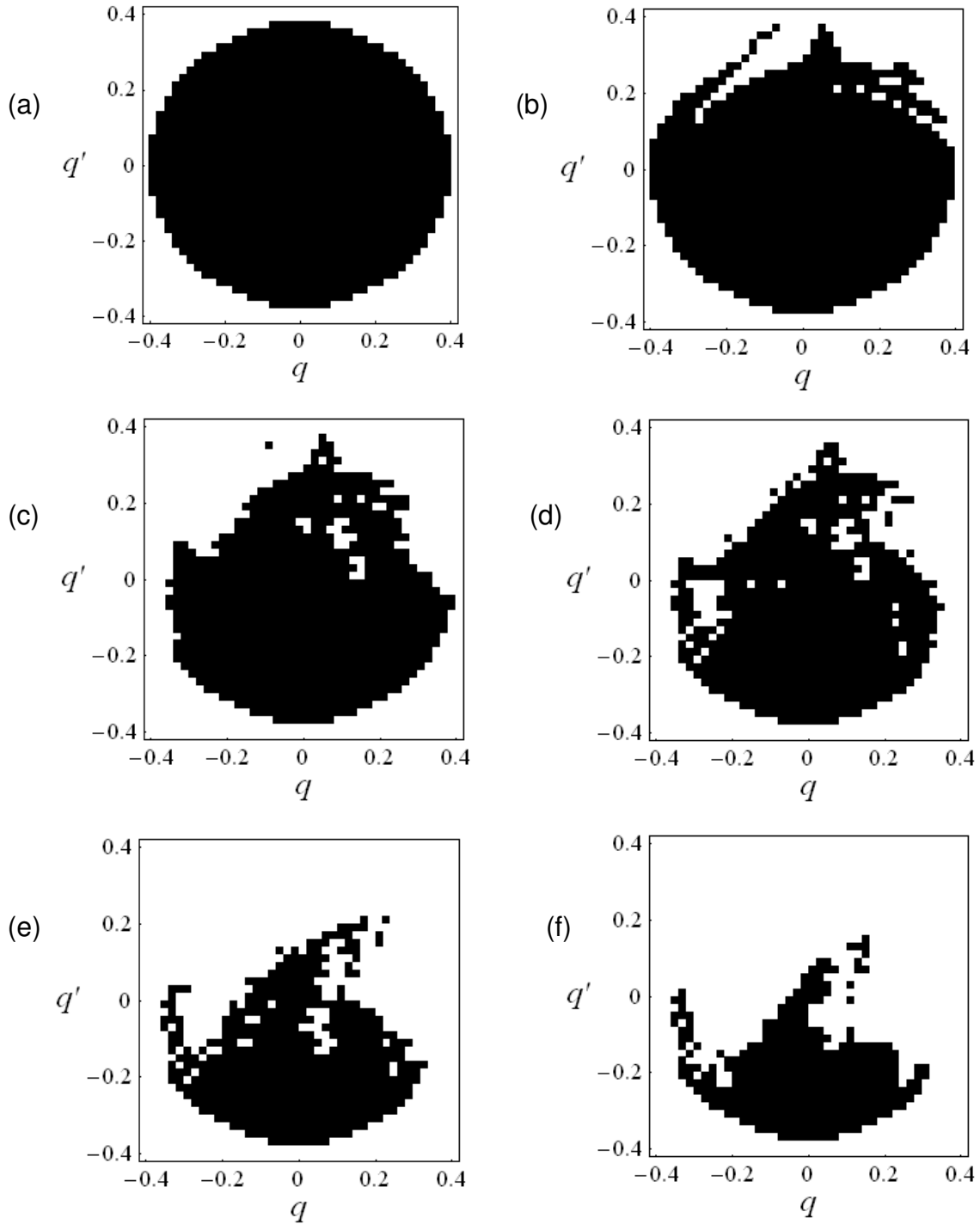


Figure 4.15. Domains of attraction for different excitation amplitudes for $v = 1.2$ as predicted by Model 1 for inelastic impact ($e = 0.8$); (a) $a = 0.04$, (b) $a = 0.064$, (c) $a = 0.096$, (d) $a = 0.104$, (e) $a = 0.12$, and (f) $a = 0.136$; Black region: bounded (safe) motion, and empty space: rollover dynamics.

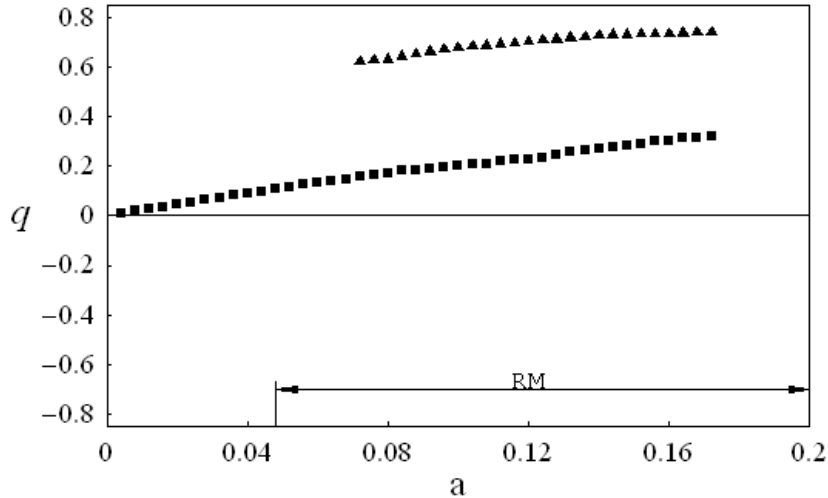


Figure 4.16. Bifurcation diagram for $\nu = 1.2$ as predicted by Model 1 for inelastic impact ($e = 0.8$); ■ Period-one response, ▲ Period-one response experiencing impact, and RM= Rollover Motion.

4.3 Non-Smooth Coordinate-Velocity Transformation (Model 2)

The previous section emphasizes the significance of damping associated with inelastic impact. However, the approach developed is efficient within the condition that the coefficient of restitution e is close to unity, such that $(1-e)$ is a small parameter. Ivanov (1994) developed another non-smooth coordinate transformation that avoids the problem of Dirac delta function. This section adopts this transformation. A comparison between the ship roll response characteristics as predicted by both Model 1 and Model 2 is carried out for same conditions and coefficient of restitution in order to determine the effectiveness of both transformations.

4.3.1 ANALYTICAL MODELING

The nonlinear equation of roll motion of ship under sinusoidal excitation takes the form

$$q'' + \bar{\zeta}q' + \gamma q' |q'| + q + \bar{C}_3 q^3 + \bar{C}_5 q^5 = Z(\tau) \quad (4.5)$$

A modified non-smooth transformation of state variables, including both coordinates and velocities, was developed by Ivanov (1994) for the case of inelastic impact. Equation (4.5) can be written in terms of the state vector form

$$u = q', \text{ and}$$

$$u' = -\bar{\zeta}q' - \gamma q' |q'| - q - \bar{C}_3 q^3 - \bar{C}_5 q^5 + Z(\tau) \quad (4.6)$$

Adopting Iv.T. for one dimensional case the following transformation can be used for inelastic impact

$$q = s \operatorname{sgn}(s) - q_i, \text{ and}$$

$$u = \operatorname{sgn}(s) [1 - K \operatorname{sgn}(s\upsilon)] \upsilon \quad (4.7)$$

where s and υ are the new coordinates whose values are not restricted, and $K = (1-e)/(1+e)$, and e is the coefficient of restitution. Alternatively, equations (4.7) may be written in the form

$$s = (q + q_i) \operatorname{sgn}(s), \text{ and}$$

$$\upsilon = \frac{\operatorname{sgn}(s)}{1 - K^2} [1 + K \operatorname{sgn}(s\upsilon)] u \quad (4.8)$$

Taking the time derivative of equations (4.8), using equations (4.6) and (4.7), consider sinusoidal excitation $Z(\tau) = a \sin \nu \tau$, gives the ship equation of motion in terms of s and υ coordinates

$$s' = [1 - K \operatorname{sgn}(s\upsilon)] \upsilon, \text{ and}$$

$$\begin{aligned} \dot{v} = & -\bar{\zeta}v - \gamma v |1 - K \operatorname{sgn}(sv)| v + \operatorname{sgn}(s) \times \left[\frac{1 + K \operatorname{sgn}(sv)}{1 - K^2} \right] \times \\ & \left\{ -(s \operatorname{sgn}(s) + q_i) - \bar{C}_3 (s \operatorname{sgn}(s) + q_i)^3 - \bar{C}_5 (s \operatorname{sgn}(s) + q_i)^5 + a \sin v \tau \right\} \end{aligned} \quad (4.9)$$

Equation (4.9) describes the ship roll dynamics with one-sided inelastic impact on the entire time interval, where conditions of reflection from the barrier and impact energy loss are already included through transformation (4.8). Substituting for $\bar{\zeta} = 0.01$, $\gamma = 0.005$, $\bar{C}_3 = -1.1$, $\bar{C}_5 = 0.1$, and $q_i = -0.4$, equation (4.9) is solved numerically for different values of excitation amplitude and excitation frequency, a comparison between Model 1 and Model 2 will be made. The results discussed in the next subsection.

4.3.2 NUMERICAL SIMULATION

A comparison of ship response as predicted by both models 1 and 2 is shown in Figure 4.17 for excitation frequency ratio $\nu = 0.88$, excitation amplitude $a = 0.084$, and initial conditions $z_o = 0.01$, $z_o' = 0.01$ and coefficient of restitution $e = 0.8$. It is seen that Model 1 yields multi-periodic response while Model 2 gives modulated response. At the same time, the maximum roll amplitude predicted by Model 1 is greater than that predicted by Model 2. Figures 4.18 through 4.20 show a comparison of the response characteristics as predicted by the Model 1 and Model 2 for $\nu = 0.88$, and $a = 0.12$. For initial conditions $z_o = 0.01$, $z_o' = 0.01$, Figure 4.18 (a) reveals chaotic response while Figure 4.18 (b) exhibits period-three response. For $z_o = 0.01$, $z_o' = 0.03$, Figure 4.19 (a) shows chaotic response as predicted by Model

1, however Model 2 predicts modulated response as shown in Figure 4.19 (b). It can be noted that for the last two conditions, the maximum roll amplitude predicted by Model 1 is greater than that predicted by Model 2. For other initial conditions, Model 1 yields rollover or ship capsizing, while Model 2 yields safe ship motion. For example for initial conditions $z_o = 0.19$, $z_o' = 0.13$ Model 2 yields modulated response and multi-periodic response as shown in Figures 4.20. The influence of initial conditions for excitation amplitude $a = 0.12$ on the ship safety is better understood through basins of attraction shown in Figure 4.21. Figure 4.21(a) shows the domains of attraction generated by Model 1. It reveals relatively larger eroded area to the region of ship capsizing than the one generated by Model 2.

For excitation frequency ratio $\nu = 0.88$, and different values of excitation amplitude, the domains of attraction generated for inelastic impact ($e = 0.8$) according to Model 2 is shown in Figure 4.22. It is seen that for relatively small values of excitation amplitude ($a < 0.116$) the entire domain experiences bounded oscillations as shown in Figure 4.22(a). As the excitation amplitude gradually increases, for instance for $a = 0.128$ the domain is eroded indicating rollover motion as shown in Figure 4.22(b). By increasing the excitation amplitude, the eroded area representing the ship capsizing increases as shown in Figures 4.22(c) through 4.22(f) up to excitation amplitude $a \leq 0.278$. Above that excitation amplitude the entire region belongs to ship capsizing. Comparing the safe basins of attraction generated by Model 2 to those generated by Model 1 shown in Figure 4.11, one may conclude that for same excitation parameters the eroded area representing regions of rollover dynamics predicted by Model 2 is smaller than that predicted by Model 1.

A summary of different response regimes for inelastic impact $e=0.8$, and excitation frequency ratio $\nu=0.88$ as predicted by Model 2 is summarized in the bifurcation diagram shown in Figure 4.23. This diagram reveals the coexistence of different solutions for the same excitation level depending on initial conditions; non-impact bounded oscillations of period-one as shown by the black square, modulated motion shown by the symbol \diamond , and multi-periodic oscillation shown by empty squares. Also, it can be seen from Figure 4.23 that rollover motion exists for excitation amplitude $a \geq 0.116$. Comparing the bifurcation diagram shown in Figure 4.23 to the corresponding one for predicted by Model 1 shown in Figure 4.12, reveals that Model 1 predicts that rollover motion exists for $a \geq 0.092$. However, the value of excitation amplitude at which rollover motion exists as predicted by Model 2 increases to $a \geq 0.116$. On the other hand, Model 1 predicts that the entire domain yield ship capsizing for $a \geq 0.196$. Meanwhile, for Model 2, this value is raised up to $a \geq 0.24$. On the other hand, Model 2 does not exhibit chaotic motion as Model 1.

The safety fraction S_f for excitation frequency $\nu=0.88$ for purely elastic impact, $e=1$, and inelastic impact, $e=0.8$ predicted by Model 1 and Model 2 is shown in Figure 4.24. It can be seen that the critical value of excitation amplitude at which ship capsizing occurs (i.e. $S_f < 1$) for purely elastic impact is $a \geq 0.084$. Meanwhile for inelastic impact, $e=0.8$, $S_f < 1$ for $a \geq 0.092$ as predicted by Model 1; and for $a \geq 0.116$ as predicted by Model 2. Also, it can be seen that the value of excitation amplitude that gives an entire domain of unsafe motion (i.e. $S_f = 0$) for elastic impact, $e=1$, is $a \geq 0.132$. For inelastic impact, $e=0.8$, $S_f = 0$ for $a \geq 0.196$

and 0.24 as predicted by Model 1 and Model 2, respectively. On the other hand, the slope of the curve predicted by Model 2 is smaller than that predicted by Model 1 which in turn is smaller than that for purely elastic impact. One may conclude that Model 2 expresses more contribution of the additional damping associated with inelastic impact than Model 1. Moreover it can be seen that Model 2 preserves the value of unity over a value of excitation amplitude larger than that of model 1 and the case of elastic impact.

A selected number of domains of attraction for excitation frequency ratio $\nu = 0.94$ and different values of excitation amplitude are shown in Figures 4.25. Comparing the safe basins of attraction generated by Model 2 to those generated by Model 1 shown in Figure 4.13, one may conclude that as excitation amplitude increases, the eroded area increases for both cases, meanwhile it is larger in case of Model 1 than that predicted by Model 2. For instance $a = 0.096$, relatively large eroded area is predicted by Model 1 than that predicted by model 2 as shown in Figures 4.13(e) and 4.25(b), respectively. A summary of different response regimes for inelastic impact $e = 0.8$, and excitation frequency ratio $\nu = 0.94$ as predicted by Model 2 is summarized in the bifurcation diagram shown in Figure 4.26. This diagram reveals the coexistence of different solutions; non-impact bounded oscillations of period-one as shown by the black square, period-one motion experiencing impact shown by the black triangle, modulated motion shown by the symbol \diamond , and multi-periodic oscillation shown by empty squares. Also, it can be seen from Figure 4.26 that rollover motion exists for excitation amplitude $a \geq 0.092$. Comparing the bifurcation diagram shown in Figure 4.26 to the corresponding one

for predicted by Model 1 shown in Figure 4.14, reveals that Model 1 predicts that rollover motion exists for $a \geq 0.068$. However, the value of excitation amplitude at which rollover motion exists as predicted by Model 2 increases to $a \geq 0.092$. On the other hand, Model 1 predicts that the entire domain yields ship capsizing for $a \geq 0.216$. Meanwhile, for Model 2, this value is raised up to $a \geq 0.28$. Moreover, Model 2 does not exhibit the modulated response but exhibits period-one and period-two motions.

The safety fraction S_f for excitation frequency $\nu = 0.94$ for purely elastic impact, $e = 1$, and inelastic impact, $e = 0.8$ predicted by both models 1 and 2 is shown in Figure 4.27. The critical value of excitation amplitude at which ship capsizing occurs (i.e., $S_f < 1$) for purely elastic impact is $a \geq 0.064$. Meanwhile, for inelastic impact, $e = 0.8$, $S_f < 1$ for $a \geq 0.068$ as predicted by Model 1, and $a \geq 0.092$ as predicted by Model 2. Also, it can be seen that the value of excitation amplitude that gives an entire domain of unsafe motion (i.e. $S_f = 0$) for elastic impact, $e = 1$, is $a \geq 0.192$. For inelastic impact, $e = 0.8$, $S_f = 0$ for $a \geq 0.216$ as predicted by Model 1, and $a \geq 0.28$ as predicted by Model 2. On the other hand, the value of excitation amplitude that gives an entire domain of unsafe motion has smaller value for elastic impact than that for inelastic impact. It can be seen that Model 2 preserves the value of unity over a value of excitation amplitude larger than that of model 1 and the case of elastic impact.

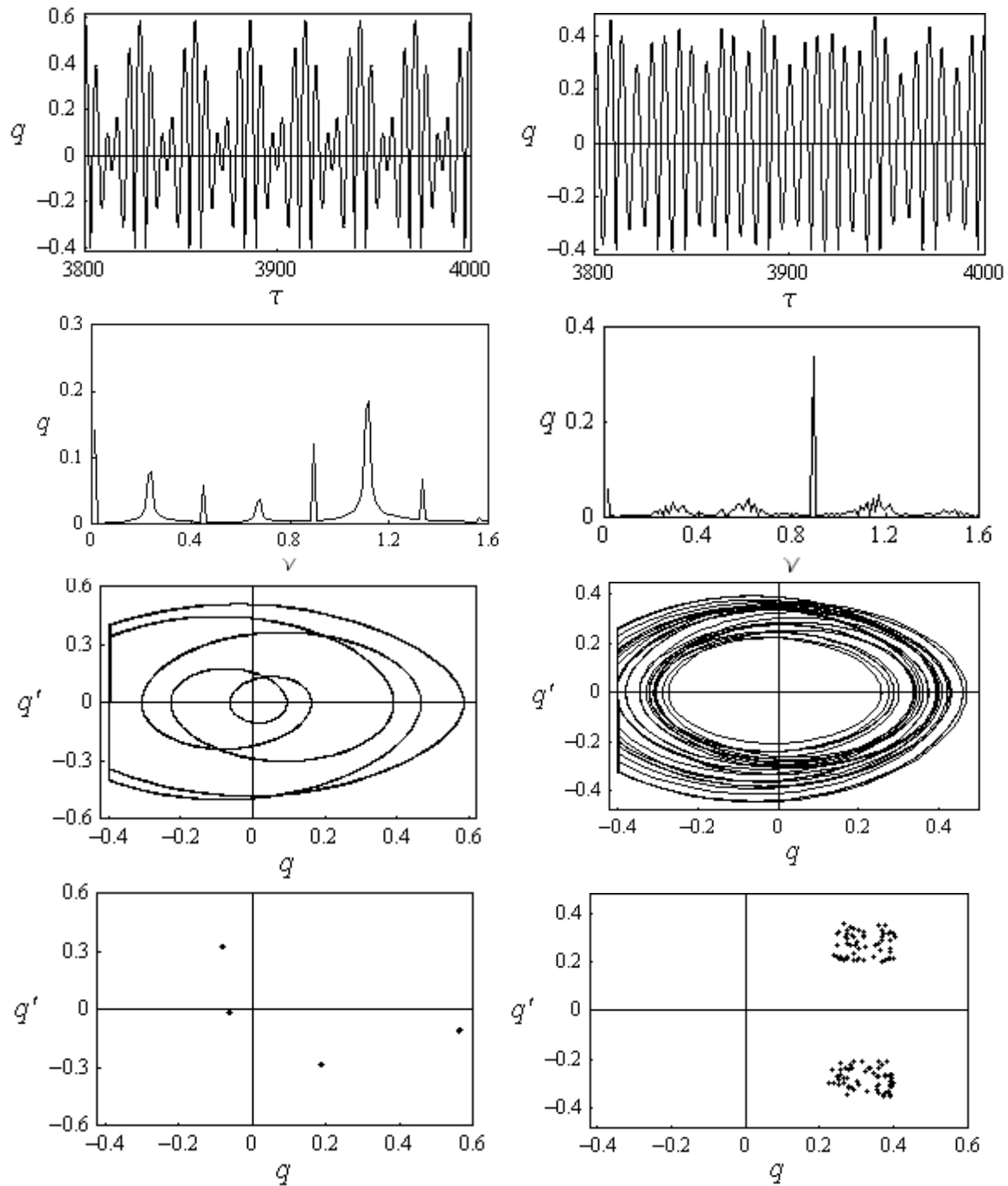
For excitation frequency ratio $\nu = 1.2$, and for different values of excitation amplitude, the domains of attraction generated by Model 2 are shown in Figure 4.28.

Comparing the safe basins of attraction generated by Model 2 to those generated by Model 1 shown in Figure 4.15, reveals that the eroded area to the region of rollover dynamics is less in case of Model 2 than that predicted by Model 1. Different response regimes for inelastic impact $e = 0.8$, and excitation frequency ratio $\nu = 1.2$ as predicted by Model 2 are summarized in the bifurcation diagram shown in Figure 4.29. This diagram reveals the coexistence of two response regimes; non-impact bounded oscillations of period-one, and period-one motion experiencing impact. Also, it can be seen from Figure 4.29 that rollover motion exists for excitation amplitude $a \geq 0.084$. Comparing the bifurcation diagram shown in Figure 4.29 to the corresponding one for predicted by Model 1 shown in Figure 4.16, reveals that Model 1 predicts that rollover motion exists for $a \geq 0.048$. However, the value of excitation amplitude at which rollover motion exists as predicted by Model 2 increases to $a \geq 0.084$. On the other hand, Model 1 predicts that the entire domain yields ship capsizing for $a \geq 0.176$, while, for Model 2, this value is raised up to $a \geq 0.2$.

A comparison between the safety factor as generated by Model 1, and Model 2 for inelastic impact for coefficient of restitution $e = 0.8$, and for purely elastic impact $e = 1$ is given in Figure 4.30. For purely elastic impact, $e = 1$, the stability index factor $S_f = 1$ is maintained for $a \leq 0.044$, and $S_f = 0$ for $a \geq 0.16$. For inelastic impact, $e = 0.8$, Model 1 predicts that $S_f = 1$ for $a \leq 0.048$ and $S_f = 0$ for $a \geq 0.176$, while Model 2 predicts that $S_f = 1$ for $a \leq 0.084$ and $S_f = 0$ for $a \geq 0.216$.

The excitation amplitude at which unbounded motion (Ship capsizing) occurs defines the ship stability boundary and depends on the excitation frequency ratio ν .

The stability boundaries for elastic $e=1$, and inelastic $e=0.8$, impact cases are shown in Figure 4.31. It is seen that the bounded region of the inelastic impact is expanded than that of the purely elastic impact region due to the inherent damping associated for all cases of $e=1$. It is more expanded for model 2 than for model 1 for the same coefficient of restitution $e=0.8$. Comparing the results for inelastic impact as predicted by Model 1 and Model 2, one may notice that Model 2 provides more significant damping. Also, for some conditions, both transformations yield different response regimes. In the next section, the equation of motion is solved explicitly using R.K. method, and the solution will be compared with the results of both models 1 and 2 in order to judge the effectiveness of both transformations.



(a)

(b)

Figure 4.17. Ship time history records, FFT plots, phase portraits, and Poincaré Maps according to (a) Model 1, and (b) Model 2 for $\nu = 0.88$, $a = 0.084$, $e = 0.8$, and initial conditions $z_0 = 0.01$, $z'_0 = 0.01$.

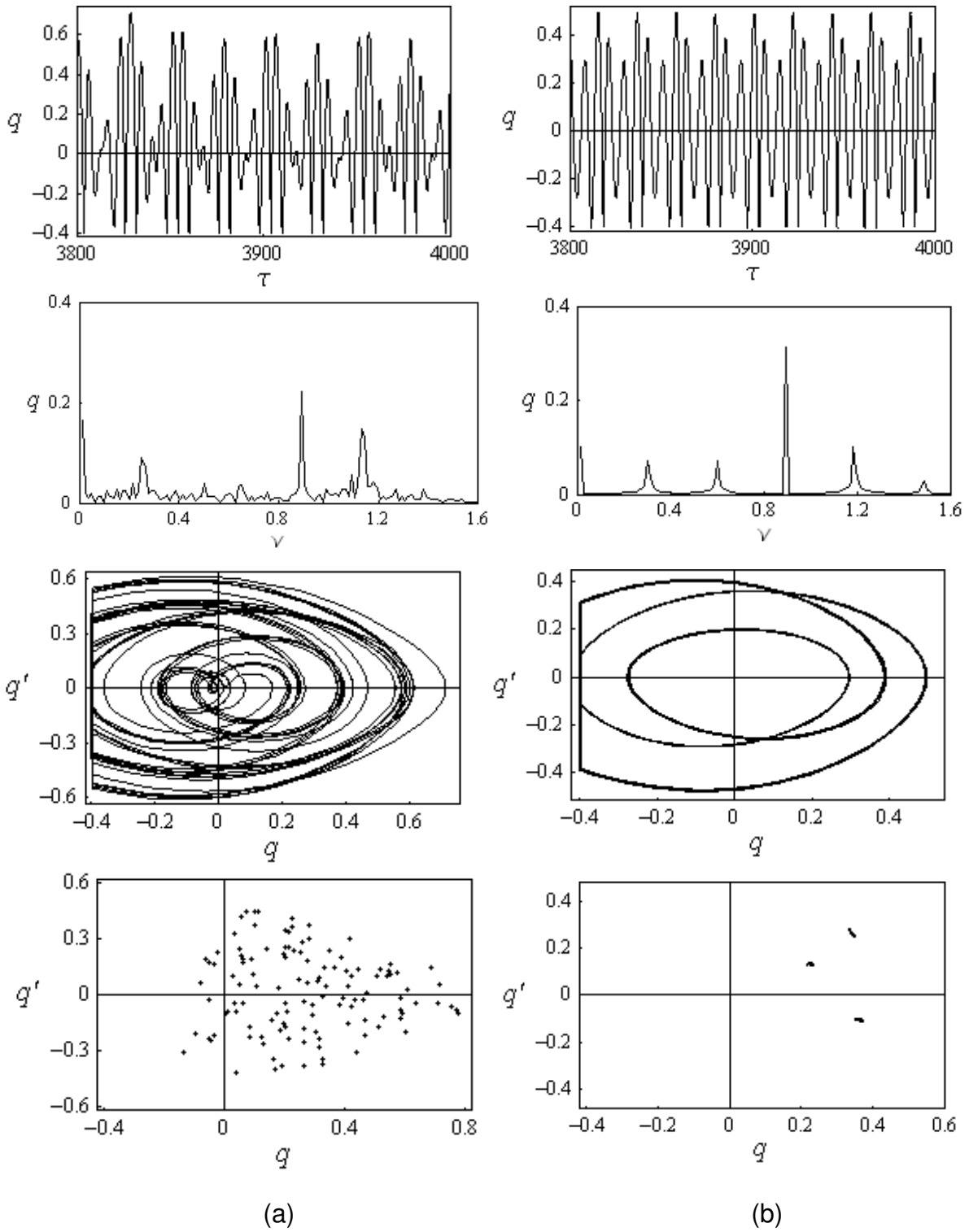


Figure 4.18. Ship time history records, FFT plots, phase portraits, and Poincaré Maps according to (a) Model 1, and (b) Model 2 for $\nu = 0.88$, $a = 0.12$, $e = 0.8$, and initial conditions $z_o = 0.01$, $z_o' = 0.01$.

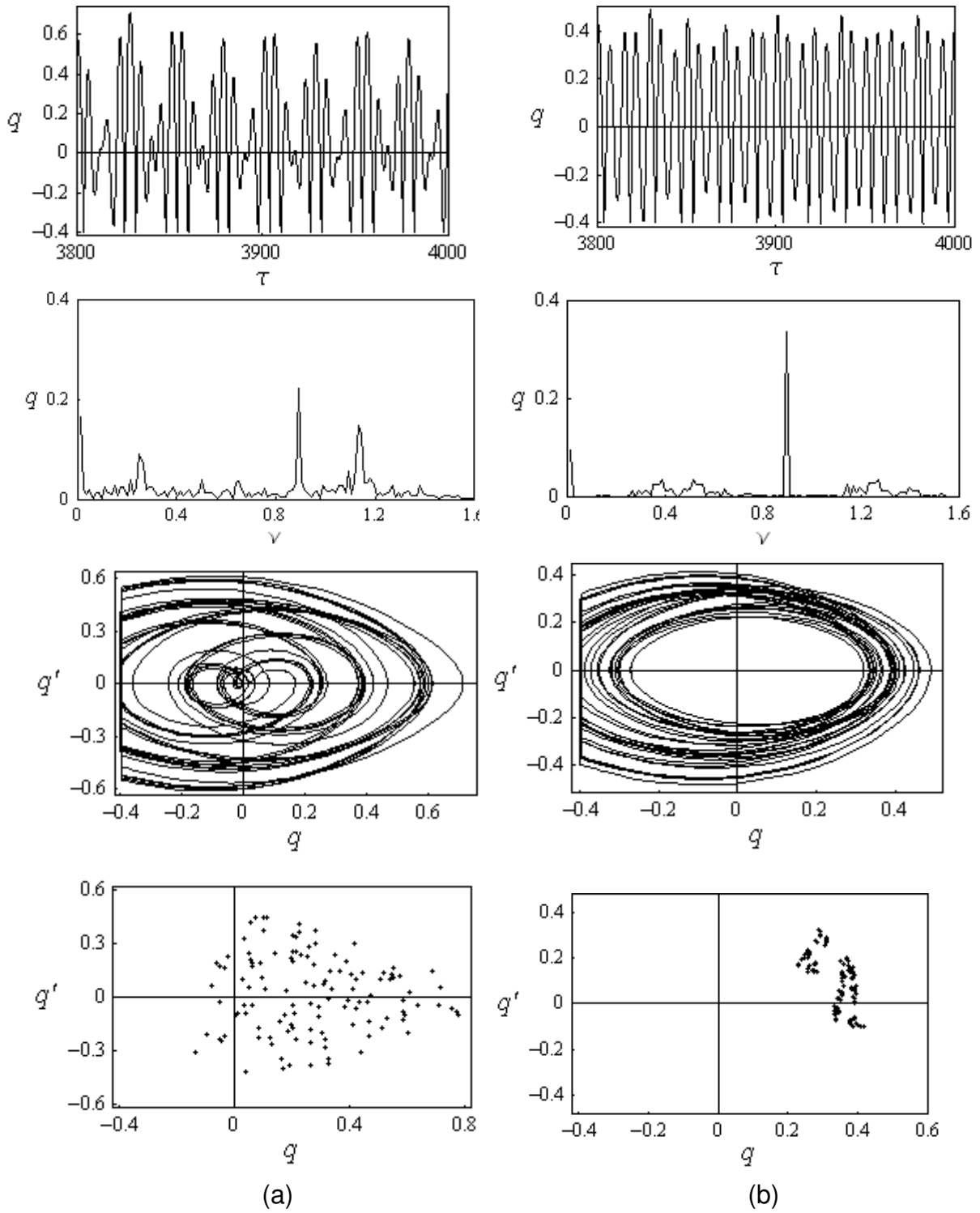


Figure 4.19. Ship time history records, FFT plots, phase portraits, and Poincaré Maps according to (a) Model 1, and (b) Model 2 for $\nu = 0.88$, $a = 0.12$, $e = 0.8$, and initial conditions $z_o = 0.01$, $z_o' = 0.03$.

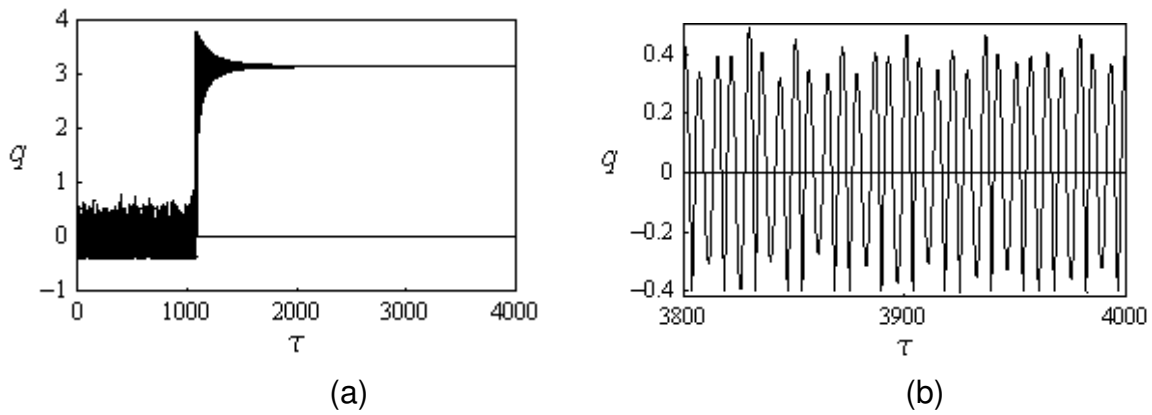


Figure 4.20. Ship time history records, FFT plots, phase portraits, and Poincaré Maps according to (a) Model 1, and (b) Model 2 for $\nu = 0.88$, $a = 0.12$, $e = 0.8$, and initial conditions $z_o = 0.19$, $z_o' = 0.13$.

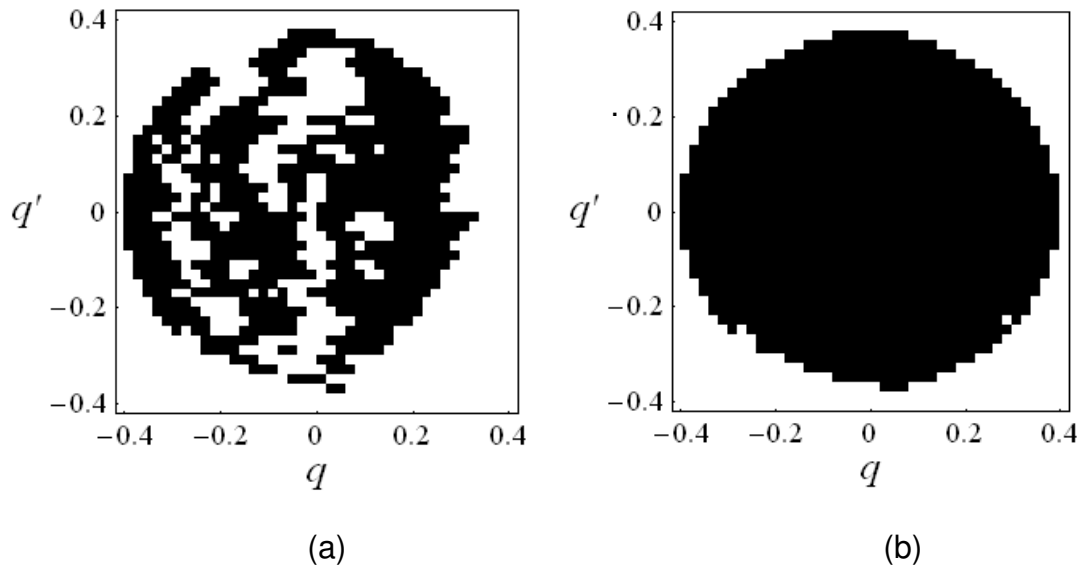


Figure 4.21. Domains of attraction according to (a) Model 1, and (b) Model 2 for $\nu = 0.88$, $a = 0.12$, $e = 0.8$, Black region: bounded (safe) motion, and empty space: rollover dynamics.

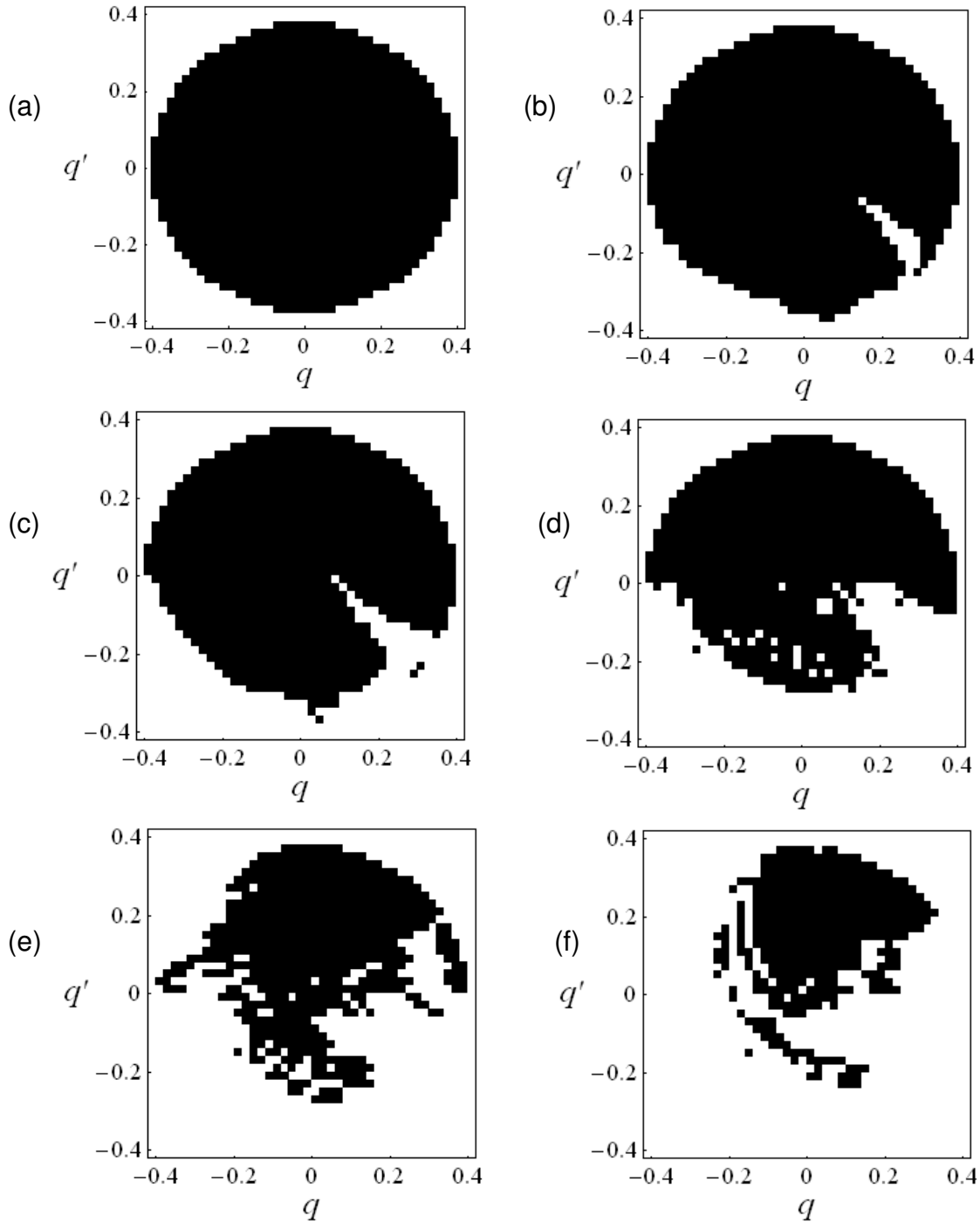


Figure 4.22. Domains of attraction for different excitation amplitudes for $v = 0.88$ as predicted by Model 2 for inelastic impact ($e = 0.8$); (a) $a = 0.08$, (b) $a = 0.128$, (c) $a = 0.14$, (d) $a = 0.16$, (e) $a = 0.18$, and (f) $a = 0.22$; Black region: bounded (safe) motion, and empty space: rollover dynamics.

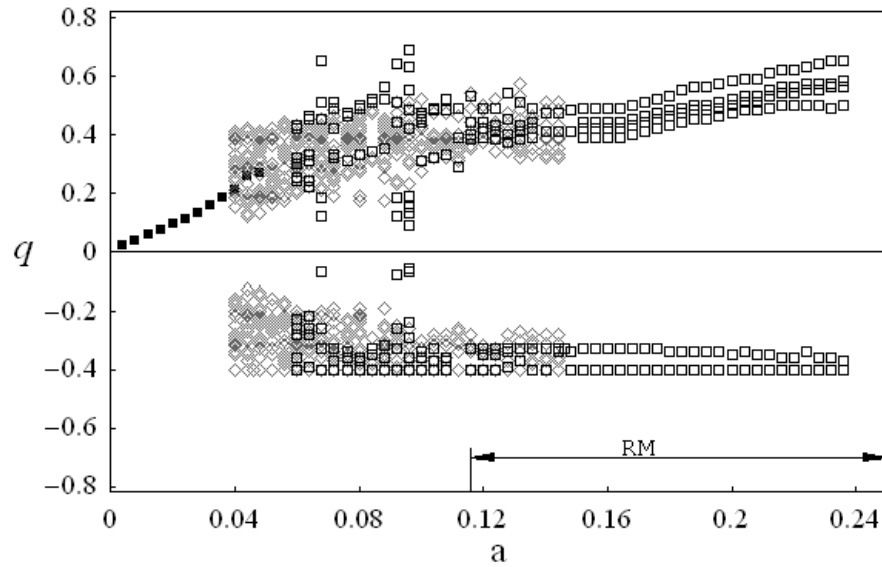


Figure 4.23. Bifurcation diagram for $\nu = 0.88$ as predicted by Model 2 for inelastic impact ($e = 0.8$); ■ Period-one response, ◇ Modulated response, □ Multi-periodic response, and RM= Rollover Motion.

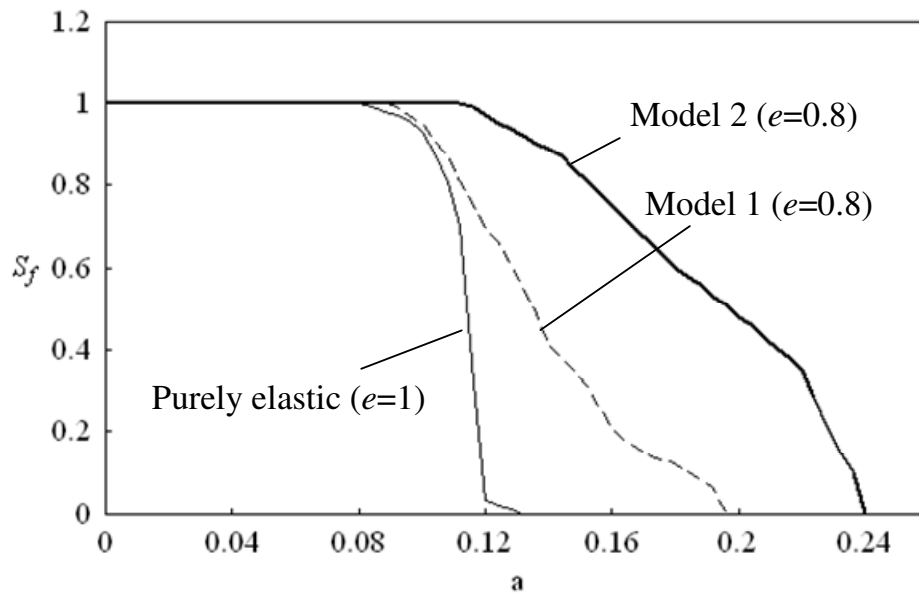


Figure 4.24. Safety factor diagram for excitation frequency $\nu = 0.88$; — Purely elastic impact ($e=1$), and inelastic impact ($e=0.8$); --- Model 1, and — Model 2

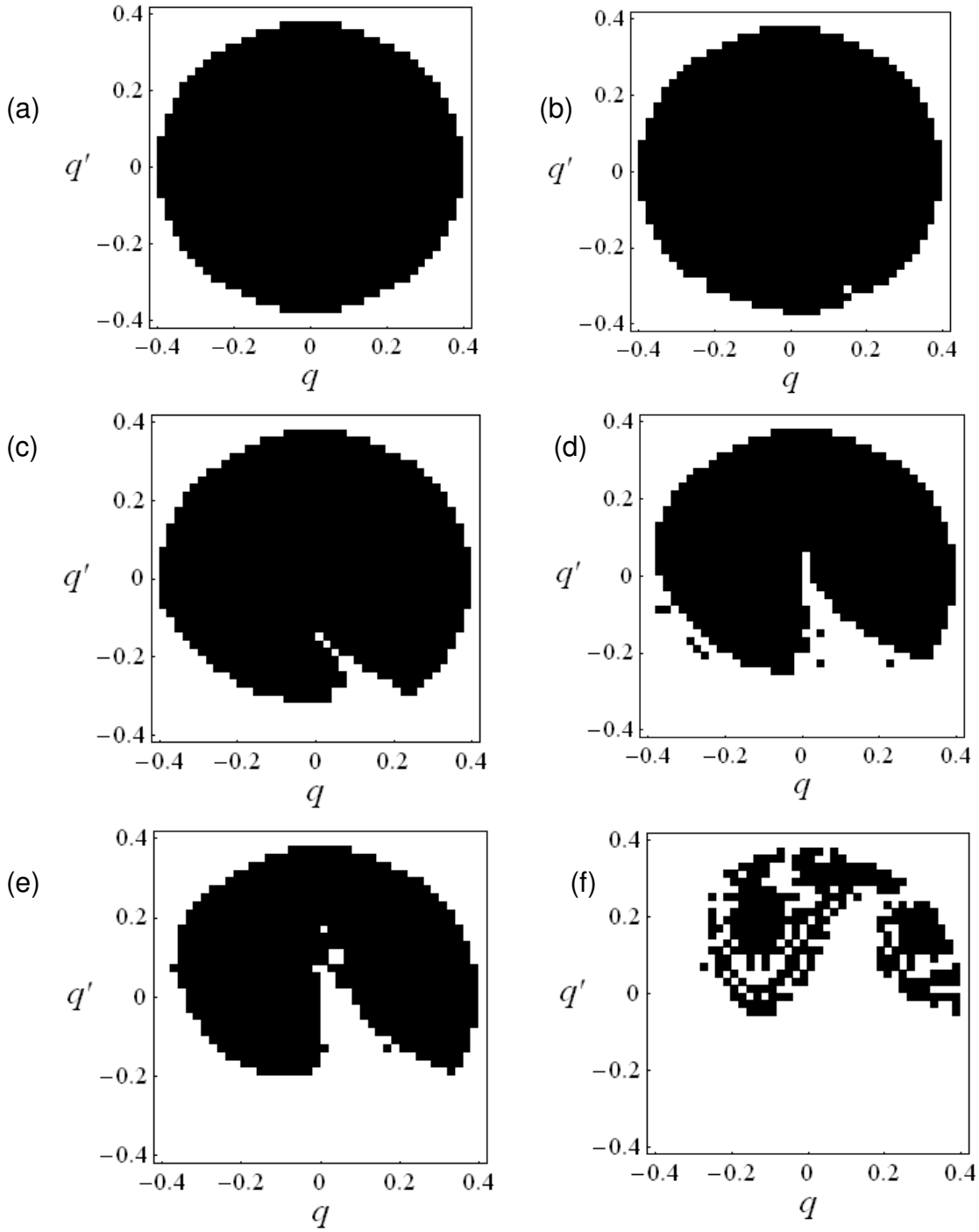


Figure 4.25. Domains of attraction for different excitation amplitudes for $\nu = 0.94$ as predicted by Model 2 for inelastic impact ($e = 0.8$); (a) $a = 0.088$, (b) $a = 0.096$, (c) $a = 0.104$, (d) $a = 0.12$, (e) $a = 0.128$, and (f) $a = 0.136$; Black region: bounded (safe) motion, and empty space: rollover dynamics.

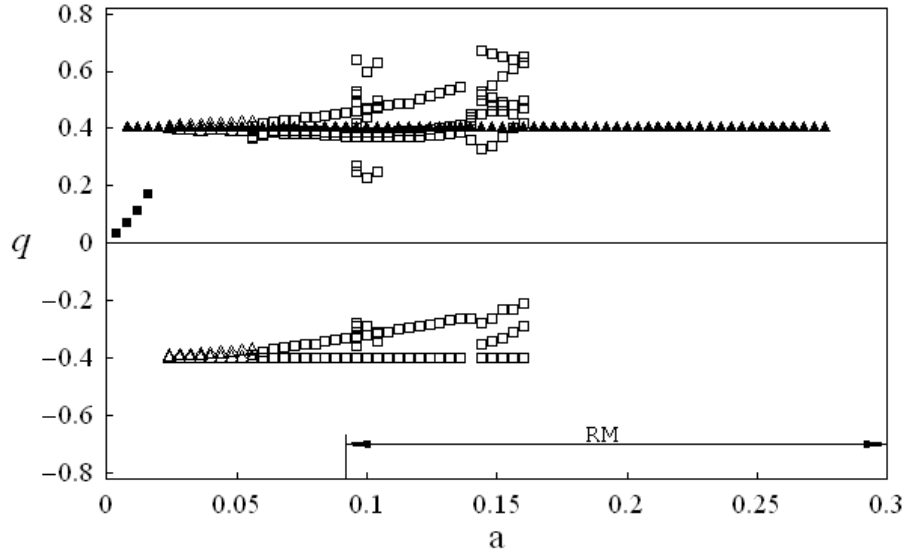


Figure 4.26. Bifurcation diagram for $\nu = 0.94$ as predicted by Model 2 for inelastic impact ($e = 0.8$); ■ Period-one response, ▲ Period-one response experiencing impact, Δ Period-two response, □ Multi - periodic response, and RM= Rollover Motion.

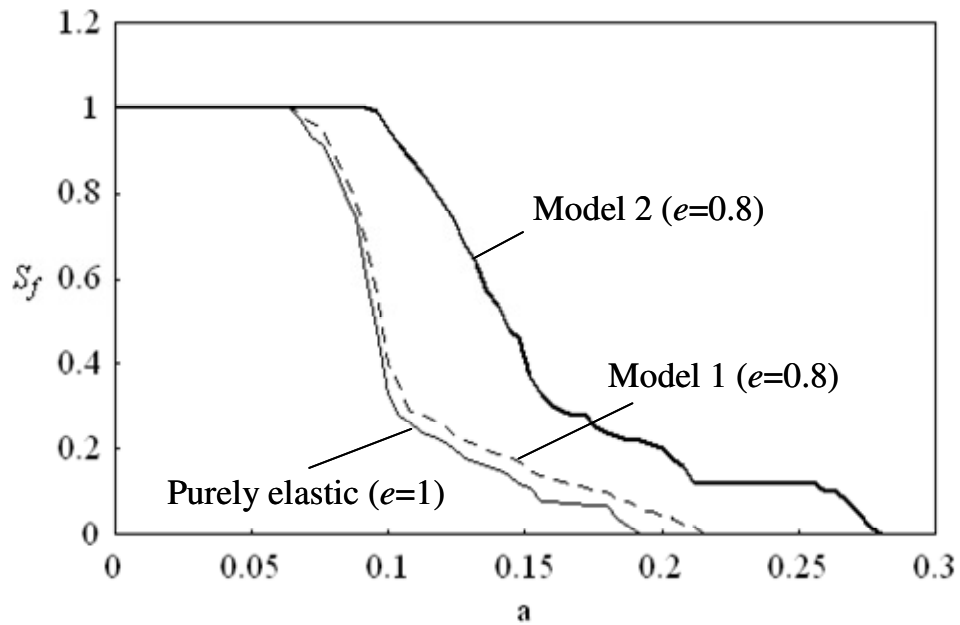


Figure 4.27. Safety factor diagram for excitation frequency $\nu = 0.94$; — Purely elastic impact ($e = 1$), and inelastic impact ($e = 0.8$); --- Model 1, and — Model 2

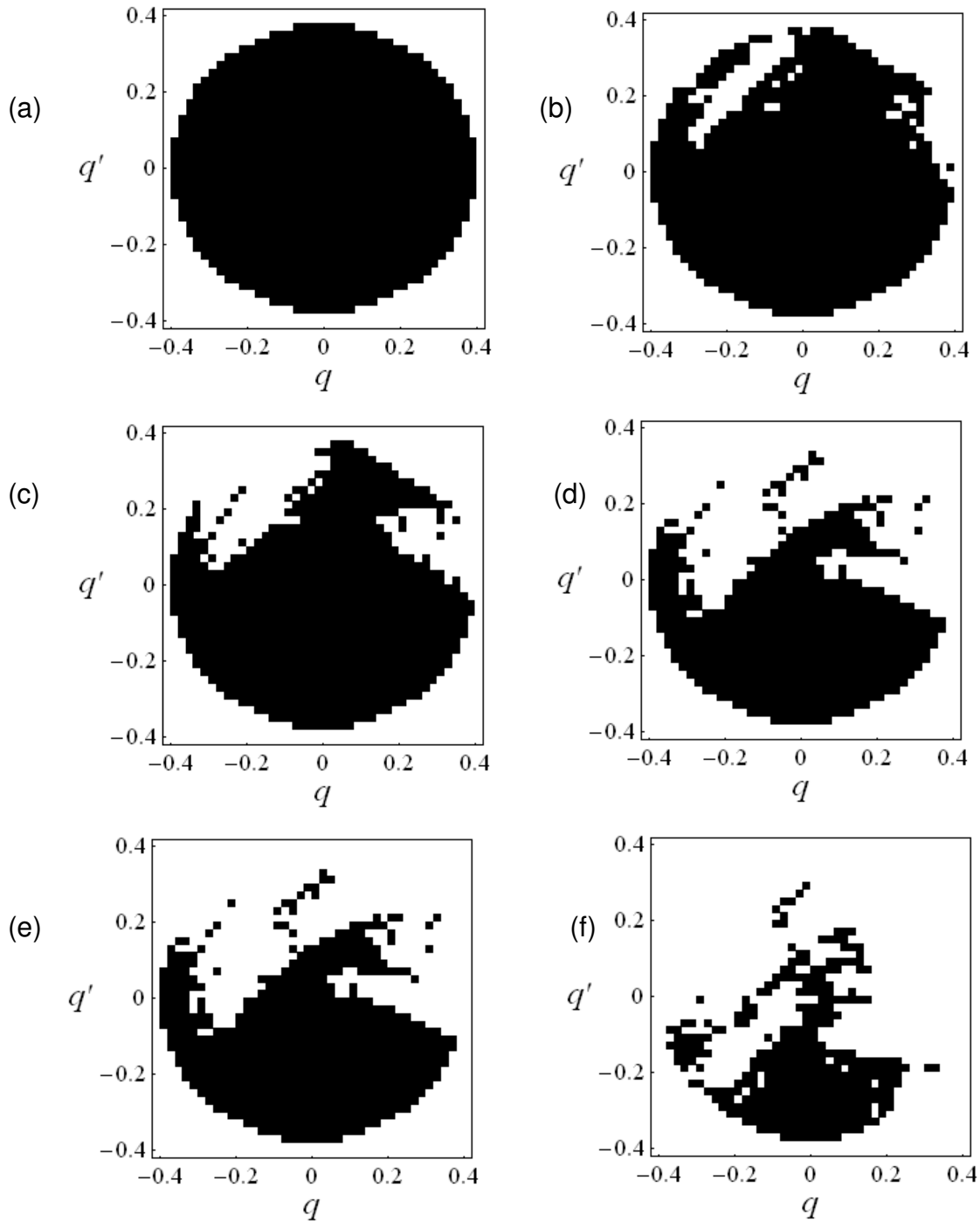


Figure 4.28. Domains of attraction for different excitation amplitudes for $\nu = 1.2$ as predicted by Model 2 for inelastic impact ($e = 0.8$); (a) $a = 0.04$, (b) $a = 0.096$, (c) $a = 0.104$, (d) $a = 0.12$, (e) $a = 0.136$, and (f) $a = 0.144$; Black region: bounded (safe) motion, and empty space: rollover dynamics.

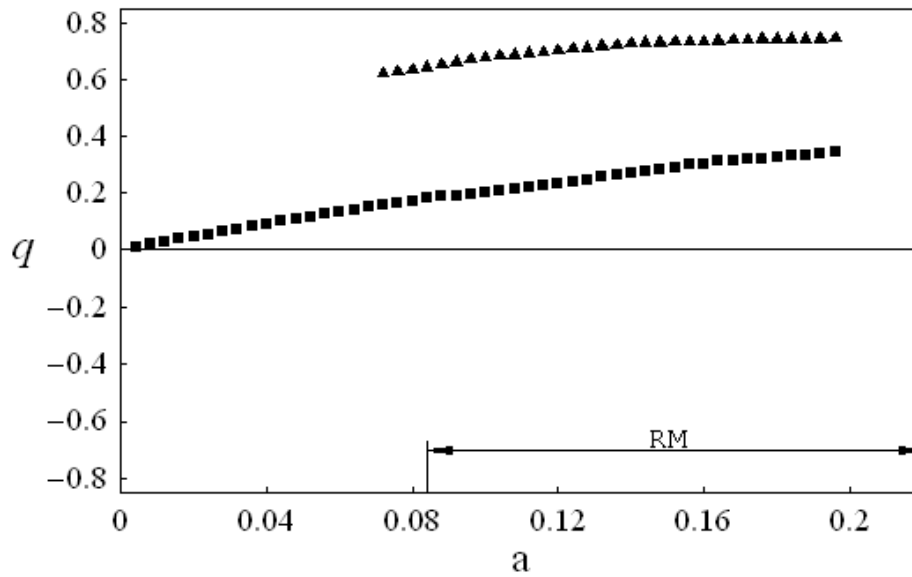


Figure 4.29. Bifurcation diagram for $\nu = 1.2$ as predicted by Model 2 for inelastic impact ($e = 0.8$); ■ Period-one response, ▲ Period-one response experiencing impact, and RM= Rollover Motion.

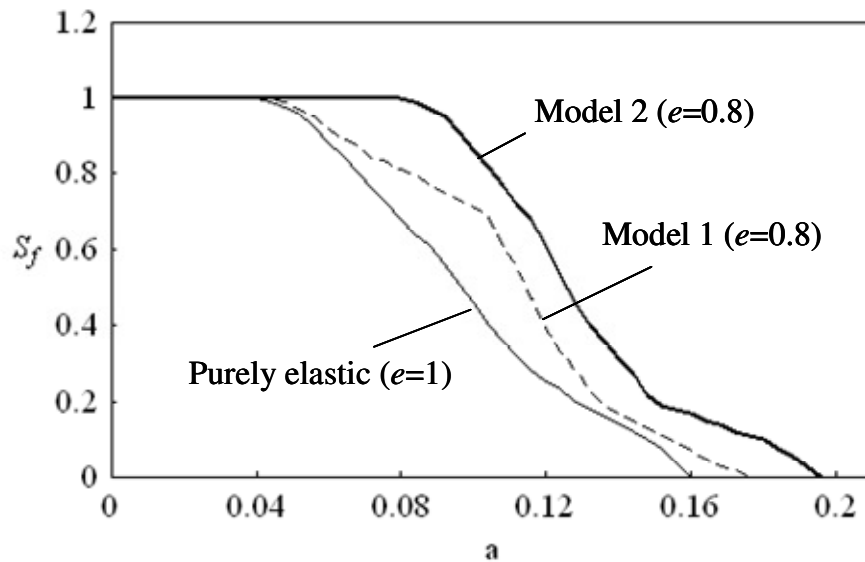


Figure 4.30. Safety factor diagram for excitation frequency $\nu = 1.2$; — Purely elastic impact ($e=1$), and inelastic impact ($e=0.8$); --- Model 1, and — Model 2.

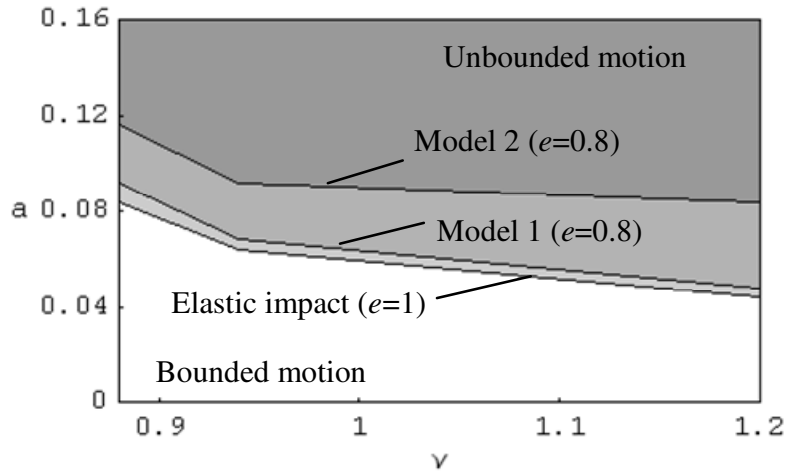


Figure 4.31. Estimates for stability boundaries due ship elastic impact ($e = 1$), and inelastic impact ($e = 0.8$) as predicted by Model 1 and Model 2. Unbounded motion is shown by grey area.

4.4 Explicit Solution and validation of the Results

Model 2 adopted Iv.T. in modeling the case of inelastic impact of ships with stationary ice. Extensive numerical simulations were carried out and the results were compared to those predicted by Zh.T. The comparison showed that for same conditions, both transformations may yield different response regimes. In this section, the equation of motion will be solved explicitly using Runge-Kutta method, and the solution will be compared with both transformations in order to highlight the effectiveness of both transformations.

4.4.1 RUNGE-KUTTA METHOD

The nonlinear equation of motion of ship in beam see under sinusoidal excitation is given by

$$q'' + \bar{\zeta}q' + \gamma q' |q'| + q + \bar{C}_3 q^3 + \bar{C}_5 q^5 = a \sin v\tau \quad (4.10)$$

Equation (4.11) can be written in terms of the state vector form

$$\dot{q} = u, \text{ and}$$

$$\dot{u} = -\bar{\xi}q' - \gamma q' \left| q' \right| - \bar{C}_3 q^3 - \bar{C}_5 q^5 + a \sin \nu \tau \equiv g(q, u, \tau) \quad (4.11)$$

with initial conditions $q(\tau_0) = q_0$, and $u(\tau_0) = u_0$,

Applying 4th order Runge-Kutta method to the system of equations (4.11) one may write

$$q_{n+1} = q_n + \frac{1}{6}(p_0 + 2p_1 + 2p_2 + p_3) + h.o.t., \text{ and}$$

$$u_{n+1} = u_n + \frac{1}{6}(w_0 + 2w_1 + 2w_2 + w_3) + h.o.t. \quad , \quad n = 0, 1, 2, \dots (\tau_f - \tau_0 / d\tau) \quad (4.12)$$

where

$$p_0 = d\tau u_n, \quad p_1 = d\tau(u_n + \frac{1}{2}w_0), \quad p_2 = d\tau(u_n + \frac{1}{2}w_1), \quad p_3 = d\tau(u_n + w_2),$$

and

$$w_0 = d\tau g(\tau_n, q_n, u_n), \quad w_1 = d\tau g(\tau_n + \frac{1}{2}d\tau, q_n + \frac{1}{2}p_0, u_n + \frac{1}{2}w_0),$$

$$w_2 = d\tau g(\tau_n + \frac{1}{2}d\tau, q_n + \frac{1}{2}p_1, u_n + \frac{1}{2}w_1),$$

$$w_3 = d\tau g(\tau_n + d\tau, q_n + p_2, u_n + w_2)$$

Thus, one may write equation (4.12) as follows

$$q_{n+1} = q_n + d\tau u_n + \frac{1}{6}d\tau(w_0 + w_1 + w_2) + h.o.t., \text{ and}$$

$$u_{n+1} = u_n + \frac{1}{6}(w_0 + 2w_1 + 2w_2 + w_3) + h.o.t. \quad (4.13)$$

where

$$w_0 = d\tau g(\tau_n, q_n, u_n),$$

$$w_1 = d\tau g\left(\tau_n + \frac{1}{2}d\tau, q_n + \frac{1}{2}u_n, u_n + \frac{1}{2}w_0\right),$$

$$w_2 = d\tau g\left(\tau_n + \frac{1}{2}d\tau, q_n + \frac{1}{2}u_n + \frac{1}{4}d\tau w_0, u_n + \frac{1}{2}w_1\right),$$

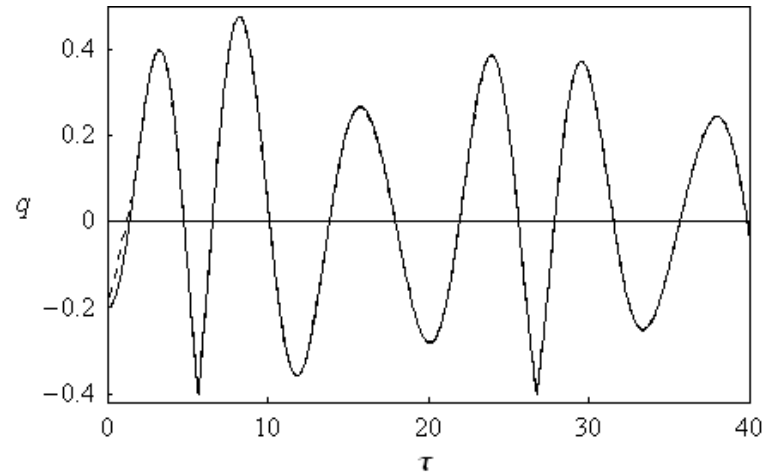
$$w_3 = d\tau g(\tau_n + d\tau, q_n + d\tau u_n, u_n + w_2)$$

It should be noted that $d\tau$ is chosen to be very small ($d\tau \leq 0.001$). In the program used in numerical analysis, impact is detected by setting a condition that whenever $q_n = q_i$ occurs at time τ_n , then the initial conditions for time $\tau_n + d\tau$ should be taken as $q_{n+1} = q_i$, and $u_{n+1} = -eu_n$.

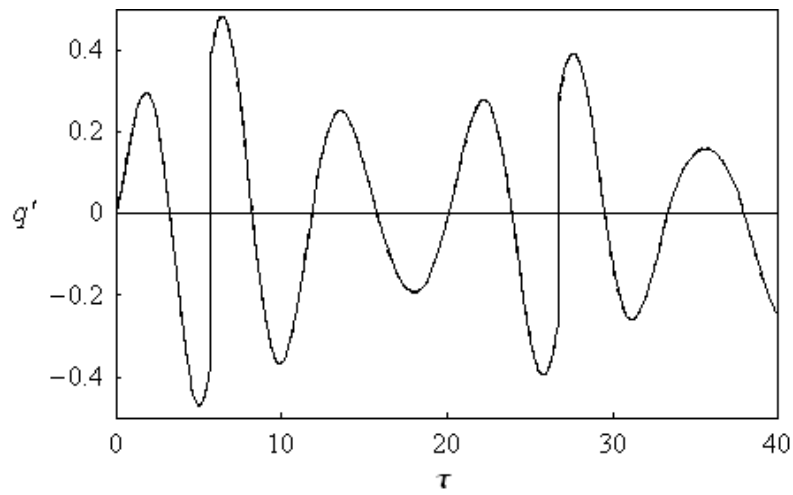
4.4.2 RESULTS AND DISCUSSION

Equations (4.13) are solved for excitation frequency ratio $\nu = 0.88$ and amplitude $a = 0.12$, and for three different values of coefficient of restitution $e = 1, 0.9$, and 0.8 . Figures 4.32 (a) and (b) show amplitude and velocity history records respectively for $e = 1$. The gray curve represents Model 1 solution, the solid curve represents Model 2 solution, and the dashed curve represents the R.K. solution. It is seen that there is a good agreement of the three solutions for purely elastic case $e = 1$. Figures 4.33 and 4.34 show the results for inelastic impact for $e = 0.9$ and $e = 0.8$, respectively. It is seen that for inelastic impact cases, (for $e < 1$), Model 2 and R.K. solutions are in good agreement, on the other hand, Model 1 solution experiences slight deviation from the other solutions. This deviation increases as the

coefficient of restitution decreases. For $e=0.9$, Model 2 and R.K. solutions give almost the same response characteristics, meanwhile Model 1 shows a slight deviation as shown in Figure 4.33. For $e=0.8$, the error involved in Model 1 solution gets larger as shown in Figure 4.34. This is due to the fact that Model 1 provides approximate description for the energy loss at the barrier, and is justified only for large values of coefficient of restitution, i.e. $(1-e) \ll 1$, hence, the error coming from the term involving the damping due to inelastic impact becomes negligible. However, for other cases, Model 2 gives more accurate description.



(a)

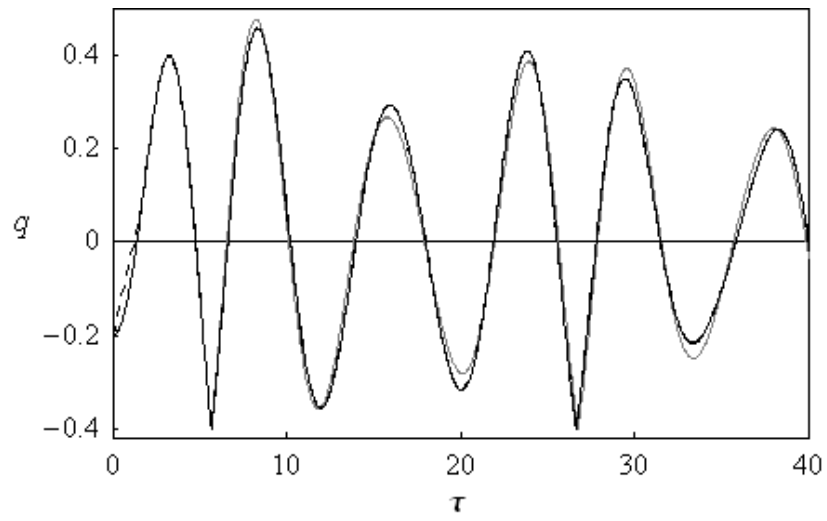


(b)

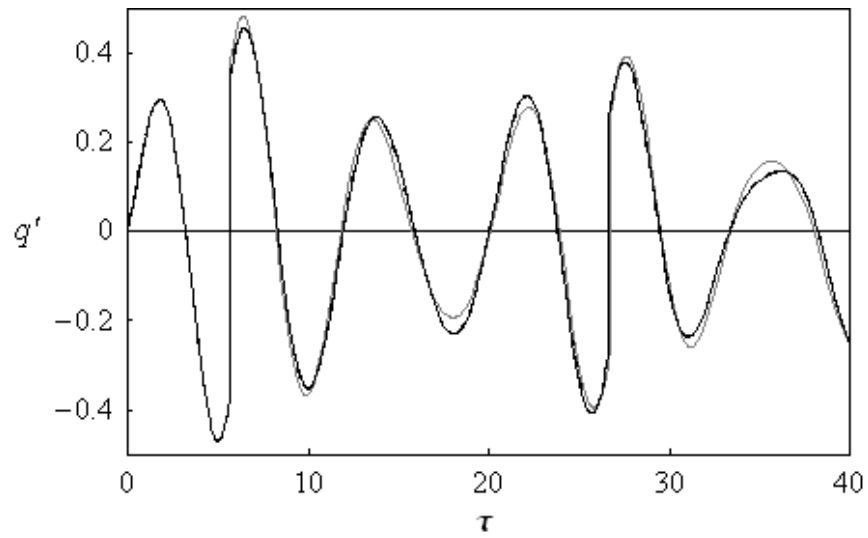
Figure 4.32 (a) Amplitude history record, and (b) Velocity history record for

$\nu = 0.88$, $a = 0.12$ and $e = 1$. Initial conditions $z_o = 0.2$, $z_o' = 0.0$.

— : Model 2, — — : Model 1, and - - - : R.K.



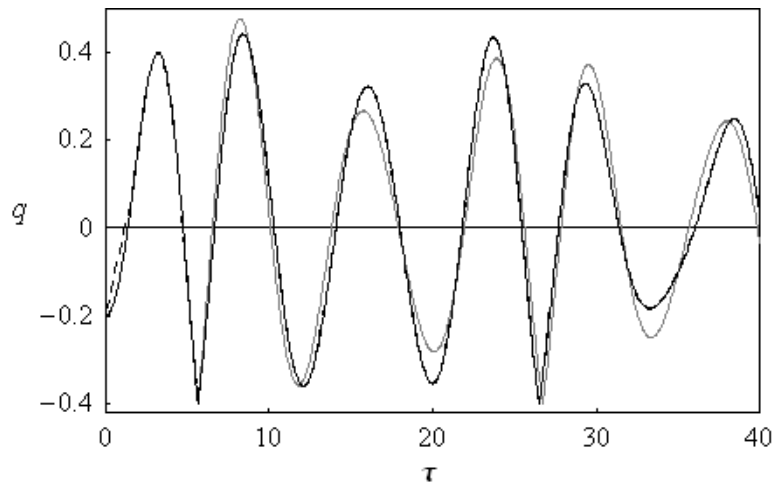
(a)



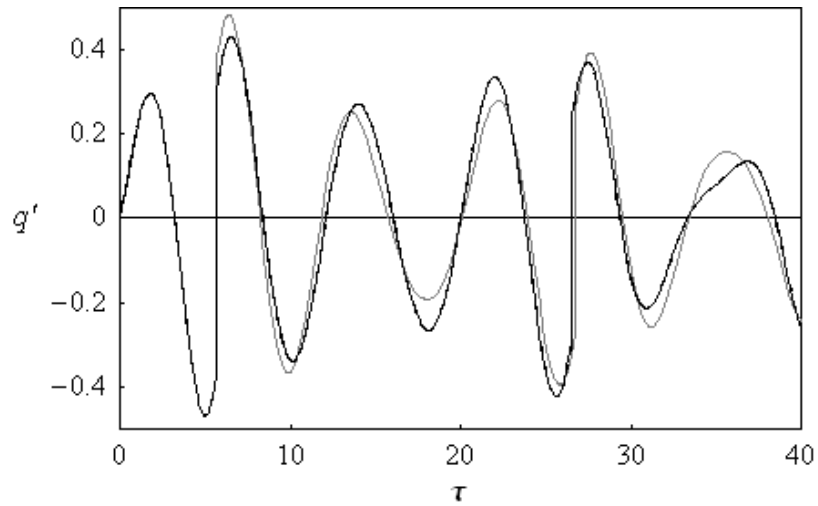
(b)

Figure 4.33 (a) Amplitude history record, and (b) Velocity history record for $v=0.88$, $a=0.12$ and $e=0.9$. Initial conditions $z_o = 0.2$, $z_o' = 0.0$.

— : Model 2, — : Model 1, and - - - : R.K.



(a)



(b)

Figure 4.34 (a) Amplitude history record, and (b) Velocity history record for $\nu = 0.88$, $a = 0.12$ and $e = 0.8$. Initial conditions $z_o = 0.2$, $z_o' = 0.0$.
 — : Model 2, — — : Model 1, and - - - : R.K.

4.5 Equivalent Viscous Damping Method

The purpose of this section is to present an alternative approach to determine the response of ship roll experiencing inelastic impact with a barrier utilizing physical basis. This method is based on simulating the impact phenomenon with a viscous damper in terms of the coefficient of restitution such that the energy dissipated by the viscous damper is equivalent to energy loss due to inelastic impact. In this case, the linear damping term included in the equation of motion of the system is the summation of two terms; the linear damping term inherent to the system, and the viscous damping term equivalent to damping associated with inelastic impact. It should be noted that energy loss accompanied by impact phenomenon is assumed to be instantaneous and occurs at the instant of impact; however, the equivalent viscous damping distributes the energy loss over the entire vibration cycle. The main advantage of such modeling is that it eliminates singularities associated with sudden energy outflows and hence simplifies analytical description and increases effectiveness of numerical codes. It will be shown, however, that the validity of such approach may depend on the type of motion – the fact which is usually ignored in the literature. Therefore, general qualitative analyses of system dynamic states must be conducted before any equivalent damping is used for modeling.

4.5.1 DERIVATION OF THE EQUIVALENT DAMPING TERM

For a ship experiencing impact with a barrier, one may simulate the energy loss due to inelastic impact with a viscous damping. One may illustrate the corresponding analytical procedure based on the simplified case of harmonic

oscillator whose displacements are restricted on one side by a perfectly stiff barrier. The linear equation of motion of the system can be written as

$$\ddot{\phi} + 2\zeta_{eq}\omega_n\dot{\phi} + \omega_n^2\phi = 0 \quad (4.14)$$

where ζ_{eq} is the equivalent damping ratio to be determined. The total energy of the linear oscillator (4.14) under no damping condition is the sum of the kinetic and restoring energies

$$E_{eq} = \frac{1}{2}\dot{\phi}^2 + \frac{1}{2}\omega_n^2\phi^2 \quad (4.15)$$

Differentiating both sides of equation (4.15) with respect to time, gives the rate of energy change as follows

$$\dot{E}_{eq} = \dot{\phi}\ddot{\phi} + \omega_n^2\phi\dot{\phi} = (\ddot{\phi} + \omega_n^2\phi)\dot{\phi} \quad (4.16)$$

Then, enforcing equations (4.14) and (4.16), gives

$$\dot{E}_{eq} = -2\zeta_{eq}\omega_n\dot{\phi}^2 \quad (4.17)$$

Assuming that the damping coefficient is small and thus integrating equation with respect to time over one period of undamped motion, gives the energy loss

$$\Delta E_{eq} = -2\zeta_{eq}\omega_n \int_0^T \dot{\phi}(t)^2 dt \quad (4.18)$$

In the case of zero damping, a typical response of oscillating ship experiencing impact with a barrier is shown in Figure 4.35. During one vibration cycle, such motion is described by

$$\phi(t) = \phi_A \sin(\omega_n t + \arcsin(\phi_i / \phi_A)) \quad (4.19)$$

where ϕ_i is angle of impact, and ϕ_A is the response amplitude.

Differentiating equation (4.19) with respect to time, gives the velocity

$$\dot{\phi}(t) = \omega_n \phi_A \cos(\omega_n t + \arcsin(\phi_i / \phi_A)) \quad (4.20)$$

The period of oscillation is given by

$$T = \frac{\pi}{\omega_n} - \frac{2}{\omega_n} \arcsin(\phi_i / \phi_A) \quad (4.21)$$

Substituting equations (4.20) and (4.21) in equation (4.18), brings the energy loss to the form

$$\Delta E_{eq} = -\phi_A^2 \zeta_{eq} \omega_n^2 \left\{ 2 \arccos(\phi_i / \phi_A) - \sin(2 \arcsin(\phi_i / \phi_A)) \right\} \quad (4.22)$$

One may expand the second term on L.H.S. in equation (4.22) as; $\sin(2 \arcsin(\phi_i / \phi_A)) = 2 \sin(\arcsin(\phi_i / \phi_A)) \cos(\arcsin(\phi_i / \phi_A))$. Making use of the following trigonometric relations;

$$\sin(\arcsin(\phi_i / \phi_A)) = (\phi_i / \phi_A), \text{ and}$$

$$\cos(\arcsin(\phi_i / \phi_A)) = \sqrt{1 - \sin^2(\arcsin(\phi_i / \phi_A))} = \sqrt{1 - (\phi_i / \phi_A)^2},$$

hence, equation (4.22) can be written as

$$\Delta E_{eq} = -2\phi_A^2 \zeta_{eq} \omega_n^2 \left\{ \arccos(\phi_i / \phi_A) - (\phi_i / \phi_A) \sqrt{1 - (\phi_i / \phi_A)^2} \right\} \quad (4.23)$$

The change in energy due to an inelastic impact (ΔE_{in}) is the difference between kinetic energies just before and just after the impact, so that

$$\Delta E_{in} = \frac{1}{2} (v_+^2 - v_-^2) = \frac{1}{2} v_-^2 (e^2 - 1) \quad (4.24)$$

where v_+ is the velocity after impact, and v_- is the velocity before impact. The relation between velocities before and after impact is given by $v_+ = -ev_-$, where e is the coefficient of restitution.

In our case $v_- = \dot{\phi}$, therefore equation (4.24) can be written as

$$\Delta E_{in} = \frac{1}{2} \dot{\phi}^2 (e^2 - 1) \quad (4.25)$$

Taking into account equations (4.20) and (4.25), gives

$$\Delta E_{in} = -\frac{1}{2} \omega_n^2 (\phi_A^2 - \phi_i^2) (e^2 - 1) \quad (4.26)$$

According to the idea of equivalent damping, one has the equation $\Delta E_{in} = \Delta E_{eq}$, where both sides are calculated according to expressions (4.22) and (4.26). Then, solving the above equation with respect to the equivalent viscous damping coefficient, gives

$$\zeta_{eq} = \frac{(\phi_A^2 - \phi_i^2)(e^2 - 1)}{4\phi_A^2 \left\{ \arccos(\phi_i / \phi_A) - (\phi_i / \phi_A) \sqrt{1 - (\phi_i / \phi_A)^2} \right\}} \quad (4.27)$$

One must assume that $|\phi_i| \ll |\phi_A|$, introducing the notation $\varepsilon = \frac{\phi_i}{\phi_A}$, brings equation

(4.27) to the form

$$\zeta_{eq} = \frac{(1 - \varepsilon^2)(1 - e^2)}{4 \left(\arccos(\varepsilon) - \varepsilon \sqrt{1 - \varepsilon^2} \right)} \quad (4.28)$$

One may expand $\arccos(\varepsilon) = \frac{\pi}{2} - \sum_0^{\infty} \frac{(2n)!}{2^{2n} (n!)^2} \frac{\varepsilon^{2n+1}}{(2n+1)}$, under the condition $|\varepsilon| \ll 1$, i.e.

$|\phi_i| \ll |\phi_A|$, and neglecting higher order terms, the following estimate for ζ_{eq} holds

$$\zeta_{eq} = \frac{1 - e^2}{2\pi} \quad (4.29)$$

It should be noted that relation (4.29) is valid under the condition that initial barrier position is much smaller than the response amplitude. Adding the equivalent viscous damping term (4.29) to the linear damping term in equation (3.2), one may write the equation of motion of the ship under sinusoidal excitation as

$$\ddot{\phi} + (2\zeta\omega_n + 2\zeta_{eq}\Omega)\dot{\phi} + a\dot{\phi}|\dot{\phi}| + \omega_n^2\phi + C_3\phi^3 + C_5\phi^5 = a_0\sin(\Omega t) \quad (4.30)$$

where a_0 is the excitation amplitude, and Ω is the excitation frequency.

Adopting Zh.T. and following same steps as in Section 3.2, the equation of motion of the ship is written as

$$z'' + \left(\bar{\zeta} + \frac{1-e^2}{2\pi} \nu \right) z' + \gamma z'^2 \operatorname{sgn}(z') + z + \operatorname{sgn}(z)[q_i + \bar{C}_3(z \operatorname{sgn}(z) + q_i)^3 + \bar{C}_5(z \operatorname{sgn}(z) + q_i)^5] = a \operatorname{Sin}(\nu\tau) \operatorname{sgn}(z) \quad (4.31)$$

The second term in the equation (4.31) is a summation of two damping terms; linear damping term and viscous damping term equivalent to damping associated with inelastic impact. Indeed, the major issue with equivalent damping is that it is always present in the differential equation of motion, whereas the original system may vibrate with or without impacts. However, introducing the condition $\phi_i \ll \phi_A$ guarantees the possibility of impact at every cycle of vibration. If the amplitude becomes small to reach the barrier then the equivalent damping of inelastic impact must be set to zero.

4.5.2 NUMERICAL SIMULATION

Extensive numerical simulations are carried out to examine the applicability of the equivalent damping approach. A comparison between direct numerical solutions

using R.K. method, solutions by Model 2 and the equivalent damping model under different system parameters is carried out. It is found that the applicability of equivalent damping depends on different parameters; excitation frequency, excitation amplitude, coefficient of restitution, and position of the barrier. For example, for $q_i = -0.2$, $v = 1.2$, $a = 0.08$, and $z_o = 0.01$, $z_o' = 0.01$, Figures 4.36 through 4.40 show comparison between the three solutions for $e = 0.9$, 0.8, 0.7, 0.6, and 0.5, respectively. It is seen that for a high value of coefficient of restitution ($e = 0.9$), there is a good match between the curves as shown in Figure 4.36. However, as the coefficient of restitution decreases, an error occurs in equivalent damping method. This error increases as the value of the coefficient of restitution decreases as shown in Figures 4.37 through 4.39. Finally, for $e = 0.5$, equivalent damping method yields period-one motion without impact, meanwhile, both Model 2 and direct R.K. method still predict period-one motion experiencing impact; see Figure 4.40. This is due to the fact that the equivalent viscous damping distributes the energy loss over the entire period of oscillation. For a relatively small coefficient of restitution, the equivalent energy loss is large, and the ship does not sustain enough energy to reach the barrier. Also, note quite perfect agreement between the model adapted by Model 2 and the direct numerical solution by R.K. method for different parameters. This is not surprising since Model 2 just brings the system to another form by means of exact analytical manipulations. Such a new form may be more or less convenient for further analyses according to a problem formulation. In our case, both solutions are numerical; therefore some mismatch between the

corresponding solutions may have only a numerical nature. So the next subsection compares only the equivalent viscous damping method to Model 2

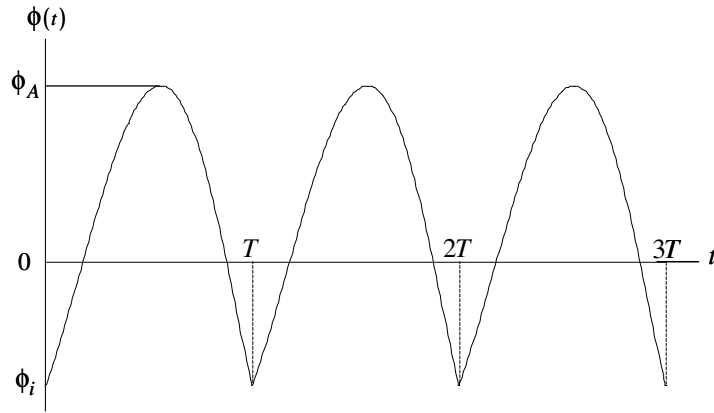


Figure 4.35. Typical response of ship roll experiencing impact with a barrier.

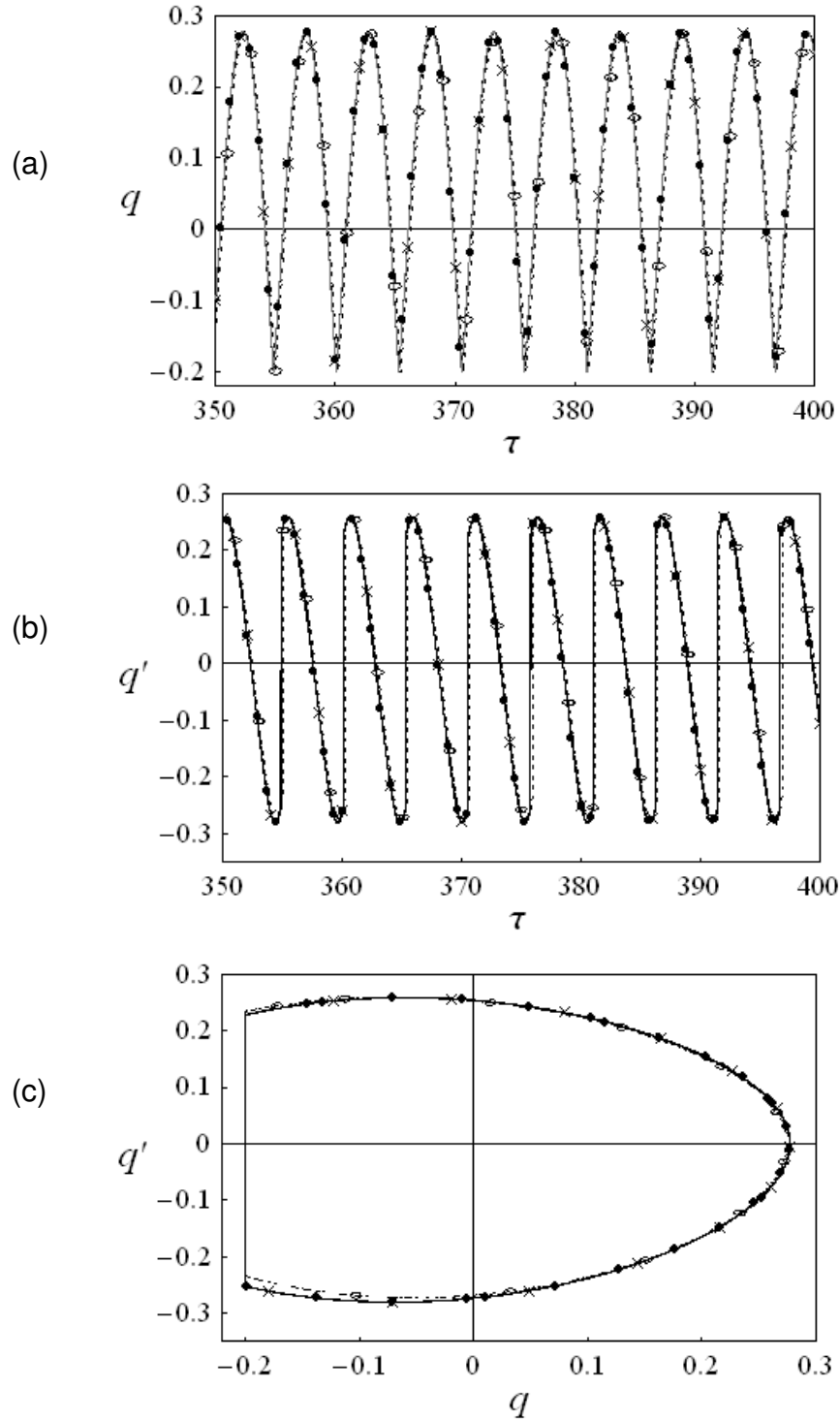


Figure 4.36. (a) Amplitude history record, (b) Velocity history record, and (c) Phase Plot for $q_i = -0.2$, $\nu = 1.2$, $a = 0.08$, $z_o = 0.01$, $z_o' = 0.01$, and $e = 0.9$:
 —●— : R.K., —×— : Model 2, and —○— : Equivalent damping method.

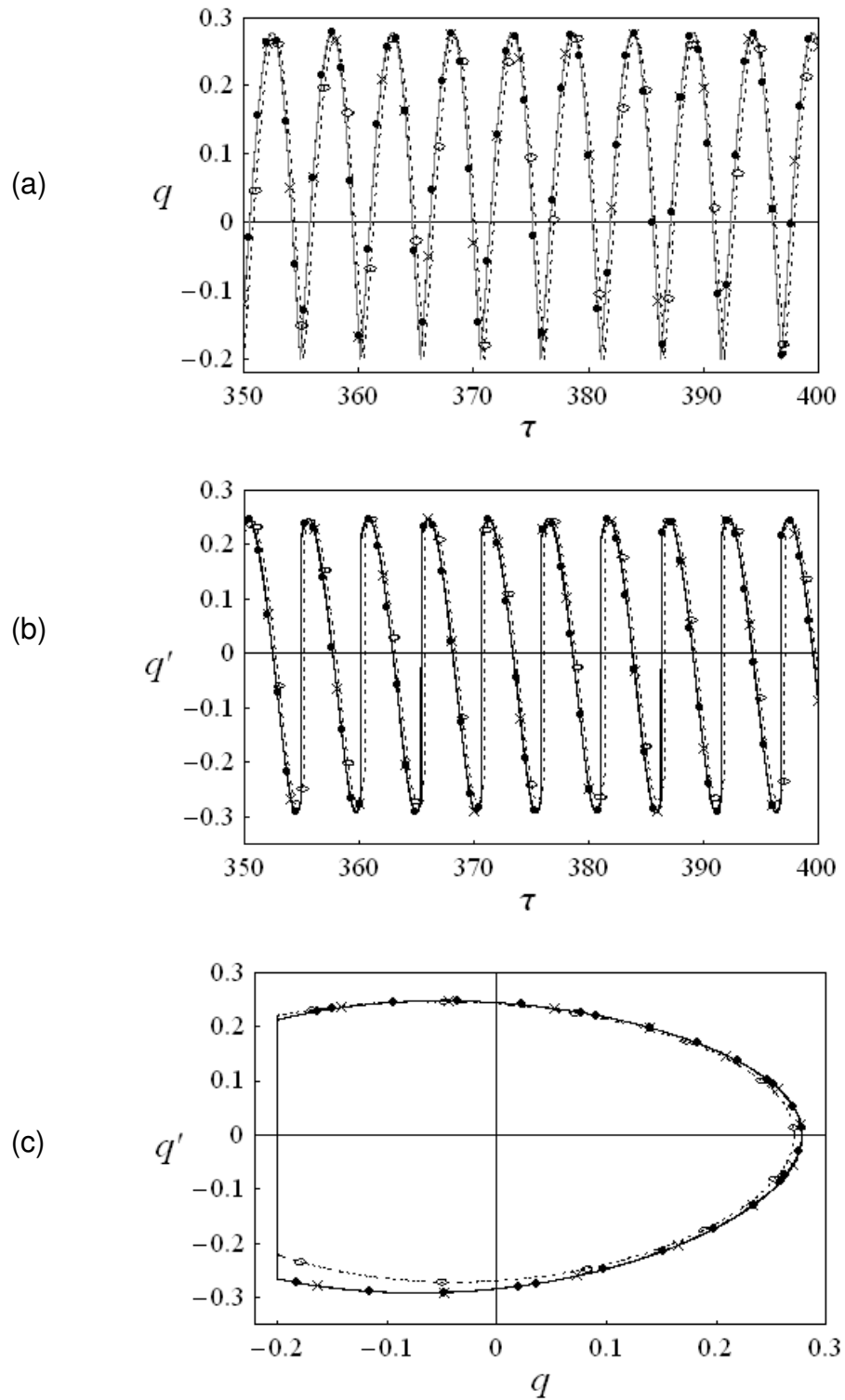


Figure 4.37. (a) Amplitude history record, (b) Velocity history record, and (c) Phase Plot for $q_i = -0.2$, $\nu = 1.2$, $a = 0.08$, $z_o = 0.01$, $z_o' = 0.01$, and $e = 0.8$:
 —●— : R.K., —×— : Model 2, and —○— : Equivalent damping method.

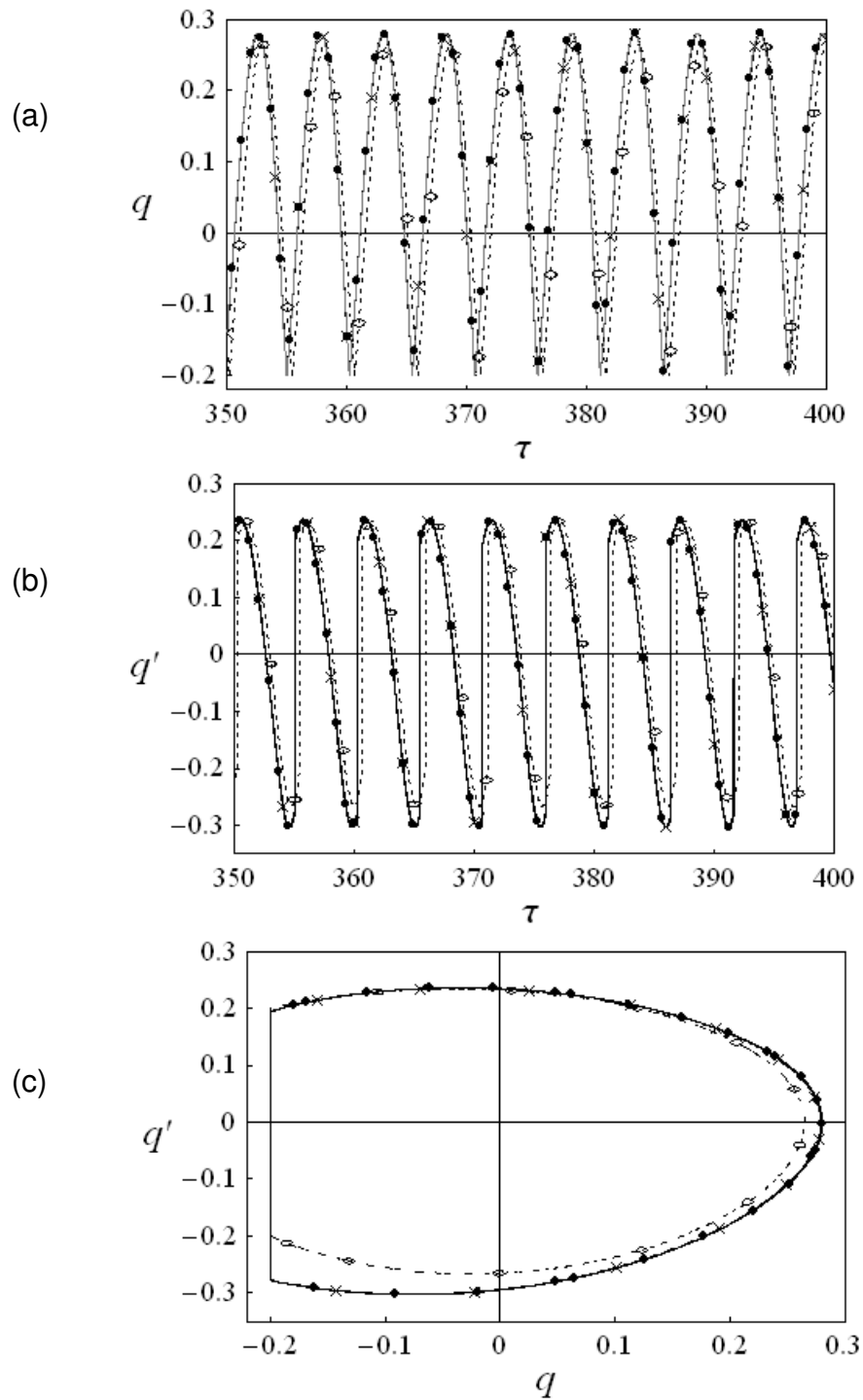


Figure 4.38. (a) Amplitude history record, (b) Velocity history record, and (c) Phase Plot for $q_i = -0.2$, $v = 1.2$, $a = 0.08$, $z_o = 0.01$, $z_o' = 0.01$, and $e = 0.7$:
 —●—●— : R.K., —×—×— : Model 2, and —○—○— : Equivalent damping method.

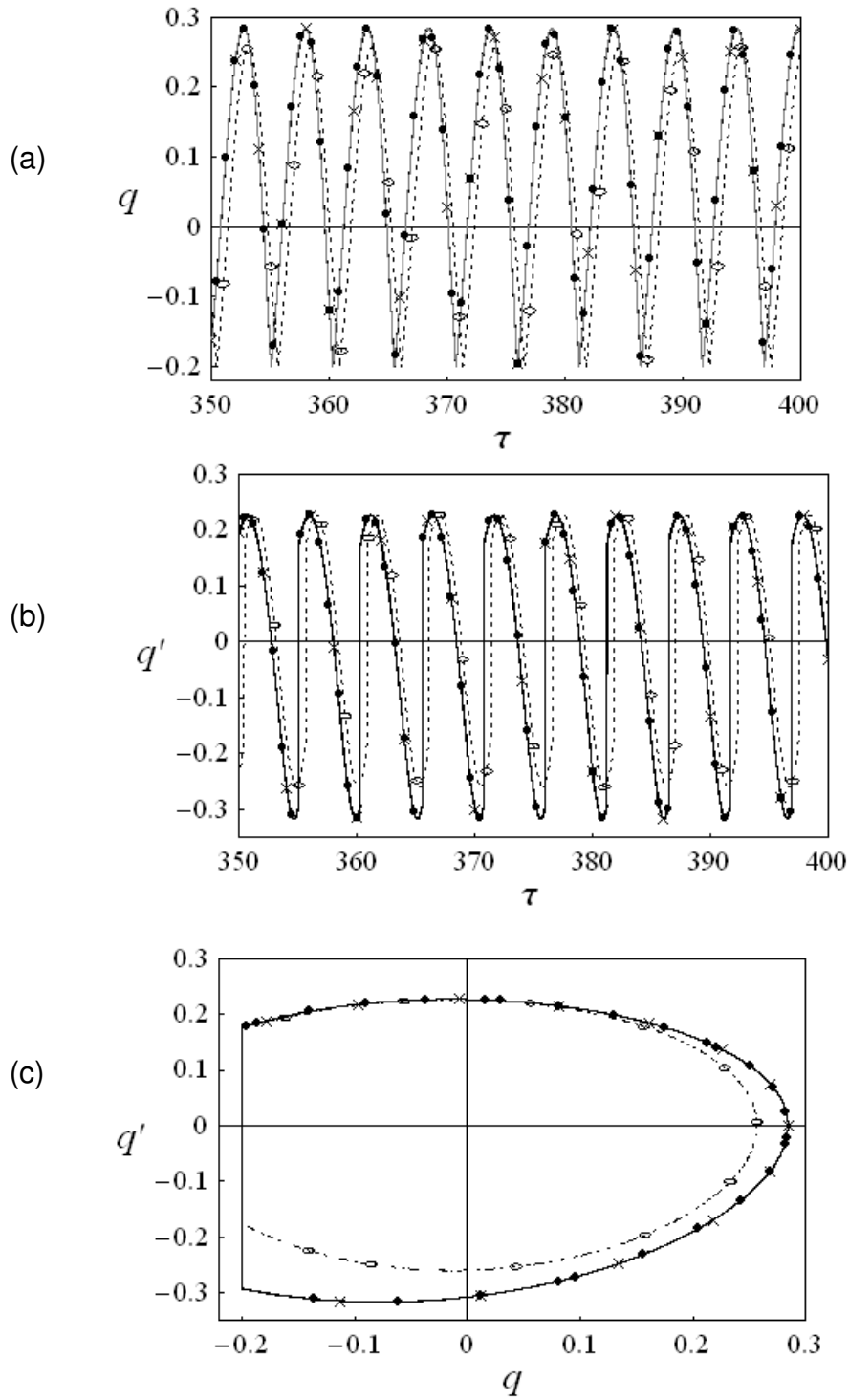


Figure 4.39. (a) Amplitude history record, (b) Velocity history record, and (c) Phase Plot for $q_i = -0.2$, $\nu = 1.2$, $a = 0.08$, $z_o = 0.01$, $z_o' = 0.01$, and $e = 0.6$:
 —●— : R.K., —×— : Model 2, and —○— : Equivalent damping method.

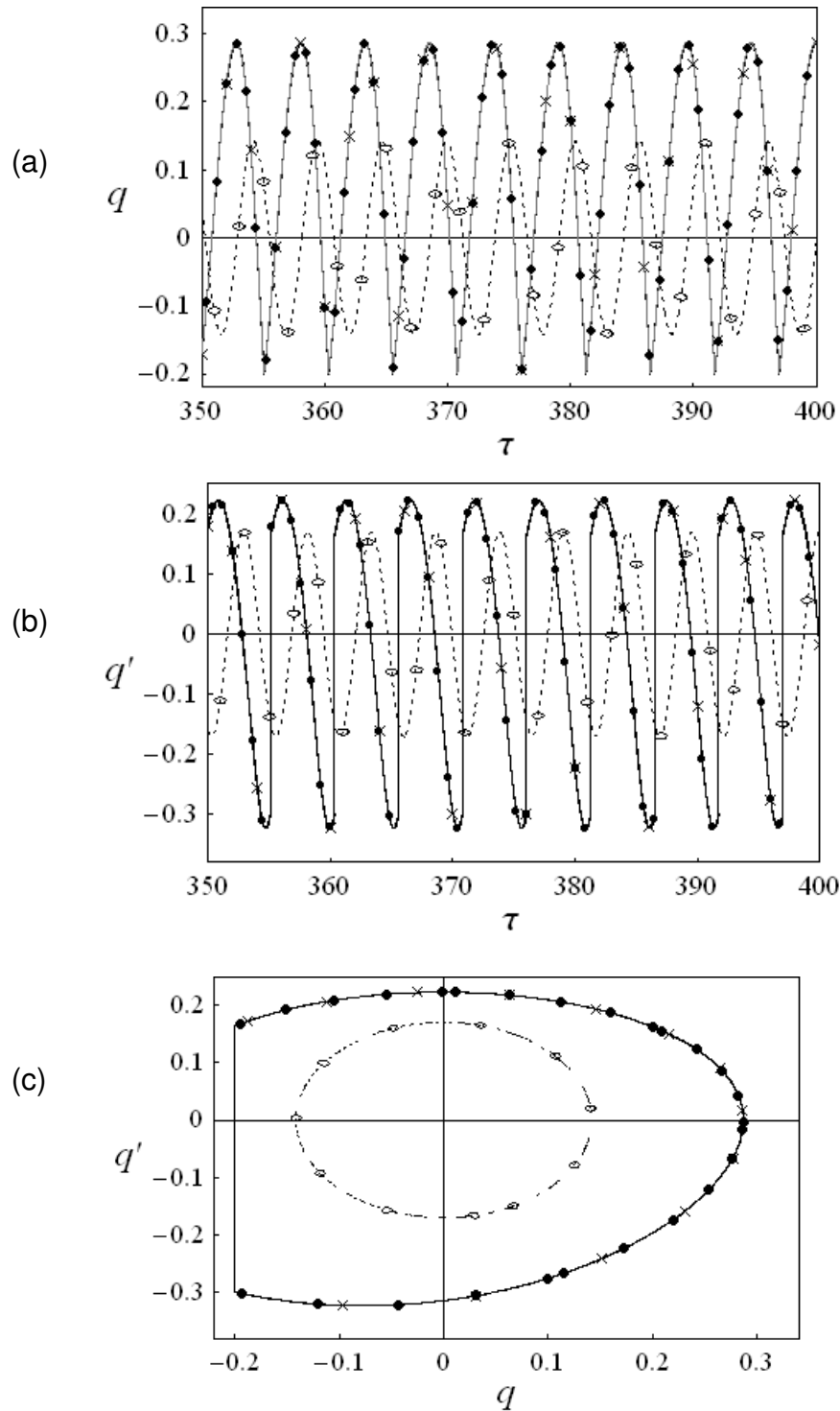


Figure 4.40. (a) Amplitude history record, (b) Velocity history record, and (c) Phase Plot for $q_i = -0.2$, $\nu = 1.2$, $a = 0.08$, $z_o = 0.01$, $z_o' = 0.01$, and $e = 0.5$:
 —●— : R.K., —×— : Model 2, and —○— : Equivalent damping method.

4.5.3 VALIDATION OF THE EQUIVALENT DAMPING MODEL UNDER DIFFERENT DYNAMIC CONDITIONS

The results obtained from equivalent damping term method will be compared with results of direct numerical simulations based on the model adapted from Iv.T. state variables. As mentioned in Sections 4.5.1 and 4.5.2, such adaptation itself represents exact analytical manipulations within the class of non-smooth functions and should not contribute any error. Further numerical solutions therefore can be viewed as test solutions for evaluating the equivalent damping approximation. Error in terms of root-mean-square (rms) of the total energy of the corresponding free, undamped system will be calculated for different parameters.

The total energy of the system is the sum of kinetic and restoring energies. For the nonlinear system given by equation (4.5), the total energy $E(\tau)$ is calculated as

$$E(q, q') = \frac{1}{2} q'^2 + \frac{1}{2} q^2 \left(1 + \frac{1}{2} \bar{c}_3 q^2 + \frac{1}{3} \bar{c}_5 q^4 \right) \quad (4.32)$$

Equation (4.32) is used to calculate total energy for both equivalent damping term and direct numerical simulation methods. For equivalent damping method, total energy is calculated as $E_{eq}(\tau) = E(q_1(\tau), q'_1(\tau))$ where $q_1(\tau)$, and $q'_1(\tau)$ are determined based on Model 1 given by equation (3.4); $q = z \operatorname{sgn}(z) + q_i$, and $q' = z' \operatorname{sgn}(z)$. For direct numerical simulation, total energy is calculated as $E_I(\tau) = E(q_2(\tau), q'_2(\tau))$ where $q_2(\tau)$, and $q'_2(\tau)$ are determined based on Model 2 given by equation (4.7); $q = s \operatorname{sgn}(s) - q_i$, and $u = \operatorname{sgn}(s) [1 - K \operatorname{sgn}(sv)] v$. In this case, the root mean square energy predicted by Model 2 is taken as

$$\bar{E}_I = \sqrt{\frac{1}{n_{max}} \sum_{i=1}^{n_{max}} E_I(\tau_i)^2}, \quad i = 1, 2, \dots, n_{max} \quad (4.33)$$

where $\tau_i = \frac{i}{n} \left(\frac{2\pi}{v} \right)$, n is the number of points per one period for calculating the error, n_{max} is maximum number of points for calculating the error over the entire period; i.e., $n_{max} = n \frac{\tau_{max}}{(2\pi/v)}$, approximated to nearest integer, and τ_{max} is the time of the whole interval.

One may define the error involved in using equivalent damping method with respect to Model 2 as follows

$$\text{Error} = \frac{\sqrt{\sum_{i=1}^{n_{max}} \{E_I(\tau_i) - E_{eq}(\tau_i)\}^2}}{\bar{E}_I} \quad (4.34)$$

Equation (4.34) may be used to determine parameters leading to relatively small error, i.e., regions where equivalent damping method can be applied.

4.5.3.1 Results and Discussion

Figures 4.41 and 4.42 show a good agreement between equivalent damping method and Model 2 in terms of time history response and energy records, respectively, for the following set of parameters and initial conditions: $q_i = -0.2$, $v = 1.2$, $a = 0.08$, $e = 0.998$, and $z_o = 0.01$, $z_o' = 0.01$. In this case, the error involved is 0.54%. However, after a slight decrease of the coefficient of restitution to $e = 0.995$, the error reaches 75.3% in the steady state, while still remaining low during the transient period. This error increase can be seen in both coordinate and energy

responses; as seen in Figure 4.43 (b), and Figure 4.44 (b), respectively. As mentioned, both solutions are in a good match during the transient period shown in Figures 4.43 (a) and 4.44 (a).

From the physical standpoint, such a divergence in long-term records could be due to the beat-like character of the dynamics as clearly seen from fragment (a) of Figure 4.43. Namely, at some cycles the near resonance beat motion, the amplitudes become so small that the oscillator is missing one or few impacts. Since the effective damping is still pumping the energy out, then the corresponding error is accumulated from one beat cycle to another, so that eventually the two models become attracted by different areas of the dynamics. Further, more different scenarios may develop for different system parameters. As the barrier coordinate increases; $q_i = -0.3$, and coefficient of restitution decreases; $e = 0.90$, and for $v = 0.8$, $a = 0.08$, $z_o = 0.01$, $z_o' = 0.01$, the error in steady state is 50.4%. Model 2 yields periodic response experiencing impact, however, equivalent damping method yields lower response value and the ship does not reach the barrier in the steady state as shown in Figure 4.45. Lower energy levels are predicted by equivalent damping method as shown in Figure 4.46.

Figures 4.47 through 4.50 give 3D diagrams illustrating sensitivity of the effective damping approach to different parameter variations. Namely, peaks of the diagrams indicate quite abrupt error increases, whereas bottoms correspond to areas, where the effective damping appears to be adequate to the system dynamic behaviors. In particular, it can be seen from Figure 4.47 that for $q_i = -0.1$, $a = 0.08$, and $z_o = 0.01$, $z_o' = 0.01$, the error is relatively small as the excitation frequency ratio

approaches the natural frequency of the system. However, significant errors occur as the input frequency is very close to resonance. This conclusion is confirmed for $q_i = -0.2$, -0.3 , and -0.4 as shown in Figures 4.48, through 4.50 respectively. On the other hand, the system should not be too far away from the resonance excitation, otherwise the assumption taken for the derivation of effective damping will be violated.

A common feature of the three-dimensional diagrams is the presence of “channels” and “ridge” indicating a high sensitivity of the model to the type of dynamics rather than variations of the coefficient of restitution. Small error values occur at excitation frequency near the natural frequency of the system. Meanwhile, as the excitation frequency is far from natural frequency, the error gets larger. This observation confirms the importance of satisfying the condition that excitation frequency should be near the natural frequency of the system in order to avoid errors of approximation during the derivation of equivalent damping coefficient. For all the parameters, the error reaches practically 0% as the coefficient of restitution equals one, which corresponds to perfectly elastic impacts. Another result may be concluded from comparing Figures 4.47 through 4.50 is that areas indicating small error are essentially reduced as the distance between the ship and barrier increases. This is in line with another assumption of the modeling, which is that the amplitude parameter should exceed the distance to the barrier on the opposite side of the ship.

As a two-dimensional visualization, Figures 4.51 through 4.54 show the contour plots for different distances to the barriers, such as $q_i = -0.1$, -0.2 , -0.3 , and -0.4 , respectively. Black regions represent 0% error, while white regions

represent 100% error. It can be seen that the entire plot becomes black at $e=1$. An important characteristic can be seen from the plots is that the contour lines at different error levels are almost horizontal. This confirms the remark that the equivalent damping method is sensitive to the excitation frequency (and thus the type of dynamics) rather than the coefficient of restitution.

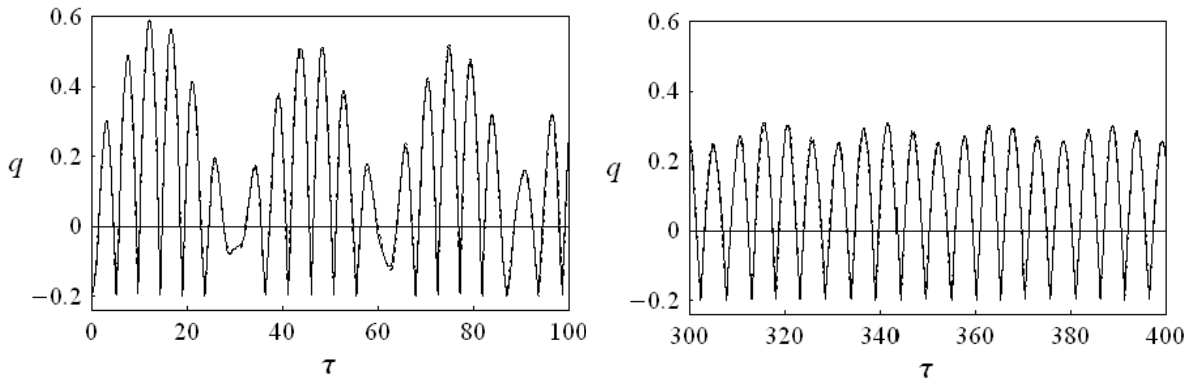
4.5.4 CONCLUSIONS AND CLOSING REMARKS

The equivalent damping method is useful in modeling vibro-impact systems since it eliminates singularities of modeling in terms of the velocity, and thus reduces computational time and avoids conditioning in the corresponding numerical schemes. However, equivalent damping method is sensitive to different system parameters such as coefficient of restitution, excitation frequency, excitation amplitude and initial barrier position. Two important conditions must be satisfied by the system to apply equivalent damping method. Firstly, the distance to the barrier should be much smaller than response amplitude to guarantee the possibility of impact at every cycle of vibration. Secondly, temporal mode shapes of the vibrations must be sufficiently stable and simple enough to describe for derivation of effective damping coefficient.

In this chapter, two different models for roll dynamics of ships interacting with one-sided barriers were introduced. Both models are based on the idea of elimination of constraints by means of the specific non-smooth transformations of the coordinates and velocities. First of the two transformations, suggested by Zhuravlev, effectively apply to the positional coordinates with further adaptation to

account for impact damping (Model 1). Another version was suggested by Ivanov and incorporates the impact damping effect through the transformation itself (Model 2). Such a combined approach gave the basis for analyses of possible variations in dynamic behaviors due to different models of impact damping, including the most direct way of spreading the energy loss over the full cycle of vibration through the effective damping.

The results obtained from the two models are found almost identical for water waves of relatively small amplitude. However, model 1 is found to yield more conservative stability regions than those of model 2. A comparison between direct numerical simulations using Runge-Kutta method, solutions for model 2 and the equivalent damping model under different system parameters were found to reveal that the applicability of equivalent damping depends on different parameters; excitation frequency, excitation amplitude, coefficient of restitution, and position of the barrier. The corresponding error analysis was conducted to establish the extent over which the equivalent viscous damping can be used in terms of excitation frequency and coefficient of restitution. Generally the error appears to be very small for relatively large coefficient of restitution. The validation of the predicted results will be examined experimentally in Chapter 5.



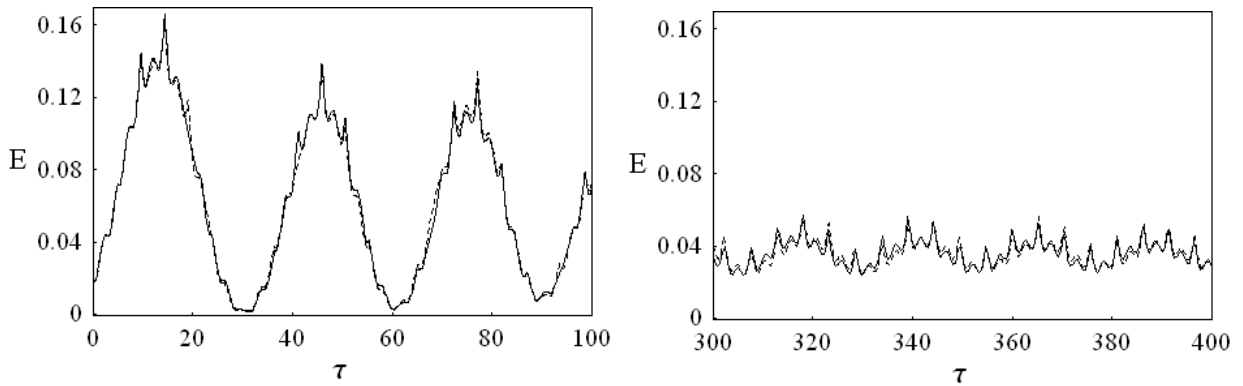
(a) Transient State

(b) Steady State

Figure 4.41. Amplitude history record for $q_i = -0.2$, $\nu = 1.2$, $a = 0.08$,

$$z_o = 0.01, z_o' = 0.01, \text{ and } e = 0.998;$$

_____ : Model 2, and - - - - : Equivalent damping method.



(a) Transient State

(b) Steady State

Figure 4.42. Total Energy for $q_i = -0.2$, $\nu = 1.2$, $a = 0.08$,

$$z_o = 0.01, z_o' = 0.01, \text{ and } e = 0.998;$$

_____ : Model 2, and - - - - : Equivalent damping method.

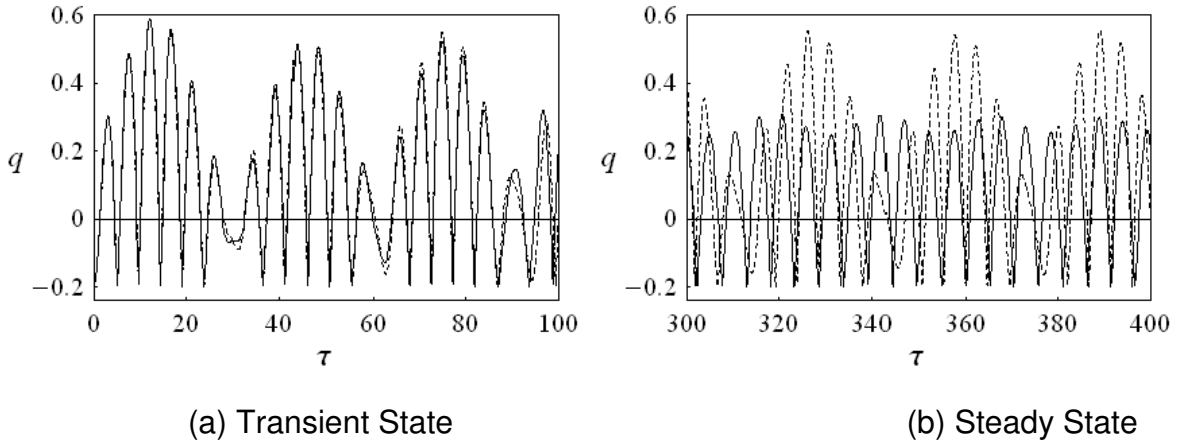


Figure 4.43. Amplitude history record for $q_i = -0.2$, $\nu = 1.2$, $a = 0.08$,
 $z_o = 0.01$, $z_o' = 0.01$, and $e = 0.995$;
 _____ : Model 2, and - - - - : Equivalent damping method.

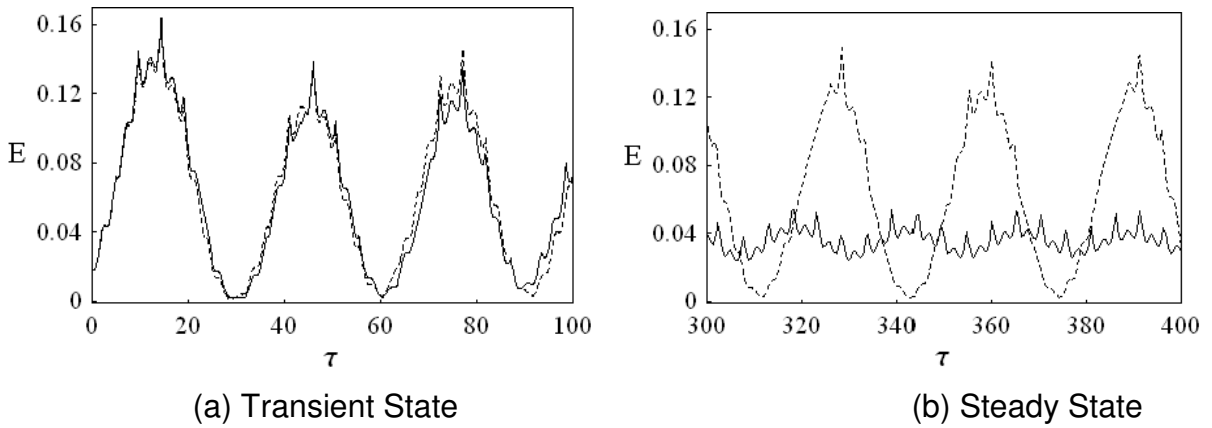


Figure 4.44. Total Energy for $q_i = -0.2$, $\nu = 1.2$, $a = 0.08$,
 $z_o = 0.01$, $z_o' = 0.01$, and $e = 0.995$;
 _____ : Model 2, and - - - - : Equivalent damping method.

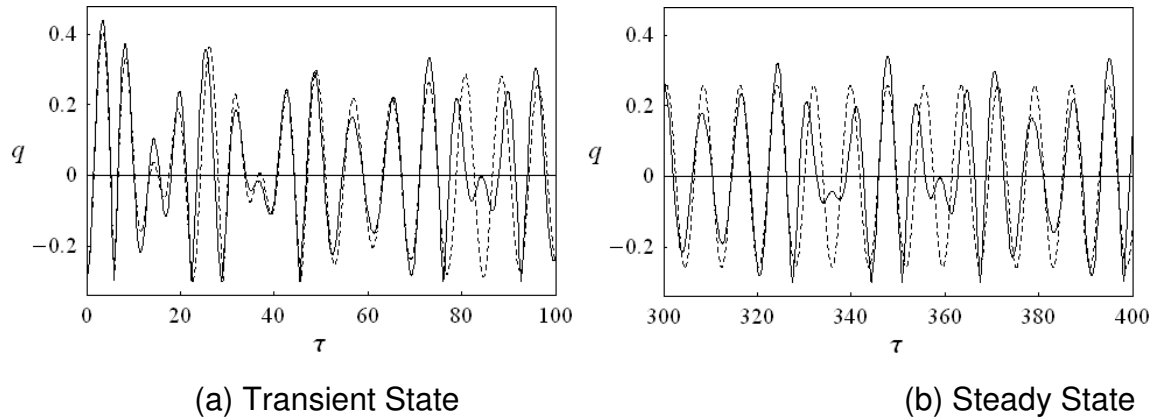


Figure 4.45. Amplitude history record for $q_i = -0.3$, $\nu = 0.8$, $a = 0.08$,

$$z_o = 0.01, z_o' = 0.01, \text{ and } e = 0.90;$$

_____ : Model 2, and - - - : Equivalent damping method.

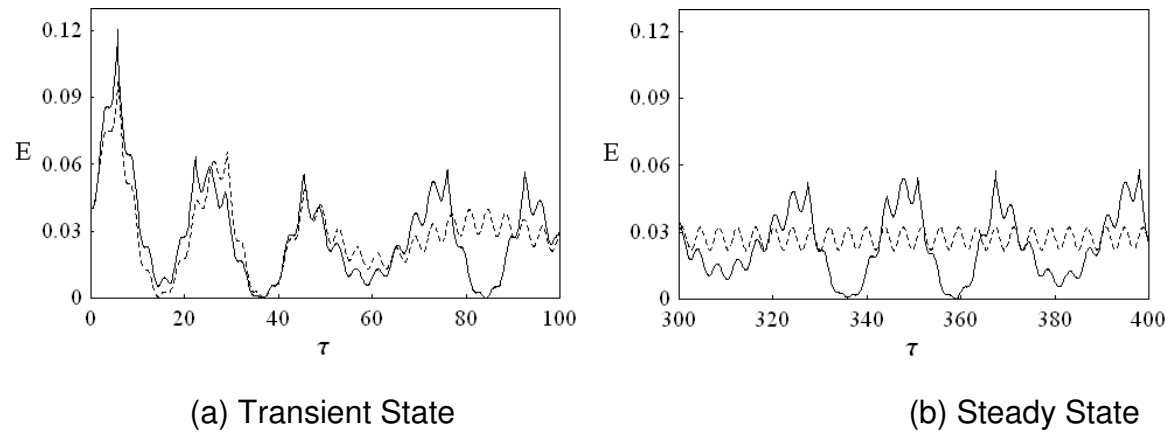


Figure 4.46. Total Energy for $q_i = -0.3$, $\nu = 0.8$, $a = 0.08$,

$$z_o = 0.01, z_o' = 0.01, \text{ and } e = 0.90;$$

_____ : Model 2, and - - - : Equivalent damping method.

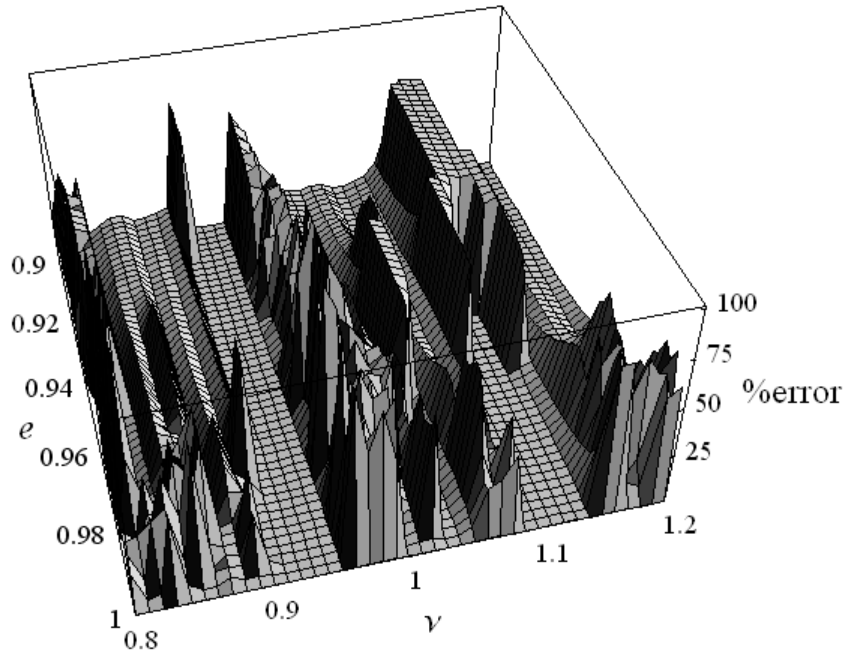


Figure 4.47. Error involved in equivalent damping method as a function of excitation frequency ratio ν and coefficient of restitution e for $a = 0.08$,

$$z_o = 0.01, z_o' = 0.01, \text{ and } q_i = -0.1.$$

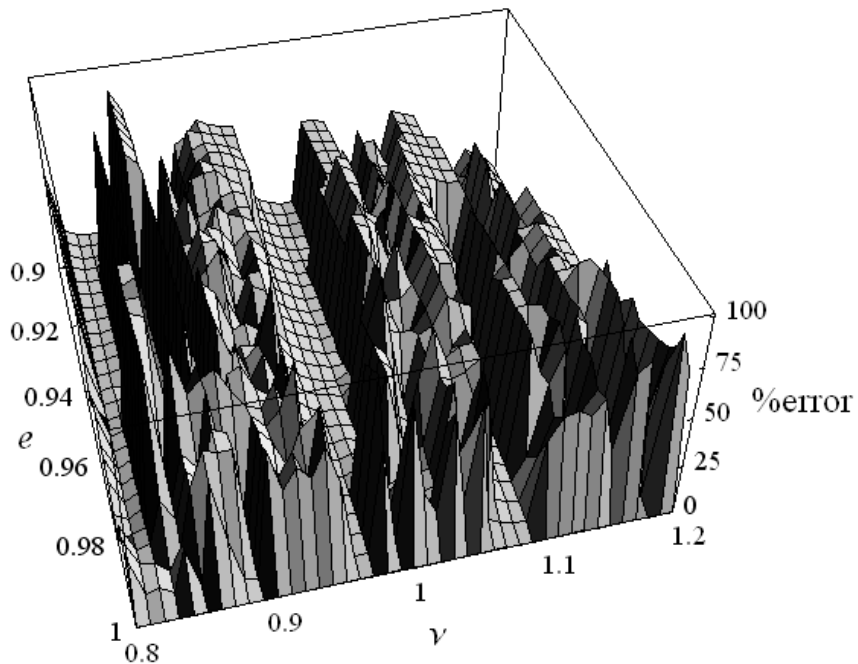


Figure 4.48. Error involved in equivalent damping method as a function of excitation frequency ratio ν and coefficient of restitution e for $a = 0.08$,

$$z_o = 0.01, z_o' = 0.01, \text{ and } q_i = -0.2.$$

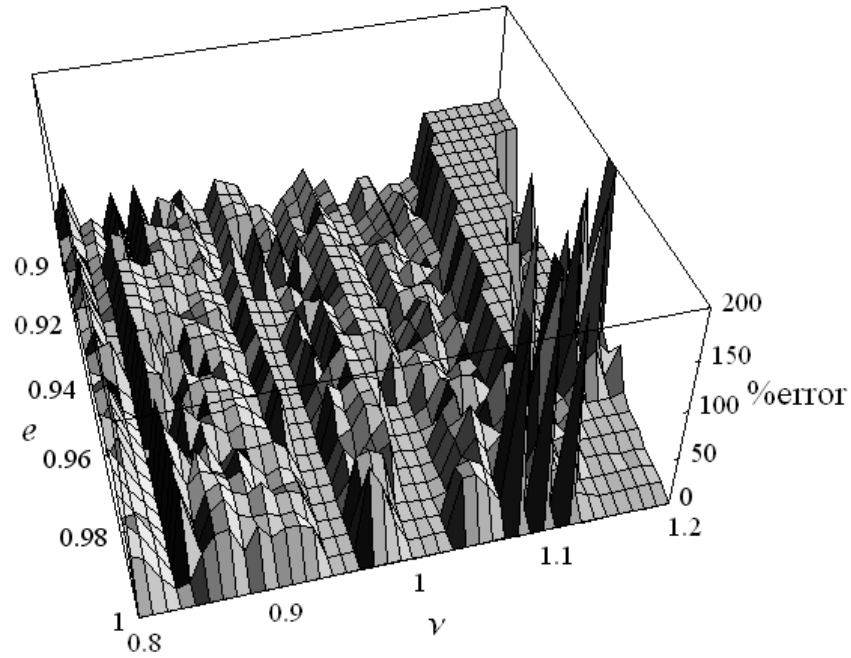


Figure 4.49. Error involved in equivalent damping method as a function of excitation frequency ratio ν and coefficient of restitution e for $a = 0.08$,

$$z_o = 0.01, z_o' = 0.01, \text{ and } q_i = -0.3.$$

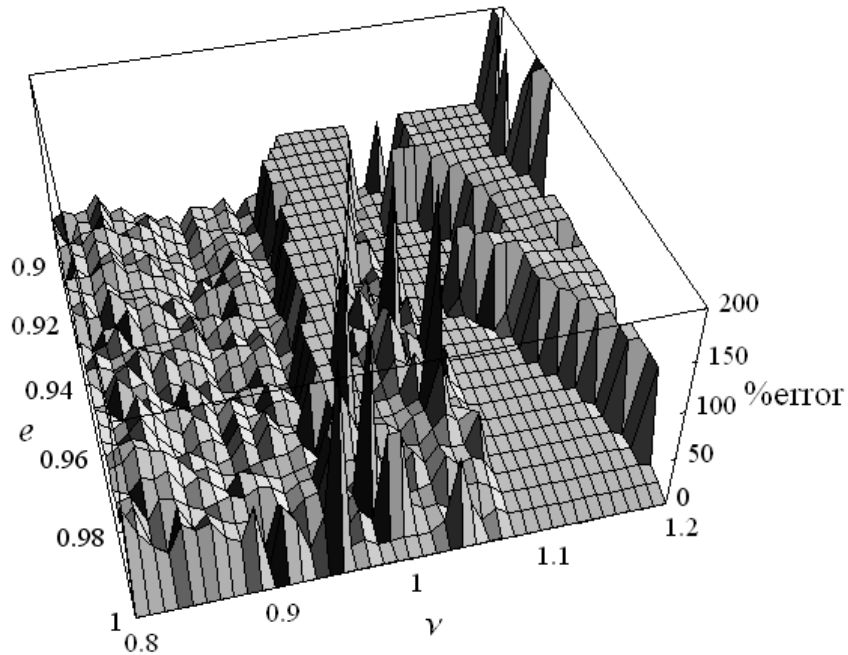


Figure 4.50. Error involved in equivalent damping method as a function of excitation frequency ratio ν and coefficient of restitution e for $a = 0.06$,

$$z_o = 0.01, z_o' = 0.01, \text{ and } q_i = -0.4.$$

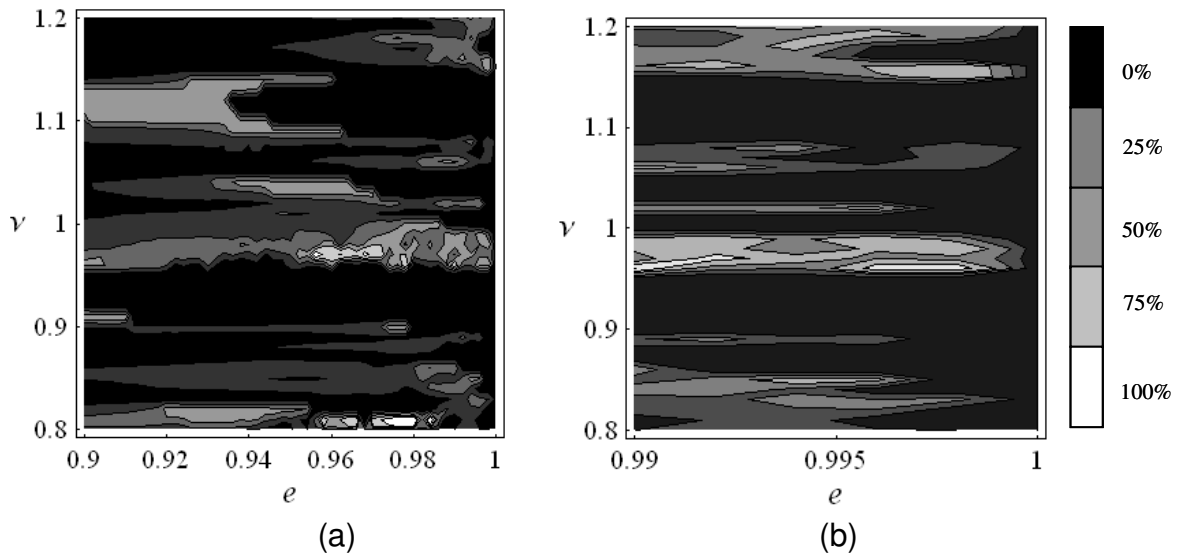


Figure 4.51. Contour Plot for error involved in equivalent damping method for $a = 0.08$, $z_o = 0.01$, $z_o' = 0.01$, and $q_i = -0.1$: (a) $e = 0.9-1.0$, (b) $e = 0.99-1.0$.

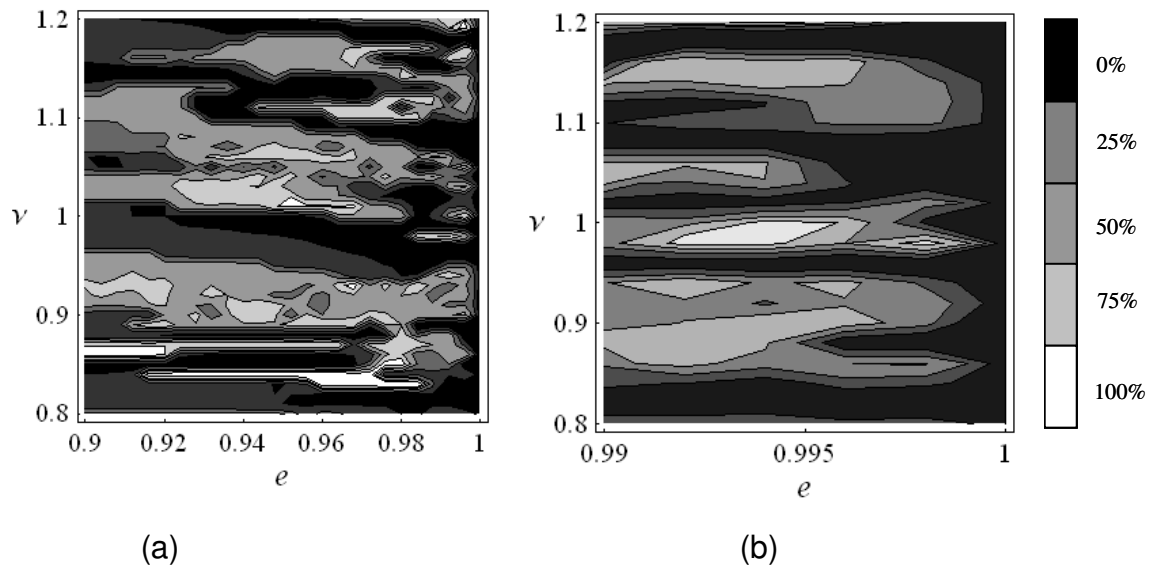


Figure 4.52. Contour Plot for error involved in equivalent damping method for $a = 0.08$, $z_o = 0.01$, $z_o' = 0.01$, and $q_i = -0.2$: (a) $e = 0.9-1.0$, (b) $e = 0.99-1.0$.

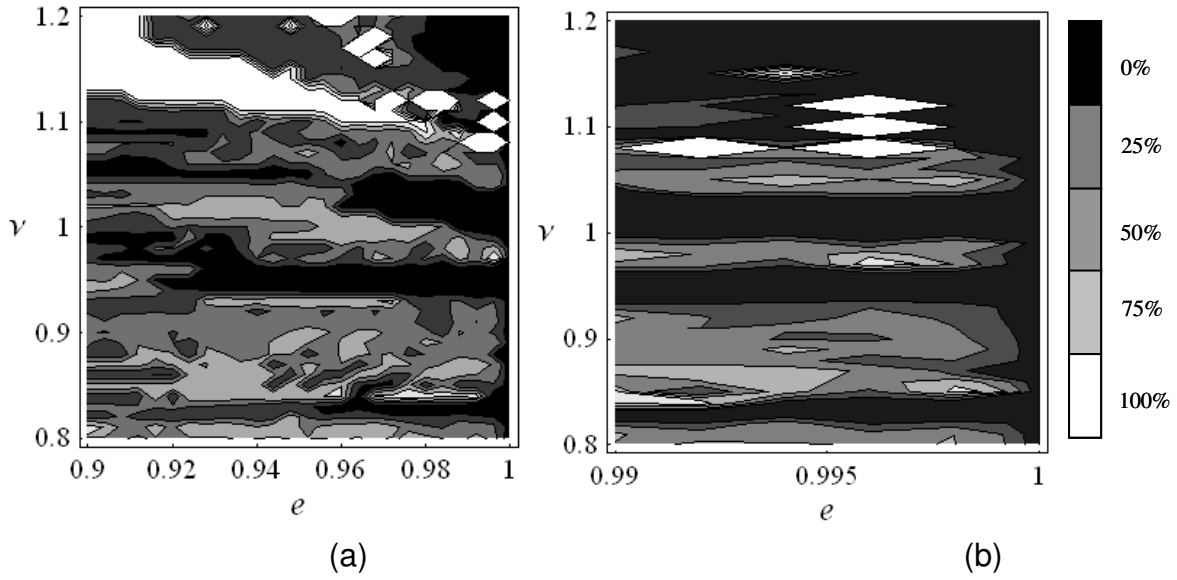


Figure 4.53. Contour Plot for error involved in equivalent damping method for $a = 0.08$, $z_o = 0.01$, $z'_o = 0.01$, and $q_i = -0.3$: (a) $e = 0.9 - 1.0$, (b) $e = 0.99 - 1.0$.

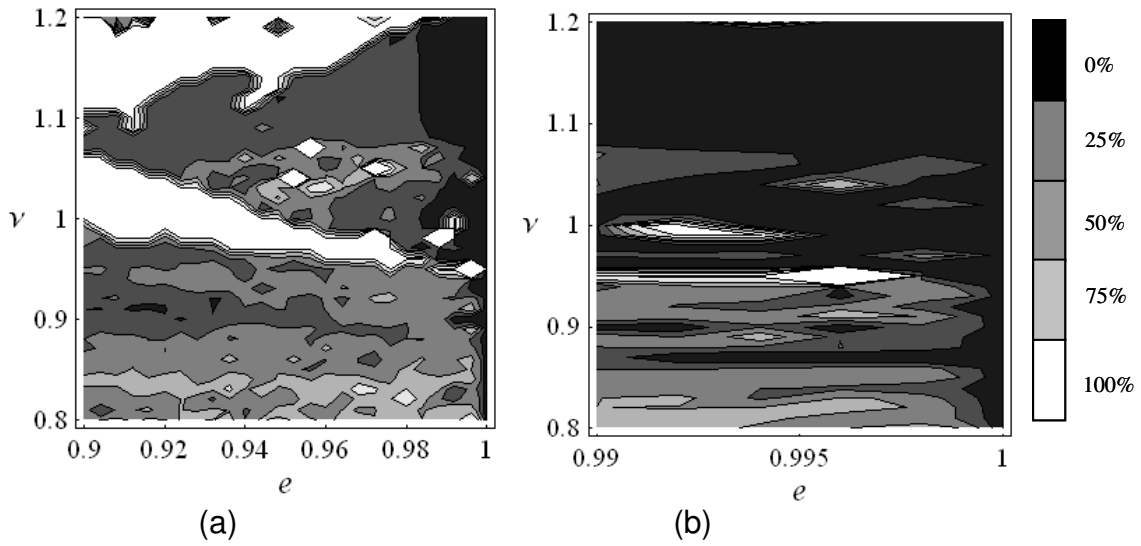


Figure 4.54. Contour Plot for error involved in equivalent damping method for $a = 0.06$, $z_o = 0.01$, $z'_o = 0.01$, and $q_i = -0.4$: (a) $e = 0.9 - 1.0$, (b) $e = 0.99 - 1.0$.

CHAPTER 5

EXPERIMENTAL INVESTIGATION

5.1 Introduction

The analytical and numerical results presented in Chapters 3 and 4 need to be validated experimentally. This chapter reports the experimental results of a ship model and provided a comparison with predicted results. Although full-scale tests provide more accurate results than model tests due to scale effects, however, it is not only difficult, but rather very expensive to conduct full-scale tests since they are useful only for vessels of similar geometry. Furthermore, full-scale tests for ships subjected to impact with a rigid barrier may lead to considerable damage. A series of experiments are conducted using the towing tank at Wayne State University. The experimental setup is designed such that the ship model is allowed to roll about the longitudinal axis that passes through its center of gravity, at the same time all other degrees of freedom are constrained. The towing tank is equipped with a wave maker that can generate water waves at different wave heights and wavelengths. In order to simulate the impact phenomenon, a metallic barrier is positioned in the neighborhood of the ship model. The experimental setup is versatile to provide different initial impact angles. In order to minimize wave reflections from the tank wall, a porous wooden plate is placed at a given slope on the opposite side of the wave maker.

5.2 Ship Model

A wooden ship model with relatively small scale was selected to satisfy two-dimensional waves' condition. Figure 5.1 shows the model and its dimensions. The ship model metacentric height, mass moment of inertia, and center of gravity are determined experimentally. Detailed calculations are given in the next subsections.

5.2.1 THE METACENTRIC HEIGHT

The metacentric height of the ship is defined as the distance from the metacenter to the center of gravity and is determined following the same procedure outlined in Bhattacharya (1978) as follows:

1. The model was placed to float on calm water.
2. A weight w was placed at right angle to the centerline athwartships¹ of the model to a distance d as shown in Figure 5.2.
3. The shifted weight produced a roll moment $M = w \times d$. The resulting roll angle ϕ was measured.
4. Taking the moments about G , one may write $W \overline{GG_1} = w \times d$ (see Figure 5.2), substituting for $\overline{GG_1} = \overline{GM} \tan \phi$ and rearranging, gives

$$\overline{GM} = \frac{w \times d}{W \tan \phi} \quad (5.1)$$

¹ Athwartships means across the vessel in a direction at right angle to the fore-and-aft line of the vessel.

where $w = 0.67 \text{ N}$ is the shifted weight, $d = 38 \text{ mm}$ is the distance from the weight w to the center of gravity, $\phi = 21^\circ$ is the roll angle, and $W = 8.6 \text{ N}$ is the weight of the ship model. From equation (5.1) the height of the metacenter is $\overline{GM} = 7.7 \text{ mm}$.

5.2.2 MASS MOMENT OF INERTIA

Since the geometry of the ship model is not possible to determine analytically its mass moment of inertia about its roll axis, J_G , one can measure its mass moment of inertia experimentally. This was carried out by placing the model to float on calm water, the model was given an initial roll angle $\phi_0 = 10^\circ$ and left to oscillate freely about its longitudinal axis passing through its center of gravity G . It should be noted that a small initial roll angle was given to the ship to keep the ship motion in the linear range. Neglecting the damping term, the equation of motion for can be written as

$$(J_G + J_A)\ddot{\phi} + W\overline{GM} \sin \phi = 0 \quad (5.2)$$

where J_A is the added inertia. One can set an average value for the added inertia as 20% of the moment of inertia of the ship as recommended by Bahattacharya (1978). Referring to Equation (5.2), the natural frequency of the model ω_n is given

by $\omega_n = \sqrt{\frac{W\overline{GM}}{J_G + J_A}}$, setting $J_A = 0.2J_G$ and rearranging

$$J_G = \frac{W\overline{GM}}{1.2\omega_n^2} \quad (5.3)$$

In order to estimate the natural frequency of the model, the time period for three complete cycles is recorded with the aid of a stop watch. This step is repeated three times and the average time is taken. The recorded time periods are $T = 3.98\text{s}$, 3.84s , and 3.89s . The average period of one oscillation is calculated as $T = 1.3\text{ s}$. The natural frequency of the model is estimated to be $\omega_n = 2\pi/T = 4.83\text{ rad/s}$. Substituting in equation (5.3) for $W = 8.6\text{ N}$, $\overline{GM} = 7.7\text{ mm}$, the mass moment of inertia of the model is found to be $J_G = 0.00237\text{ Kg m}^2$.

5.2.3 CENTER OF GRAVITY

The coordinates of the model center of gravity are recorded in the vertical and longitudinal coordinates. The vertical position of the center of gravity of the model is determined as follows:

1. The ship model is suspended to roll freely about point D , see Figure 5.3, where $\overline{KD} = 79\text{ mm}$.
2. The initial roll angle is measured by angular displacement gage as $\phi_0 = 10^\circ$.
3. In order to determine the time period of oscillation, time for five complete oscillations is recorded with the aid of a stop watch. To reduce the human error, this step is repeated three times, and time for four complete oscillations is taken as average of these readings. The recorded time periods are 3.24s , 3.18s , and 3.19s . The average time period for one oscillation is taken as $T = 0.8\text{ s}$. Hence, the natural frequency of roll about axis passes through point D is $\omega_{nD} = 2\pi/T = 7.85\text{ rad/s}$

4. Applying Newton's second law of motion on the system shown in Figure 5.3, the equation of motion can be written as

$$J_D \ddot{\phi} + W \overline{DG} \sin \phi = 0 \quad (5.4)$$

where J_D is the mass moment of inertia of the ship model about the longitudinal axis through D . For a small angle ϕ , one may set $\sin \phi = \phi$, hence, Equation (5.4) takes the form

$$\ddot{\phi} + \frac{W \overline{DG}}{J_D} \phi = 0 \quad (5.5)$$

Equation (5.5) gives the natural frequency ω_{nD} to be

$$\omega_{nD} = \sqrt{W \overline{DG} / J_D}, \text{ or}$$

$$\overline{DG} = \frac{J_D}{W} \omega_{nD}^2 \quad (5.6)$$

where $J_D = J_G + \frac{W}{g} \overline{DG}^2$, substituting in equation (5.6) and rearranging,

gives

$$\overline{DG}^2 - \frac{g}{\omega_{nD}^2} \overline{DG} + \frac{g J_G}{W} = 0 \quad (5.7)$$

where g is the gravitational acceleration.

5. Solving equation (5.7) gives $\overline{DG} = 19mm$.
6. Referring to Figure 5.3 the vertical location of the center of gravity can be estimated by setting $\overline{KG} = \overline{KD} - \overline{DG} = 60mm$.

The longitudinal position of the center of gravity of the model is determined by placing one end of the ship model on a knife edge, while the other end is placed on

another knife edge placed on the digital scale, as shown in Figure 5.4. Let x be the distance from model's center of gravity G to the plane of the aft support passing through point A and taking moments about A gives,

$$W \times x = p \times l \quad (5.8)$$

where $p = 4.6 \text{ N}$ is the pressure of the model on the scale, and $l = 201 \text{ mm}$ is the distance from the knife edge on the scale to the support. Substituting in equation (5.8), the longitudinal position of center of gravity from the plane of support A is calculated as $x = 107.5 \text{ mm}$.

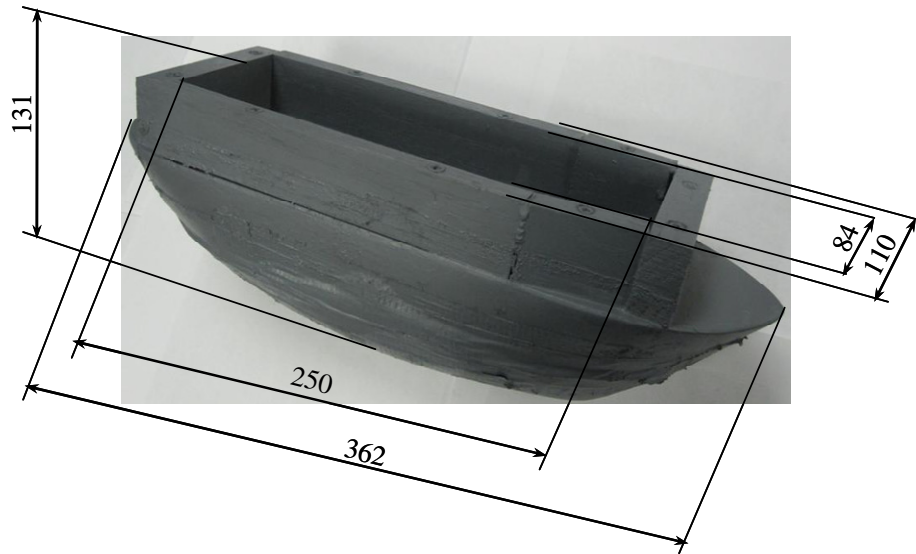


Figure 5.1. The ship model used in the experiments and its dimensions (dimensions are in mm).

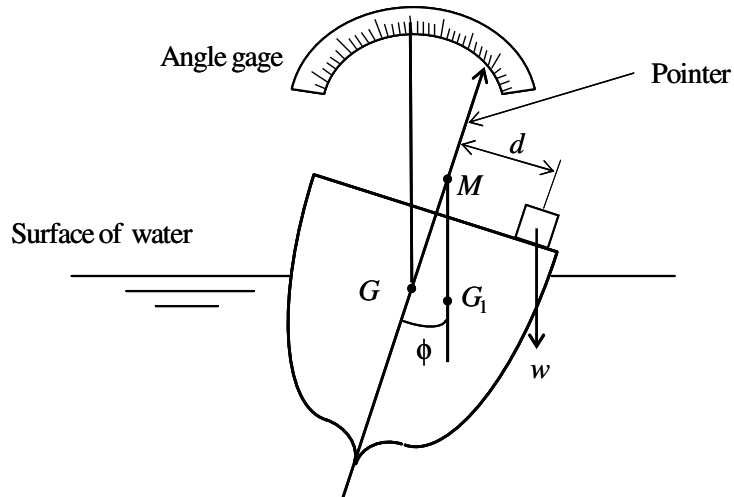


Figure 5.2. Inclination experiment to determine the metacentric height.

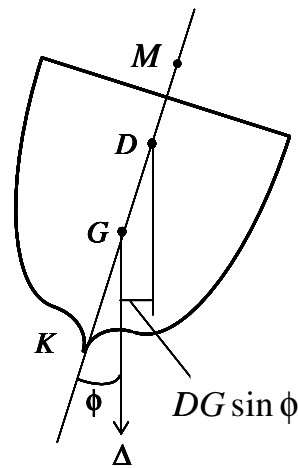


Figure 5.3. Determination of the vertical position of center of gravity of the ship model.

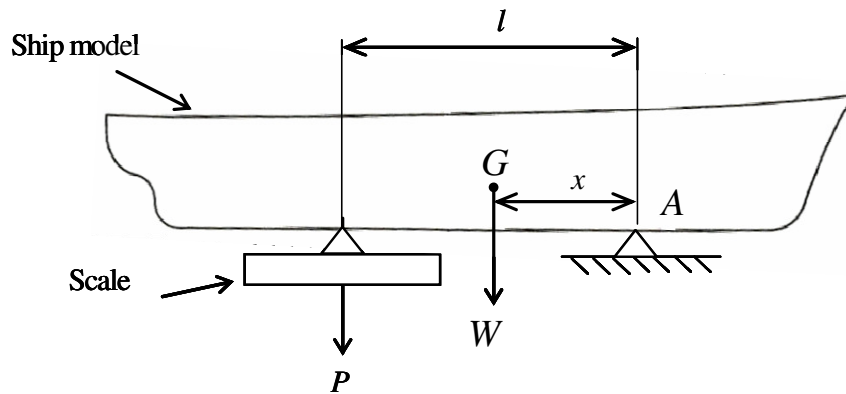


Figure 5.4. Determination of the longitudinal position of the center of gravity of the ship model.

5.3 Experimental Setup

Figure 5.5 shows a block diagram of the experiment setup. The towing tank is made of Plexiglas sheets with dimensions $3.05 \times 1.22 \times 1.22m$ and thickness $0.03175m$. The tank is fixed to a steel frame with six adjustable legs, as shown in Figure 5.6. The frame is designed such that the length of each leg can be adjusted separately in order to keep the tank in a horizontal level regardless the irregularities in the floor surface. The walls of the tank are tightened with the aid of tension belts to sustain the hydrodynamic loads of waves on tank walls. The experiment setup is designed such that the ship model is only allowed to roll about the longitudinal axis that passes through its center of gravity against one-sided barrier as shown in Figure 5.7. The model is mounted through an axle along the longitudinal axis, which is linked with a metallic beam that is fixed to the carriage, as shown in Figure 5.8. For other purposes, the carrying carriage is allowed to move forward and backwards in a straight line parallel to longitudinal axis of the tank through a DC gear motor.

The towing tank is equipped with a flap-type wave maker (see Figure 5.8) that can generate water waves at different wave heights and wavelengths. The speed of the gear motor is controlled by a speed control unit such that the motor speed can be adjusted up to 34 rpm. It should be noted that the experiments are carried out at a speed in the vicinity of resonant frequency of the free surface of water to generate large wave heights. Neglecting the surface tension, the natural frequency of the free surface in a rectangular tank is given by (see e.g., Ibrahim, 2005)

$$\omega_m^2 = \frac{2m\pi}{L} g \tanh\left(\frac{2m\pi}{L} H\right), \quad m = 1, 2, \dots \quad (5.9)$$

where L is the inside length of the tank, and H is the water depth. The first natural frequency of the free surface for water depth $H = 0.89m$ is estimated to be $\omega_1 = 4.4 \text{ rad/s}$.

5.3.1. MAGNETIC ANGLE SENSOR

The amplitude of the roll angle of the ship model is measured by analog magnetic angle sensor (ASM PTAS2) with a range of -90° to 90° . An input voltage of 5V D.C. is applied to the sensor through a power supply. The relation between output voltage of the sensor and roll angle is found to be linear. The calibration of the sensor is carried out by measuring minimum and maximum output voltages corresponding to -90° and 90° , respectively. Figure 5.9 shows the calibration curve of the magnetic angle sensor. The calibration curve may be described by the following equation

$$\phi \text{ (deg)} = 18V \text{ (V)} \quad (5.10)$$

where V is the output voltage of the angle sensor in volts.

5.3.2. RESISTIVE-TYPE WAVE GAUGE

Measurements of water surface elevation variations are commonly referred to as *wave measurements* and various instruments used to obtain the measurements are called *wave gauges*. The most common wave gauges are based on the variation of one parameter in an electrical circuit, caused by the variation of the water depth. According to Hudson et al. (1979) these parameters may be resistive or capacitive. The main advantages of the resistance wave gauge are; it exhibits good linear

response, it achieves a very high accuracy of about $\pm 0.1\text{mm}$, it has low construction cost and long service life. Therefore, for the purpose of the present study, it is found that the resistive type wave gauge is convenient.

Figure 5.10 shows a schematic diagram for the electric circuit of the resistance wave gauge. The gauge consists of two electrical resistance wires (material C72150, 0.287mm diameter, and resistance 7.62 ohms/m) uniformly spaced at a separating distance of 4mm . The pair of wires is stretched between the tank bottom and its top and attached to the inside wall of the tank. An A.C. signal of 9.5 kHz at 5 r.m.s. is applied across R_1 and the probe in series. This signal is modulated according to the wave height across the probe. To block any D.C. signal, an A.C. coupling capacitor C_1 is provided through which the modulated signal passes to the amplifier, A_1 , R_2 , R_3 , and R_4 . The ratio R_4/R_2 determines the gain of the amplifier. RV_1 is the offset null control and the amplifier supply is $+15\text{V}$ and -15V D.C. The amplified output is then applied to a diode detector (D_1, C_2 , and R_5). The original signal is extracted from the carrier and this signal represents the wave height.

The calibration is carried out by recording the wave gage output voltage corresponding to the maximum wave height at a certain motor speed. The wave height is changed by changing the motor speed. Due to the sensitivity of the resistance with water salinity and temperature, the calibration is carried out for each set of experiments. For example, for first set of experiments, the calibration curve of wave gauge is shown in Figure 5.11, and is given by

$$\eta \text{ (mm)} = 50.194V \text{ (V)} + 327.55 \quad (5.11)$$

where η is the wave height in mm, and V is the output voltage in volts.

Both outputs; the amplitude of the roll angle of the ship model, and the wave height are collected by data acquisition (NI-PCI 6251) and processed by Labview software. As a result, two sets of data are recorded; excitation-time history record and ship response time history record. Post processing of time history records to determine frequencies, and the plot phase diagrams are processed by MATHEMATICA.

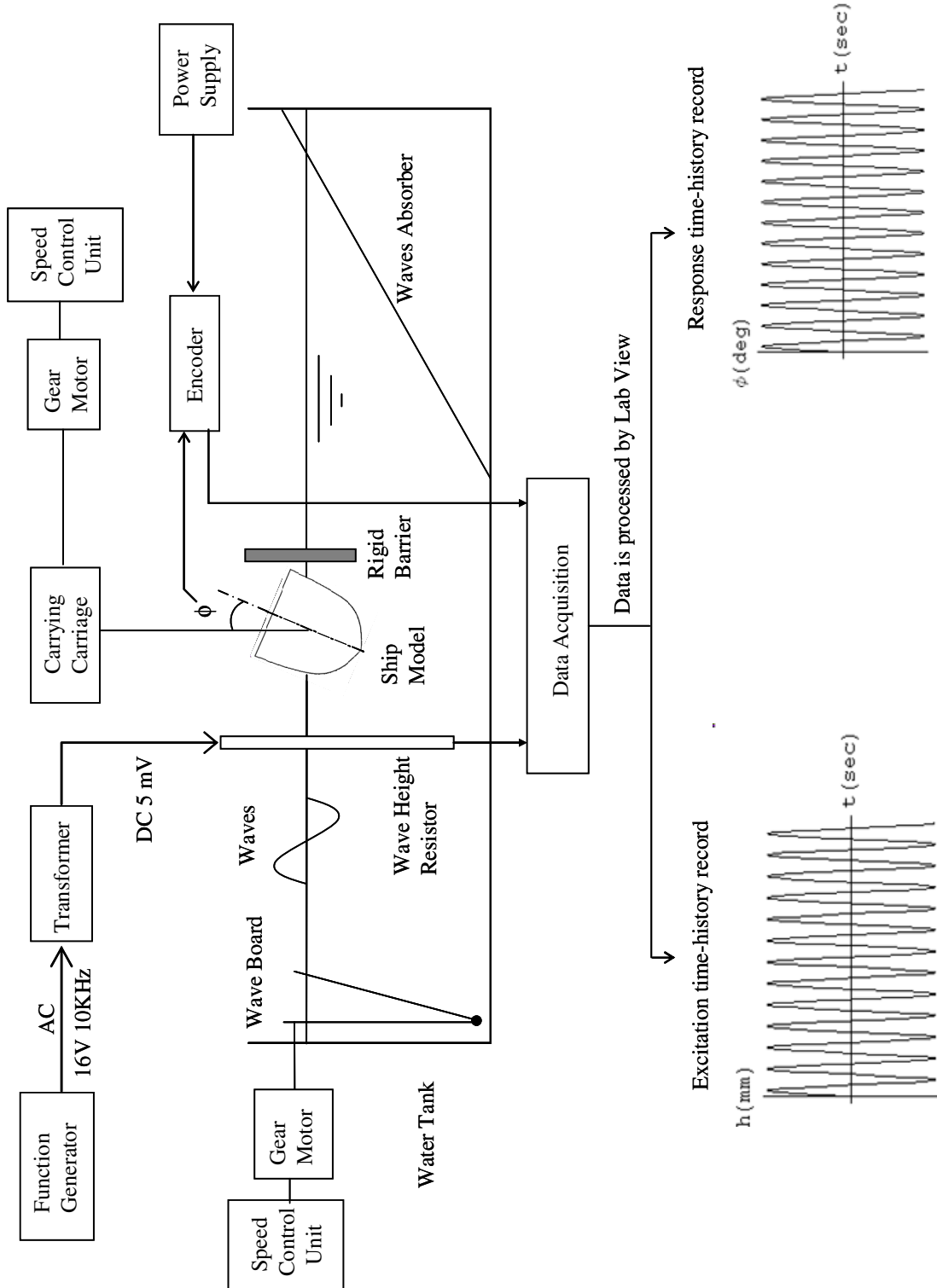


Figure 5.5. Block diagram showing the experiment layout.

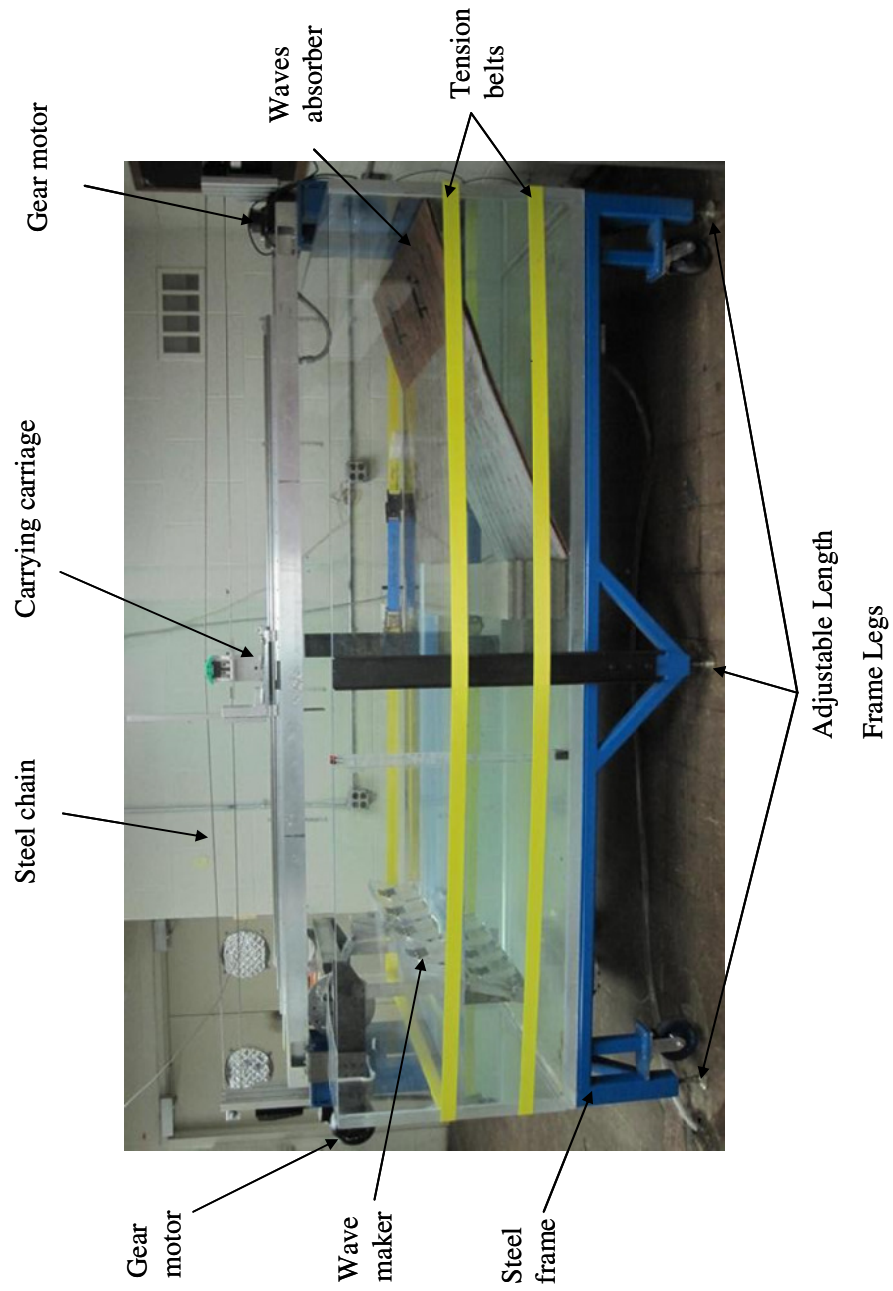


Figure 5.6. A front view of the towing tank showing the tank, wave absorber, and the wave maker.

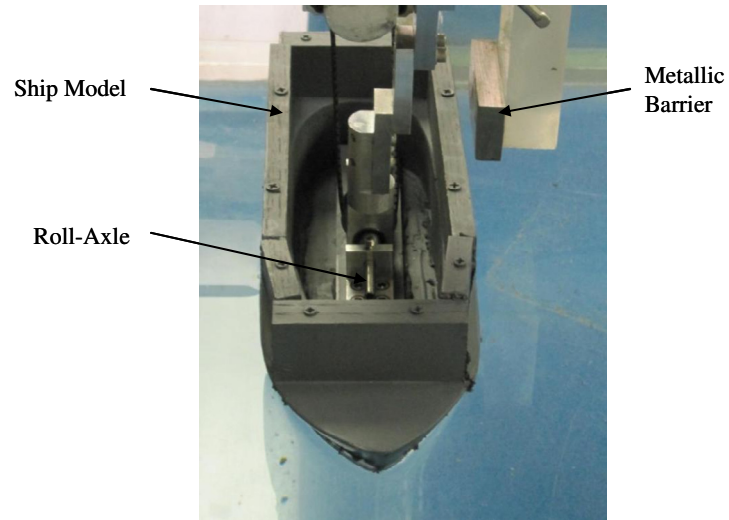


Figure 5.7. The ship model showing the installed axle about which the model is restricted to roll against the one-sided barrier shown on the right side.

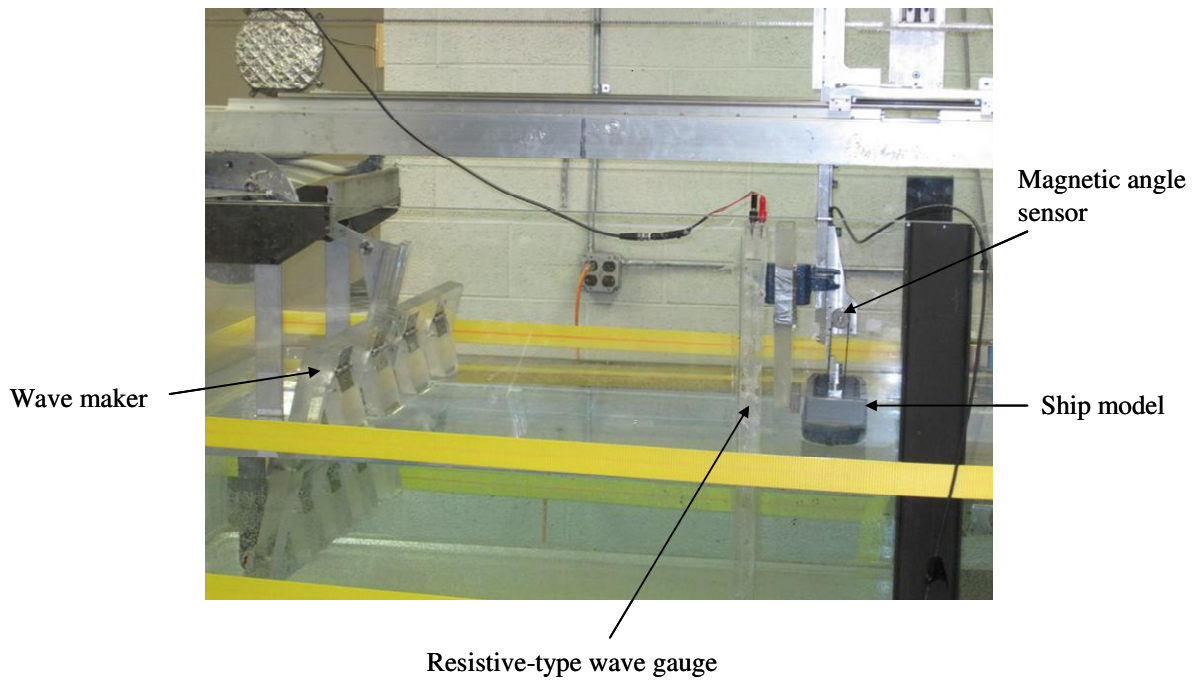


Figure 5.8. A side view of the towing tank showing the wave maker and the resistive-type wave gauge.

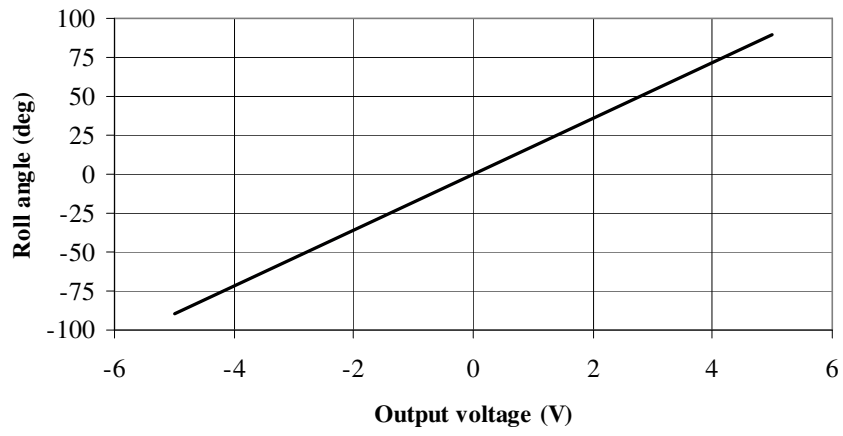


Figure 5.9. Calibration curve of the magnetic angle sensor.

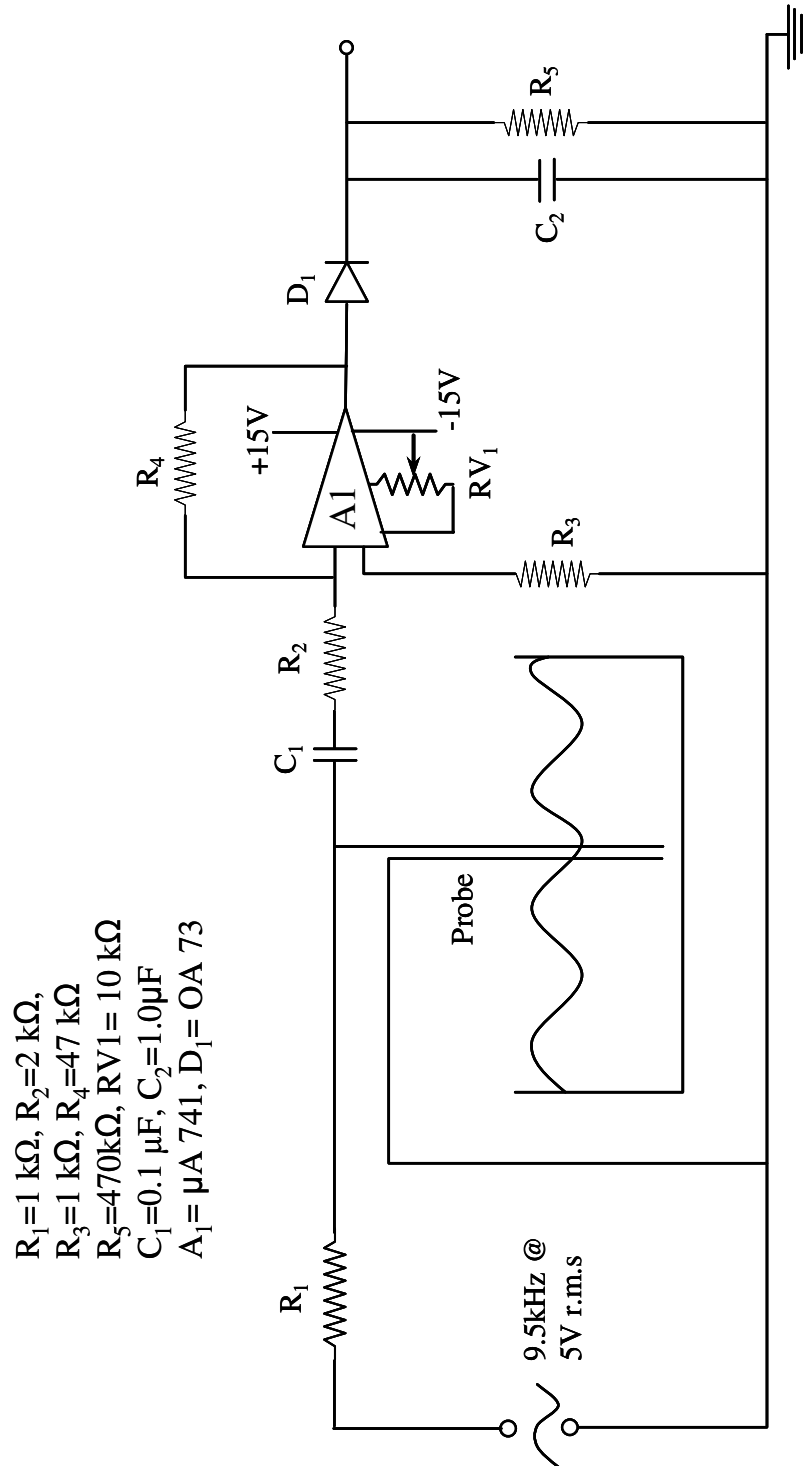


Figure 5.10. Schematic diagram for the electric circuit of the resistive-type wave gauge.

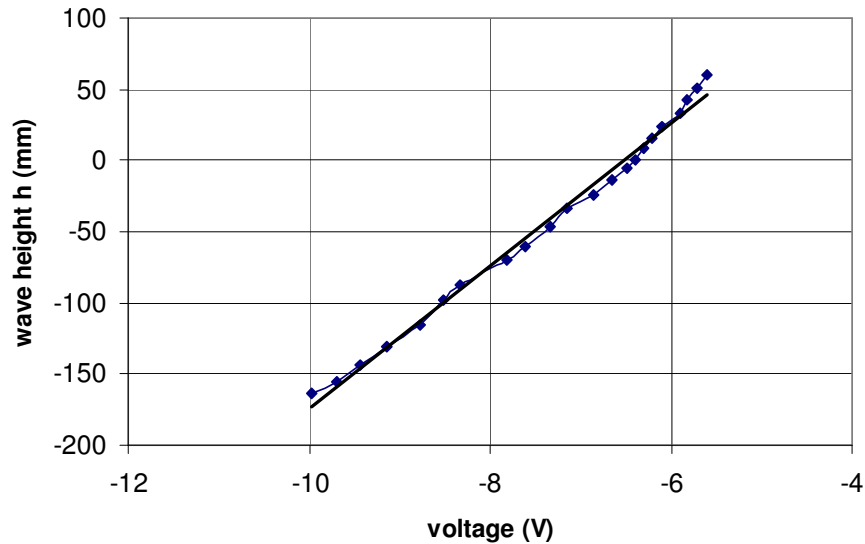


Figure 5.11. Calibration curve of the wave gauge.
 ◆◆ Experimental data, and — Fitting straight line.

5.4 Results and Discussion

In order to determine the effect of the position of the barrier on the ship response, each set of tests is carried out at the same motor speed at different values of initial impact angle. The first set of tests is carried out at a motor speed $N_m = 2.4$ rad/s. Figures 5.12(a) and (b) show the time history record and magnification of few cycles revealing the longer time duration of the wave elevation than trough. The areas under the positive and negative portions of the diagram are same giving zero average mean of the wave profile. This is confirmed by the FFT of the time history record as given in Figure 5.12(c). It is seen that the free surface wave height is periodic with two major frequencies, which may be attributed to the wave reflection from the opposite wall of the wave maker. The roll angle response of the model experiences amplitude modulation with the roll angle varies between -54° to 58° as shown in Figures 5.13(a) and 5.15(a). Figures 5.12(c) and 5.14(a) show

FFT plots of liquid surface elevation and the roll angle response, respectively. The non-zero mean amplitude is revealed in the FFT plots at zero frequency. Moreover, it can be seen that the ship response represents amplitude modulated cycles whose frequency content complies with those of the liquid surface elevation. The first frequency is 4.8 rad/s, which is twice the motor speed. This is due to the fact that for every one motor' cycle, there are two effective strokes by the wave maker board: one in the forward direction, and another one in the backward direction.

By placing the rigid barrier in the vicinity of the model at four different positions, $\phi_i = -40^\circ$, -30° , -20° , and -10° for the same motor speed; $N_m = 2.4$ rad/s, the time history records for the ship roll angle response are shown in Figures 5.13(b)-(e). It is seen that the ship experiences an impact every excitation period. With reference to Figures 5.13(b), the maximum roll angle amplitude in the positive direction is 46° which is greater than the absolute value of the impact angle $\phi_i = |-40^\circ|$, and yet smaller than the maximum positive angle in the absence of the barrier. This effect may be contributed by both energy loss at the barrier and phase shift variations induced by interactions with the barrier corresponding FFT and phase plots of the model response shown in Figures 5.14(b)-(e), and Figures 5.15(b)-(e), respectively. In particular, Figures 5.15 (b) shows the 'phase plot' of the model response for impact angle $\phi_i = -40^\circ$, at which the velocity jump occurs. It should be noted that a small velocity jump that occurs at $\phi = 46^\circ$ is possibly attributed to the stick- slip phenomenon between the ship model and the shaft about which the model rolls. This feature appears in the time history record for the case of impact angle

$\phi_i = -10^\circ$. It can be seen that the maximum roll amplitude is close 22° . Also, the model response shown in Figure 5.13(e) exhibits flattening at the positive peak at an angle less than 20° . By looking at the signal of the water free surface waves at this instant one may conclude that the forward wave and reflected wave are having opposing effect and keep the position of the model for duration less than 0.5 sec. This is reflected in the corresponding phase diagram by the near zero velocity near $\phi = 20^\circ$ as shown in Figure 5.15(e).

Another set of experiments is conducted at a motor speed of $N_m = 2.8$ rad/s. This frequency is close to the resonance of the water free surface leading to large wave heights with the possibility of nonlinear effects. Figure 5.16 shows the time history record of the water free surface wave, while Figures 5.17(a), 5.18(a) and 5.19(a) show the model time history record, its FFT plot and its phase portrait, respectively, in the absence of the barrier. In particular, it can be seen from Figure 5.16(c) that in this case, the wave generates a multiple frequency excitation on the ship model with the possibility of nonlinear effects. The FFT plots of the water free surface wave and model response are displayed in Figures 5.16(c) and 5.18(a), respectively. The principle frequency of waves is 5.6 rad/s, which is twice the motor speed. Also, the model response is modulated with two frequencies. The with the possibility of nonlinear effects response of the ship model is quite close to periodic; see Figure 5.19(a).

For the barrier placed at four different positions, $\phi_i = -40^\circ$, -30° , -20° , and -10° , and under the same motor speed, $N_m = 2.8$ rad/s, the time history records for

the ship roll angle response are shown in Figures 5.17(b)-(e). It is seen from these plots that the impact interaction with the barrier may occur in a regular or irregular way and with different cyclicity rate as the barrier position is varying. Furthermore, as the impact angle is reduced towards $\phi_i = -10^\circ$ the model experiences multi-frequency oscillations as reflected in the FFT plots and phase portraits shown in Figures 5.18 and 5.19, respectively.

The Fourier spectra presented in Figure 5.18 may not reveal possible non-stationary effects in the frequency response caused by impact events. This can be obtained either by using the windowed Fourier transform or the wavelet transform. The present work will adopt wavelet transform because the windowed Fourier transform relies on the selected length of the window. Thus, any special features occur during short time-scales smaller than the length of the window, or with small frequencies than those contained in the window are lost and cannot be captured by the windowed Fourier transform. On the other hand, the wavelet transform (see Appendix B) has the advantage in that it follows the rapid variations of the instantaneous frequencies since it adjusts the length of the window according to the frequency content of the signal. Figure 5.20 shows Morlet wavelet plots of the model response shown in Figure 5.17 under motor speed $N_m=2.8$ rad/s. These plots are generated using the MATLAB command: `ccfs = cwt(x,1:128,'morl','lvlabs');` where x is the input signal. While the wavelet scale content is quite stationary in the fragments of Figures 5.20(a) and 5.20(b), related to larger impact angles, observable non-stationary effects occur when the barrier is shifted towards the ship's port side; see fragments of Figures 5.20(c) through 5.20(e). At a very small impact angle, the

non-stationary features are less clear as shown in Figure 5.20(e). Since the motor speed is fixed, such non-stationary effects may be due to redistribution in the component amplitudes rather than varying frequencies.

Another set of experiments is conducted at a motor speed of $N_m = 2.2 \text{ rad/s}$. Figures 5.21, 5.22(a), 5.23(a) and 5.24(a) show profiles of the water free surface wave and the model response in the absence of a barrier. In particular, it can be seen from Figure 5.21 that the wave generates a multiple frequency excitation of the ship model with three major frequencies. The FFT plots of the water free surface wave and model response are displayed in Figures 5.21(c) and 5.23(a), respectively. The principle frequency of waves is 4.4 rad/s , which is twice the motor speed. Also, the model response is modulated with three major frequencies, which correspond to the three major excitation frequencies.

For the barrier placed at four different positions, $\phi_i = -40^\circ$, -30° , -20° , and -10° , and under the same motor speed, $N_m = 2.2 \text{ rad/s}$, the time history records for the ship roll angle response are shown in Figures 5.22(b)-(e). It is seen that as the impact angle is reduced towards $\phi_i = -20^\circ$, the model experiences multi-frequency oscillations as reflected by the FFT plots and phase portraits shown in Figures 5.23 and 5.24, respectively. It can be concluded that as the magnitude of impact angle decreases, the model amplitude response in the positive direction decreases. However, for small impact angle, $\phi_i = -10^\circ$, at the instant of impact, the model sticks with the barrier for certain interval of time as shown in Figure 5.22(e). Meanwhile the model response reaches a surprisingly large value in the positive direction. The model sticks to the barrier until the excitation waves are acting with a large moment

on the model in the opposite direction. For better understanding of this phenomenon, a 3-D phase plot is generated as shown in Figure 5.25. It can be seen that as the model hits the barrier with a relatively small speed, the model sticks to the barrier for uncertain interval of time.

A summary for the above results is given in Figure 5.26. The % reduction in amplitude of response experiencing impact with respect to amplitude of response with no barrier is calculated for each impact angle. Results for motor speed $N_m = 2.4$ rad/s are shown in black, and those for $N_m = 2.8$ rad/s are shown in gray. It can be seen that for both cases; $N_m = 2.4$ rad/s, and $N_m = 2.8$ rad/s, the % reduction in amplitude of model response increases as the magnitude of impact angle decreases, i.e., the significance of the damping due to inelastic impact is increased as the magnitude of initial impact angle decreases. Furthermore, for motor speed $N_m = 2.8$ rad/s, which simulates severe sea conditions, the significance of damping due to inelastic impact is dropped dramatically.

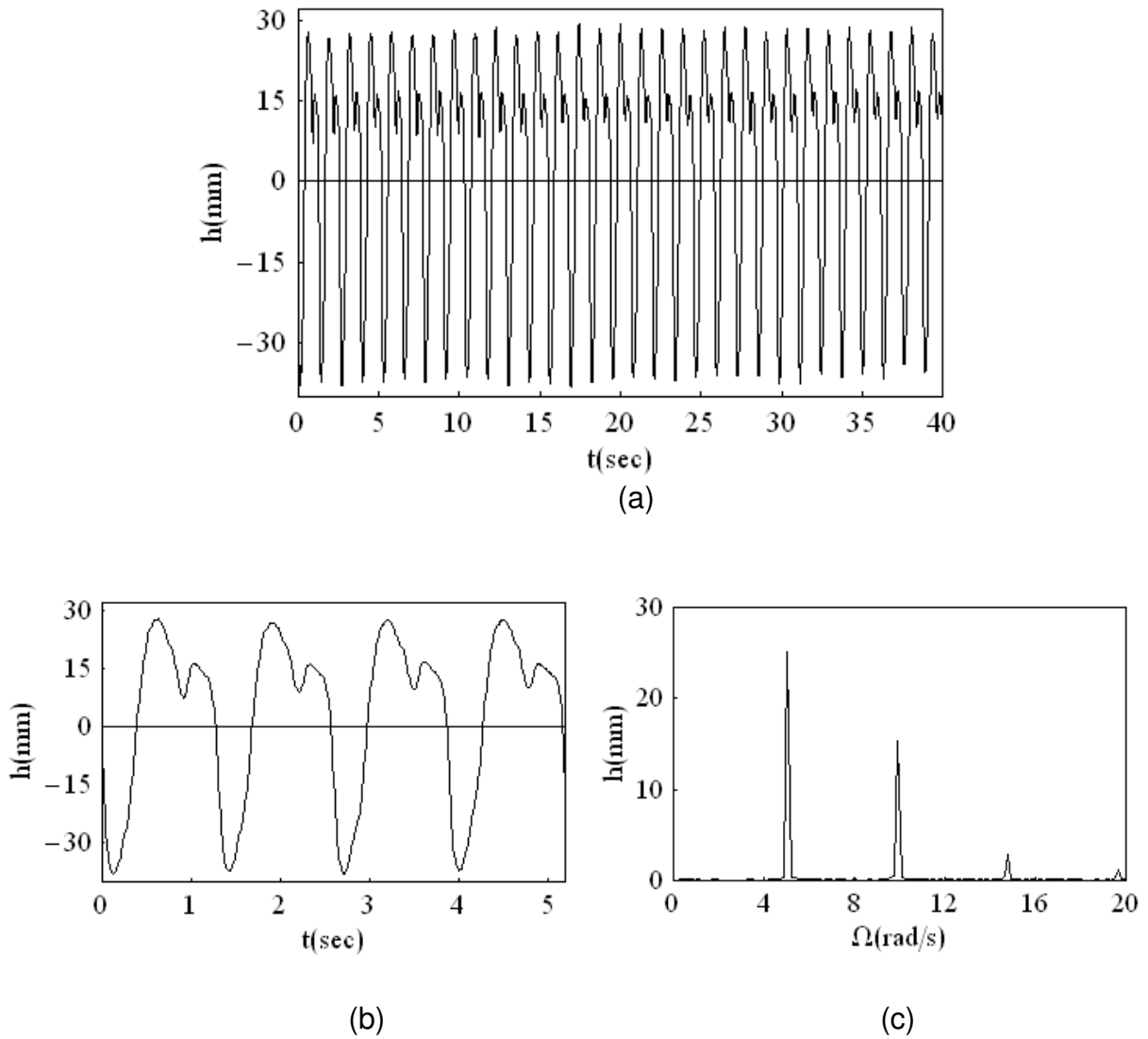


Figure 5.12. Free surface wave at wave maker motor speed $N_m = 2.4$ rad/s :
 (a) time history record of the water free surface, (b) magnification of few cycles showing the wave profile, and (c) FFT plot.

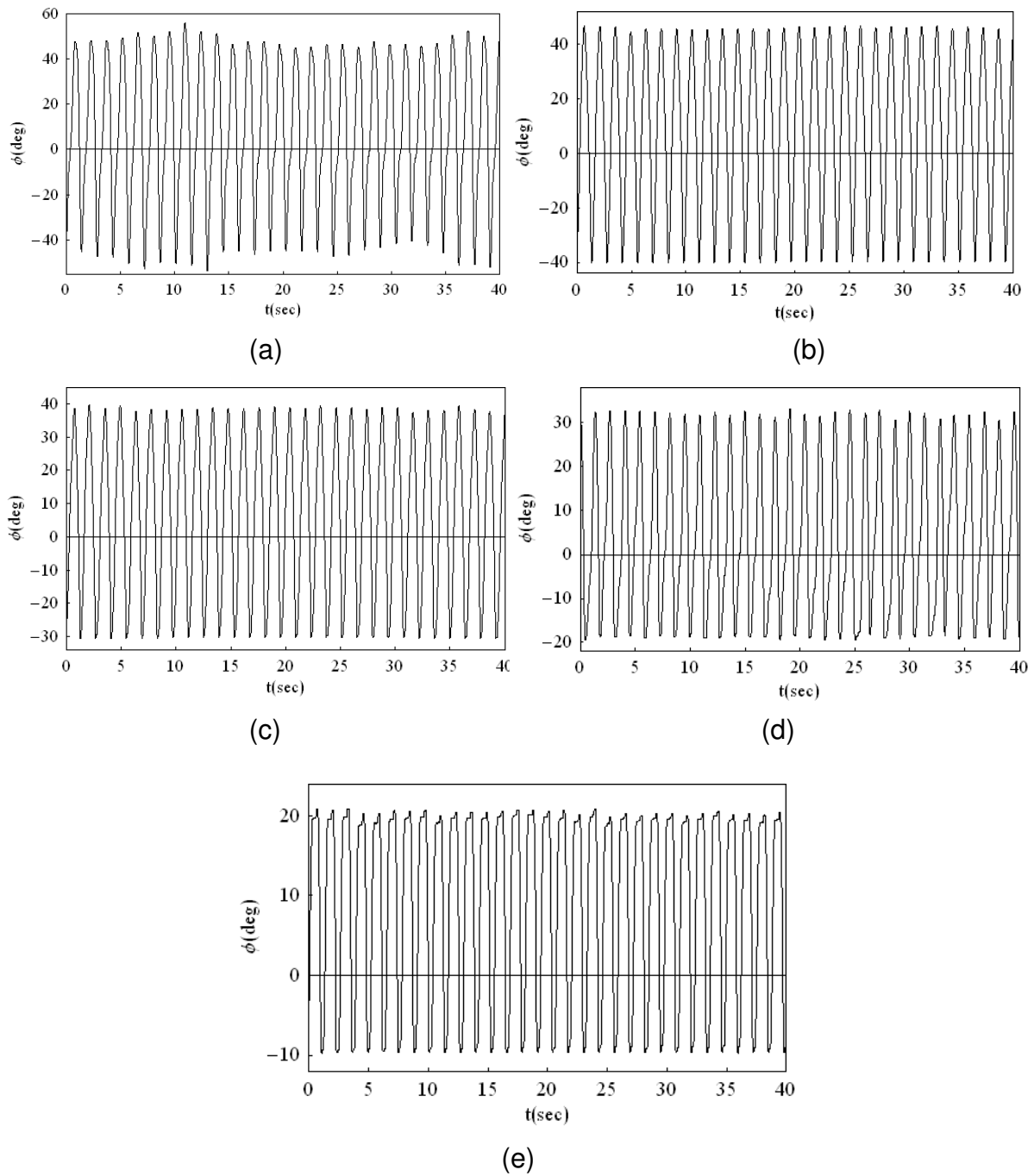


Figure 5.13. Measured time history records of the model response under motor speed $N_m = 2.4$ rad/s : (a) in the absence of barrier, (b) in the presence of one-sided barrier at -40° , (c) at -30° , (d) at -20° , (e) at -10° .

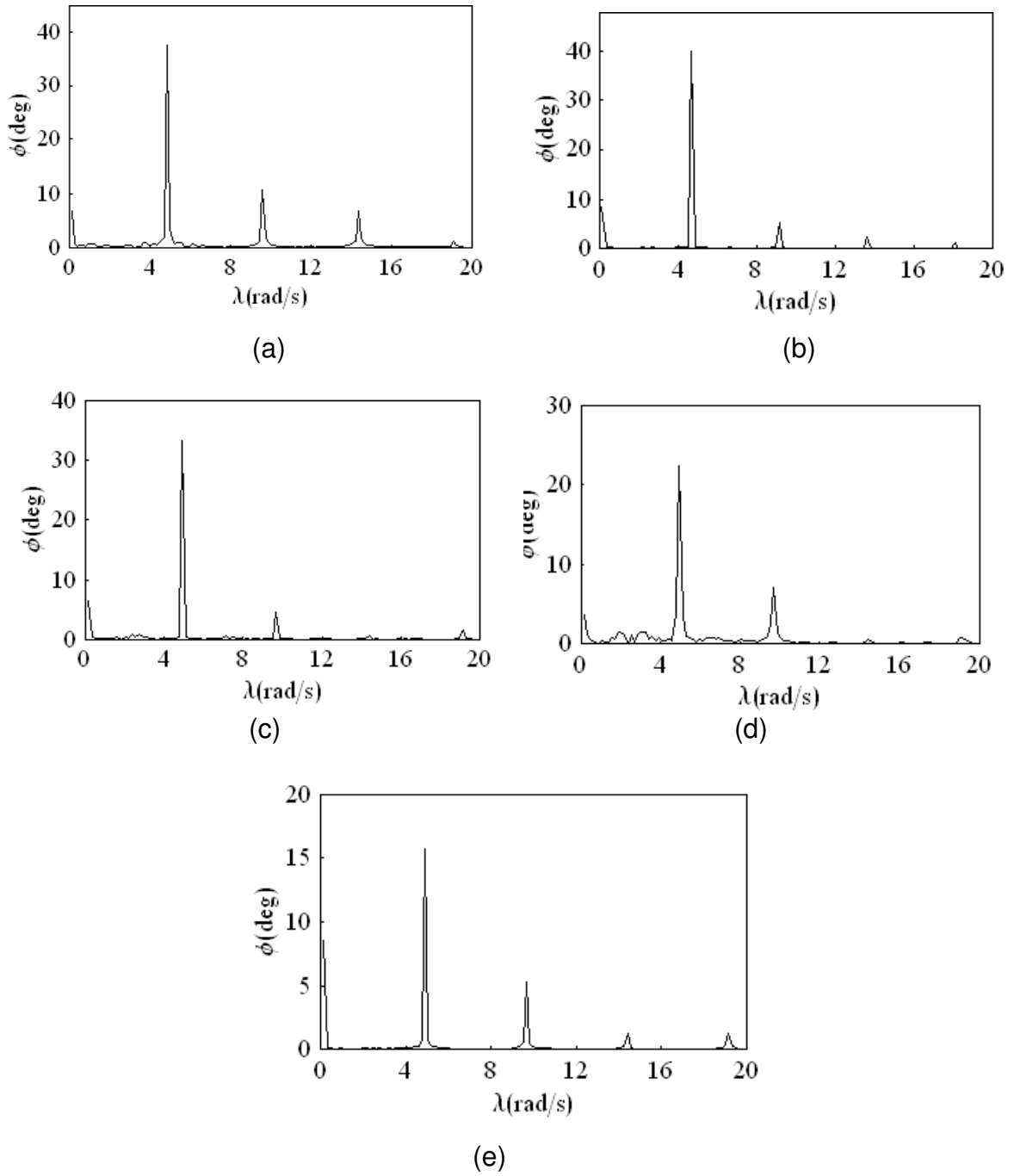


Figure 5.14. FFT plots of the model response of Figure 5.13. under motor speed $N_m = 2.4$ rad/s : (a) in the absence of barrier, (b) in the presence of one-sided barrier at -40° , (c) at -30° , (d) at -20° , (e) at -10° .

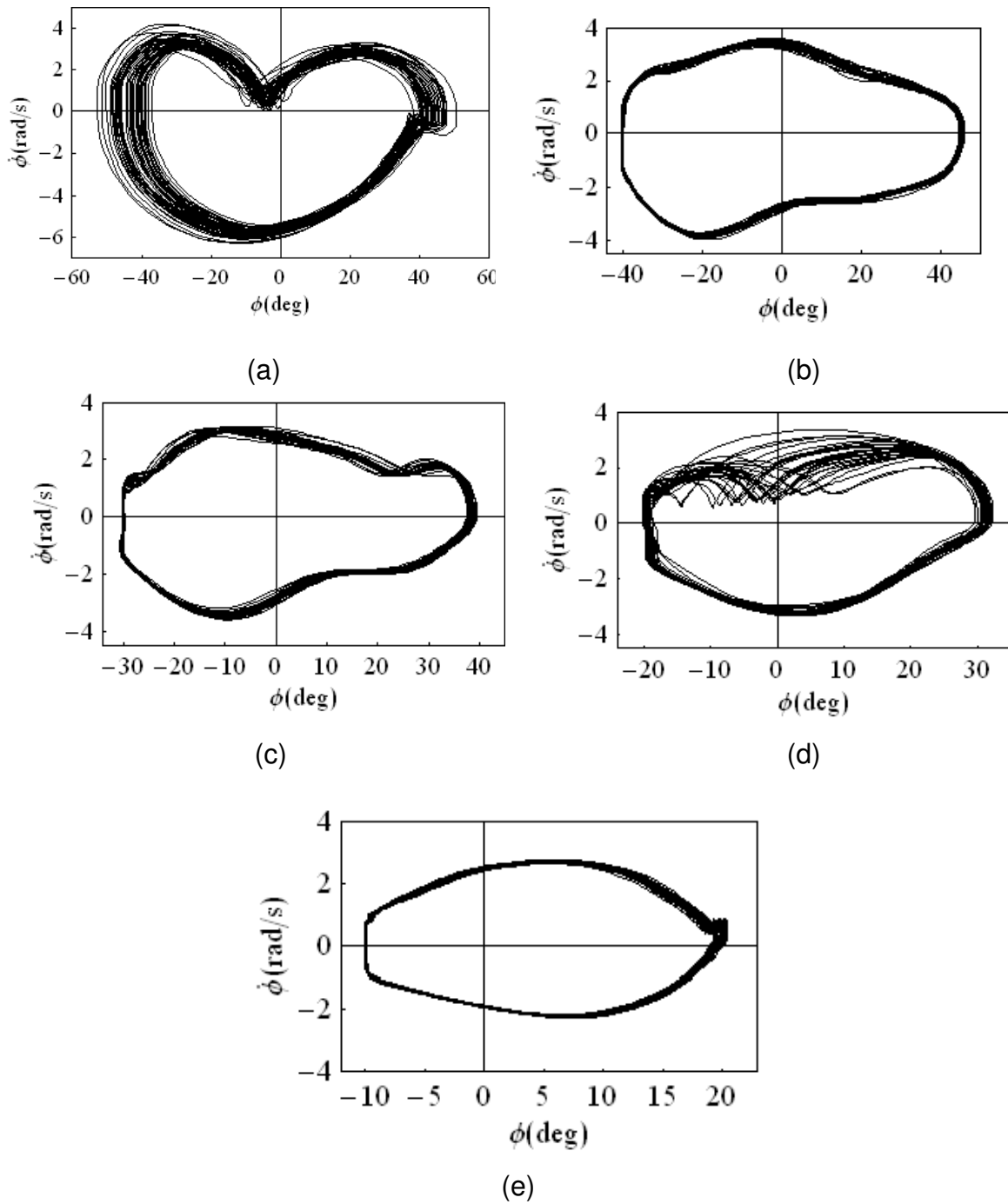
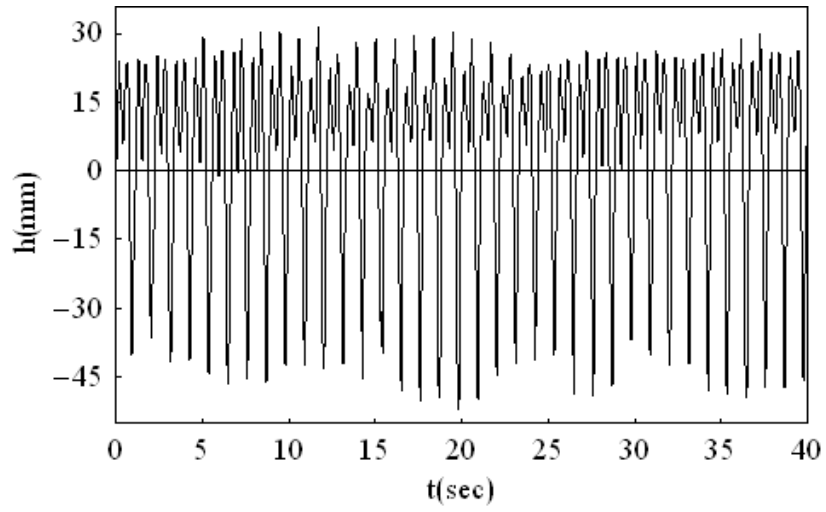
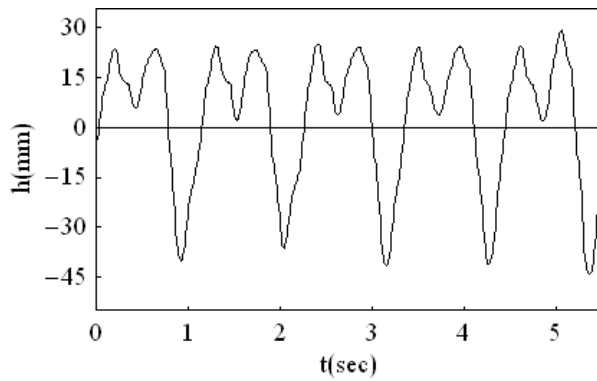


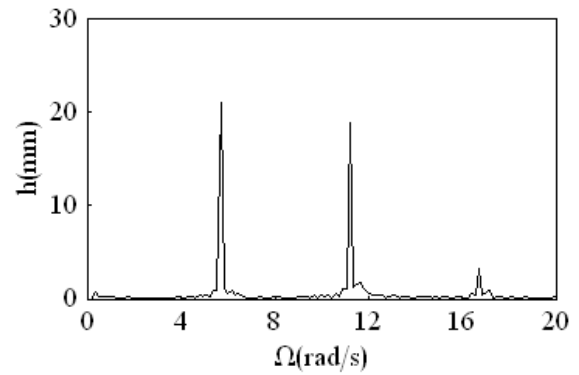
Figure 5.15. Phase trajectory projections of the model response of Figure 5.13 under motor speed $N_m = 2.4$ rad/s : (a) in the absence of barrier, (b) in the presence of one-sided barrier at -40° , (c) at -30° , (d) at -20° , (e) at -10° .



(a)



(b)



(c)

Figure 5.16. Free surface wave at wave maker motor speed $N_m = 2.8$ rad/s :
 (a) time history record of the water free surface, (b) magnification of few cycles showing the wave profile, and (c) FFT plot.

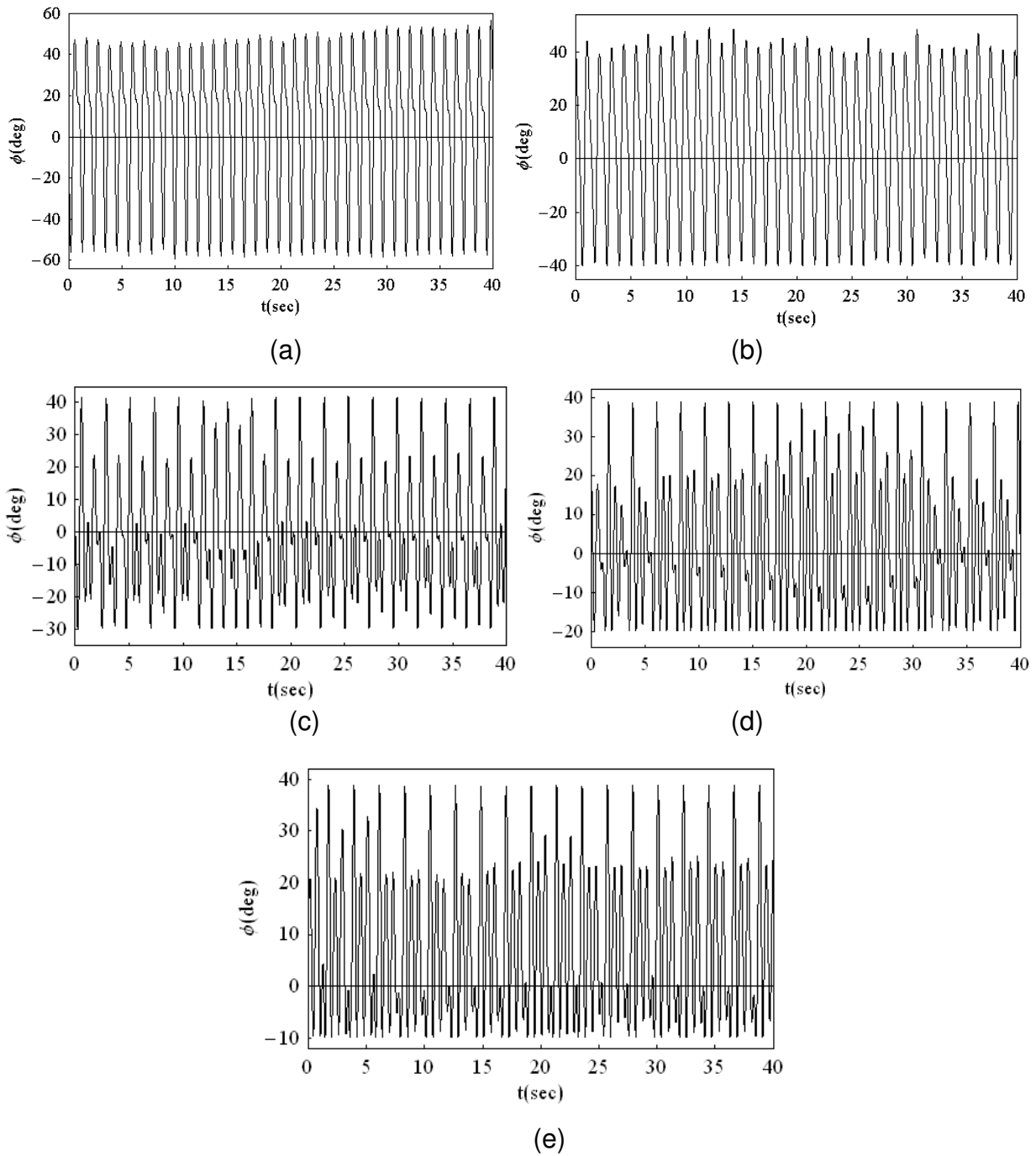


Figure 5.17. Measured time history records of the model response under motor speed $N_m = 2.8$ rad/s : (a) in the absence of barrier, (b) in the presence of one-sided barrier at -40° , (c) at -30° , (d) at -20° , (e) at -10° .

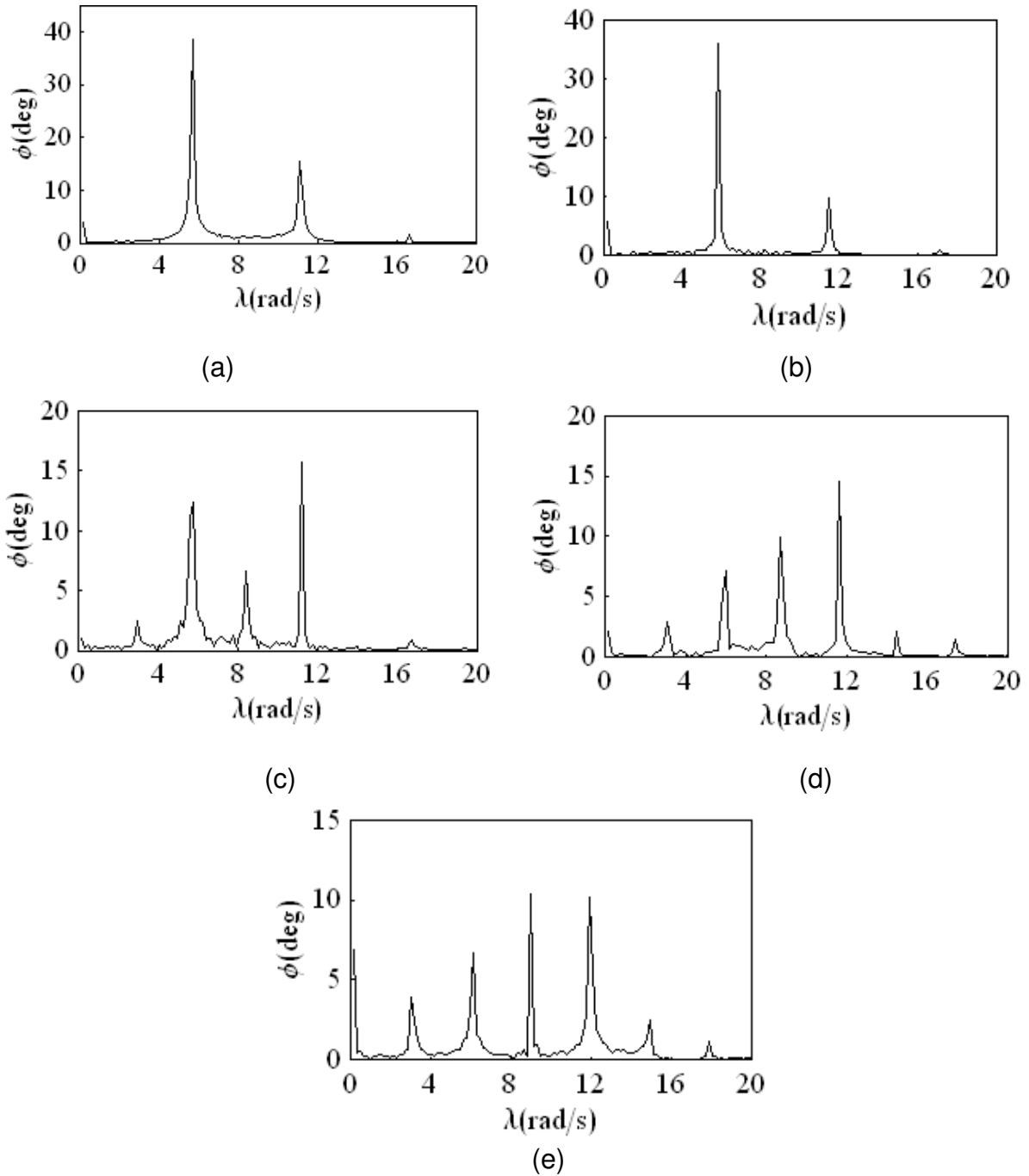


Figure 5.18. FFT plots of the model response shown in Figure 5.17 under motor speed $N_m = 2.8$ rad/s: (a) in the absence of barrier, (b) in the presence of one-sided barrier at -40° , (c) at -30° , (d) at -20° , (e) at -10° .

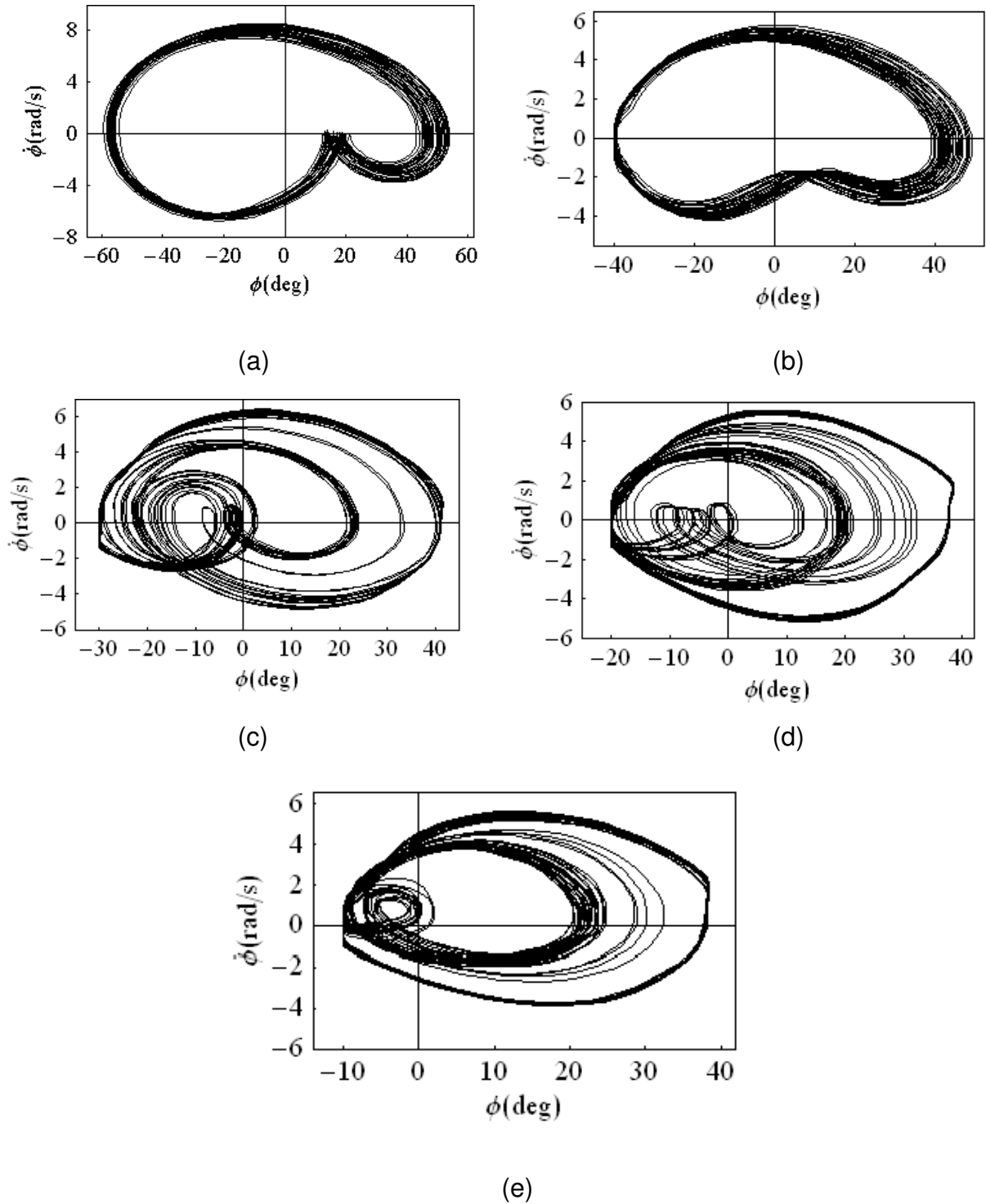


Figure 5.19. Phase trajectory projections of the model response shown in Figure 5.17 under motor speed $N_m = 2.8 \text{ rad/s}$: (a) in the absence of barrier, (b) in the presence of one-sided barrier at -40° , (c) at -30° , (d) at -20° , (e) at -10° .

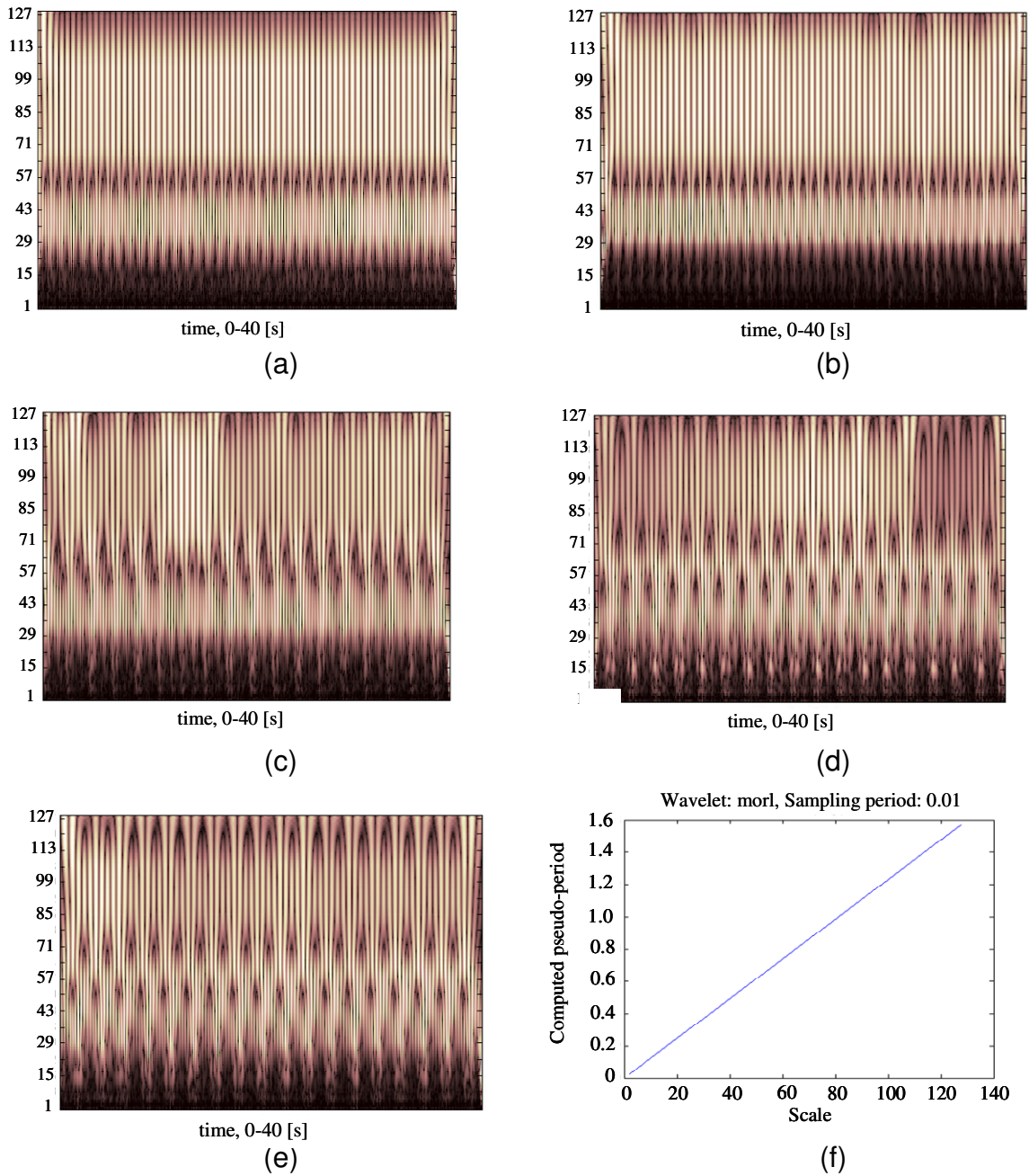


Figure 5.20. Morlet wavelet plots of the model response shown in Figure 5.16 under motor speed $N_m = 2.8$ rad/s : (a) in the absence of barrier, (b) in the presence of one-sided barrier at -40° , (c) at -30° , (d) at -20° , (e) at -10° , and (f) shows the quasi period versus scale relationship.

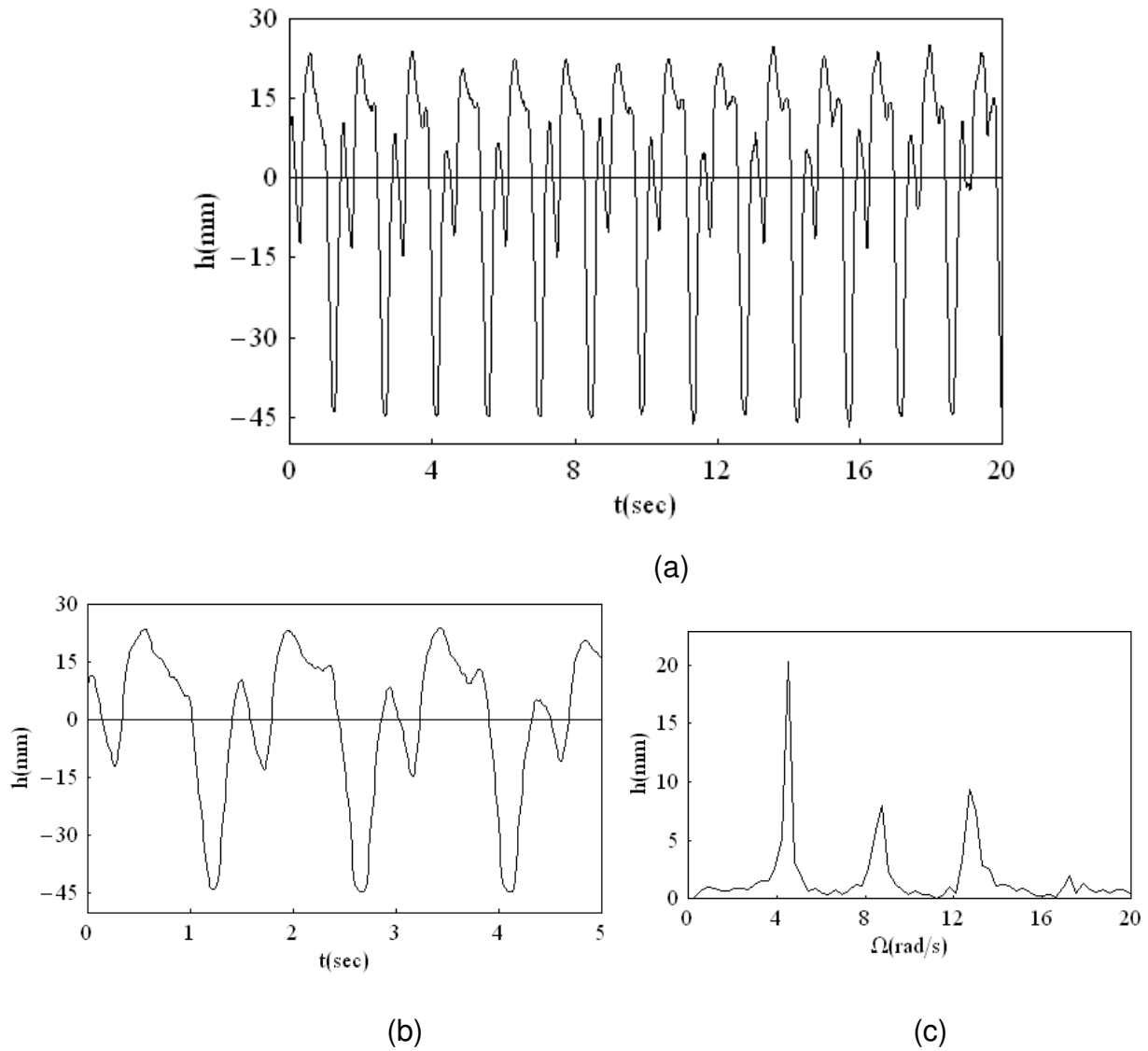


Figure 5.21. Free surface wave at wave maker motor speed $N_m = 2.2$ rad/s :
 (a) time history record of the water free surface, (b) magnification of few cycles showing the wave profile, and (c) FFT plot.

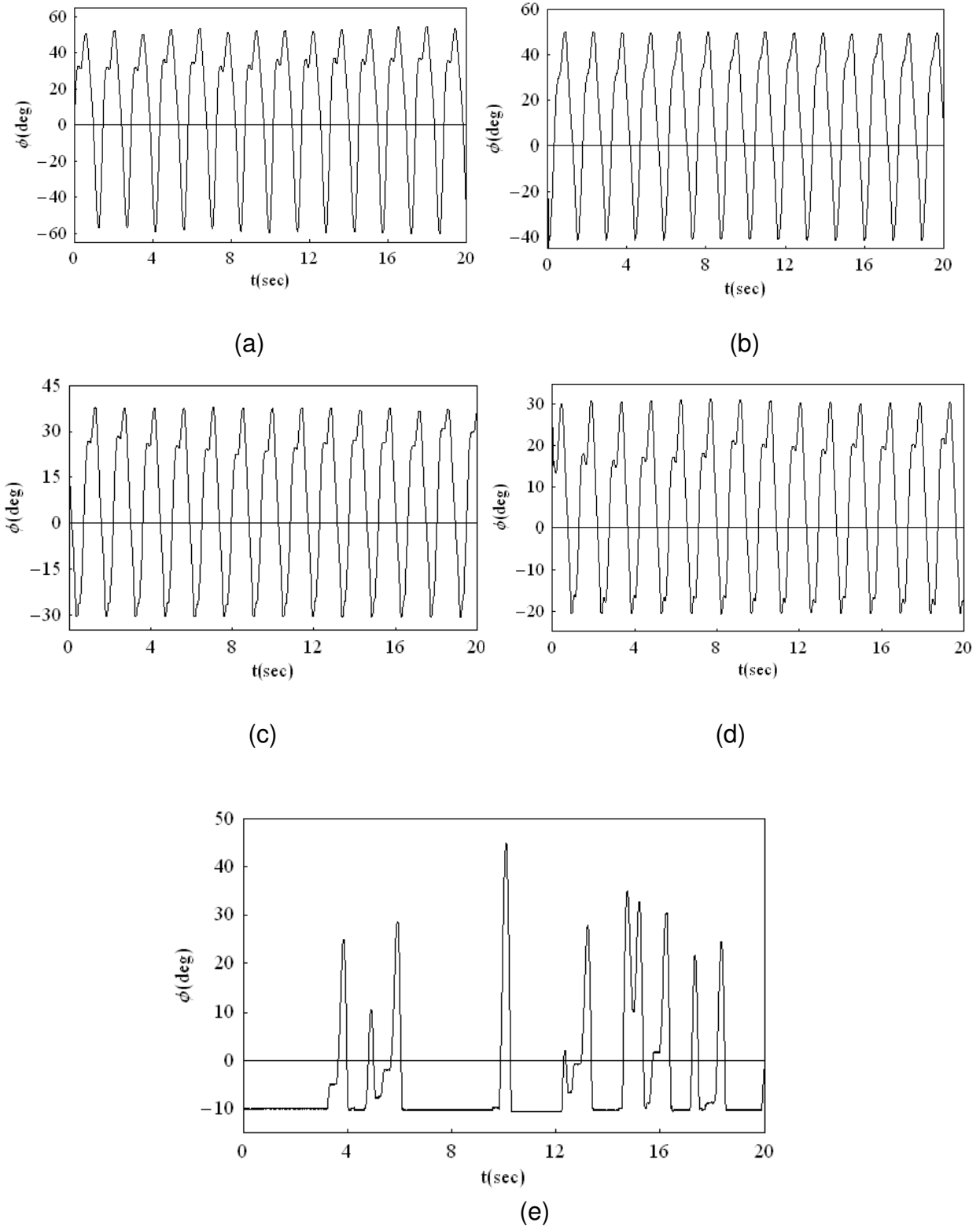


Figure 5.22. Measured time history records of the model response under motor speed $N_m = 2.2$ rad/s : (a) in the absence of barrier, (b) in the presence of one-sided barrier at -40° , (c) at -30° , (d) at -20° , (e) at -10° .

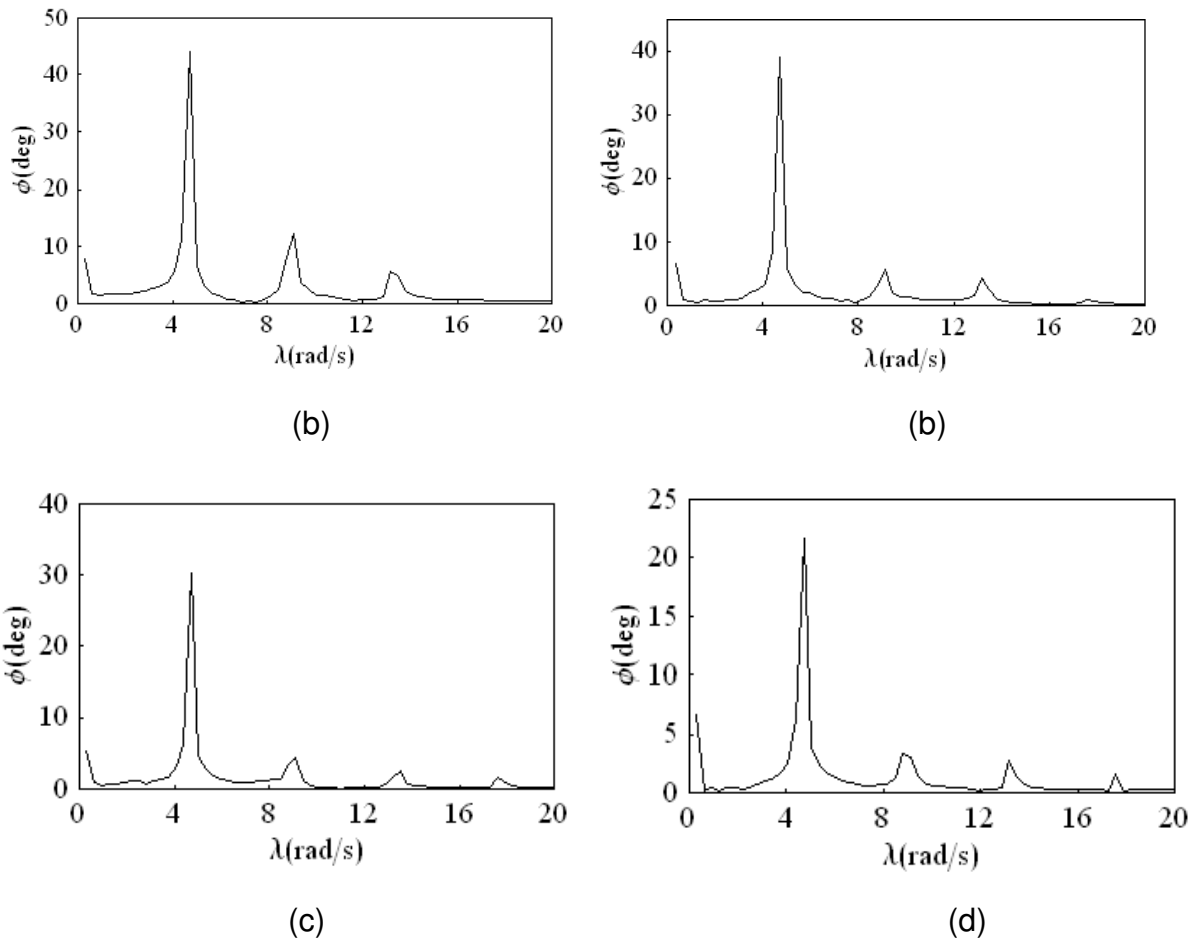


Figure 5.23. FFT plots of the model response of Figure 5.22. under motor speed $N_m = 2.2$ rad/s : (a) in the absence of barrier, (b) in the presence of one-sided barrier at -40° , (c) at -30° , and (d) at -20° .

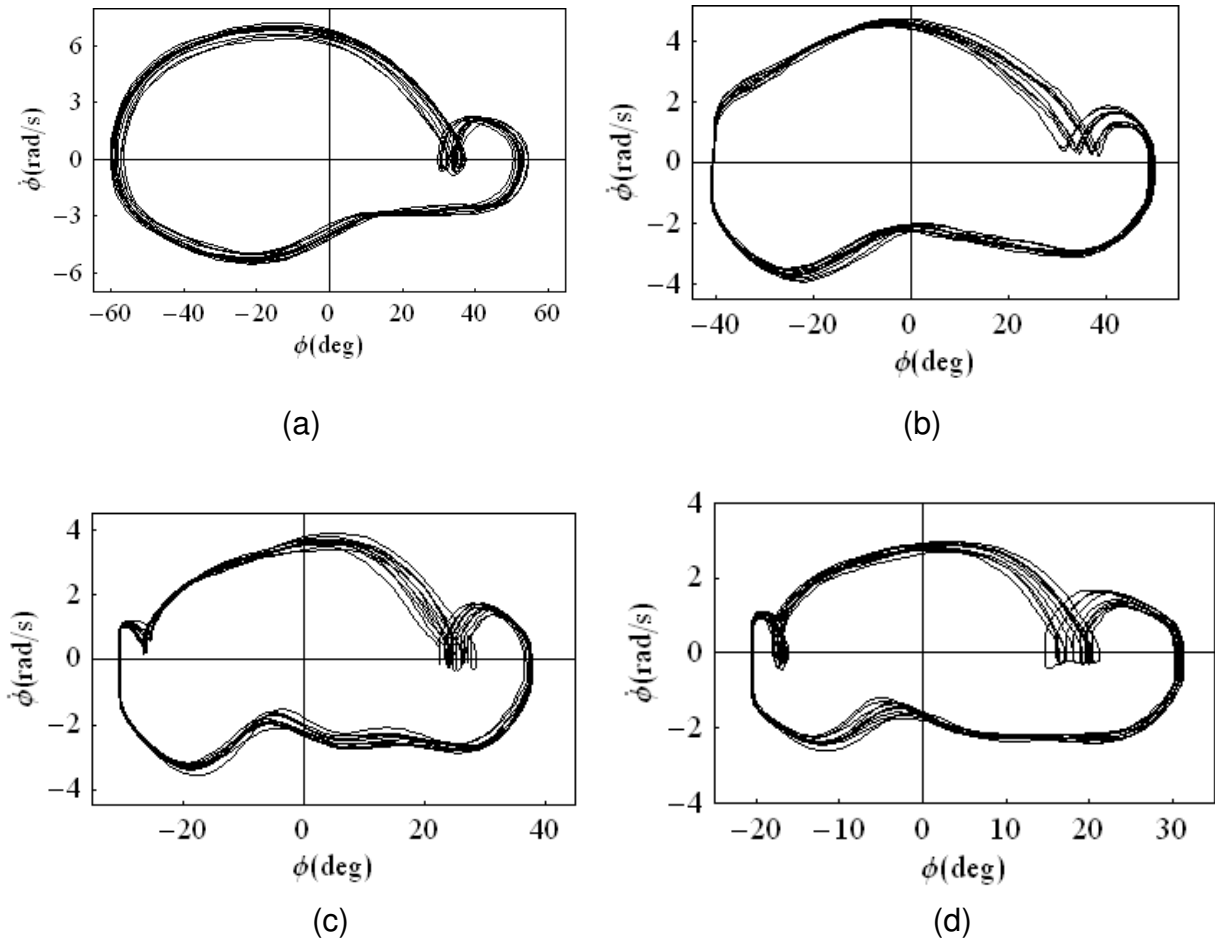


Figure 5.24. Phase trajectory projections of the model response of Figure 5.22 under motor speed $N_m = 2.2$ rad/s : (a) in the absence of barrier, (b) in the presence of one-sided barrier at -40° , (c) at -30° , and (d) at -20° .

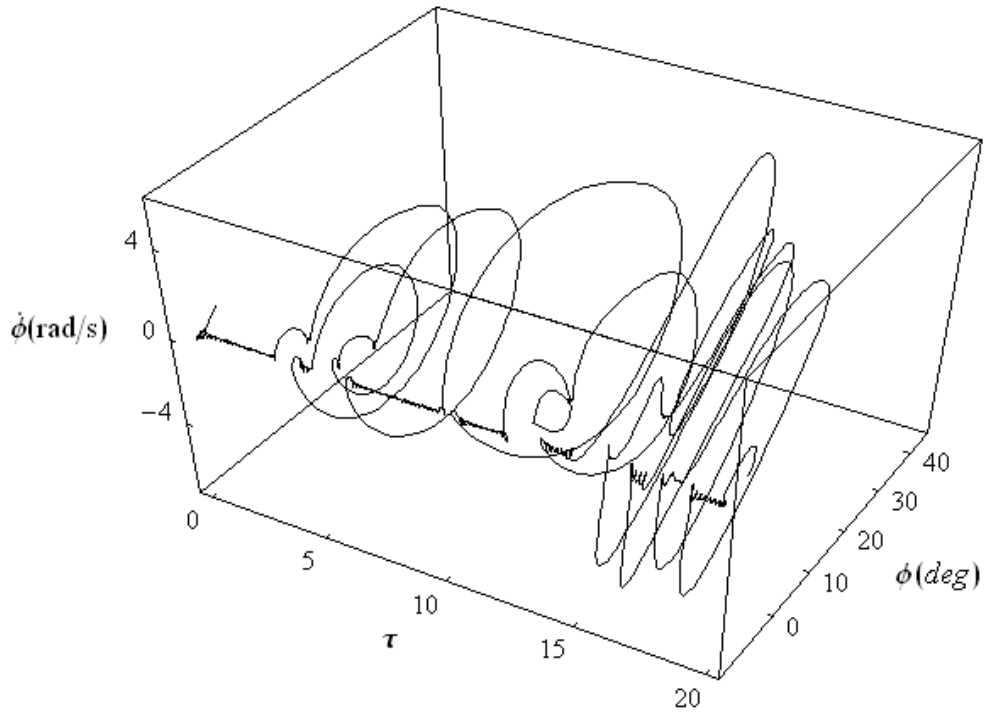


Figure 5.25. Phase trajectory projections of the model response of Figure 5.22(e) under motor speed $N_m = 2.2$ rad/s in the presence of one-sided barrier at -10° .

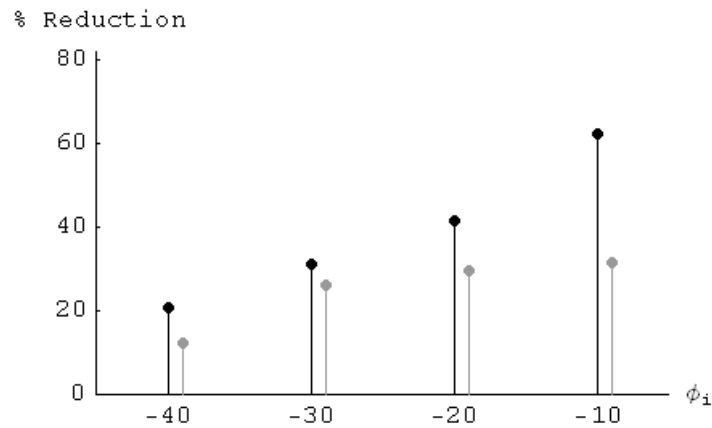


Figure 5.26. % Reduction in response amplitude vs impact angle. Black: $N_m = 2.4$ rad/s, and Gray: $N_m = 2.8$ rad/s.

5.5 Comparing Experimental Results to Analytical Solutions

The main purpose of this section is to compare the analytical results to the experimental ones in order to determine the usefulness of the analytical approaches. The nonlinear equation of motion of ship roll given in chapter 3 by equation (3.2) needs to be modified to account for possible influence of the dry friction damping between the ship model and the shaft about which the model rolls, in addition to the magnetic sensor resistance. Since the friction force acts in an opposite direction to the velocity, as well as the magnetic sensor resistance, one may define a total effective dry friction moment N_{eff} of constant amplitude and the opposite direction to the velocity, see Figure 5.27. Hence, the dry friction damping term may be written as $N_{eff} \text{sgn}(\dot{\phi})$, where N_{eff} can be identified experimentally. Adding the dry friction damping term to equation (3.2), the equation of motion becomes

$$\ddot{\phi} + 2\zeta\omega_n\dot{\phi} + N_{eff}\text{sgn}(\dot{\phi}) + a\dot{\phi}|\dot{\phi}| + \omega_n^2\phi + c_3\phi^3 + c_5\phi^5 = \xi(t) \quad (5.12)$$

The excitation moment $\xi(t)$ can be represented as follows (see Senjanovic, et al. 1997, and Liqin et al., 2007)

$$\xi(t) = \alpha_0\omega_n^2\pi\sum_{i=1}^N\frac{\eta_i}{\lambda_i}\text{Cos}(\Omega_i t + \varepsilon_i) \quad (5.13)$$

where α_0 is the effective wave slope coefficient, η_i is wave amplitude of i^{th} component, and ε_i is corresponding phase angle, and λ_i is the wavelength and is given by

$$\lambda_i = \frac{2\pi g}{\Omega_i^2} \quad (5.14)$$

Substituting (5.14) in equation (5.13), gives

$$\xi(t) = \alpha_0 \omega_n^2 \pi \sum_{i=1}^N \frac{\eta_i}{2\pi g} \Omega_i^2 \text{Cos}(\Omega_i t + \epsilon_i) \quad (5.15)$$

Adopting Ivanov transformation for one dimensional case, the following transformation can be used for inelastic impact

$$\phi = S \text{sgn}(S) - \phi_i, \text{ and}$$

$$\dot{\phi} = \text{sgn}(S) [1 - K \text{sgn}(S.V)] V \quad (5.16)$$

where S and V are the new coordinates whose values are not restricted, $K = (1-e)/(1+e)$, and e is the coefficient of restitution. Following same steps as subsection 4.3.1, equation (5.12) is written in terms of S and V coordinates as

$$\dot{S} = [1 - K \text{sgn}(SV)] V, \text{ and}$$

$$\begin{aligned} \dot{V} = & -2\zeta\omega_n V - aV |[1 - K \text{sgn}(S.V)] V| + \text{sgn}(S) \times \left[\frac{1 + K \text{sgn}(SV)}{1 - K^2} \right] \times \\ & \left\{ -\omega_n^2 (S \text{sgn}(S) + \phi_i) - c_3 (S \text{sgn}(S) + \phi_i)^3 - c_5 (S \text{sgn}(S) + \phi_i)^5 - N_{eff} \text{sgn}(\dot{\phi}) + \xi(t) \right\} \end{aligned} \quad (5.17)$$

Equation (5.17) is solved numerically and a comparison with the measured results is carried out. The identification of the coefficients of equation (5.12) is carried out in the following subsections.

5.5.1 IDENTIFICATION OF THE MODEL PARAMETERS

5.5.1.1 Free Vibration Test

A free vibration test is carried out to determine the coefficients of the linear terms; the natural frequency of the ship model ω_n and the linear damping factor ζ . An initial angular displacement $\phi_0 = 10^\circ$ is applied to the ship model; the ship is left to oscillate freely. The response of the ship model is recorded as shown in Figure 5.28.

For small roll angles one can ignore the nonlinearities and equation (5.12) in absence of wave excitation takes the form as

$$\ddot{\phi} + 2\zeta\omega_n\dot{\phi} + \omega_n^2\phi = 0 \quad (5.18)$$

From the free vibration test, the parameters of linear terms can be determined as follows:

- The linear damping factor ζ is

$$\zeta = \frac{\ln(\phi_i / \phi_{i+1})}{2\pi} \quad (5.19)$$

where ϕ_i , and ϕ_{i+1} are the roll amplitude for two successive cycles,

see Figure 5.23.

- The damped natural frequency ω_{nd} is

$$\omega_{nd} = \frac{2\pi}{T_{nd}} \quad (5.20)$$

where T_{nd} is the time period for one cycle of the damped oscillation.

- The undamped natural frequency of the ship model ω_n is

$$\omega_n = \frac{\omega_{nd}}{\sqrt{1-\zeta^2}} \quad (5.21)$$

Referring to free vibration test results shown in Figure 5.28, the values of parameters are calculated as $\zeta = 0.14$, and $\omega_n = 4.2$ rad/sec.

5.5.1.2 Nonlinear Restoring Moment Coefficients

The restoring moment is given by

$$\Gamma(\phi) = \omega_n^2\phi + C_3\phi^3 + C_5\phi^5 \quad (5.22)$$

where the restoring moment vanishes (i.e. $\Gamma(\phi)=0$) at the ship model capsizing angle which is measured with the aid of an angular displacement gauge as $\phi_c = 82^\circ$. Also, the restoring moment vanishes at $\phi = 180^\circ$. Equation (5.22) is solved for $\Gamma(\phi)=0$, and the nonlinear restoring terms are calculated as $C_3 = -10.42 \text{ 1/sec}^2$, and $C_5 = 0.87 \text{ 1/sec}^2$.

5.5.1.3 Coefficient of Restitution

The coefficient of restitution is measured from impact tests described in the previous subsection using the basic definition $e = \phi_+ / \phi_-$, where ϕ_+ and ϕ_- are the ship model velocities just after and before impact, respectively. In most engineering applications, the coefficient of restitution has been assumed to be a constant that depends on the geometry and material properties of colliding bodies. However, in the present experimental investigation it is found the coefficient of restitution e depends also on the velocity just before impact and its value is unrepeatably in every cycle and in every test. Some studies in other applications have confirmed this observation. For example, in impact analysis of multibody dynamics, Schiehlen and Seifried (2007) showed that the multiple impacts in every test are the source of uncertainty of the coefficient of restitution and depend on the velocity. It was shown that for the case of rod impacts, the coefficient of restitution decreases monotonically with increasing initial velocity. Ronsse and Sepulchre (2006) showed that the acceleration of the table with a bouncing ball at impact is an important parameter for the robustness of the feedback system to model uncertainty, in particular to the uncertainty on the coefficient of restitution. Figure 5.29 shows the scatter of the

coefficient of restitution. The curve fitting of the measured points reveal a monotonic decrease with the coefficient of restitution and dependence on the velocity of the model just before impact velocity. The curve fitting is based on selecting the exponential form

$$e = \text{Exp}\left\{c_1|\dot{\phi}_-| + c_2|\dot{\phi}_-|^2\right\} \quad (5.23)$$

where c_1 and $c_2 < 0$ which satisfy the boundary conditions: $e = 1$ at $|\dot{\phi}_-| = 0$, and $e = 0$ at $|\dot{\phi}_-| = \infty$. The reason for selecting function (5.23) is that it provides a natural and smooth transition between the two asymptotic limits. For motor speed $N_m = 2.4$ rad/s, the average value of the coefficient of restitution estimated from the time history records shown in Figures 5.13(b)-(e) is found $e = 0.73$. This value is adopted for the numerical simulation.

5.5.1.4 Forced Vibration Test

In order to determine the nonlinear damping coefficient a and the effective friction parameter N_{eff} , the test results at motor speed $N_m = 2.4$ rad/s given in Figures 5.12, 5.13(a) and 5.14(a) are used. System (5.17) is solved numerically for different values of a and N_{eff} , and the value of a and N_{eff} are chosen to minimize the error in response when compared to the experimental result given in Figure 5.31(a). Such parameter optimization procedure gives $a = 0.05$, and $N_{eff} = 0.84$ 1/sec².

5.5.2 NUMERICAL SIMULATION

A comparison between experimental results and numerical simulation adopting Ivanov transformation is carried out. For wave excitation generated by motor speed $N_m = 2.4 \text{ rad/s}$, and impact angle $\phi_i = -40^\circ$, the wave amplitude history record shown in Figure 5.12(c) is represented as sum of harmonic wave amplitudes;

$$\sum_{i=1}^N h_i \text{Cos}(\Omega_i t + \varepsilon_i)$$
 A comparison between FFT corresponding to the experimental record and that corresponding to Fourier series representation is shown in Figure 5.30. It can be seen that Fourier series representation perfectly agrees with the experimental data. A comparison between experimental results and numerical simulations based on the parameters determined equations (5.17) are solved numerically to predict the model response. Figure 5.31 shows the time history records of the steady state response measured experimentally and those predicted numerically for different barrier positions. Figure 5.32 shows the FFT plots related to Figure 5.31 and both plots reveal multi-periodic response with the same frequency components. However, It is seen that the predicted amplitude in both time history record and FTT plot is larger than the measured one. Such deviation may be attributed to the uncertainty in the coefficient of restitution.

5.6 Closing Remarks

This chapter presented an experimental investigation conducted on a ship model impacting with a stationary one-sided barrier. A series of experiments were conducted to study the influence of impact on the ship's roll motion. Experiments showed that the impact of the ship with the barrier reduced the amplitude of

response, i.e., the impact of a ship roll with a rigid barrier acted as damper, hence, was helpful to the ship motion provided it does not result in a structural damage of the ship. In this case, the ship outer surface must be equipped with a layer of isolated material.

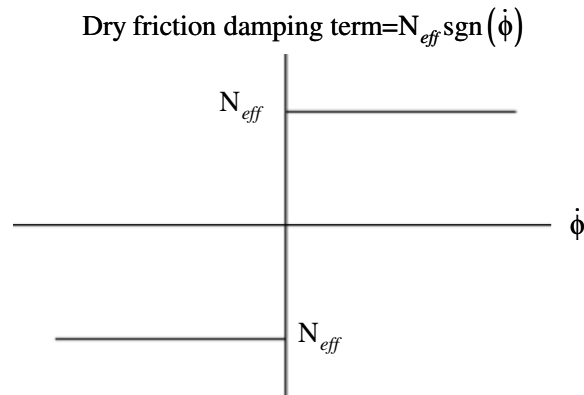


Figure 5.27. Dry friction damping term.

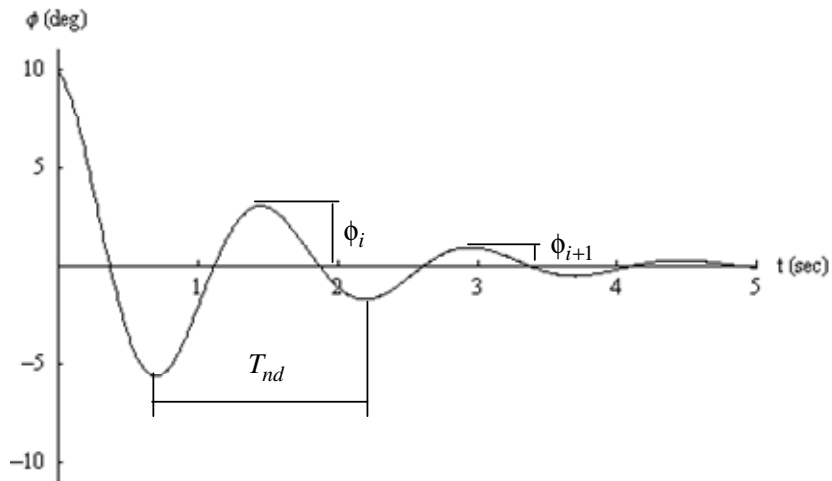


Figure 5.28. Free vibration test result.

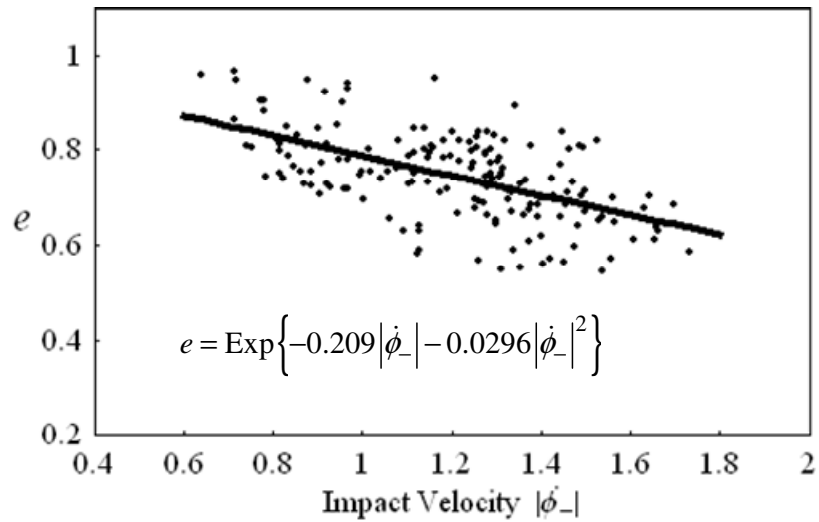


Figure 5.29. Dependence of the coefficient of restitution on the impact velocity (with the fitting curve is: $e = \text{Exp}\{-0.209|\dot{\phi}_-| - 0.0296|\dot{\phi}_-|^2\}$)

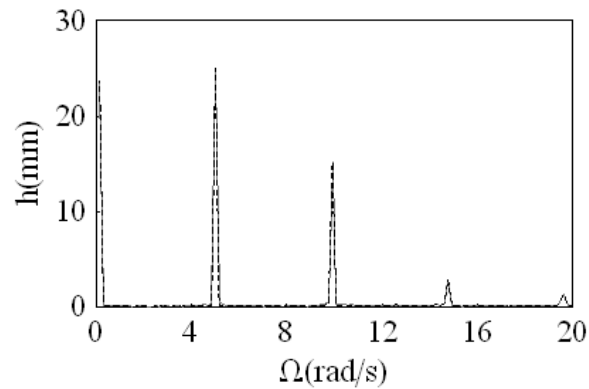


Figure 5.30. FFT of excitation waves corresponding to — Experimental record, and - - - - - Fourier series representation.

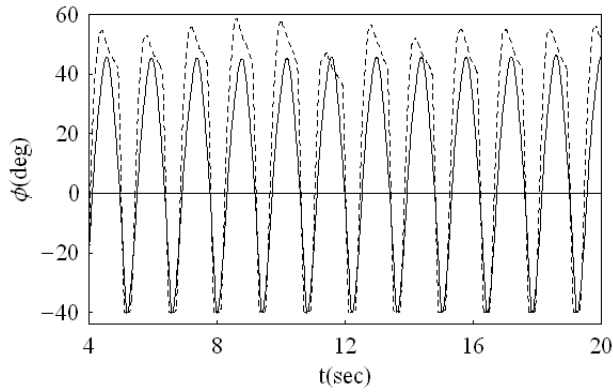
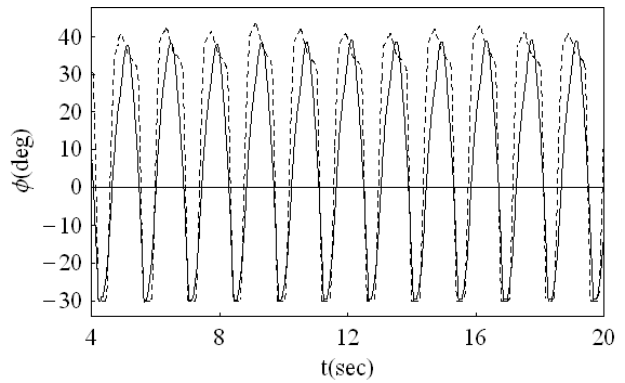
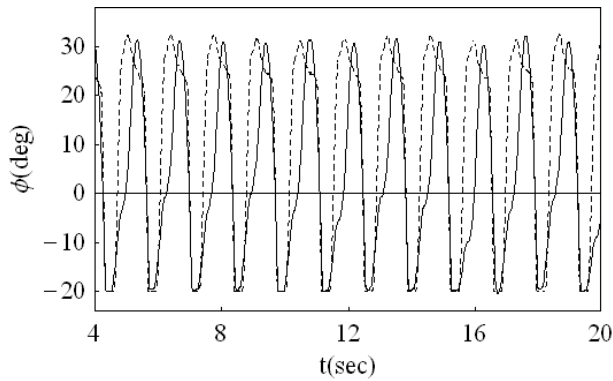
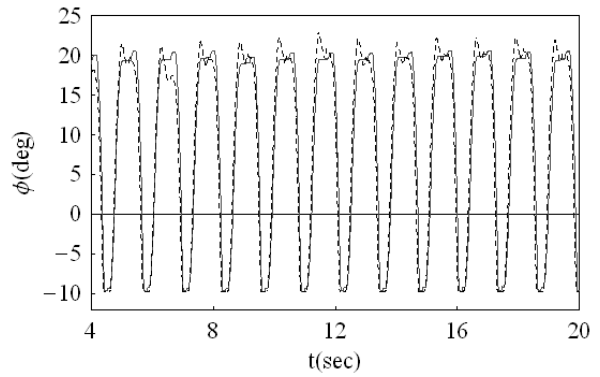
(a) $\phi_i = -40^\circ$ (b) $\phi_i = -30^\circ$ (c) $\phi_i = -20^\circ$ (d) $\phi_i = -10^\circ$

Figure 5.31. Comparison between measured and predicted time-history record of ship response for $N_m = 2.4$ rad/s and different barrier positions, — experimental measurement, and - - - numerical simulation.

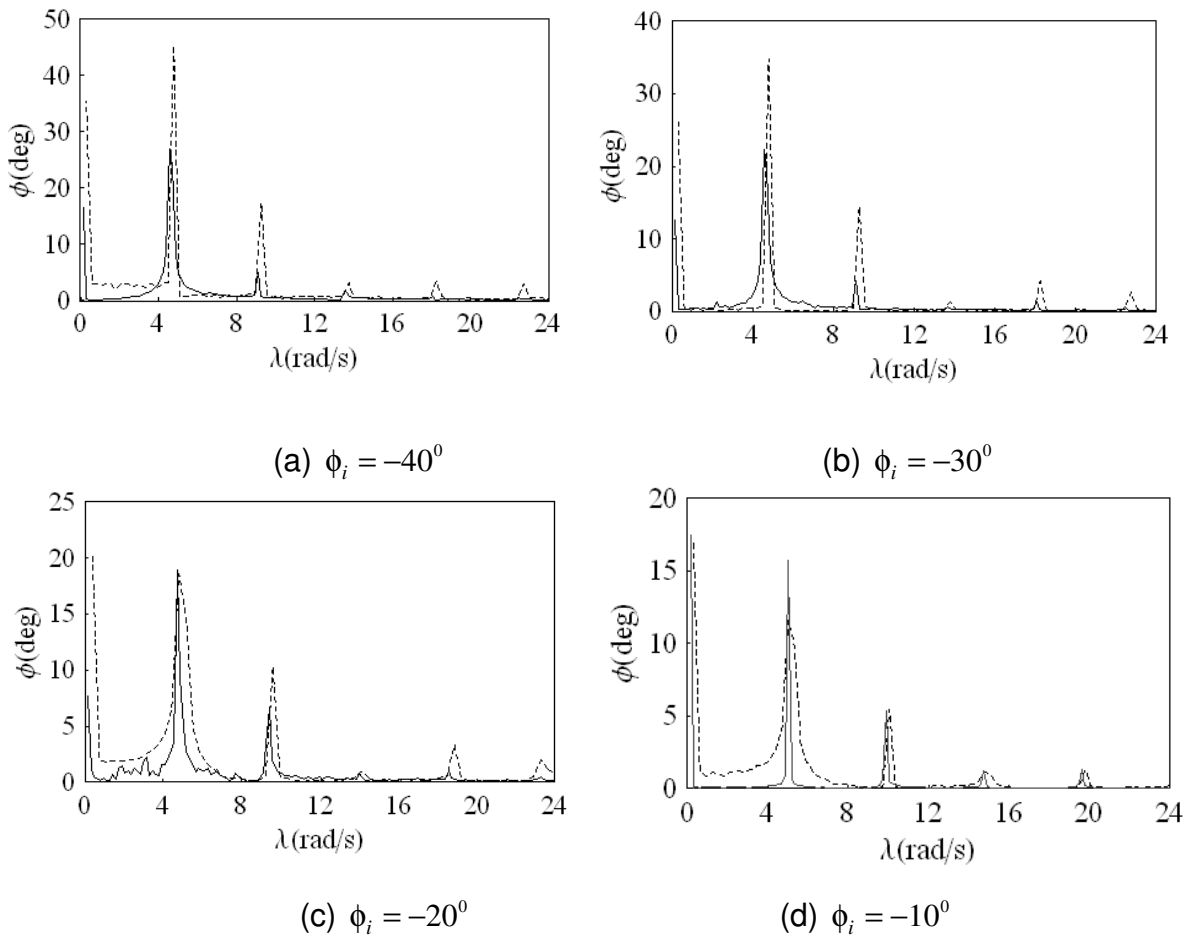


Figure 5.32. Comparison between measured and predicted results FFT of ship time history responses shown in Figure 5.31. for $N_m = 2.4$ rad/s and different values of barrier position.
 — experimental measurement, and - - - - numerical simulation.

CHAPTER 6
CONCLUSIONS AND RECOMMENDATIONS
FOR FUTURE RESEARCH

The dynamic behavior of ship roll motion under both elastic and inelastic impact with a stationary one-sided barrier was studied. Different analytical models of ship roll motion interacting with one-sided barrier were developed. First, an analytical model of ship roll motion interacting with a rigid barrier was developed based on Zhuravlev (1976) non-smooth coordinate transformation. The impact was considered purely elastic (i.e. no energy loss due to impact). This transformation has the advantage of converting the vibro-impact oscillator into an oscillator without barriers such that the corresponding equation of motion does not contain any impact term, hence reducing time required for numerical simulation. Following conclusions were observed:

- The dynamic behavior of ship roll motion under impact depends on excitation parameters and initial conditions. Different response regimes such non-impact periodic oscillations, modulation impact motion, period added impact oscillations, chaotic impact motion and unbounded rollover dynamics (ship capsizing) were observed.
- For a certain excitation frequency, there exists a critical value of excitation amplitude above which the stability fraction decreases. As the excitation amplitude increases the stability fraction decreases until it reaches a zero.
- As the excitation frequency ratio increases, the excitation amplitude leading to ship capsizing decreases. This is attributed to the fact that less force is

required to cause large response amplitude as the excitation frequency increases.

In case of inelastic impact, different analytical models of ship roll motion interacting with stationary ice were developed. Two models of ship roll motion interacting with ice were developed. Model 1 adapted Zhuravlev (1976) non-smooth coordinate transformation. This transformation effectively applies to the positional coordinates with further adaptation to account for impact damping. Model 2 adopted Ivanov (1994) transformation that incorporates the impact damping effect through the transformation itself. Such a combined approach gave the basis for analyses of possible variations in dynamic behaviors due to different models of impact damping, including the most direct way of spreading the energy loss over the full cycle of vibration through the effective equivalent damping. The following conclusions were observed:

- Additional damping associated with inelastic impact plays an important role in ship response and results in reducing the ship tendency for capsizing when compared to purely elastic impact.
- The results obtained from the two models were found almost identical for water waves of relatively small amplitude. However, model 1 was found to yield more conservative stability regions than those of model 2.
- Model 2 and Runge-Kutta solutions are in good agreement, on the other hand, Model 1 solution experiences slight deviation from the other solutions. This deviation increases as the coefficient of restitution decreases. This is due to the fact that Model 1 provides approximate description for the energy

loss at the barrier, and is justified only for large values of the coefficient of restitution, i.e. $(1-e) \ll 1$. However, for other cases, Model 2 gives more accurate description.

- A comparison between direct numerical simulations using Runge-Kutta method, solutions for model 2 and the equivalent damping model under different system parameters were found to reveal that the applicability of equivalent damping depends on different parameters; such as excitation frequency, excitation amplitude, coefficient of restitution, and position of the barrier. Generally, the error appears to be very small for relatively large coefficient of restitution. Therefore, general qualitative analyses of system dynamic states must be conducted before any equivalent damping is used for modeling.

Experimental investigation on a ship model interacting with a stationary barrier was conducted using the towing tank. Experiments showed that the impact of the ship with the barrier reduces the amplitude of response, i.e., the impact of a ship roll with a rigid barrier acted as damper, hence, was helpful to the ship motion. A comparison between analytical and experimental results was carried out in order to determine the usefulness of the analytical models. For small angles of the barrier relative to the ship unbiased position, the solutions predicted by the analytical approaches showed good agreement with the experimental measurements. As the impact angle increases, predicted results showed some deviation from the measured results. This deviation is mainly attributed to the uncertainty of the coefficient of restitution, which is found to depend on the velocity of impact in

addition to the geometry and material properties of the model and barrier. The importance of this study is that it shows the usefulness of analytical approaches in studying impact of ship roll dynamics with rigid barriers. This saves time and high cost required by experimental analysis.

The present research did not address the influence of stochasticity of ocean waves and ice impact loads. This is a potential topic for future research. It was reported in the literature that ice loads are of impact type and have been assumed as a Poisson arrival process of loading events. Thus, one must deal with probabilistic approaches when studying ships' stochastic stability, response, and reliability. The treatment can be carried out using one of the available techniques such as:

- The path integral method (Köylüoğlu et al., 1995),
- Monte Carlo simulation, and
- Equivalent linearization method.

These techniques are well documented by Dimentberg (1988) and Ibrahim (2009). Strongly related to repeated impact is the structural integrity and health monitoring. Structural health monitoring of ship structure whether metallic or composite is another open area particularly in cold regions.

APPENDIX A

A list of the main terms of naval architecture terminology is provided as follows (see Figure A.1):

Aft: Toward the stern of the boat.

Beam: The width of a vessel; also a structural component. Both Uses come from the Anglo-Saxon word beam, meaning, "tree,"

Beam Sea: Sea coming on the side of the ship.

Bilge: The lower point of inner hull of a ship.

Bow: The forward part of a boat. The word may come from the Old Icelandic bogr, meaning "shoulder"

Broach: The action of turning a vessel broadside to the waves.

Broadside: Presenting the side of the ship.

Buoyancy: The upward push of water pressure, equal to the weight of the volume of water the ship displaces (W).

Capsize: To turn over.

Center of Buoyancy (B): The geometric center of the submerged hull, acting vertically upward.

Center of Flotation (F): The geometric center of the waterline plane, about which the ship trims fore-and-aft.

Center of Gravity (G): The center of all mass of the ship, acting vertically downward.

Displacement Volume (V): The volume of the underwater hull at any given waterline.

Displacement (W): The weight of water of the displaced volume of the ship, which equals the weight of the ship and cargo.

Draft: The depth of water a boat draws.

Fathom: Six feet.

Following Sea: Sea coming on the stern.

Forecastle: Pronounced "fo'c's'l", and usually now spelled that way. Now the foredeck of a vessel, the term originally referred to a raised and fortified platform at the ship's bow. Used by archers in combat at sea as early as the 13th century.

Freeboard: That part of a ship's sides above water, from the Anglo-Saxon *fram-bord*, meaning 'the frame's side.'

Head: (1) The uppermost or forward-most part of a ship (or of some specific part of a ship, such as the masthead, beakhead, stemhead, or whatever.

(2) The bathroom. In the age of sail, the crew was quartered forward in the forecastle, and their latrine was located on the beakhead, over hanging the water (for obvious reasons).

Heading: The direction in which a vessel's bow points at any given time.

Headway: The forward motion of a boat. Opposite of sternway.

Heel: Constant roll angle - such as caused by a side wind or turning of the vessel.

Hull: The main body of a vessel.

Keel: The centerline of a boat running fore and aft; the backbone of a vessel.

Knot: A measure of speed equal to one nautical mile (6076 feet) per hour.

Lee: The side sheltered from the wind.

Leeward: The direction away from the wind. Opposite of windward.

Leeway: The sideways movement of the boat caused by either wind or current.

List, Heel, and Roll: It is both a noun and a verb referring to a ship's upping to one side or the other due to poor trim, shifting cargo, or sinking. The word comes from the Anglo-Saxon *lystan*, meaning "to lean". Angular transverse inclinations. List describes a static inclination such as list due to side damage. Heel describes a temporary inclination generally involving motion, such as wind or turning, while roll indicates periodic inclination from side to side such as wave action.

Metacenter (M): When the ship is inclined at small angles, the metacenter is the intersection of the buoyant force with the ship centerline. If the metacenter is above the center of gravity then the ship is stable.

Midship: Approximately in the location equally distant from the bow and stern.

Nautical Mile: One minute of latitude; approximately 6076 feet: about 1/8 longer than the statute mile of 5280 feet.

Naval Architecture: Ship design: especially hull design, overall layout with attention to stability, sea-keeping and strength.

Port: The left side of a boat looking forward.

Quarter: The sides of a boat aft of amidships.

Quarter Sea: Sea coming on a boat's quarter.

Reserve Buoyancy: The watertight volume between the waterline and the uppermost continuous watertight deck.

Starboard: The right side of a boat when looking forward.

Stern: The rear of any vessel. The word came from the Norse Stjorn (pronounced "Stjorn"), meaning "steering". It is the after part of the boat.

Thwartships: means across the ship.

Trim: Longitudinal tilt. Stern draft - bow draft

Wake: Moving waves, track or path that a boat leaves behind it, when moving across the waters.

Waterline: A line painted on a hull which shows the point to which a boat sinks when it is properly trimmed

Way: Movement of a vessel through the water such as headway, sternway or leeway.

Windward: Toward the direction from which the wind is coming.

Yaw: To swing or steer off course, as when running with a quartering sea.

Definition of incident wave directions is given in Figure A.2.

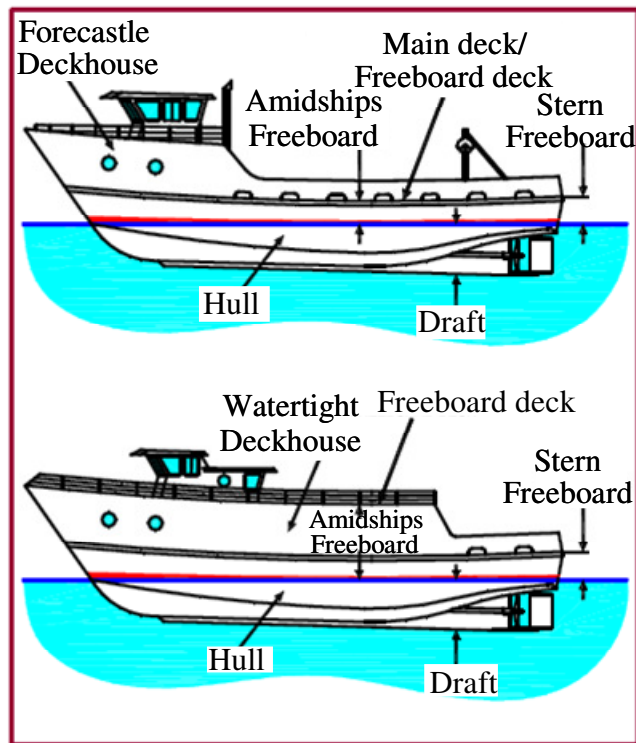


Figure A.1. Key parts of a ship structure.

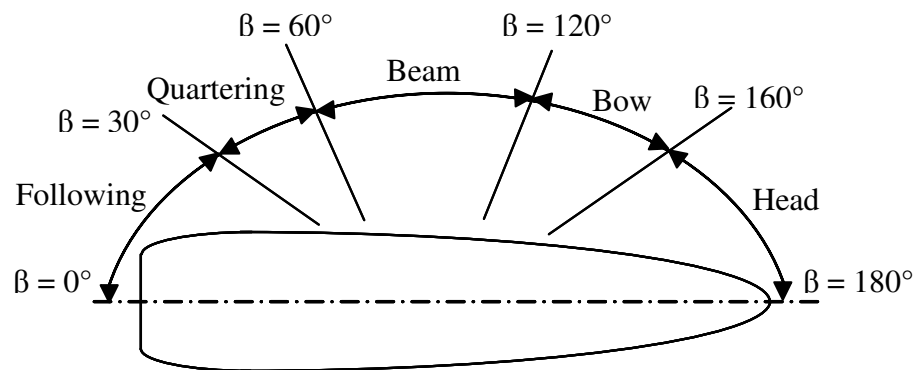


Figure A.2. Definition of incident wave directions.

APPENDIX B

The wavelet transform of a continuous time signal, $x(t)$, is obtained by using discrete values of the dilation (or scale) s , and time translation u of the wavelet function $\Psi_{u,s}(t)$. The wavelet transform of a continuous signal, $x(t)$, using discrete wavelets is

$$T_{u,s}x(u,s) = \int_{-\infty}^{\infty} x(t)\Psi_{u,s}(t)dt \quad (\text{B.1})$$

where, $\Psi_{u,s}(t)$ is a wavelet function for which the family

$$\Psi_{u,s}(t) = \frac{1}{\sqrt{s}}\Psi\left(\frac{t-u}{s}\right) \quad (\text{B.2})$$

forms an orthonormal basis. By choosing an orthonormal wavelet basis, $\Psi_{u,s}$, one can reconstruct the original signal in terms of wavelet coefficients, $T_{u,s}$, using the inverse discrete wavelet transform as follows

$$x(t) = \sum_{s=-\infty}^{+\infty} \sum_{u=-\infty}^{+\infty} T_{u,s}\Psi_{u,s}(t) \quad (\text{B.3})$$

Orthonormal dyadic discrete wavelets are associated with scaling functions, $\phi_{u,s}(t)$, which have the same form as the wavelet functions described by equation (B.3)

$$\phi_{u,s}(t) = \frac{1}{\sqrt{s}}\phi_{u,s}\left(\frac{t-u}{s}\right) \quad (\text{B.4})$$

A continuous approximation signal $x(t)$ at scale index s can be generated as a sum of a sequence of scaling functions at the scaling factor by the approximation coefficients as follows, (see, e.g. Addison, 2002),

$$x_s(t) = \sum_{s=-\infty}^{+\infty} S_{u,s} \phi_{u,s}(t) \rightarrow x(t) \text{ as } s \rightarrow -\infty \quad (\text{B.5})$$

where $S_{u,s}$ are the *approximation coefficients* and $x_s(t)$ is a smooth scaling-function-dependent version of the original signal $x(t)$ at scale index s . The scaling functions can be convoluted with the signal to produce the approximation coefficients

$$S_{u,s} = \int_{-\infty}^{\infty} x(t) \phi_{u,s}(t) dt \quad (\text{B.6})$$

The continuous approximation given by equation (6) approaches $x(t)$ at small scales, i.e., as $s \rightarrow -\infty$. In the present work, the *Morlet wavelet*, is adopted and is defined by the expression (Addison, 2002)

$$\Psi(t) = \pi^{-1/4} \left[e^{i2\pi f_0 t} - e^{(2\pi f_0)^2} \right] e^{-t^2/2} \quad (\text{B.7})$$

where f_0 is the central frequency of the mother wavelet. The second term in the brackets is known as the correction term, as it corrects for the non-zero mean of the complex sinusoid of the first term. In practice it becomes negligible for values of $f_0 \gg 0$ can be ignored, in which case, the Morlet wavelet can be written in a simpler form as

$$\Psi(t) = \frac{1}{\pi^{1/4}} e^{i2\pi f_0 t} e^{-t^2/2} \quad (\text{B.8})$$

The Morlet wavelet is simply a complex wave within a Gaussian envelope, $e^{-t^2/2}$. The real and imaginary sinusoids, $e^{i2\pi f_0 t}$, differ in phase by a quarter period. The $\pi^{1/4}$ term is a normalization factor which ensures that the wavelet has unit energy. Note that the function given by equation (B.4) is not really a wavelet as it has a non-

zero mean, i.e., the zero frequency term of its corresponding energy spectrum is non-zero and hence it is inadmissible, however, it can be used in practice with $f_0 \gg 0$ with minimal error. The graphical representation of the wavelet transform in time-scale plane is referred to as *scalogram* and it reveals the time evolution of the signal frequency. If the wavelet is complex, then the square modulus represents the energy density distribution of the signal over the time-scale plane.

REFERENCES

- [1] Abkowitz, M. A., 1964, "Lectures on Ship Hydrodynamics - Steering and Maneuverability," Technical Report Hy-5. Hydro and Aerodynamics Laboratory. Lyngby, Denmark.
- [2] Abkowitz, M. A., 1975, "System Identification Techniques For Ship Maneuvering Trials," *Proceedings of Symposium on Control Theory and Navy Applications. Monterey, California*, 337-393.
- [3] Abkowitz, M. A., 1980, "Measurements of Hydrodynamic Characteristics From Ship Maneuvering Trials By System Identification," *Transactions of the Society of Architects and Marine Engineering (SNAME)*, **88**, 283-314.
- [4] Abrate, S., 1998, *"Impact on Composite Structures,"* Cambridge University Press, Cambridge, UK.
- [5] Aboulazm, A. F., 1989, *"Ship Resistance in Ice Floe Covered Waters,"* PhD Dissertation, Memorial University of Newfoundland, Canada.
- [6] Aboulazm, A. F., and Williams, A. N., 1992, "Approximation of Interference Effects and Dynamic Ice-structure Interactions," *Journal of Offshore Mechanics and Arctic Engineering*, **114**(4), 299-309.
- [7] Aldwinckle, D. S., and Lewis, K. J., 1984, "Prediction of Structural Damage, Penetration and Cargo Spillage due to Ship Collisions with Icebergs," *SNAME Ice Tech'84*, Calgary, **D**, 1-14.
- [8] Arnold, L., Chueshov, I., and Ochs, G., 2004, "Stability and Capsizing of Ships in Random Sea - A Survey," *Nonlinear Dynamics*, **36**, 135-179.
- [9] Arockiasamy, M., El-Tahan, H., Swamidas, A. S. J., Russell, W. E. and

- Reddy, D. V., 1984, "Semi Submersible Response to Transient Ice Forces," *Ocean Engineering* **11**(5), 463-490.
- [10] Bass, D., Gaskill, H., and Riggs, N., 1985, "Analysis of Iceberg Impact With Gravity-base Structures at Hibernia," *Proceedings of the 4th International Conference on Offshore Mechanics and Arctic Engineering (OMAE'85)* **3**, 255-259.
- [11] Bass, D. W. and Haddara, M. R., 1987, "On the Modeling Of The Nonlinear Damping Moment For Tthe Rolling Motion Of a Ship," *Proceedings of the International Association of Scientific Technology (IASTED) Symposium: Identification, Modeling and Simulation, Paris, France*, 346-349.
- [12] Bass, D. W. and Haddara, M. R., 1988, "Nonlinear Models Of Ship Roll Damping," *International Shipbuilding Progress*, **35**(401), 5-24.
- [13] Bhat, S. U., 1988, "Analysis of Splitting of Ice Floes During Summer Impact," *Cold Regions Science and Technology* **5**(1), 53-63.
- [14] Bhattacharya, R., 1978, "*Dynamics of Marine Vehicles*," John Wiley & Sons, New York.
- [15] Bishop, R. D., and Price, W. G., 1978, "Note on Structural Damping of Ship Hulls," *Journal of Sound and Vibration*, **56**(4), 495-499.
- [16] Bjerkas, M., 2006, "Wavelet Transforms and Ice Actions on Structures," *Cold Regions Science and Technology*, **44**, 159-169.
- [17] Blenkarn, K. A., 1970, "Measurements and Analysis of Ice Forces on Cook Inlet Structures," *Proceedings of Offshore technology Conference (OTC)*, Houston, Texas, 1261, **II**, 365-378.

- [18] Bryan, G. H., 1900, "The Action of Bilge Keels," *Transactions of the Institute of Naval Architects*, **42**, 198-239.
- [19] Bulian, G., 2005, "Nonlinear Parametric Rolling in Regular Waves - A General Procedure for the Analytical Approximation of the GZ Curve and its Use in Time Domain Simulations," *Ocean Engineering*, **32**, 309-330.
- [20] Cai, G. Q. and Lin Y. K., 1994, "On Statistics of First-passage Failure," *ASME Journal of Applied Mechanics*, **61**, 93-99.
- [21] Cai, G. Q., Yu, J. S., Lin, Y. K., 1994, "Ship Rolling in Random Sea," In *Stochastic Dynamics and Reliability of Nonlinear Ocean Systems*, Ibrahim, R. A., and Lin, Y. K. (eds.), *ASME WAM GE*, **77**.
- [22] Cammaert, A. B. and Muggeridge, D. B., 1988, "*Ice Interaction with Offshore Structures*," Van Nostrand Reinhold, New York.
- [23] Cammaert, A. B. and Tsinker, G. P., 1981, "Impact of Large Ice Floes and Icebergs on Marine Structures," *Proceedings of the International Conference on Port and Ocean Engineering under Arctic Conditions-POAC'81*, **2**, 653-662.
- [24] Cammaert, A. B., Wong, T. T., and Curtis, D. D., 1983, "Impact of Icebergs on Offshore Gravity and Floating Platforms," *Proceedings of the International Conference on Port and Ocean Engineering under Arctic Conditions-POAC*, **4**, 519-536.
- [25] Cardo, A., 1982, "On damping models in free and forced rolling motion," *Ocean Engineering*, **9** (2), 171-179.
- [26] Chakrabarti, S., 2001, "Empirical Calculations of Roll Damping for Ships and

- Barges," *Ocean Engineering*, **28**, 915-932.
- [27] Chu, H., 1998, "Numerical Modeling of Ship Motions in Shallow Water Waves," Ph.D. Thesis, Florida Institute of Technology, Florida.
- [28] Chung, J. S. and Bernitsas, M. M., 1997, "Hydrodynamic Memory Effect on Stability, Bifurcation, and Chaos of Two-point Mooring Systems," *Journal of Ship Research*, **41**(1), 26-44.
- [29] Contento, G., Francescutto, A., and Piciullo, M., 1996, "On the Effectiveness of Constant Coefficients Roll Motion Equation," *Ocean Engineering*, **23**(7), 597-618.
- [30] Croasdale, K. R. and Marcellus, R. W., 1981, "Ice Forces on Large Marine Structures," *Proceedings of International Association of Hydraulic Engineering and Research (IAHR) Symposium on Ice*, **2**, Quebec, 755-765.
- [31] Cummins, W. E., 1962, "The Impulse Response Function and Ship Motions," *Schiffstechnik* **9**.
- [32] Curtis, D. D, Cammaert, A. B., Wong, T. T., and Bobby, W., 1984, "Numerical Analysis of Impact of Small Icebergs on Semi-submersibles," Int. Spec. Conf. Cold Regions Eng., Edmonton.
- [33] Daley, C. G. Philips, L. D., McCallum, J. S., 1986, "Dynamic Ship/Ice Impact; Results of Parametric Model Testing," *Proceedings of the 1st International Conference on Ice Technology*, Cambridge, MA., 349-363.
- [34] Dalzell, J. F., 1978, "A Note on the Form of Ship Roll Damping," *Journal of Ship Research*, **22**, 178-185.
- [35] De Kat, J. O., Paulling, J. R., 1989, "The Simulation of Ship Motions and

- Capsizing in Severe Seas,” *Transactions of the Society of Architects and Marine Engineering (SNAME)*, **117**, 127-135.
- [36] Denise, J. F., 1983, “On the Roll Motion of Barges,” *Transactions of the Royal Institution of Naval Architects (RINA)*, **125**, 255-268.
- [37] Dimentberg, M. F., 1988, “*Statistical Dynamics of Nonlinear and Time-Varying Systems*,” Wiley, New York.
- [38] Duthinh, D. and Marsden, S., 1986, “Iceberg Impact Load on a Gravity-Based Structure,” *Proceedings of the 4th International Conference on Cold Regions Engineering*, Anchorage, Alaska, 82-92.
- [39] Edward, L. V., 1989, “*Principles of Naval Architecture*,” The Society of Naval Architects and Marine Engineers, Jersey City, New Jersey.
- [40] El-Bassiouny, A. F., 2007, “Nonlinear Analysis for a Ship with a General Roll-Damping Model,” *Physica Scripta*, **75**, 691-701.
- [41] El-Tahan, H., Swamidas, A. S., Arockiasamy, M., and Reddy D. V., 1984, “Strength of Iceberg and Artificial Snow Ice Under High Strain Rates and Impact Loads,” *Proceedings of the International Offshore Mechanics and Arctic Engineering*, New Orleans, **3**, 158-165.
- [42] El-Tahan, H., Swamidas, A. S., and Arockiasamy, M. 1985, “Response of Semi-Submersible Models to Bergy-Bit Impact,” *Proceedings of the International Conference on part and Ocean Engineering under Arctic Conditions (POAC)*, Narssarssuaq, 544-554.
- [43] Eranti, E., 1992, “Ice Forces in Dynamic Ice Structure Interaction,” *International Journal of Offshore and polar Engineering*, **2**(3), 204-211.

- [44] Falzarano, J. and Zhang, F., 1993, "Multiple Degree-of-freedom Global Analysis of Transient Ship Rolling Motion," *ASME Winter Annual Meeting*, New York, Nonlinear Dynamics of Marine Vehicles, DSC **51**, 57-72.
- [45] Fossen, T. I., 1994, "*Guidance and Control of Ocean Vehicles*," John Wiley & Sons, New York.
- [46] Fossen, T. I., 2002, "*Marine Control Systems: Guidance, Navigation and Control of Ships, Rigs and Underwater Vehicles*," Marine Cybernetics AS. Trondheim, Norway, ISBN 82-92356-00-2.
- [47] Francescutto, A. and Contento, G., 1999, "Bifurcations in Ship Rolling: Experimental Results and Parameter Identification Technique," *Ocean Engineering* **26**(11), 1095-1123.
- [48] Francescutto, A., Contento, G., Biot, M., Schiffrer, L., and Caprino, G., 1998, "Effect of Excitation Modeling in the Parameter Estimation of Nonlinear Rolling," *Proceedings of the 8th International Offshore and Polar Engineering Conference*, Montreal, Canada, **3**, May 24-29, 490-498.
- [49] Francescutto, A., Serra, A., and Scarpa, S., 2001, "A Critical Analysis of Weather Criterion for Intact Stability of Large Passenger Vessels," *Proceedings of the International Conference on Offshore Mechanics and Arctic Engineering - OMAE* **1**, 829-836.
- [50] Frederking, R., and Timco, G., 2000, "Sea Ice Floes-Large Scale Basin Experiments," *Proceedings of the 10th International Offshore and Polar Engineering Conference*, **1**, 640-645.
- [51] Froude, W. 1863, "Remarks on Mr. Scott Russell's Paper on Rolling,"

- Transactions of the Institute of Naval Research*, **4**, 232-275.
- [52] Fuglem, M., Muggeridge, K. and Jordaan, I. J., 1999, "Design Load Calculations for Iceberg Impacts," *Interactional Journal of Offshore and Polar Engineering*, **9**, 298-306.
- [53] Gagnon, R., 2004a, "Physical Model Experiments to Assess the Hydrodynamic Interaction Between Floating Glacial Ice Masses and a Transiting Tanker," *ASME Journal of Offshore Mechanics and Arctic Engineering*, **126**, 297-309.
- [54] Gagnon, R., 2004b, "Analysis of Laboratory growler impact tests," *Cold Regions Science & Technology*, **39**, 1-17.
- [55] Gaskill, H. S., and Rochester, J., 1984, "A New Technique for Iceberg Drift Prediction," *Journal of Cold Regions and Science Technology*, **8**, 223-234.
- [56] Gu, J. Y., 2004, "Nonlinear Rolling Motion of Ship in Random Beam Seas," *Journal of Marine Science and Technology*, **12**(4), 273-279.
- [57] Gu, J. Y., 2006a, "Calculation of Ship Rolling Probability using a New Path Integration Method," *Chuan Bo Li Xue/Journal of Ship Mechanics*, **10**(6), 43-52.
- [58] Gu, J. Y., 2006b, "Probability Analysis of Ship Nonlinear Roll-motion Excited by White Noise," *Chuan Bo Li Xue/Journal of Ship Mechanics*, **10**(3), 17-25.
- [59] Haddara, M. R., 1971, "On the Stability of Ship Motion in Regular Oblique Waves," *International Ship Building Progress*, **18**(207), 416-434.
- [60] Haddara, M. R., 1975, "A Study of Stability of the Mean and Variance of Rolling Motion in Random Waves." *Proceedings of the International*

Conference on Stability of Ships and Ocean Vehicles, University of Strathclyde, Glasgow.

- [61] Haddara, M. R., 1983, "Note on the Power Spectrum of Nonlinear Rolling Motion," *International Shipbuilding Progress*, **30**(342), 41-44.
- [62] Haddara, M. R., 1992, "On the Random Decrement for Nonlinear Rolling Motion," *Proceedings of the 11th International Offshore Mechanics and Arctic Engineering Symposium*, **2**, Safety and Reliability, Calgary, Alberta, 321-324.
- [63] Haddara, M. R. and Zhang, Y., 1994, "On the Joint Probability Density Function of Nonlinear Rolling Motion," *Journal of Sound and Vibration*, **169**(4), 562-569.
- [64] Himeno, Y., 1981, "Prediction of Ship Roll Damping: State-of-the-Art," Report No. 239, Department of Naval Architecture and Marine Engineering, The University of Michigan, Ann Arbor, MI, September.
- [65] Hishida, T., 1952, "Study on the Wave Making Resistance for Rolling Ships, Parts 1 and 2," *Journal of Society of Naval Architecture of Japan*, **85**, 45-61.
- [66] Hishida, T., 1954, "Study on the Wave Making Resistance for Rolling Ships, Parts 3 and 4," *Journal of Society of Naval Architecture of Japan*, **86**, 277-283.
- [67] Hishida, T., 1955, "Study on the Wave Making Resistance for Rolling Ships, Parts 5 and 6," *Journal of Society of Naval Architecture of Japan*, **87**, 67-68.
- [68] Huang, G., and Liu P., 2009, "A Dynamic Model for Ice-Induced Vibration of Structures," *Journal of Offshore Mechanics and Arctic Engineering*, **131**, 1-6.
- [69] Huang, X., Gu, X., and Bao, W., 1994, "The Probability Distribution of Rolling

- Amplitude of a Ship in High Waves," *5th International Conference on Stability of Ships and Ocean Vehicles*, Melbourne, Florida.
- [70] Hwang, W. Y., 1980, "*Application of System Identification to Ship Maneuvering*," Ph.D. Dissertation, Massachusetts Institute of Technology, Cambridge, MA.
- [71] Ibrahim, R. A., 2005, "*Liquid Sloshing Dynamics: Theory and Applications*," Cambridge University Press, Cambridge, U.K.
- [72] Ibrahim, R. A., 2009, "*Vibro-Impact Dynamics: Modeling, Mapping and Applications*," *Lecture Notes in Applied and Computational Mechanics* **43**, Springer-Verlag, Berlin.
- [73] Ibrahim, R. A., Chalhoub, N. G., and Falzarano, J., 2007, "Ice Interaction with Ships and Ocean Structures and their Control," *ASME Applied Mechanics Reviews* **60**(5), 246-289.
- [74] Ibrahim, R. A., and Grace, I. M., 2010, "Modeling of Ship Roll Dynamics and its Coupling with Heave and Pitch," *Mathematical Problems in Engineering* 2010 (934714), 1-32.
- [75] Ikeda, Y., 1984, "Roll Damping of Ships," (in Japanese) *Proceedings of Ship Motions, Wave Loads and Propulsive Performance in a Seaway*, First Marine Dynamics Symposium, The Society of Naval Architecture in Japan, 241-250.
- [76] Ikeda, Y., Fujiwara, T. and Katayama, T., 1993, "Roll Damping of a Sharp-cornered Barge and Roll Control by a New-type Stabilizer," *Proceedings of the 3rd International Offshore and Polar Engineering Conference*, Singapore, 634-539.

- [77] Ikeda, Y., Himeno, Y. and Tanaka, N., 1978a, "Components of Roll Damping of Ships at Forward Speed," (in Japanese), Report No. 00404, Department of Naval Architecture, University of Osaka Prefecture, Osaka, Japan (August); (also in *Journal of Society of Naval Architecture of Japan*, **143**).
- [78] Ikeda, Y., Himeno, Y. and Tanaka, N., 1978b, "A Prediction Method for Ships Roll Damping," (in Japanese), Report No. 00405, Department of Naval Architecture, University of Osaka Prefecture, Osaka, Japan.
- [79] Isaacson, M., and Mc-Taggart, K., 1990, "Influence of Hydrodynamic Effects in Iceberg Collisions," *Canadian Journal of Civil Engineering*, **17**, 329-337.
- [80] Ivanov, A. P., 1994, "Impact Oscillations: Linear Theory of Stability and Bifurcations," *Journal of Sound and Vibrations*, **178**, 361-378.
- [81] Izumiyama, K. Kitagawa, H., Koyama, K., and Uto, S., 1996, "On the Interaction between the Conical Structure and Ice Sheet," *Proceedings of the 11th International Conference on Port and Ocean Engineering under Arctic Conditions, POAC*, St. John's Newfoundland, **1**, 155-166.
- [82] Izumiyama, K., Irani, M.P., Timco, G.W., 1994, "Influence of Compliance of Structure on Ice Load," *Proceedings of the 12th International Symposium on Ice*, **1**, 229-238.
- [83] Jebaraj, C., Swamida, A. S. J., and Shih, L. Y., 1988, "Numerical Modeling of Ship/ice Interaction," *ASME Petroleum Division (Publication), Offshore and Arctic Operations Symposium*, Jan 22-25, Houston, TX **26**, 199-205.
- [84] Jiang, C., Troesch, A. W., and Shaw, S. W., 1996, "Highly Nonlinear Rolling Motion of Biased Ships in Random Beam Seas," *Journal of Ship Research*,

- 40(2)**, 125-135.
- [85] Jiang, C., Troesch, A. W. and Shaw, S. W., 2000, "Capsize Criteria for Ship Models with Memory Dependent Hydrodynamics and Random Excitation," *Philosophical Transactions of the Royal Society London*, **A 358**, 1761-1791.
- [86] Jiang, T., Schellin, T. E., and Sharma, S.D., 1997, "Maneuvering Simulation of a Tanker Moored in a Steady Current Including Hydrodynamic Memory Effect and Stability Analysis," *Proceedings of the Royal Institution of Naval Architects (RINA) International Conference on Ship Maneuvering*, London.
- [87] Jin, D. P., and Hu, H. Y., 1998, "Ice Induced Nonlinear Vibration of an Offshore Platform," *Journal of Sound and Vibration*, **214(3)**, 431-442.
- [88] Johnson, R. J., and Prodanovic, A., 1989, "Calculations of Iceberg Impact Forces," *Proceedings of the International Conference on Port and Ocean Engineering under Arctic Conditions-POAC'89*, **2**, 546-556.
- [89] Jones, H., 1978, "Bilge Keel Size Investigation for an Attack Aircraft Carrier (CVA-41)," David Taylor Model Basin Technical Report, West Bethesda, DTNSRDC/SPD-0861-01.
- [90] Jones, H., 1979, "Bilge Keel Size Investigation for an Attack Aircraft Carrier and VSTOL (Vertical Short Takeoff and Landing)," David Taylor Model Basin Technical Report, West Bethesda, DTNSRDC/SPD-0861-02.
- [91] Jones, S. J., 2007, "A Review of the Strength of Iceberg and Other Freshwater Ice and the Effect of Temperature," *Journal of Cold Regions Science and Technology*, **47**, 256-262.
- [92] Jordaan, I. J., 2001, "Mechanics of Ice-Structure Interaction," *Journal of*

- Engineering Fracture Mechanics*, **68**, 1923-1960.
- [93] Jordann, I. J., 2001, "Mechanics of Ice-structure Interaction," *Engineering Fracture Mechanics*, **68**, 1923-1960.
- [94] Källström, C. G. and Åström, K. J., 1981, Experience of System Identification Applied to Ship Steering," *Automatica*, **17**(1), 187-198.
- [95] Kärnä, T., 1992, "A Procedure for Dynamics Soil-structure-ice Interaction," *Proceedings 2nd International Offshore and Polar Energy Conference (ISOPE'92)*, San Francisco, **II**, 764-770.
- [96] Kärnä, T., 2001, "Simplified Modeling of Ice-Induced Vibrations of Offshore Structures," *Proceedings of 16th International Symposium on Okhotsk Sea & Sea Ice*, Mombetsu, Japan, 114-122.
- [97] Kärnä, T., and Turunen, R., 1990, "A Straightforward Technique for Analyzing Structural Response to Dynamic Ice Action," *Proceedings of the 9th International Conference on Offshore Mechanics and Arctic Engineering (OMAE)*, Houston, **4**, 135-142.
- [98] Kärnä, T., Jochmann, P., Maattanen, M., Evers, K. U., Kolari, K., Xiangjun, B., and Martonen, P., 2003, "Tests on Dynamic Ice-structure Interaction," *Proceedings of the 22nd International Conference on Offshore Mechanics and Arctic Engineering - OMAE, Materials Technology Ocean Engineering Polar and Arctic Sciences and Technology Workshops*, Jun 8-13, 2001, Cancun, Mexico, **3**, 823-829.
- [99] Kärnä, T., Kamesaki, K., and Tsukuda, H., 1990, "A Numerical Model for Dynamic Ice-structure Interaction," *Computer and Structures*, **72**, 645-658.

- [100] Kärnä, T., Kamesaki, K. and Tsukuda, H. 1999, "A Numerical Model for Dynamic Ice-Structure Interaction," *Journal of Computers and Structures*, **72**, 645-658.
- [101] Karr, D. G., Troesch, A. W., and Wingate, W. C., 1992, "Nonlinear Dynamic Response of a Simple Ice-structure Interaction Model," Proceedings of the 11th International Conference on Offshore Mechanics and Arctic Engineering-Symposium, 4, Arctic/Polar Technology, Calgary, Alberta, 231-237.
- [102] Kato, H., 1965, "Effect of Bilge Keels on the Rolling of Ships," *Journal of Society of Naval Architecture of Japan*, **117**, 93-114.
- [103] Khalid, M. S., 2007, "*Simulation of Euler Equations of Motion and Blended - Nonlinear Hydrodynamics for Multi-Hulled Vessels*," PhD. Thesis, University of Michigan, Ann Arbor, Michigan.
- [104] Kinney, W. D., 1961, "On the Unstable Rolling Motions of Ships Resulting from Nonlinear Coupling with Pitch Including the Effect of Damping in Roll," Institute of Engineering Research, University of California, **173**(3), Berkeley, California.
- [105] Kirchhoff, G., 1869, "*Advanced Engineering Mathematics*," John Wiley & Sons, New York.
- [106] Koehler, P. E., and Jorgensen, L., 1985, "Ship Ice Impact Analysis," *Proceedings of the International Offshore Mechanics and Arctic Engineering Symposium*, **2**, 344-350.
- [107] Köylüoğlu, H. U., Nelson, S. R. K., and Iwankiewicz, R., 1995, "Response and Reliability of Poisson-Driven Systems by Path Integration," *ASCE Journal of*

Engineering Mechanics **12**(1), 117-130.

- [108] Kreider, J. R., 1984, "Summer Ice Impact Loads from Multiyear Floes," *Proceedings of International Association of Hydraulic Engineering and Research (IAHR) Symposium on Ice*, Hamburg, **2**, 55-66.
- [109] Kwon, S. H., Kim, D. W., Chung, H., 1993, "Application of Path Integral Solution to Ship Rolling Motion," *Proceedings 3rd International Offshore and Polar Engineering Conference (ISOPE)*, Singapore, **3**, 657-660.
- [110] Lansbury, A. N., Thompson, J. M., and Stewart, H. B., 1992, "Basin Erosion in the Twin-well Duffing Oscillator: Two Distinct Bifurcations Scenarios," *Journal of Bifurcation and Chaos*, **2**, 505-532.
- [111] Lee, Y., 2001, "Non Linear Ship Motion Models to Predict Capsize in Regular Beam Seas," Ph.D. Thesis, University of Michigan, Ann Arbor, Michigan.
- [112] Lewandowski, E. M., 2004, "The Dynamics of Marine Craft Maneuvering and Seakeeping," *Advanced Series on Ocean Engineering*, **2**, Worldscientific, Singapore.
- [113] Lin, H., and Yim, S. S., 1995, "Chaotic Roll Motion and Capsize of Ships under Periodic Excitation with Random Noise," *Applied Ocean Research*, **17**(3), 185-204.
- [114] Lin, R-Q., and Kuang, W., 2006, "Numerical Modeling of Nonlinear Interactions Between Ships And Surface Gravity Waves II: ship boundary conditions," *Journal of Ship Research*, **50**(2), 181-186.
- [115] Lin, R-Q., and Kuang, W., 2008, "Modeling Nonlinear Roll Damping with Self-Consistent, Strongly Nonlinear Ship Motion Model," *Journal of Marine*

Science and Technology, **13**, 127-137.

- [116] Lin, R-Q., Kuang, W., Reed, A. M., 2005, "Numerical Modeling of Nonlinear Interactions between Ships and Surface Gravity Waves I: ship waves in calm water," *Journal of Ship Research*, **49**(1),1-11.
- [117] Lin, W. M. and Salvesen, N., 1997, "Nonlinear Time-domain Simulation of Ship Capsizing in Beam Seas," Final Report, *Science Applications International Corp.*, Annapolis, MD.
- [118] Lin, W. M., Meinhold, M. J., and Salvesen, N., 1998, "Nonlinear Time-Domain Simulation of Fishing Vessel Capsizing in Quartering Seas," *Science Applications International Corp.*, Annapolis, MD, Report SAIC-CG-D-17-98.
- [119] Liqin, L. and Yougang, T., 2007, "Stability of Ships with Water on Deck in Random Beam Waves," *Journal of Vibration and Control*, **13**(3), 269-280.
- [120] Liu, L. Q., Tang, Y. G., and Li, H. X., 2007, "Stochastic Chaotic Motion of Ships in Beam Seas," *Journal of Marine Science and Technology*, **15**(2), 123-128.
- [121] Liu, L. Q., Tang, Y.G., Zheng, H. Y., and Gu, J. Y., 2006, "Analysis Method of Capsizing Probability in Time Domain for Ships in Random Beam Waves," (in Chinese) *Tianjin Daxue Xuebao (Ziran Kexue yu Gongcheng Jishu Ban)/Journal of Tianjin University Science and Technology*, **39**(2), 165-169.
- [122] Liu, y., Wu, Y., Song, L., Shen, Z., and Duan, M., 2001, "A Dynamic Model for Ice-Structure Interaction," *Proceedings of 20th Conference on Offshore Mechanics and Arctic Engineering*, **1**, 29-36.
- [123] Lloyd, A. M., 1989, "*Seakeeping - ship Behavior in Rough Weather*," Ellis

Howood, Chichester, U.K.

- [124] Luk, C. H., 1984, "In-Plane Ice Structure Vibration Analysis by Two-Dimensional Elastic Wave Theory," *Journal of Energy Resources Technology*, **106**, 160-168.
- [125] Määttänen, M., 1978, "On Conditions for the Rise of Self-Excited Ice Induced Autonomous Oscillations in Slender Marine Pile Structures," Finnish-Swedish Winter Navigation Research Board, Research Report No. 25.
- [126] Määttänen, M., 1980, "Ice Force on Fixed, Flexible Structure," A State-of-the-art report by Working group on Ice Forces on Structures," *International Association of Hydraulic Engineering and Research (IAHR)*, U.S. Army Cold Regions Research and Engineering Laboratory, Hanover, NH 03755, Special Report 80-26, ASA 089674.
- [127] Määttänen, M., 1981, "Ice Structure Dynamic Interaction - Ice Forces Versus Velocity, Ice-induced Damping," Proceedings of Quebec 1981 International Association of Hydraulic Research International Symposium on Ice Problems, 27-31 July, Quebec, Canada, Laval University, 783-796.
- [128] Määttänen, M., 1983, "Dynamic Ice-structure Interaction during Continuous Crushing," U.S. Army Cold Regions Research and Engineering Laboratory, Hanover, NH 03755, CREL Report 83-5.
- [129] Maes, M. A. and Jordaan, I. J., 1984, "Probabilistic Analysis of Iceberg Loads on Offshore Structures," *Proceedings of the International Association of Hydraulic Engineering and Research Symposium (IAHR) on Ice*, Haburg, **2**, 175-188.

- [130] Mahfouz, A. B., 2004, "Identification of the Nonlinear Ship Rolling Motion Equation Using the Measured Response at Sea," *Ocean Engineering*, **31**, 2139-2156.
- [131] Manotov, E. and Naess, A., 2009, "An Analytical-numerical Method for Fast Evaluation of Probability Densities for Transient Solutions of Nonlinear Stochastic Differential Equations," *International Journal of Engineering Science*, **47**(1), 116-130.
- [132] Marcellus, R. W., Sander, M., Sinha, N. K., and Shah, V. K., 1990, "A Theoretical Dynamic Ice Structure Interaction Model for Crushing with Extrusion," *Proceedings of 9th Conference on Offshore Mechanics and Arctic Engineering*, Huston, Tx, **IV**, 95-101.
- [133] Martin, M., 1958, "Roll Damping Due to Bilge Keels," Technical Report, Iowa University, Institute of Hydraulics Research, Iowa.
- [134] Mathisen, J. B. and Price, W. G., 1984, "Estimation of Ship Roll Damping Coefficients," *Transactions Royal Institution of Naval Architects (RINA)*, **127**, 295-307.
- [135] Matlock, G., Dawkins, W., and Panak, J., 1971, "Analytical Model for Ice Structure Interaction," *Journal of Engineering Mechanics*, EM4, 1083-1092.
- [136] Matsushi, M., and Ettema, R., 1986, "Model Tests on Dynamic Behavior of a Floating Cable-Moored Platform by Floes of Annual Ice," *Proceedings of the International Conference on Offshore Mechanics and Arctic Engineering Symposium*, Tokyo, **4**, 561-568.
- [137] McCreight, W. R., 1986, "Ship Maneuvering in Waves," *Proceedings 16th*

- Symposium on Naval Hydrodynamics: Ship Wakes; Large Amplitude Waves; Real Fluid Effects in Ship Hydrodynamics; Fluid-Structure Interaction; Frontier Problems in Hydrodynamics. Sponsor: US Office of Naval Research, USA; National Research Council, US Naval Studies Board, University of California, Berkeley, 456-469.*
- [138] Meyers, W. G., Sheridan, D. J., and Salvesen, N., 1975, "Manual: NSRDC Ship-Motion and Sea-load Computer Program," *Naval Ship Research and Development Center, Maryland, USA, Report No. 3376.*
- [139] Milne-Thomson, L. M., 1968, "*Theoretical Hydrodynamics,*" MacMillan Education, London.
- [140] Minorsky, V. U., 1959, "An Analysis of Ship Collision with Reference to Protection of Nuclear Powered Plants," *Journal of Ship Research*, **3**, 1-4.
- [141] Moody, C. G., 1961, "The Effect of Bilge Keels on the Roll Damping Characteristics of the Large Bulk-oil Carrier SS World Glory," David Taylor Model Basin Technical Report, West Bethesda, p1515.
- [142] Morison, J. P., O'Brien, M. P., Johnson, J. W., and Schaaf, S. A., 1950, "The Force Exerted by Surface Waves on a Pile," *Petroleum Transactions*, **189**, 149-154.
- [143] Morsy, U.A., and Brown, T. G., 1993, "Modeling for Ice Structure Interactions," *Proceedings of 12th Conference on Offshore Mechanics and Arctic Engineering*, **4**, 119-125.
- [144] Moshchuk, N. K., Ibrahim, R. A., Khasminskii, R. Z., and Chow, P. L., 1995a, "Asymptotic expansion of ship capsizing in random sea waves, Part I: First-

- order approximation," *International Journal of Nonlinear Mechanics*, **30**(5), 727-740.
- [145] Moshchuk, N. K., Khasminskii, R. Z., Ibrahim, R. A., and Chow P., 1995b, "Asymptotic Expansion of Ship Capsizing in Random Sea Waves, Part II: Second-Order Approximation," *International Journal of Nonlinear Mechanics*, **30**(5), 741-757.
- [146] Motter, L. E., 1967, "Ship Motion and Bilge Keel Studies for the CVA," David Taylor Model Basin Technical Report, West Bethesda, OPNAVINST S5513.3A-17.
- [147] Muhuri, P. K., 1980, "A Study of the Stability of the Rolling Motion of a Ship in an Irregular Seaway." *International Shipbuilding Progress*, **27**, 139-142.
- [148] Nayfeh, A. H. and Balachandran, B., 1995, "*Applied Nonlinear Dynamics*," Wiley Series in Nonlinear Science, New York.
- [149] Nayfeh, A. H., and Mook, D. T., 1979, "*Nonlinear Oscillations*," Pure and Applied Mathematics, John Wiley and Sons, New York.
- [150] Nayfeh, A. H., Mook, D. T., and Marchall, L. R., 1973, "Nonlinear Coupling of Pitch and Roll Modes in Ship Motions," *Journal of Hydronautics*, **7**(4), 145-152.
- [151] Nayfeh, A. H., Mook, D. T., and Marshall, L. R., 1974, "Perturbation Energy Approach for the Development of the Nonlinear Equations of Ship Motion," *Journal of Hydronautics*, **8**(4), 130 - 136.
- [152] Nayfeh, A. H., Ragab, S. A., and Al-Maaitah, A. A. 1988, "Effect of Bulges on the Stability of Boundary Layers," *Physics of Fluids*, **31**(4), pp. 796-806.

- [153] Neil, C., 1976, "Dynamic Ice Forces on Piers and Piles: An Assessment of Design Guidelines in Light of Recent Research," *Canadian Journal of Civil Engineering*, **3**, 305-341.
- [154] Nevel, D. E., 1986, "Iceberg Impact Forces," Proceedings of the International Association of Hydraulic Engineering and Research Symposium (IAHR) on Ice, Iowa City, **3**, 345-365.
- [155] Neves, M. A., and Rodriguez, C. A., 2006, "On Unstable Ship Motions Resulting from Strong Nonlinear Coupling," *Ocean Engineering*, **33**, 1853-1883.
- [156] Neves, M. A., and Rodriguez, C. A., 2007, "Influence of Nonlinearities on the Limit Stability of Ships Rolling in Head Seas," *Ocean Engineering*, **34**, 1618-1630.
- [157] Newman, J. N., 1977, "*Marine Hydrodynamics*," The MIT Press, Cambridge, Massachusetts.
- [158] Paulling, J. R. and Rosenberg, R. M. 1959, "On Unstable Ship Motions Resulting from Nonlinear Coupling," *Journal of Ship Research*, **2**, 36-46.
- [159] Pedersen, P. T., Hansen, P. F., and Nielsen L. P., 1996, "Collision Risk and Damage after Collision," RINA International Conference on the Safety of Passenger RoRo Vessels, 1.
- [160] Pedersen, P. T., and Zhang, S., 1998, "On Impact Mechanics in Ship Collisions," *Marine Structures*, **11**, 429-449.
- [161] Perez, T., 2005, "*Ship Motion Control; Course Keeping and Roll Stabilization Using Rudder and Fins*," Advances in Industrial Control, Springer-Verlag,

Berlin.

- [162] Petersen, M. J., 1982, "Dynamics of ship collision," *Ocean Engineering*, **9**(4), 295-329.
- [163] Philips, L., 1994, "*Simulation of Ship-Ice Collision Dynamics*," PhD. Thesis, University of Ottawa, Canada.
- [164] Philips, L., and Tanaka, H., 1994, "Simulation of Ship-Ice Collision Dynamics; Ice Interface Modeling Considerations," *Journal of Marine, Offshore and Ice Technology*, 295-302.
- [165] Pontryagin, L. S., Andonov, A. A., and Vitt, A. A., 1933, "On Statistical Consideration of Dynamical Systems," *Journal of Experimental and Theoretical Physics*, **3**(3), 165-172.
- [166] Price, W. G. and Bishop, R. E., 1974, "*Probabilistic Theory of Ship Dynamics*," Chapman and Hall, London.
- [167] Price, W.G., 1975, "A Stability Analysis of the Roll Motion of a Ship in an Irregular Seaway." *International Shipbuilding Progress*, **22**, 103-112.
- [168] Ralph, F., McKenna, R., and Gagnon, R., 2008, "Iceberg Characterization for the Bergy-Bit Impact Study," *Journal of Cold Regions Science and Technology*, **52**, 7-28.
- [169] Robert, J. B., 1982, "Effect of Parametric Excitation on Ship Rolling Motion in Random Waves," *Journal of Ship Research*, **26**, 246-253.
- [170] Roberts, J. B., 1982a, "A Stochastic Theory for Nonlinear Ship Rolling in Irregular Seas," *Journal of Ship Research*, **26**(4), 229-245.
- [171] Roberts, J. B., 1982b, "Effect of Parametric Excitation on Ship Rolling

- Motion," *Journal of ship Research*, **26**(4), 246-253.
- [172] Roberts, J. B., and Dacunha, N. C., 1985, "Roll Motion of a Ship in Random Beam Waves: Comparison between Theory and Experiment," *Journal of Ship Research*, **29**, 112-126.
- [173] Rong, Z., 1994, "*Studies of Weak and Strong Nonlinear Sea Loads on Floating Marine Structures*," Thesis, NEI-NO-465, Norges Tekniske Hoegskol, Trodheim.
- [174] Ronsse, R., Sepulchre, R., 2006, "Feedback Control of Impact Dynamics: The Bouncing Ball Revisited," *Proceedings 45th IEEE Conference on Decision and Control*, San Diego, CA, 4807-4812.
- [175] Ross, A., 2009, "*Nonlinear Maneuvering Models for Ships: a Lagrangian Approach*," Ph.D. Thesis, Norwegian University of Science and Technology, Trondheim, Norway.
- [176] Salvaggio, M. A., and Rojansky, M., 1986, "The Importance of Wave-driven Icebergs Impacting an Offshore Structure," *Proceedings of the Offshore Technology Conference OTC'86*, Paper OTC 5086, **1**, 29-38.
- [177] Salvesen, N., 1979, "Five Years of Numerical Naval Ship Hydrodynamics at DTNSRDC," David W. Taylor Naval Ship Research and Development Center, Bethesda, MD, Report: DTNSRDC-79/082.
- [178] Salvesen, N., Tuck, O. E., and Faltinsen, O., 1970, "Ship Mmotions and Sea Loads," *Transactions Society of Architects and Marine Engineering (SNAME)*, **78**, 250-287.
- [179] Sarpkaya, T. and Isaacson, M., 1981, "*Mechanics of Wave Forces on*

- Offshore Structures*," Van Nostrand Reinhold, New York.
- [180] Schiehlen, W., Seifried, R., 2007, "Impact systems with uncertainty." *Proceedings IUTAM Symposium on Dynamics and Control of Nonlinear Systems*, Springer, Berlin, 33-44.
- [181] Schmiechen, M., 1974, "Zur kollisionsdynamik von Schiffen," Jahrbuch der Schiffbautechnischen Gesellschaft 68.
- [182] Schmiechen, M., 1975, "Equation for Non-Quasi-Steady Ship Motion," Seaking Committee Report, *Proceedings of the 14th International Towing Tank Conference*, Ottawa, Canada.
- [183] Senjanović, I., Ciprić, G., and Parunov, J., 2000, "Survival Analysis of Fishing Vessels Rolling in Rough Seas," *Transactions of the Royal Society of London*, series A, **358**, 1943-1965.
- [184] Senjanović, I., Parunov, J. Ciprić, G, 1997, "Safety Analysis of Ship Rolling in Rough Sea. *Chaos*," *Solitons & Fractals*, **8**(4), 659-680.
- [185] Sharma, S. D., Jiang, T., and Schellin, T. E., 1988, "Dynamic Instability and Chaotic Motions of a Single-point-moored Tanker," *Proceedings 17th Office of Naval Research (ONR) Symposium on Naval Hydrodynamics*.
- [186] Shih, L. Y., 1991, "Analysis of Ice-Induced Vibrations on a Flexible Structure," *Journal of Applied Mathematical Modeling*, **15**, 632-638.
- [187] Sodhi, D. S., 1991, "Ice-Structure Interaction during Indentation Tests," *Proceedings of IUTAM-IAHR Symposium*, Springer-Verlag, Berlin, 619-640.
- [188] Sodhi, D. S, 1994, "A Theoretical Model for Ice-Structure Interaction," *Proceedings of the OMAE-94 Conference* , ASME, New York, **IV**, pp. 29-34.

- [189] Son, K. H. and Nomoto, K., 1982, "On the Coupled Motion of Steering and Rolling of a High Speed Container Ship," *Naval Architect of Ocean Engineering*, **20**, 73-83. From J.S.N.A. Japan.
- [190] Spyrou, K, 2002, "A Basis for Developing a Rational Alternative to the Weather Criterion: Problems and Capabilities," *6th International Ship Stability Workshop Proceedings*, October, 13-16.
- [191] Suleiman, B. M., 2000, "*Identification of Finite-Degree-of-Freedom Models for Ship Motions*," PhD. Thesis, Virginia Polytechnic Institute and State University, Blacksburg, Virginia.
- [192] Sunder, S. S., 1986, "An Integrated Constitutive Theory for the Mechanical Behavior of Sea Ice; Micromechanical Interpretation," *Proceedings of International Conference on Ice Technology*, Cambridge, Mass.
- [193] Surendran, S. and Reddy, V. R., 2002, "Roll dynamics of a Ro-Ro ship," *International Shipbuilding Progress*, **49**(4), 301-320.
- [194] Surendran, S., Lee, S. K., Reddy, J. V., and Lee, G., 2005, "Nonlinear Roll Dynamics of a Ro-Ro Ship in Waves," *Ocean Engineering*, **32**, 1818-1828.
- [195] Surendran, S., Reddy, V. R., 2003, "Numerical Simulation of Ship Stability for Dynamic Environment," *Ocean Engineering*, **30**(10), 1305-1317.
- [196] Tanaka, M., 1957, "A study on the Bilge Keel, Part 1," *Journal of Society of Naval Architecture of Japan*, **101**, 99-105.
- [197] Tanaka, M., 1958, "A study on the Bilge Keel, Part 2," *Journal of Society of Naval Architecture of Japan*, **103**, 343.
- [198] Tanaka, M., 1959, "A study on the Bilge Keel, Part 3," *Journal of Society of*

- Naval Architecture of Japan*, **105**, 27-32.
- [199] Tanaka, M., 1961, "A study on the Bilge Keel, Part 4," *Journal of Society of Naval Architecture of Japan*, **104**, 205-212.
- [200] Tang, Y. G., Gu, J. Y., Zheng, H. Y., and Li, H. X., 2004, "Study on the Ship Capsize in Random Beam Seas using Melnikov Method," (in Chinese) *Chuan Bo Li Xue/Journal of Ship Mechanics*, **8**(5), 27-34.
- [201] Taylan, M., 2000, "The Effect of Nonlinear Damping and Restoring in Ship Rolling," *Ocean Engineering*, **27**, 921-932.
- [202] Taylan, M., 2004, "Effect of Forward Speed on Ship Rolling and Stability," *Mathematical and Computational Applications*, **9**(2), 133-145.
- [203] Thompson, J. M. and McRobie, F. A., 1993, "Intermediate Bifurcations and Global Dynamics of Driven Oscillators," *1st European Nonlinear Oscillations Conference*, Hamburg, eds. E. Kreuzer and G. Schmidt, Akademie-Verlag, Berlin, 107-128.
- [204] Thompson, J. M., 1989a, "Loss of Engineering Integrity Due to the Erosion of Absolute and Transient Basin Boundaries, *Proceedings IUTAM Symposium 'Nonlinear Dynamics in Engineering Systems,'* Stuttgart 21-25 August 1989, W. Schiehlen (editor), Springer, Berlin.
- [205] Thompson, J. M., 1989b, "Chaotic Phenomena Triggering the Escape from a Potential Well," *Proceedings Royal Society London*, **A 421**, 195-225.
- [206] Thompson, J. M., 1997, "Designing Ships against Capsize in Beam Seas: Recent Advances and New Insights," *ASME Applied Mechanics Review*, **50**, 307-324.

- [207] Tick, I. J., 1959, "Differential Equations with Frequency-Dependent Coefficients," *Journal of Ship Research*, **3**(2), 45-46, 1959.
- [208] Timco, G. W., and Jordaan, I. J., 1987, "Time-Series Variations in Ice Crushing," 9th International Conference on Port and Ocean Engineering and Arctic Conditions, Fairbanks, Alaska.
- [209] Timco, G. W., Irani, M. B., Tseng, J., Liu, L. K., and Zheng, C. B., 1992, "Model Tests of Dynamic Ice Loading on the Chinese JZ-20-2 Jacket Platform," *Canadian Journal of Civil Engineering*, **19**, 619-627.
- [210] Troesch, A. W., Karr, D. G., and Beier, K. P., 1992, "Global Contact Dynamics of an Ice-structure Interaction Model," *International Journal of Bifurcation and Chaos in Applied Science and Engineering* **2**(3), 607-620.
- [211] Tsuchiya, M., Kanie, S., Ikejiri, K., Yoshida, A., and Saeki, H., 1985, "An Experimental Study on Ice-Structure Interaction," *Proceedings of the 17th Offshore Technology Conference*, Huston, TX, **IV**, 321-327.
- [212] Valsgard, S., and Jorgensen, L., 1983, "Evaluation of Ship/Ship Damage Using Simplified Nonlinear Finite Element Procedure," *International Symposium on Practical Design in Shipbuilding PRADS*, Tokyo.
- [213] Vershinin, J., and Iliady, A., 1990, "A New Approach to Dynamic Ice-Flexible Structure Interaction," IAHR 10th Ice Symposium, **III**, Helsinki University of Technology, 73-80.
- [214] Vinogradov, O. C., 1986, "Simulations Methodology of Vessel-Ice Floes Interaction Problems," *Proceedings of the International Symposium on Offshore Mechanics and Arctic Engineering (OMAE)* **4**, 601-606, Tokyo.

- [215] Vugts, J. H., 1971, "The Hydrodynamic Forces and Ship Motions on Oblique Waves," Netherlands Ship Research Center, Report No. 150 S.
- [216] Witz, J. A., Ablett, C. B. and Harrison, J. H., 1989, "Roll Response of Semi-submersibles with Nonlinear Restoring Moment Characteristics," *Applied Ocean Research*, **11**, 153–166.
- [217] Wu, X., Tao, L., and Li, Y., 2005, "Nonlinear Roll Damping of Ship Motions in Waves," *ASME Journal of Offshore Mechanics and Arctic Engineering*, **127**, 205-211.
- [218] Xu, J., and Wang, L., 1986, "The Ice Force Oscillation Model for Dynamic Ice-Structure Interaction Analysis," *Proceedings of 1st ICETECH Conference*, Cambridge, Springer-Verlag, 391-397.
- [219] Yim, S. C., Nakhata, T., Bartel, W. A., and Huang, E.T., 2004a, "Coupled Nonlinear Barge Motions: Part I: Deterministic models development, identification and calibration," *Proceedings of the ASME 23rd International Conference on Offshore Mechanics and Arctic Engineering - OMAE, 1A: Offshore Technology*, Vancouver, BC, Canada, 281-291.
- [220] Yim, S. C., Nakhata, T., and Huang, E. T., (2004b), "Coupled Nonlinear Barge Motions: Part II: Deterministic Models Stochastic Models and Stability Analysis," *Proceedings of the 23rd International Conference on Offshore Mechanics and Arctic Engineering - OMAE, 1A: Offshore Technology*, Vancouver, Canada, 293-302.
- [221] Yue, Q., and Bi, X., 1998, "Full-Scale Tests and Analysis of Dynamic Interaction between Ice Sheet and Conical structures," *Proceedings of 14th*

International Association for Hydraulic Research Symposium on Ice.

[222] Yue, Q., and Bi, X., 2000, "Ice Induced Jacket Structure Vibration in Bohai Sea," *Journal of Cold Regions Engineering*, **14**, 81-92.

[223] Zhuravlev, V. P., 1976, "Investigation of Certain Vibro-impact Systems by the Method of Non-smooth Transformations," *Izvestiya AN SSSR Mehanika Tverdogo Tela (Mechanics of Solids)* **12**, 24-28.

[224] Zou, B., 1996, "*Ships in Ice: The Interaction Process and Principles of Design*," PhD Thesis, Memorial University of Newfoundland, Canada.

<http://www.tc.gc.ca/marinesafety/CES/Arctic/IMO-guidelines.pdf>.

<http://www.uscg.mil/hq/g-m/MSE4/stdimofp46-6.pdf>,

<http://www.marineengineering.org.uk/navarch/navstability.htm>

<http://www.purgit.com/shippart.html>

http://www.worldwideflood.com/ark/terms/ship_terms.htm

http://en.wikipedia.org/wiki/Bergy_bit

<http://www.uscg.mil/LANTAREA/IIP>

ABSTRACT**ANALYTICAL AND EXPERIMENTAL INVESTIGATIONS
OF SHIPS IMPACT INTERACTION WITH
ONE-SIDED BARRIER**

by

IHAB MAMDOUH FOUAD GRACE

May 2012

Advisor: Dr. Raouf A. Ibrahim**Major:** Mechanical Engineering**Degree:** Doctor of Philosophy

This study deals with impact interaction of ships with one-sided ice barrier during roll dynamics. An analytical model of ship roll motion interacting with ice is developed based on Zhuravlev and Ivanov non-smooth coordinate transformations. These transformations have the advantage of converting the vibro-impact oscillator into an oscillator without barriers such that the corresponding equation of motion does not contain any impact term. Such approaches, however, account for the energy loss at impact times in different ways. The present work, in particular, brings to the attention the fact that the impact dynamics may have qualitatively different response characteristics to different dissipation models. The difference between localized and distributed equivalent damping approaches is discussed. Extensive numerical simulations are carried out for all initial conditions covered by the ship grazing orbit for different values of excitation amplitude and frequency of external wave roll moment. The basins of attraction of safe operation are obtained and reveal the coexistence of different response regimes such as nonimpact periodic

oscillations, modulation impact motion, period added impact oscillations, chaotic impact motion and rollover dynamics.

An experimental investigation conducted on a small ship model. In particular, the experimental tests reveal complex dynamic response on multi-frequency wave motion caused by the wave reflection from the tank walls. Measured results showed a good agreement with the predicted results for small angles of the barrier relative to the ship unbiased position. However, deviation becomes significant as the angle increases. This deviation is mainly attributed to the uncertainty of the coefficient of restitution, which is found to depend on the velocity of impact in addition to the geometry and material properties of the model and barrier.

AUTOBIOGRAPHICAL STATEMENT

IHAB MAMDOUH FOUAD GRACE

Ihab M. F. Grace was born in Cairo, capital of Egypt. At the age of 6, he joined Patriarchal College (Freres) where he completed his primary, and middle School. Then, he joined St. George's College where he completed his high school. In both Colleges, he joined the scout where he learned many things as serving the community, and how to be self dependent. His father, as a Mechanical Engineer gave him the passion for Mechanical Engineering. Because of that, in 1990 he was admitted to the Mechanical Engineering Department at Helwan University. In 1995 he graduated with bachelor degree. After graduation he worked for Petroleum Company for two years. In 1997, he was admitted to Helwan University where he worked as Teaching Assistant, and completed a MS program in Mechanical Engineering. In 2006, he was admitted to Wayne State University where he fulfilled the requirements for a Ph.D. program. The author currently lives in Warren, Michigan, with his wife Amy, and his daughter Hannah. Among his hobbies include reading, swimming, listening to classical music, and theatrical art.

Selected Publications

1. Grace, I. M., Ibrahim, R. A., and Pilipchuk, V. N., 2011, "Inelastic Impact Dynamics of Ships with One-Sided Barriers; Part I: Analytical and Numerical Investigations," *Nonlinear Dynamics*, **66**, 589-607.
2. Grace, I. M., Ibrahim, R. A., and Pilipchuk, V. N., 2011, "Inelastic Impact Dynamics of Ships with One-Sided Barriers; Part II: Experimental Validation," *Nonlinear Dynamics*, **66**, 609-623.